THE NATURE OF THE OLIVINE → SPINEL TRANSITION IN THE Mg_2SiO_4-Fe_2SiO_4 SYSTEM AND ITS GEOPHYSICAL IMPLICATIONS

by

CHIEN-MIN SUNG

B.S., National Taiwan University
1972

SUBMITTED IN PARTIAL FULFILLMENT
OF THE REQUIREMENTS FOR THE
DEGREE OF DOCTOR OF
PHILOSOPHY

at the

MASSACHUSETTS INSTITUTE OF
TECHNOLOGY

June, 1976

Signature of Author_____
Department of Earth and Planetary Sciences, April, 30, 1976

Certified by_____
Thesis Supervisor

Accepted by_____
Chairman, Departmental Committee on Graduate Students

THE NATURE OF THE OLIVINE→SPINEL TRANSITION IN THE Mg_2SiO_4-Fe_2SiO_4 SYSTEM AND ITS GEOPHYSICAL IMPLICATIONS

by

CHIEN-MIN SUNG

SUBMITTED IN PARTIAL FULFILLMENT OF THE REQUIREMENTS FOR THE DEGREE OF DOCTOR OF PHILOSOPHY

ABSTRACT

Olivine is a relatively loose structure. At low pressure it is stable because unshared octahedral edges may extend far enough to reduce the repulsion force between cations in edge-sharing octahedra and tetrahedra. At high pressure the large volume in olivine makes it unfavorable, so the more compact spinel structure becomes stable. Because the octahedral site in spinel is smaller than in olivine, the crystal field stabilization free energy for Fe^{2+} ions in spinel is larger than in olivine. Consequently, the pressure for the olivine→spinel transition in Fe_2SiO_4 may be lowered by the crystal field stabilization.

The rate of the olivine→spinel transition in the Mg_2SiO_4-Fe_2SiO_4 system with $Mg/(Mg+Fe)<0.4$ has been measured by using a modified diamond anvil press with external heating. The experiments were performed at pressures well above equilibrium under isothermal and isobaric conditions. The kinetics of the olivine→spinel transition are consistent with a model of nucleation and growth. For powdered samples nucleation on grain surfaces is very fast so that grain surfaces are exhausted at an early stage of transition. Most of the transition is then due to the growth of existing nuclei. The rate of the olivine→spinel transition is therefore controlled by the growth rate of the spinel, which was found to increase exponentially with increasing temperature. The growth rate is insensitive to pressure change beyond a certain overpressure. This may imply that the activation energy of growth (Q_a) for spinel is nearly constant and the activation volume for the olivine→spinel transition is negligible. Measured Q_a increases almost linearly with the Mg/(Mg+Fe) ratio. For olivine of the possible mantle composition, the extrapolated value of Q_a is approximately 80 Kcal/mole. Because high shear stress peculiar to the diamond anvil press used in this study might reduce Q_a by changing the growth mechanism of spinel, the above value of Q_a may be a lower bound for the olivine→spinel transition in the mantle. Based on this value of Q_a and a reasonable estimate of grain sizes of olivine in the mantle, it is concluded that the olivine→spinel transition in downgoing slabs may not occur below a temperature of 500 to 600°C.

Since the temperature within a downgoing slab varies greatly according to different models of calculation, it is not clear at this stage whether the temperature is low enough to suppress the olivine→spinel transition. If the olvine→spinel transition can not be suppressed, it may not be responsible for the genesis of deep-focus earthquakes. However, the rise of the olivine-spinel boundary across the cold interior of downgoing slabs provides an additional driving force for the plunging of these slabs. The distortion of the olivine-spinel boundary may also control the stress distribution in downgoing slabs and may be responsible for the observed alignment of principal stress axes of deep-focus earthquakes.

THESIS ADVISOR: ROGER G. BURNS
PROFESSOR OF MINERALOGY AND GEOCHEMISTRY

TABLE OF CONTENTS

INDEX OF FIGURES

INDEX OF TABLES

ACKNOWLEDGMENTS

I am greatly indebted to Professor Roger G. Burns for his assistance, guidance and advice concerning my education and this thesis, as well as my personal affairs. I wish to express my gratitude to Professors F. A. Frey and J. S. Dickey for their advice on my first year graduate studies. I thank Professor W. A. Bassett for introducing me to the technique of diamind anvil press and for allowing me to use his facilities. I also thank Drs. L. C. ming and H. K. Mao for the teaching and assistance during my stay at the University of Rochester and Geophysical Laboratory, respectively.

I have benefitted from discussions with Drs. J. W. Cahn, K. C. Russel, C. Goetze, A. Parkes, P. Molnar, S. R. Hart P, M. Hurley, R. G. J. Strens, R. M. Abu-Eid, M. S. Paterson, K. Aki, Messrs M. Obata, W. P. Chen, Mrs. V. M. Burns, and others. I also greatly appreciate the following assistance: Mr. E. B. Watson, Drs. R. G. Burns and H. K. Mao have provided samples forstudy; Mr. B. M. Loeffler, Ms. C. Montgomery and K. Parkin have reviewed the manuscript; and Ms. R. Gegan has typed the thesis.

Special thanks are due to my wife for her encouragement and patience.

Chapter 1

INTRODUCTION

1-1: The 400 km Discontinuity:

Olivine of composition approximately Fo_{90} has been widely accepted as the dominant mineral in the upper mantle (O'Hara, 1970; Ringwood, 1970). The abundance of olivine in the upper mantle has been estimated to be about 60-70 wt.%. Major phase transformations in olivine will then have drastic effects on the properties of the mantle.

Goldschmidt (1931) demonstrated that Mg_2GeO_4 olivine could transform into a denser phase of the spinel structure. By analogy, Bernal (1936) predicted that olivine in the mantle might also transform into the spinel structure at high pressure. He further suggested that this olivine→spinel transition might result in the rapid rise of density in the mantle. Jeffreys (1937) suspected that the olivine→spinel transition might be responsible for a rapid increase of the compressional wave velocity in the upper transition zone. This rapid increase of P-wave velocity could explain the observed curvature in the travel-time curve associated with the so-called "20° discontinuity". Birch (1939, 1952) demonstrated that the density and seismic discontinuities in the transition zone could be due to major phase transformations of silicate minerals instead of compositional changes. Later studies (Anderson, 1967; Johnson, 1967; Kanamori, 1967; Archambeau et al., 1969; Whitcomb and Anderson, 1970; Helmberger and Wiggins, 1971) revealed that

there are two major seismic discontinuities located at depths of 400 km and 650 km (Figure 1-1). These two discontinuities could extend universally under normal tectonic provinces (oceanic and continental). The large rise of seismic velocities (about 1 km/sec for V_p) for the two discontinuities indicated that major minerals in the transition zone were involved in intensive transformations. As olivine is the most abundant mineral in the upper mantle, its transformations into denser modifications could be responsible for the two discontinuities in the transition zone, provided the transformations are intensive (large increase of density) and the P-T conditions at which they occur can be correlated with the depths of the discontinuities.

1-2: Phase Diagram in the Mg_2SiO_4-Fe_2SiO_4 System:

The first olivine→spinel transition was demonstrated by Ringwood (1958) in Fe_2SiO_4. The same transition has been repeated by other investigators, using different high pressure equipment (Wentorf, 1959; Dachille and Roy, 1960; Boyd and England, 1960; Bradley et al., 1963). Detailed experimental studies of the olivine-spinel phase boundary in Fe_2SiO_4 using tetrahedral anvil press were carried out by Akimoto et al. (1965, 1967). The phase boundary determined was later revised by Mao et al. (1969), using a more precise pressure calibration scale. The olivine→spinel transition for the whole range of compositions in the system Mg_2SiO_4-Fe_2SiO_4 was reported by Ringwood and Major (1966). They found that both olivine (the

Fig. (1-1)

Seismic velocity profiles across the mantle(After Akimoto et al, 1976). Curves designated by K, AFL and HW represent the models proposed by Kanamori(1967) for the Japanese Islands, by Archambeau, Flinn and Lambert (1966) for the Western continental United States, and by Helmberger and Wiggins(1971) for the Midwestern United States, respectively. Note the sharp increase of P wave velicity at 400 and 650 Km depth.

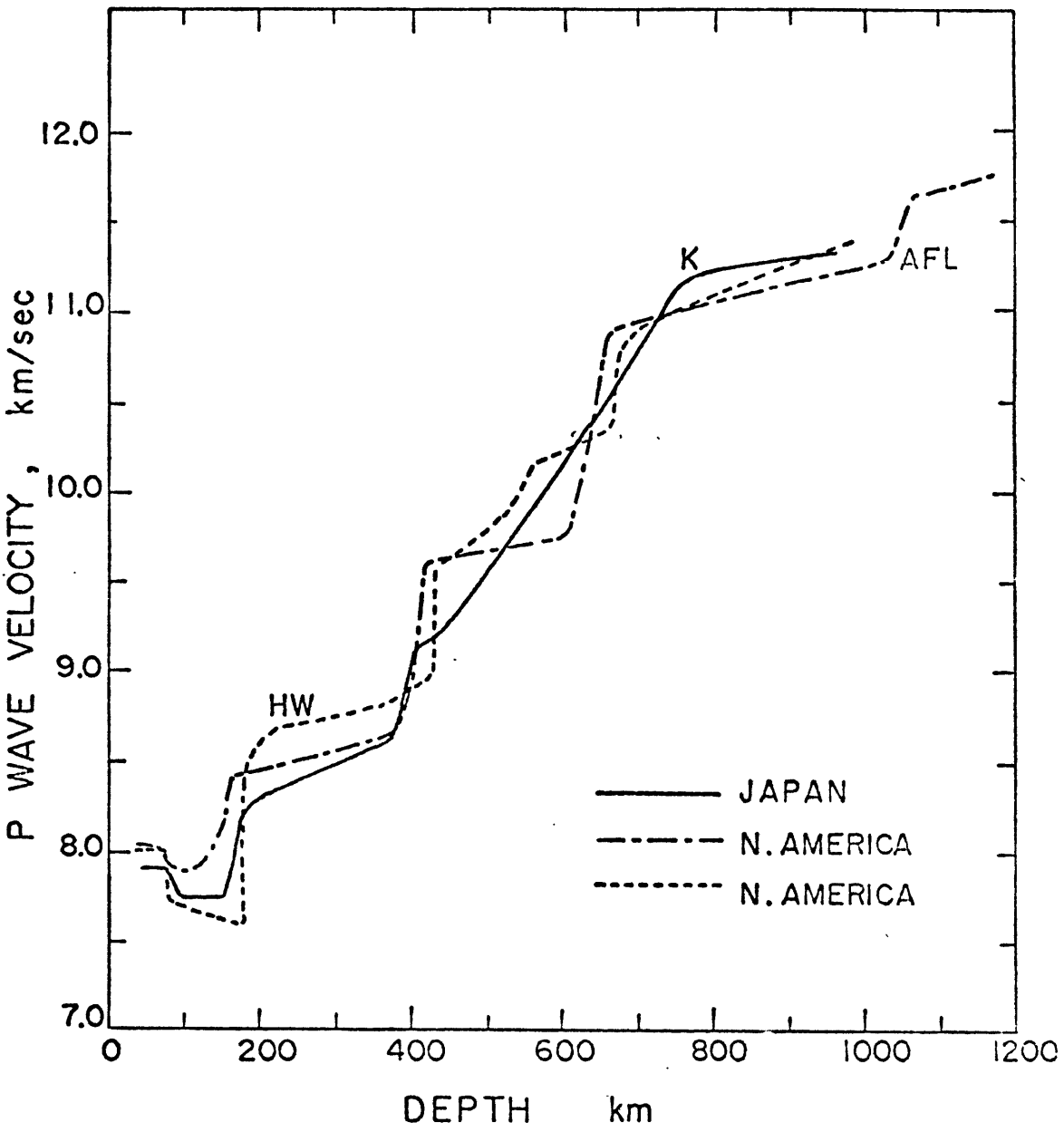
12.0
11.0
10.0
9.0
8.0
7.0
P WAVE VELOCITY, km/sec
0
200
400
600
800
1000
1200
DEPTH km
K
AFL
HW
JAPAN
N. AMERICA
N. AMERICA

α-phase) and spinel (the γ-phase) form continuous solid solutions showing close to ideal behavior, as evidenced by almost linear relationship between their lattice parameters and composition. However, they noticed that extra x-ray diffraction lines existed in the pattern of synthesized 'spinels' with Mg/(Mg+Fe) ratios greater than 0.85. They attributed this to the distortion of spinel during quenching from high pressure and temperature. Akimoto and Ida (1966) claimed the success in synthesizing Mg_2SiO_4 'spinel', using the revised Drickamer's high pressure cell. They also noticed the presence of extra lines in their 'spinel'. Detailed studies of the olivine→ spinel transition for Mg/(Mg+Fe) ratios less than 0.8 using the tetrahedral anvil press, have been reported by Akimoto and Fujisawa (1966, 1968). They confirmed that the spinel solid solution was continuous and behaved like an ideal solution. Ringwood and Major (1970) first presented a complete isothermal section of the system Mg_2SiO_4-Fe_2SiO_4 at 1000°C. They used the Bridgman anvil press as the high pressure apparatus. The phase diagram is characterized by the emergence of an orthorhombic solid solution (the β-phase) at high pressure for the Mg/(Mg+Fe) ratio greater than 0.8. They demonstrated that all the previously claimed Mg_2SiO_4 'spinels' were actually the β-phase. The existence of the stability of the β-phase in Mg-rich compositions was also reported by Kawai et al. (1970) and Ito et al. (1971) in their studies, using an octahedral anvil split-sphere press, of the high pressure transformation of a natural olivine of composition Fo_{93}. The dependence of

isothermal sections of the system Mg_2SiO_4-Fe_2SiO_4 on temperature was studied by Akimoto (1972), using a revised Bridgman anvil press. He observed a remarkable expansion of the stability field of the β-phase with temperature. The high pressure part of the isothermal section at 1000°C was completed by Suito (1972) who finally succeeded in synthesizing a true Mg_2SiO_4 spinel by using a double-stage split-sphere press. The syntheses of Mg_2SiO_4 spinels were also reported by Ito et al. (1974) and Mizukami et al. (1975), using the same type of press. Typical isothermal sections of the system Mg_2SiO_4-Fe_2SiO_4 at different temperatures are shown in Figure (1-2).

Although the phase boundary of the olivine→spinel transition in Fe_2SiO_4 can be accurately determined, the phase boundaries among the three phases, α, β, and γ, in Mg_2SiO_4 are not well known. This is because the transitions in Mg_2SiO_4 occur at higher pressure where the accuracy of the pressure measurement is low. In addition, the transitions in Mg_2SiO_4 are much more sluggish than in Fe_2SiO_4. The hysteresis of transition in Mg_2SiO_4 is very large even when fine powders, and mineralizers such as water or $Mg(OH)_2$, are used to facilitate the reaction. As a consequence, wide discrepancies exist among determinations of the relative stabilities of the three phases, α, β, and γ, in Mg_2SiO_4. However, all experimental data indicated that all the three phase boundaries have positive P-T slopes. Table (1-1) summarizes the available experimental results on phase boundaries among the three phases in Fe_2SiO_4 and Mg_2SiO_4.

Fig. (1-2)

Typical isothermal sections of the system Mg_2SiO_4-Fe_2SiO_4 (after Akimoto et al, 1976). Note the emergence of the β-phase stability field at the high magnesium composition, and the expansion of this stability field with increasing temperature. Dotted lines are compositions of olivine and its high pressure dérivatives. The increase of iron content in the high pressure phases is due to the preferential partitioning of iron between them and garnet.

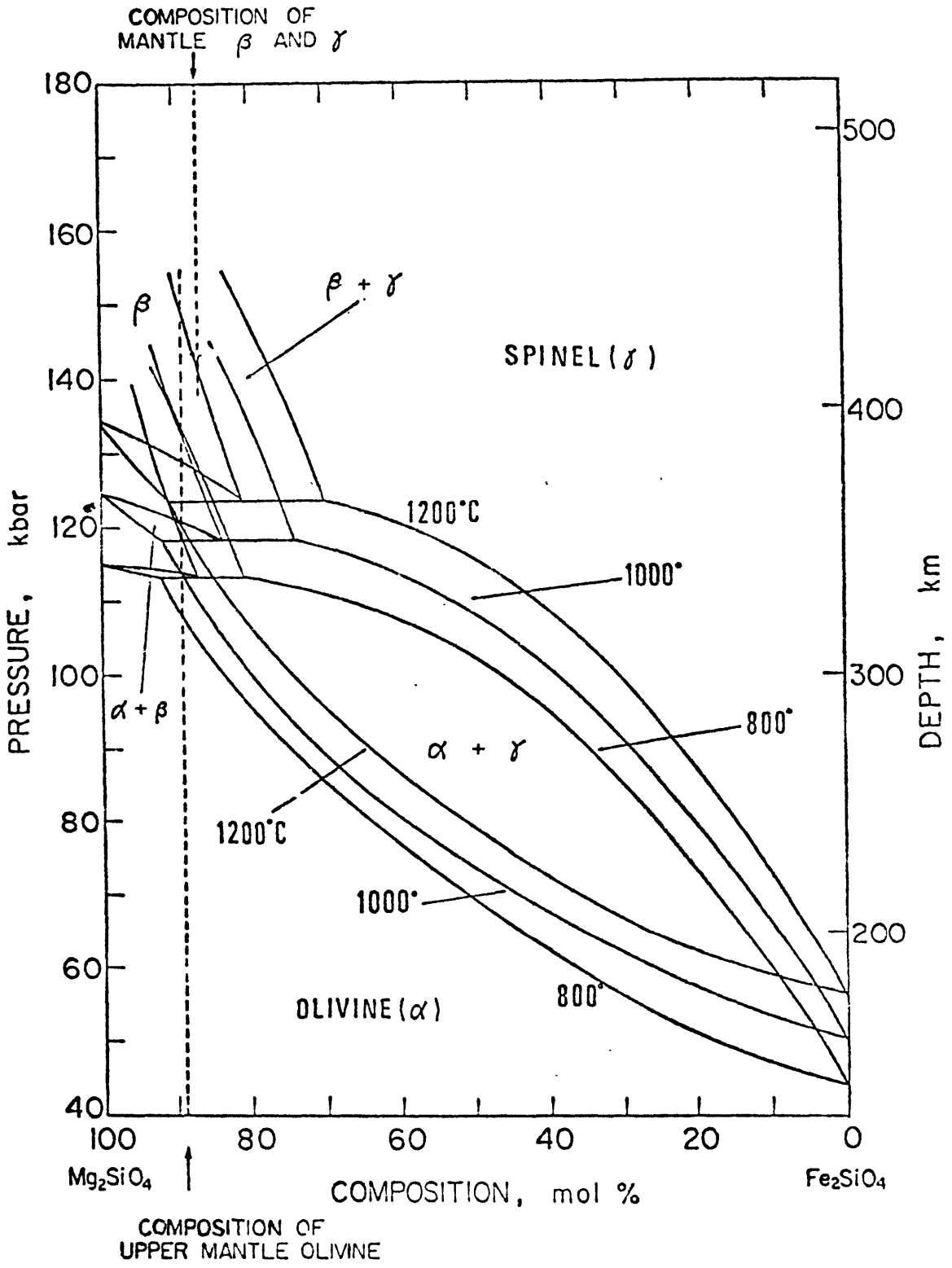
COMPOSITION OF
MANTLE β AND γ
180
160
140
120
100
80
60
40
PRESSURE, kbar
500
400
300
200
DEPTH, km
β
β + γ
SPINEL (γ)
1200°C
1000°
800°
α + β
α + γ
1200°C
1000°
800°
OLIVINE (α)
100
80
60
40
20
0
Mg2SiO4
Fe2SiO4
COMPOSITION, mol %
COMPOSITION OF
UPPER MANTLE OLIVINE

Table (1-1)

DEGENERATED UNIVARIANT PHASE BOUNDARIES AND THE THREE PHASE(α , β , γ) UNIVARIANT LINE IN THE Mg_2SiO_4-Fe_2SiO_4 SYSTEM.

Mg_2SiO_4			Fe_2SiO_4
α-β	β-γ	α-γ	α-γ
$P=2+0.13T'$ [a]	$P=390-0.227T'$ [b]	$P=87+0.048T'$ [b]	$P=21+0.028T'$ [e]
$P=77+0.048T'$ [b]	$P=138+0.047T'$ [b]	$P=78+0.062T'$ [d]	$P=25.5+0.026T'$ [f]
$P=78+0.040T'$ [c]	$P=31+0.144T'$ [c]	$P=95+0.030T'$ [e]	
		$P=72+0.053T'$ [c]	

Three phase(α , β , γ) univariant line: $P=81+0.033T'$ [c]

Unit: P(Kb), T'(^{o}C)

References: a) Suito, 1972
b) Ming, 1974
c) Sung, this work, based on the selected data of Table(1-2), also shown in Fig. (1-3)
d) Akimoto and Fujisawa, 1968
e) Ringwood and Major, 1970
f) Mao et al, 1969

At even higher pressures and temperatures, olivine and spinel phases in the Mg_2SiO_4-Fe_2SiO_4 system have been shown to decompose into magnesiowüstite solid solution and stishovite (Kumazawa et al., 1974; Ming and Bassett, 1975). The phase boundaries for this decomposition were shown to have negative P-T slopes. However, Jackson et al. (1974) have proposed that the entropy of spinel will substantially increase at high temperature due to the disordering of Mg, Fe, and Si atoms. If this effect is taken into account, the slopes of decomposition of spinel may be less negative or even positive.

Carefully selected data for high pressure transformations available in the Mg_2SiO_4-Fe_2SiO_4 system are listed in Table (1-2). These data were selected in such a way that, for each particular temperature, the transformation pressure is the minimum value for the reaction going in the forward direction, low pressure phase→high pressure phase. Conversely, the maximum pressure value is chosen for the reaction going in the reverse direction. These data usually correspond to experimental runs with the longest duration and the least degree of transformation at each temperature. The purpose of selecting data in this way is to minimize the effect of the hysteresis of the transformation. The equilibrium phase boundary should lie between the data points of forward and reverse reactions. In the case of transformations that occur at higher pressure in Mg_2SiO_4, the experimental data for the reverse reaction are not available. The phase boundary should lie on the low pressure side of the data points for the forward reaction. The

Table (1-2)

SELECTED DATA TO CONSTRUCT THE PHASE DIAGRAM OF THE SYSTEM Mg_2SiO_4-Fe_2SiO_4 SHOWN IN FIG. (1-3)

P(Kb)	T'(^{o}C)	t(min.)	Composition	Reaction	Method	Ref.
42.7±0.5	755±10	120	Fe_2SiO_4	α→α+γ(small amount)	Exp.	a
47.2±0.5	870±10	45	"	α→α+γ(80%)	"	"
44.3±0.5	885±10	26	"	γ→α	"	b
49.3±0.5	1025±15	30	"	α→γ	"	a
49.3±0.5	1145±10	15	"	γ→α	"	"
54.2±0.5	1170±10	10	"	α→α+γ(60%)	"	"
57±1	1300±5	10	"	α→α+γ(30%)	"	"
55.8±0.5	1320±5	10	"	γ→α	"	"
58.3±0.5	1340±5	10	"	α→α+γ(80%)	"	"
54.2±0.5	1355±5	10	"	γ→α	"	"
57.5±0.5	1485±5	5	"	α→α+γ(80%)	"	"
0.001	1205±5	-	"	α→α+ℓ	"	"
17.0±0.5	1315±5	5	"	α→α+ℓ(50%)	"	"
30.0±0.5	1415±10	5	"	α→α+ℓ(40%)	"	"
43.5±0.5	1455±5	5	"	α→α+ℓ(30%)	"	"
54.2±0.5	1505±10	5	"	α→α+ℓ(80%)	"	"
61.2±0.5	1575±5	4	"	α→γ(small amount)+ℓ	"	"
64.0±0.5	1615±10	4	"	α→γ+ℓ(rare)	"	"
69.0±0.5	1710±10	3	"	α→γ+ℓ(60%?)	"	"
158±5	1600±100	-	"	α→w+s	"	c
100±15	530	-	Mg_2SiO_4	α→α+γ	Ext.	d
125±13	1000±200	-	"	α→α+γ	"	"
110±11	800±20	60	"	α→α+β	Exp.	e
118±12	1000	3-5	"	α→β	"	f
175	1000	-	"	α→β+γ	Ext.	g

Table (1-2)
(CONTINUED)

P(Kb)	T'(^{o}C)	t(min.)	Composition	Reaction	Method	Ref.
0.001	1890±20	-	Mg_2SiO_4	$\alpha \rightarrow \alpha + \ell$	Exp.	h
5.5	1930	1	"	$\alpha \rightarrow \ell$	"	i
12.5	1975	1	"	$\alpha \rightarrow \ell$	"	"
18	1980	2	"	$\alpha \rightarrow \alpha(33\%) + \ell$	"	"
25	2030	2	"	$\alpha \rightarrow \alpha(50\%) + \ell$	"	"
30.5	2030	1	"	$\alpha \rightarrow \alpha(33\%) + \ell$	"	"
39.5	2105	1	"	$\alpha \rightarrow \ell$	"	"
330	1000	30	"	$\alpha \rightarrow w + s$	"	j
114±12	1000±200	3-5	$(Mg_{0.9}Fe_{0.1})_2SiO_4$	$\alpha \rightarrow \alpha + \beta + \gamma$	"	f
134	1600	-	"	$\alpha \rightarrow \alpha + \beta + \gamma$	Est.	f

References:

a) Akimoto et al(1967)
b) Akimoto et al(1965)
c) Ming and Bassett(1975)
d) Ringwood and Major(1966)
e) Suito(1972)
f) Ringwood and Major(1970)
g) Akimoto(1972)
h) Bowen and Anderson(1914)
i) Davis and England(1964)
j) Kumazawa et al(1974)

Note:

(1) The pressure calibration for Akimoto et al(1965, 1967) was based on II-III transition in Tl at 36.7 Kn, and II-IV transition in Ba at 59 Kb. The pressure for the latter transition has been revised to 55 Kb(see Mao et al(1969). Pressure between 36.7 to 55 Kb in

Table (1-2)
(CONTINUED)

their works have been recalculated by P'=36.7+(P-36.7)x((55-36.7)/(59-36.7)), where P' and P are pressures listed in this table and reported in Akimoto et al(1965, 1967), respectively.

(2) Slopes of the phase boundary $\gamma \rightarrow w+s$ shown in Fig. (1-3) are tentatively assumed to be: -0.022 Kb/^{o}C for Fe_2SiO_4(Ming and Bassett, 1975); and -0.013 Kb/^{o}C for Mg_2SiO_4(Ahrens and Syono, 1967). These slopes may be less negative or even positive due to the possible increase of entropy in spinel at high temperature(Jackson et al, 1974).

(3) Symbols in this table are:
α=olivine
β=modified spinel
γ=spinel
s=stishivite
w=wüstite or magnesiowüstite
ℓ=liquid
Exp.=Experimental
Ext.=Extrapolated from the iron rich compositions in a pressure-composition phase diagram
Est.=Estimated

selected data in Table (1-2) are self-consistent. Extrapolation of phase boundaries based on these data to the P-T conditions corresponding to depths of 400 km (130 kb and 1600°C) and 650 km (240 kb and 1800°C) has revealed that the two major phase boundaries in mantle olivine of composition $(Mg_{0.9}Fe_{0.1})_2SiO_4$ may coincide with the two major seismic discontinuities in the transition zone. The eutectoid reaction, $\alpha \rightarrow \alpha+\gamma \rightarrow \alpha+\beta \rightarrow \beta$, may be responsible for the discontinuity at 400 km depth, and the peritectoid reaction, $\gamma \rightarrow \gamma+w+s \rightarrow \beta+w+s \rightarrow w+s$, where w and s denote magnesiowüstite solid solution and stishovite, respectively, may be responsible for the discontinuity at 650 km depth. These two reactions could be intensive enough to cause the observed seismic discontinuities in the transition zone. Based on the data of Table (1-2), and the above assumptions that the two seismic discontinuities are due to the transformations of olivine and its high pressure modifications, the P-T phase diagram of the system Mg_2SiO_4-Fe_2SiO_4 is proposed as shown in Figure (1-3). The high P-T region of this diagram is purely speculative, and is subject to revision as new data becomes available.

1-3: High Pressre Transformations of Olivine in the Mantle:

Superimposed on Figure (1-3) are a range of geotherms (between X and Y) under normal tectonic provinces (Ahrens, 1972), and a possible geotherm for the cold interior of a downgoing slab, corresponding to constant shear stress on the slip zone (Turcotte and Schubert, 1973). The polythermal and poly-

Fig. (1-3)

Proposed phase diagram for the pseudo-binary system Mg_2SiO_4-Fe_2SiO_4. Plotted data and symbols for the phases are shown in Table (1-2). Fine and coarse lines are univariant lines for one component systems(Mg_2SiO_4 or Fe_2SiO_4), and for two(Mg_2SiO_4-Fe_2SiO_4, MgO-SiO_2, or FeO-SiO_2) or three (MgO-FeO-SiO_2) component systems, respectively. AB($\alpha + \beta + \gamma$) and CD($\beta + \gamma$ + w+s) are univariant lines responsible for 400 Km and 650 Km discontinuities, respectively. X and Y are the range of geotherms under continental and oceanic plates (Ahrens, 1972). Z is the geotherm of the coldest part of a rapid-plunging downgoing slab(Turcotte and Schubert, 1973).

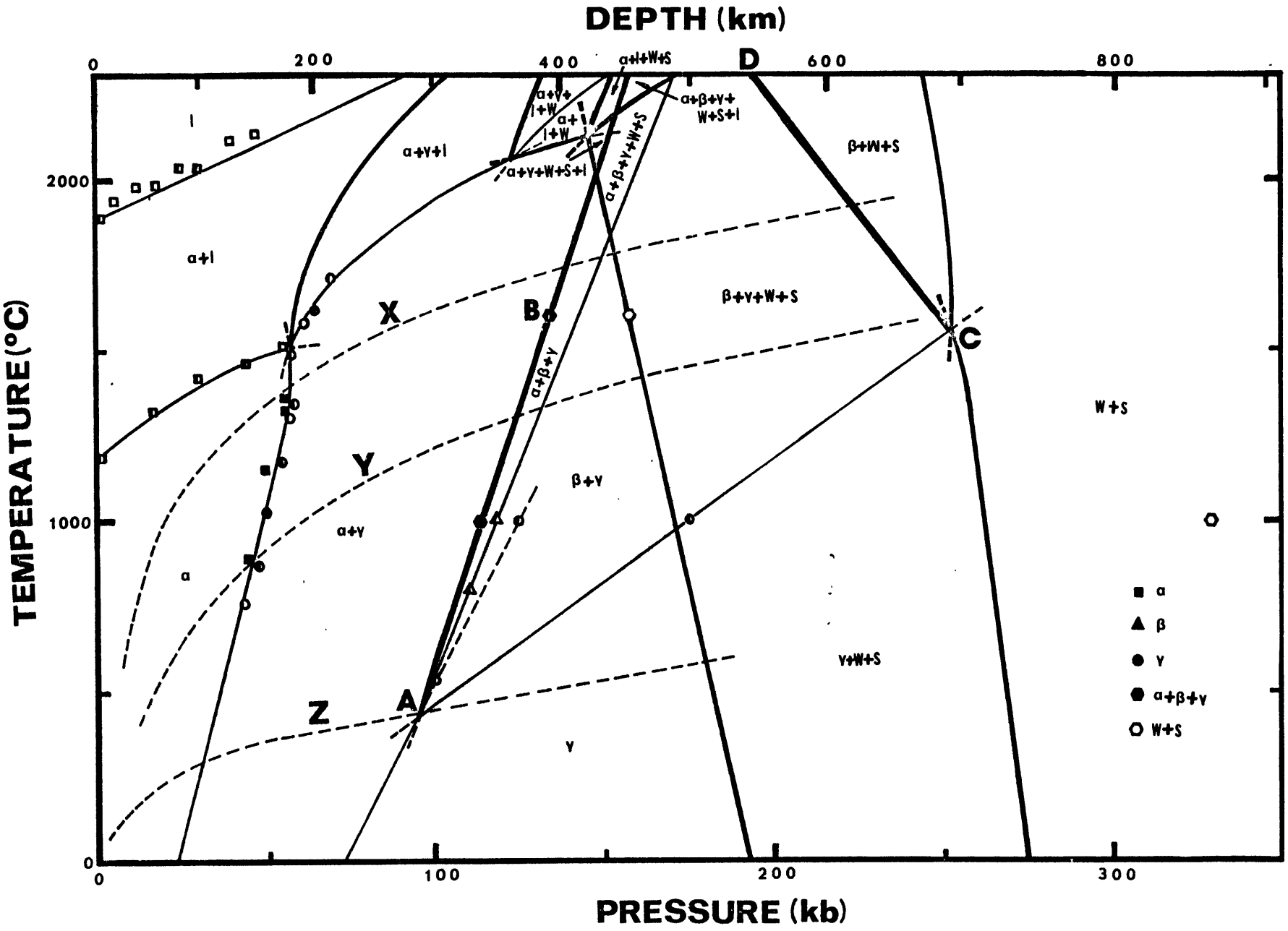
DEPTH (km)
0
200
400
600
800
D
α+I+W+S
α+γ+I+W
α+I+W
α+β+γ+W+S+I
α+γ+I
α+γ+W+S+I
α+β+γ+W+S
β+W+S
2000
α+I
X
B
β+γ+W+S
C
α+β+γ
W+S
Y
β+γ
1000
α+γ
α
Z
A
γ+W+S
γ
α
β
γ
α+β+γ
W+S
TEMPERATURE(°C)
0
100
200
300
PRESSURE (kb)

baric sections of the phase diagram along the two distinct types of geotherms are shown in Figure (1-4). Dashed lines in Figure (1-4) are the possible compositions of olivine and its high pressure modifications in the mantle. The increase of iron content in the high pressure modifications of olivine co-existing with garnet has been proposed by Akimoto et al. (1975). It is interesting to note that a series of reactions may occur under normal tectonic provinces. They are: $\alpha \rightarrow \alpha+\gamma \rightarrow \alpha+\beta \rightarrow \beta \rightarrow \beta+\gamma \rightarrow \gamma \rightarrow \gamma+w+s \rightarrow \beta+w+s \rightarrow w+s$. Whereas the first three reactions may be responsible for the 400 km discontinuity, the next two reactions are less intensive and may be responsible for the second order seismic discontinuity occasionally observed at about 550 km depth (Figure 1-1). The last four reactions may be responsible for the 650 km discontinuity. On the other hand, the reactions taking place in the cold interior of a downgoing slab could be much simpler: $\alpha \rightarrow \alpha+\gamma \rightarrow \gamma \rightarrow \gamma+w+s \rightarrow w+s$ (Figure 1-3b). The first two reactions may occur at depths shallower than 400 km depth, and the last two reactions may occur deeper than 650 km. The reactions in the cold interior of the downgoing slab may not involve the β-phase, since the stability field of the β-phase may wedge out at low temperature (Figure 1-3). It should be noted that the major phase in the transition zone could be the β-phase under normal tectonic provinces, but could be spinel in the cold interior of the downgoing slab. The reactions and the mineralogy in the cold interior of the downgoing slab may gradually

Fig. (1-4)

Polythermal and polybaric sections through the phase diagrams shown in Fig. (1-3). (A) Along geotherms under oceanic or continental plate(between X and Y in Fig. 1-3), and (B) along the cold interior of a rapid-plunging downgoing slab(along Z in Fig. 1-3). MN and PQ in (A) are traces of univariant lines AB and CD in Fig. (1-3), respectively. The composition of magnesiowüstite is projected from the silica end member in the ternary system MgO-FeO-SiO_2. Dotted lines are the proposed compositions for the system Mg_2SiO_4-Fe_2SiO_4 in the mantle with Mg/(Mg+Fe) atomic ratio of 0.89 in olivine and 0.87 in β-phase or spinel (Akimoto et al, 1976). Note that the 400 Km discontinuity is caused by the $\alpha \rightarrow \beta$ transition under oceanic and continental plates. The corresponding transition in the cold interior of a rapid-plunging downgoing slab is the $\alpha \rightarrow \gamma$ transition.

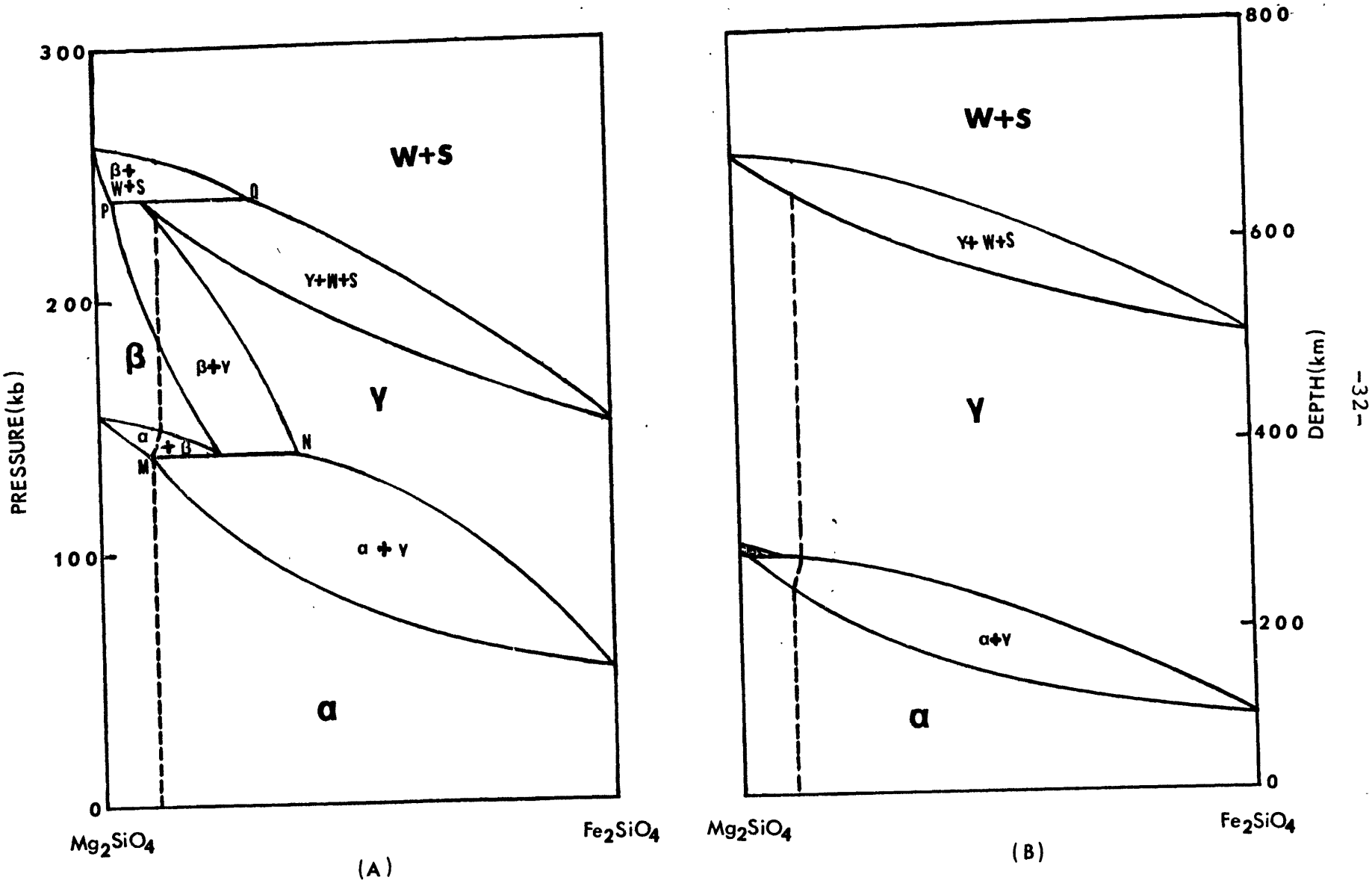
300
200
100
0
PRESSURE(kb)
W+S
β+
W+S
Q
P
Y+W+S
β
β+γ
γ
α
+ β
N
M
α + γ
α
Mg_2SiO_4
Fe_2SiO_4
(A)
800
600
400
200
0
DEPTH(km)
W+S
Y+ W+S
γ
α+γ
α
Mg_2SiO_4
Fe_2SiO_4
(B)

change into these two phases under normal tectonic provinces across the two flanks of the slab.

1-4: Thesis Objectives and Contents:

The olivine→spinel transition in the downgoing slab has important consequences in plate dynamics. It could be one of the major mechanisms that generate deep earthquakes and drive downgoing slabs (Turcotte and Schubert, 1971; Ringwood, 1972, 1973; Schubert et al., 1975). However, the exact role of the olivine→spinel transition in the downgoing slab is mainly dependent on the kinetics of its transformation. The kinetics of the olivine→spinel transition and its importance to plate dynamics has only recently been explored (Sung, 1974; Burns and Sung, 1975; Sung, 1975; Sung and Burns, 1976a, b, c). The main objective of this thesis is to develop this new frontier of research in the earth sciences. Both theoretical and experimental research are emphasized in this thesis to achieve the following major break throughs in the study of the olivine→spinel transition: (1) development of new theories; (2) design of new high pressure, high temperature apparatus; (3) measurement of rates of the olivine→spinel transition for different compositions at different temperatures; and (4) proposal of new hypothesis for the role of the olivine→spinel transition in plate dynamics.

Solid-solid transitions are very complicated proceeses, mainly because: (1) they involve highly anisotropic interfacial and strain energies, and (2) solids possess many metastable

phases and contain a variety of crystal heterogeneities. This subject has been studied by numerous metallurgists for decades, yet it is still not well understood. The subject becomes even more difficult when the material is a silicate mineral and the transition is performed at high pressure, as well as at high temperature. In this case, the transition process is more complicated and the measurement becomes much more difficult. In addition, there is a lack of both theoretical models and the experimental data to test them. Facing these tremendous difficulties, it is impossible for this thesis to arrive at a complete understanding of the kinetics of the olivine→spinel transition. Within the limited time and facilities available, we could only study the most general features of the kinetics of the olivine→spinel transition. The main efforts of this thesis were, therefore, focussed on these objectives: (1) to identify the controlling factors and their effects on the kinetics of the olivine→spinel transition; (2) to understand the general features of the kinetics of the olivine→spinel transition; and (3) to determine, as closely as possible, the range of the kinetics of the olivine→spinel transition in the mantle. To this end, it is again emphasized that this thesis is not intended to be a complete study, but serves to present a new research frontier in earth science.

Following introductory material in this chapter, Chapter 2 gives a conceptual review of crystal structures and the structural basis of the relative stabilities of olivine and spinel. Chapter 3 re-evaluates the effect of crystal field

stabilization of the olivine→spinel transition, highlighting the previously neglected contribution of electronic configurational entropy. Chapter 4 discusses the possible mechanism of the olivine→spinel transition. Chapter 5 presents a consistent picture of thermodynamic properties of olivine and spinel at elevated pressure and temperature. Chapter 6 derives semi-quantitatively the rate equations for the olivine→spinel transition and evaluates the factors controlling the kinetics of the olivine→spinel transition. Chapter 7 describes the equipment, calibration, and techniques used for the experiments. Chapter 8 summarizes the experimental results and compares them with the theories developed in Chapter 6. Chapter 9 applies both the theories and experimental data to plate dynamics. Chapter 10 suggests directions for future work.

1-5: Conventions and Symbols:

The following terminology will be adapted throughout this thesis:

A) "Phase transition" refers to a polymorphic transformation with no composition change (Roy, 1973; Heuer and Nord, 1976).

B) "Nucleation mechanism" refers to the spatial distribution of nuclei, e.g. homogeneous nucleation (volume nucleation), nucleation on grain surfaces, nucleation on dislocations, etc.

C) "Growth mechanism" refers to the path which atoms take to migrate across the interphase boundary (interface).

D) "Olivine→spinel transition" refers to either the $\alpha \rightarrow \beta$ or

the $\alpha \rightarrow \gamma$ transition. When the discussion refers to the very metastable olivine→spinel transition at low temperature (<700°C), the β-phase may not be stable (Figure 1-3), so the latter transition is implied.

In addition to the above conventions, symbols used in this thesis and their units are listed in Appendix A.

Chapter 2

CRYSTAL STRUCTURAL BASIS OF THE OLIVINE→SPINEL TRANSITION

2-1: Introduction:

In order to understand the nature of the olivine→spinel transition, we shall examine features of the crystal structures of the three polymorphs, α, β, and γ in the Mg_2SiO_4-Fe_2SiO_4 system. In this chapter, we review and present new approaches to the understanding of the structural features of these three polymorphs and the structural basis of their relative stabilities.

Crystal structures of olivine at room temperature and one atmosphere pressure (Birle et al., 1968; Brown, 1970; Finger, 1971; Wenk and Raymond, 1973), at elevated temperatures (Smyth and Hazen, 1973; Smyth, 1975), and at high pressures (Hazen, 1975) have been extensively studied. Crystal structures of the β-phase (Baur, 1971; Moore and Smith, 1970) and the γ-phase (Yagi et al., 1974; Ito et al., 1974) have also been studied. High pressure cell parameters of the β- and the γ-phases (Mao et al., 1969; Mizukami et al., 1975) are also available. Computer calculated structural data (DLS method) have been reported by Baur (1972) and by Dempsey and Strens (1975). The relative stabilities of the three polymorphs, α, β, and γ, based on their structural features, have been discussed by Kamb (1968) and by Tokonami et al. (1972).

2-2: Crystal Structural Features:

General structural parameters of the three polymorphs are summarized in Table (2-1). All three structures are based on closest packing of oxygen atoms. However, the α-structure is hexagonal close-packed (h.c.p.) while the β- and the γ-structures are cubic close-packed (c.c.p.). In all three structures, divalent cations M (Mg or Fe) are octahedrally coordinated and tetravelent cations Si are tetrahedrally coordinated. Thus, the transitions among the three phases involve no coordination change. Because the ratios of M and Si atoms to oxygen atoms are 1/2 and 1/4, respectively, only half of the octahedra and one eighth of the tetrahedra in the oxygen close-packing are occupied. This eliminates the necessity of face-sharing between occupied polyhedra and also edge-sharing between occupied tetrahedra. Thus, all three structures can be viewed by linking edges and corners of occupied polyhedra. The differences among the three structures lies in their distinctive patterns of linkage of polyhedra as shown schematically in Figure (2-1). All three structures are composed of three common polyhedral chains. They are: a continuous octahedral chain (A); a discontinuous octahedral chain (B); and a discontinuous tetrahedral chain (C), as shown in Figure (2-2). Thus, the α-structure is composed of alternating normal and overturned layers of ABCB chains; the β-structure is composed of repeating layers of ABABCBCB chains; and the γ-structure is composed of alternating layers of AB

Table (2-1)

GENERAL STRUCTURAL PARAMETERS OF THE THREE POLYMORPHS.

	Z	System	Space Group	Oxygen Packing	Silicate Type	Cell Parameter Mg_2SiO_4	Cell Parameter Fe_2SiO_4	Av. M-O Dist. Mg_2SiO_4	Av. M-O Dist. Fe_2SiO_4
α	4	Ortho.	Pbnm	h.c.p.	Neso. (SiO_4)	a=4.753[a]-4.819[b]		M1=2.101[f]	2.157[g]
						b=10.196-10.476		M2=2.126-2.182	
						c=5.979-6.086		T =1.630-1.625	
β	8	Ortho.	Imma	c.c.p.	Soro. (Si_2O_7)	a=8.247[c]		M1=2.13[h]	
						b=11.440		M2=2.05	
						5.712		M3=2.10	
								T =1.64	
γ	8	Isom.	Fd3m	c.c.p.	Neso. (SiO_4)	a=8.075[d]-8.234[e]		B =	2.137[i]
								T =	1.652

References:

a) Average value of Akimoto and Fujisawa(1968)(a=4.753,b=10.197,c=5.982), Fisher and Medris(1969)(a=4.752,b=10.197,c=5.979), and Hazen(1975)(a=4.752,b=10.193,c=5.977).

b) Average value of Akimoto and Fujisawa(1968)(a=4.821,b=10.477,c=6.086), Fisher and Medaris(1969)(a=4.817,b=10.480,c=6.086), and Hazen(1975)(a=4.818,b=10.470,c=6.086).

c) Average value of Ringwood and Major(1970)(a=8.248,b=11.45,c=5.710), Suito(1972)(a=8.242,b=11.414,c=5.731), Moor and Smith(1970)(a=8.248,b=11.444,c=5.696), and Mizukami et al (1975)(a=8.25,b=11.45,c=5.71).

Table (2-1)
(CONTINUED)

d) Average value of Ringwood and Major(1970)(a=8.071), Suito(1972)(a=8.076), Ito et al(1974)(a=8.076), and Mizukami et al(1975)(a=8.075).

e) Average value of Akimoto and Fujisawa(1968)(a=8.234), Ringwood(1958)(a=8.233), Boyd and England(1960)(a=8.235), and Yagi et al(1974)(a=8.234).

f) Hazen(1975)

g) Average value of Smith(1975)(M1=2.157,M2=2.179,T=1.628), and Hazen(1975)(M1=2.157,M2=2.184,T=1.621).

h) Moore and Smith(1970)

i) Yagi et al(1974)

Fig. (2-1)

Schematic diagram showing the different linking patterns of occupied polyhedra in the three polymorphs. The closest packed layers of oxygen atoms are parallel to the paper. (A) α-structure, (B) β-structure, and (C) γ-structure. Outlined are unit cells. The unit cell contains 2, 6, and 6 layers of occupied polyhedra in the direction perpenticular to the drawing for the α-, β- and γ-structures, respectively. (After Morimoto et al, 1974).

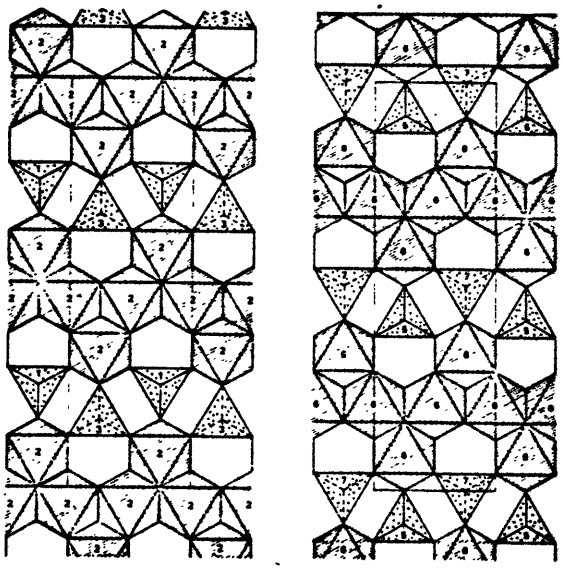

(a)

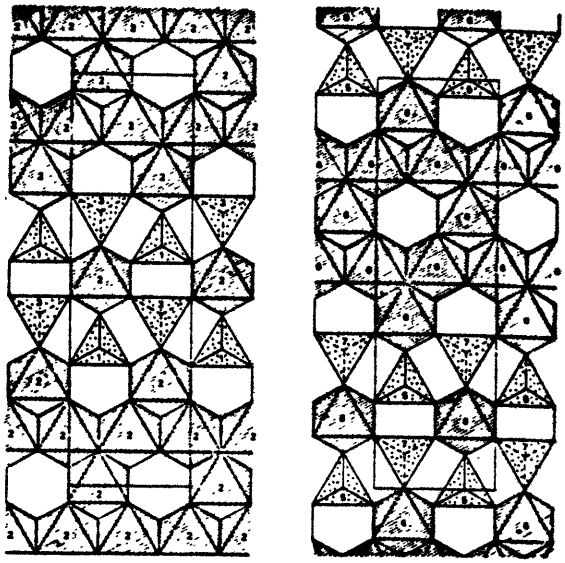

(b)

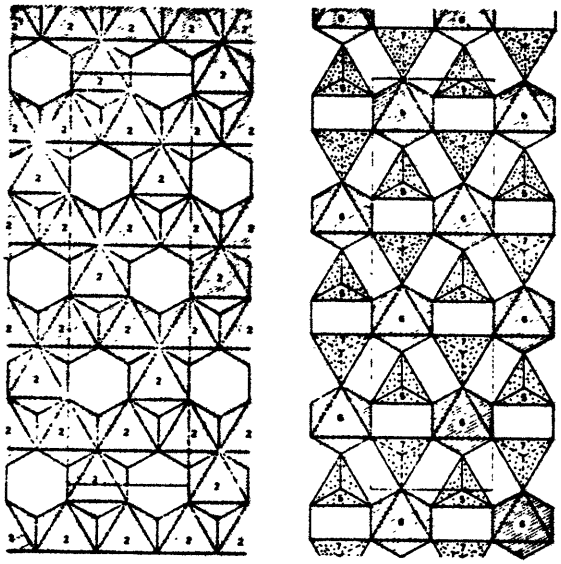

(c)

Fig. (2-2)

Three basic structural units for the three polymorphs, α , β and γ . A=continuous octahedral chain, B=discontinuous octahedral chanin, and C=discontinuous tetrahedral chain.

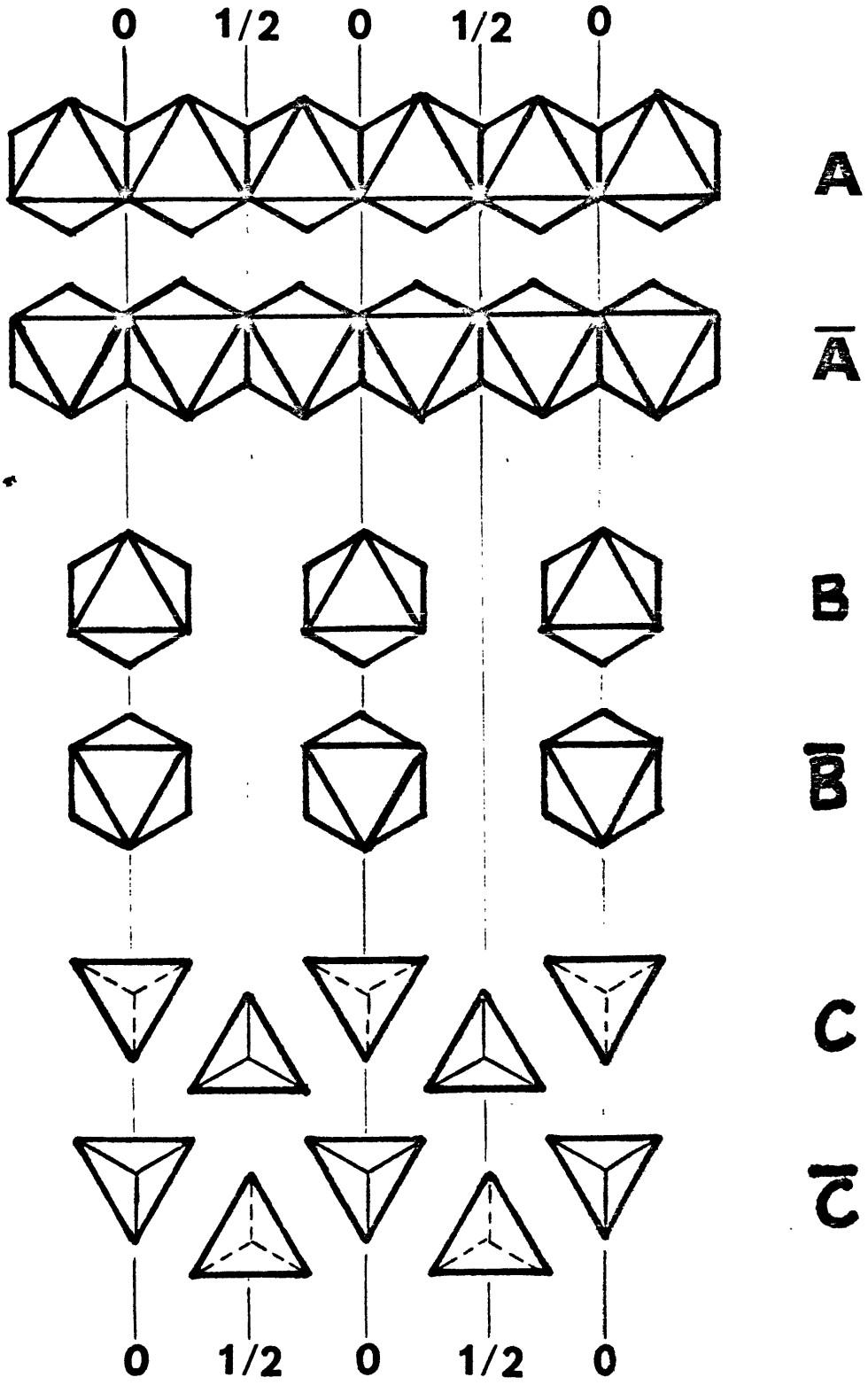
0
1/2
0
1/2
0
A
$\bar{A}$
B
$\bar{B}$
C
$\bar{C}$
0
1/2
0
1/2
0

and BC chains. The two dimensional representations of the three structures, using the three types of polyhedral chains, are shown in Figure (2-3). The three different patterns of linking polyhedra in three dimensions resulted in the distinctive 2(M1, M2), 3(M1, M2, M3), and 1(B) octahedral sites in α-, β-, and γ-structures, respectively, and one tetrahedral site (T) in each of the three structures. The six distinct octahedral sites are shown schematically in Figure (2-4), where the shared (heavy line) and the unshared (light line) edges are distinguished. The characteristics of these six sites, in terms of the number of shared edges and corners, are listed in Table (2-2).

Pauling's third rule predicts that the shared polyhedral edges will shorten relative to the unshared ones in order to reduce the unfavorable cation-cation repulsion. However, this rule will be obeyed only when the arrangement of these shared edges within the crystal structure is such that the shortening of these edges is allowed by the geometry (Kamb, 1968; Baur, 1972). In the α-structure, this condition is fulfilled because all the shared polyhedral edges coincide with the six edges of unoccupied tetrahedra. Thus, the shortening of shared polyhedral edges in the α-structure simply leads to contraction of the so-called "Leer" tetrahedra (L), which can be tolerated by the geometry of the structural framework. The contracted L site and T site in the α-structure form chains of corner-sharing trigonal dypyramids running parallel to the a-axis. These LT chains are offset and separated by

Fig. (2-3)

Two dimensional representation of the three dimensional framework of the three polymorphs, α , β and γ . A, B and C are the three basic structural units(Fig. 2-2). Subscripts are positions of these structural units as labelled in Fig. (2-2).

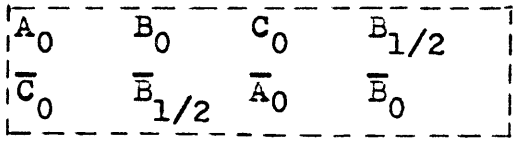

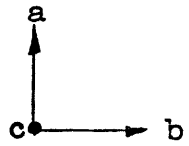

α-structure

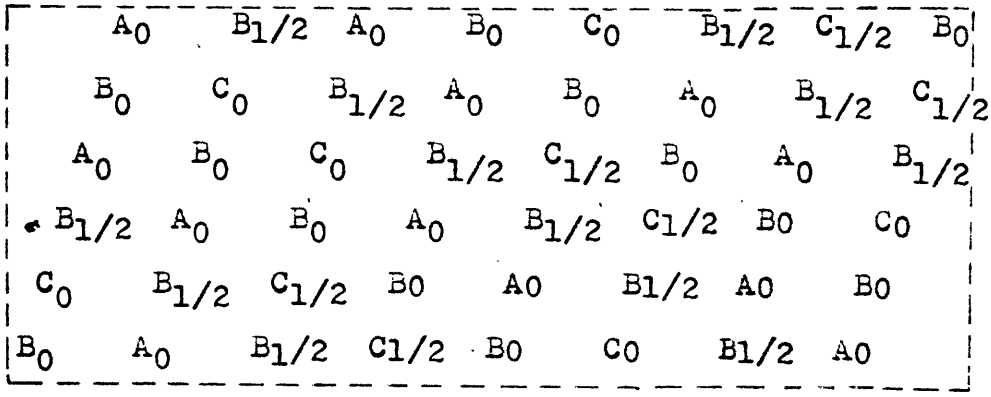

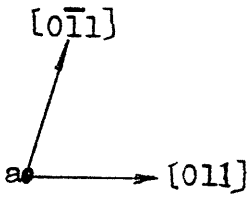

β-structure

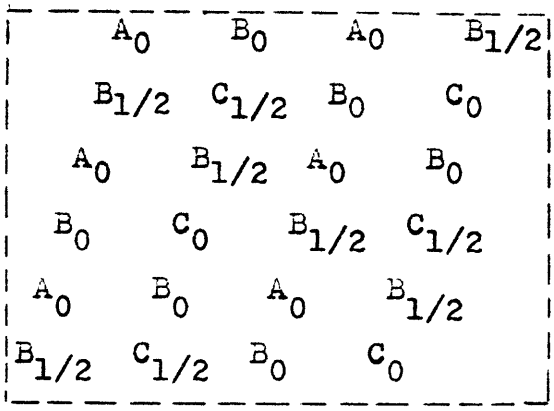

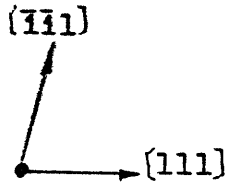

γ-structure

Fig. (2-4)

Schematic diagram showing projections of the six distinct sites in the three polymorphs. Upper row, M1 and M2 sites in the α-structure, B-site in the γ-structure; lower row, M1, M2 and M3 sites in the β-structure. Heavy and light lines are shared and unshared octahedral edges, respectively.

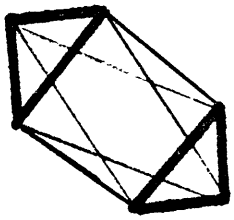

M1

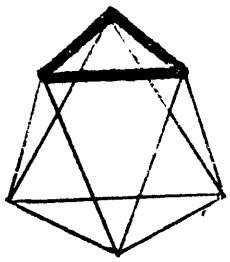

M2

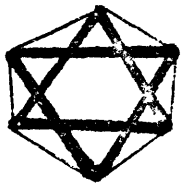

B

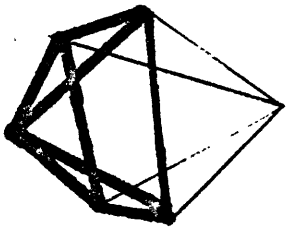

M1

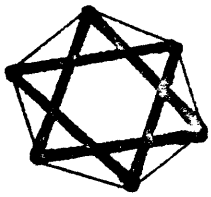

M2

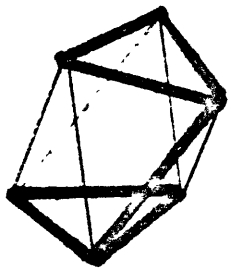

M3

Table (2-2)

STRUCTURAL DIFFERENCE OF CATION SITES IN THE THREE POLYMORPHS

Polymorph	Site	Number of shared corner per site			Number of shared edge per site		
		M-M	M-T	T-T	M-M	M-T	T-T
α	M1	4 (4M2)	2	-	4 ($^{2M1}_{2M2}$)	2	-
	M2	8 ($^{4M1}_{4M2}$)	4	-	2 (2M1)	1	-
	T	-	6 ($^{2M1}_{4M2}$)	0	-	3 ($^{2M1}_{1M2}$)	0
β	M1	0	6	-	6 ($^{4M3}_{2M2}$)	0	-
	M2	0	6	-	6 ($^{5M3}_{1M1}$)	0	-
	M3	0	4	-	7 ($^{4M3}_{2M2}$)	0	-
	T	-	10	1	- ^{1M1}	0	0
γ	B	0	6	-	6	0	-
	T	-	12	0	-	0	0

Note: Symbols: M=Octahedral site(Mg,Fe)
T=Tetrahedral site(Si)

M sites as depicted schematically in Figure (2-5). As all the octahedral edges connecting different LT chains are unshared edges, which are weaker and can be stretched for the adjustment of distances of separation among the more rigid LT chains, the α-structure is relaxed on the b-c plane in contrast to the more compact a-direction. This is demonstrated by comparing the ratios of the three cell parameters between the real structure and the ideal non-distorted structure. For the latter, a:b:c = 1:2.121:1.225. Thus, if the a-direction corresponds to the ideal length of a non-distorted structure, the b- and the c-directions are, respectively, 1.1%(Fo) - 2.5%(Fa) and 2.7%(Fo) - 3.1%(Fa) longer than the ideal lengths calculated from the data of Table (2-1). The higher expansion along the c-direction relative to the b-direction may be explained by the stronger cation-cation repulsion of the closely spaced M1 sites (A chain) parallel to the c-direction (Figure 2-1). The inequality of the distortions along the three directions characteristic of the α-structure may also be reflected in their different responses to changes of pressure and temperature. Thus, we may expect thermal expansions and compressibilities to increase in the order $c \geq b > a$ and $b \geq c > a$, respectively. The predicted trends agree in general with the experimental results shown in Table (2-3).

The contraction of L sites and the extension of unshared edges greatly distort the M1 and M2 sites in the α-structure. Because each M1 site shares six L-site edges, while each M2 site shares only three L-site edges, this makes the volume of

Fig. (2-5)

Schematic diagram showing rigid LT chains running parallel to the a-axis in the α-structure. LT chains are linked only by weak unshared octahedral edges which can be stretched or compressed to fit the structural requirement in response to P-T changes. This geometry of linked polyhedra gives the α-structure the largest thermal expansion and compressibility among the three polymorphs. The diagram shows LT chains and interstitial M-sites on three projections. Heavy lines are tetrahedral(T) edges or shared octahedral(L) edges. Light lines are unshared octahedral edges. Dotted lines are edges on the far side from the viewer.

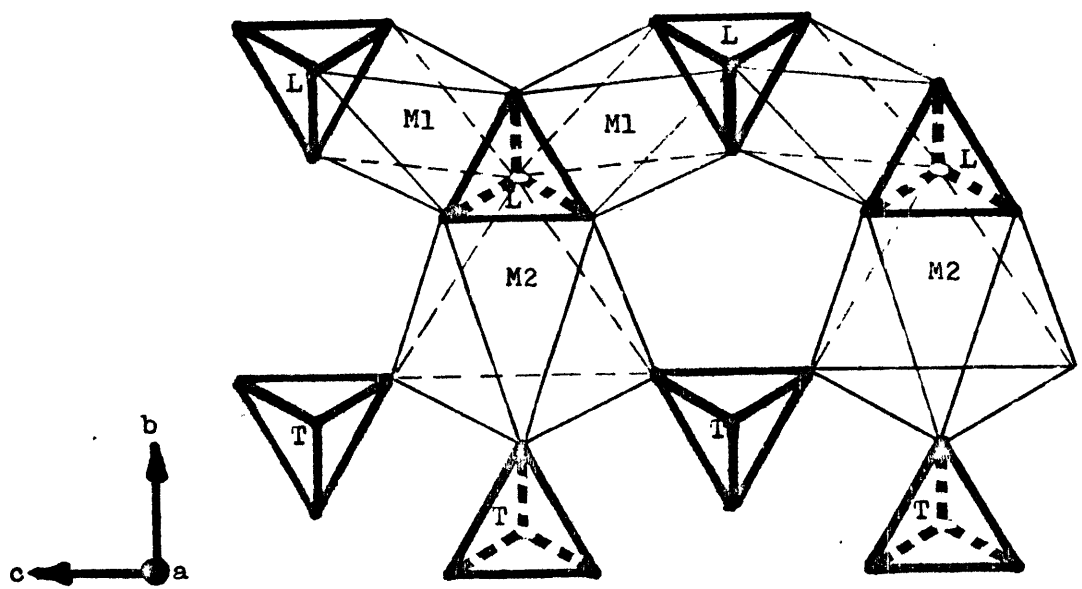
L
L
M1
M1
L
L
M2
M2
T
T
T
T
b
c
a

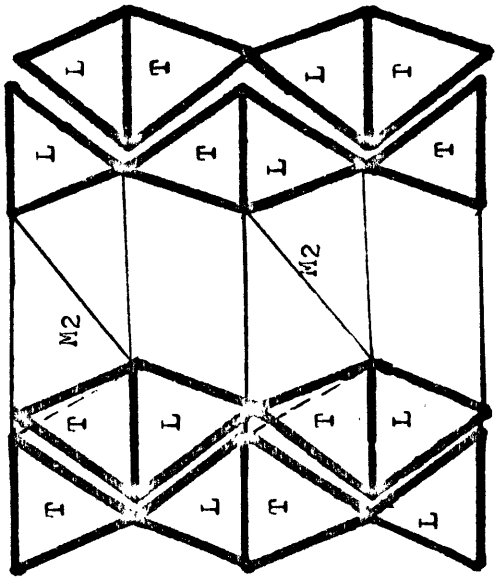
L
T
M2
M2
b
a
c

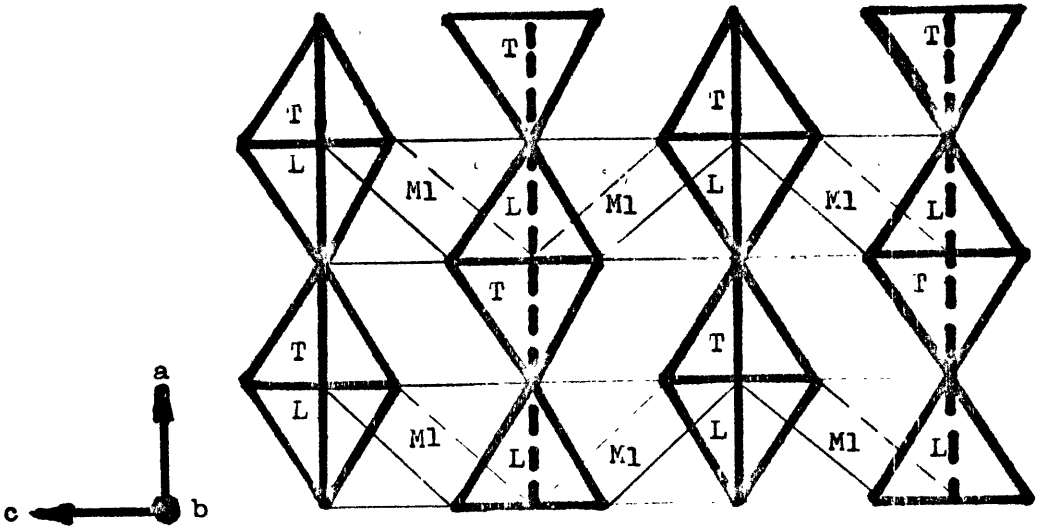
T
T
L
M1
L
M1
T
T
L
M1
L
M1
T
T
L
M1
L
M1
T
a
c
b

the M2 site slightly larger than the M1 site.

The above discussion indicates that in the α-structure, the shared edges involve the L-site exclusively. This makes the shortening of these edges required by Pauling's third rule natural. By contrast, the shared octahedral edges in the γ-structure for isolated triangles. Each triangle shares its three corners with the surrounding T sites in such a way that the shared octahedral edges and edges of T-sites alternate to form continuous lattice rows (Figure 2-6). The alternation of these two types of edges exists along all 6 directions parallel to the 6 edges of T-sites throughout the structure. This framework has made the γ-structure the most rigid of the three structures. As edges of T-sites are shorter and more rigid than shared octahedral edges, the latter can be stretched to fill up the gap in the former and make lengths of these two edges complementary. As a result, the shared octahedral edges become longer than unshared ones. This contradiction of Pauling's third rule is the major destabilizing factor of the γ-structure at low pressure, as will be discussed later.

The distribution of the shared octahedral edges is more complicated in the β-structure. In the local region around M3 sites, the geometry is similar to the γ-structure and the shared octahedral edges are not shortened. However, this is compensated by the shortening of shared octahedral edges in other regions. Thus, the β-structure is intermediate between the α- and the γ-structures.

Fig. (2-6)

Geometry of linking polyhedral edges along the three faces of form {111} in the γ-structure. Heavy, light and dotted lines are tetrahedral edges, shared octahedral edges, and unshared octahedral edges, respectively. Note that the lengths of tetrahedral enges and shared octahedral edges are complementary. This makes the latter longer than unshared octahedral edges.

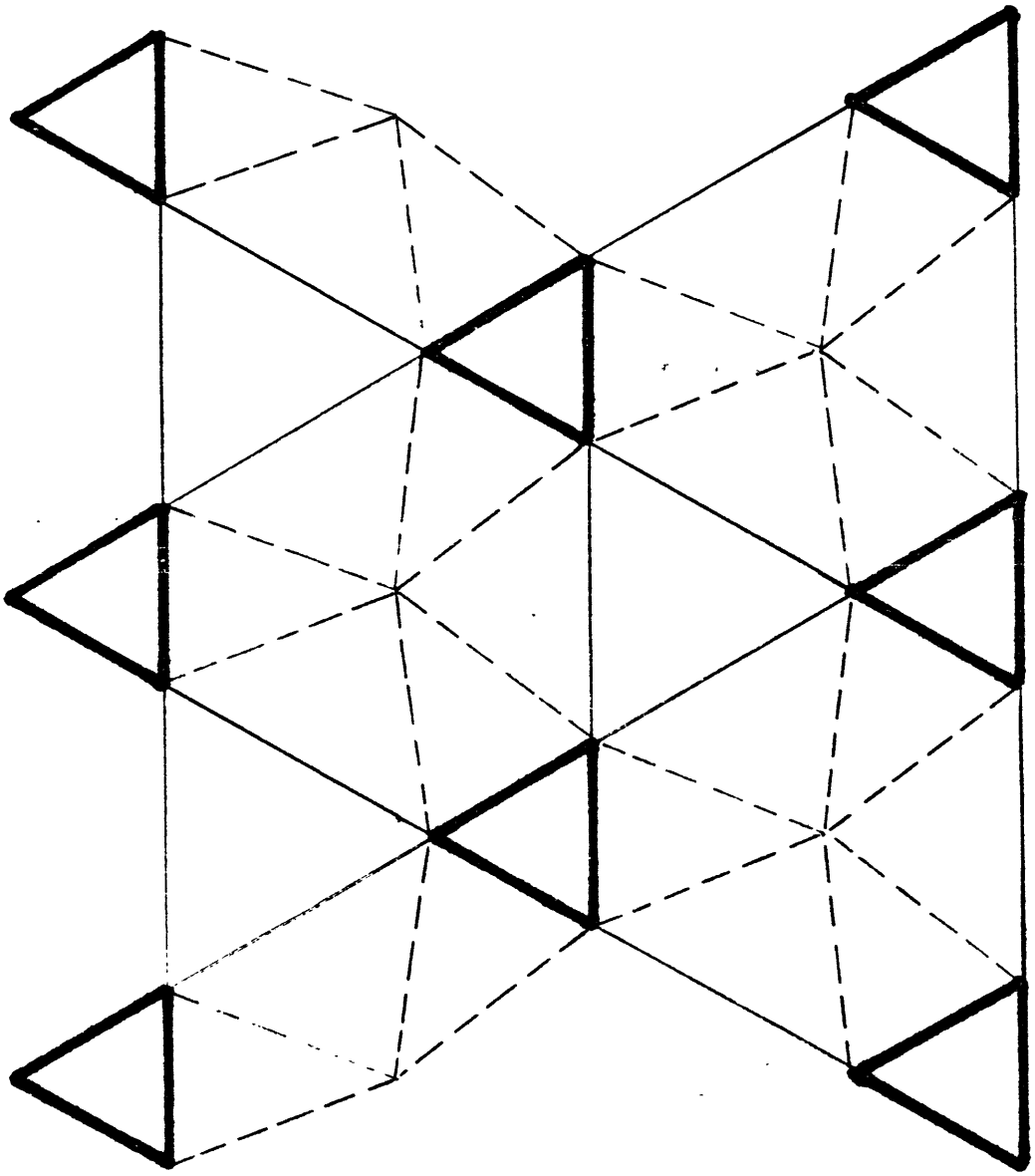

Table (2-3)

THERMAL AND PRESSURE ANISOTROPY IN OLIVINE

	Direction	Linear Thermal Expansion ($10^{-6}{}^{o}C^{-1}$)		Linear Compressibility ($10^{-5}Kb^{-1}$)	
		Mg_2SiO_4	Fe_2SiO_4	Mg_2SiO_4	Fe_2SiO_4
Fractional Length Change	a	7.9[a]	9.9[b]	7.9[c]	8.4[d]
	b	15.3	9.6	41.7	56.9
	c	13.4	11.9	16.7	14.5

References:

a) Average value between 23°C to 900°C, from Hazen's (1975) data

b) Average value between 20°C to 900°C, from Smyth's (1975) data

c) Average value between 0 to 40 Kb, from Hazen's (1975) data

d) Average value between 0 to 42 Kb, from Hazen's (1975) data

2-3: Structural Basis of Relative Stabilities:

We shall now discuss the structural basis of the relative stabilities of these three structures. The relative stabilities at a given P and T are determined by their free energies (G). We shall express the free energy in the form: G = E+U+PV-TS, where E is the part of internal energy excluding the lattice energy U, and V and S are volume and entropy, respectively. Thus, we shall evaluate relative stabilities of the three structures by comparing their U, V, and S on a structural basis.

As described previously, the weak unshared octahedral edges which separate LT chains in the α-structure are extended to allow longer cation-cation distances and thus reduce cation-cation repulsion. On the other hand, the unshared octahedral edges in the γ-structure are compressed by corner-sharing T-sites. As a consequence, the octahedral volumes (M-sites and unoccupied sites), and thus the molar volumes of the three structures, increase in the order $\gamma<\beta<\alpha$. This trend will become increasingly evident with increasing temperature. Partly because of the increase of molar volume which contributes to the volume entropy, partly because of the decrease of the rigidity which contributes to the vibrational entropy (Tokonami et al., 1972), and also partly because of the smaller energy splitting in the lower d orbitals which contributes to the electronic configurational entropy, especially at higher temperature (Chapter 3), entropies of the three structures

increase in the same order, $\gamma<\beta<\alpha$. Relative compressibilities, heat capacities, and thermal expansions for these three polymorphs will show the same trend. The decrease of rigidity in the series γ-β-α may be explained by the rigid M-M edge-sharing rows forming lines, planes, and a three-dimensional framework in the three structures, α, β, and γ, respectivley (Tokonami et al., 1972). Similar trends of increasing volume and entropy in the three structures suggest that all three phase boundaries have positive slopes, which is consistent with the experimental data (Figure 1-3). In addition, if we assume that differences in internal energies (E+U) among the three structures are small, then the α-structure will be destabilized at high pressure (large PV term) and low temperature (small TS term), and will be favored at low pressure and high temperature. The stability relation for the γ-structure is just the opposite to that for the α-structure. The stability fields of the three structures thus conform with these shown in Figure (1-3).

We shall now evaluate structural controls on the lattice energy U. According to Pauling's third rule, the lattice energy of a crystal structure which contains corner- and edge-sharing tetrahedra and octahedra may increase in the order: $C_{M-M}<C_{M-T}<E_{M-M}<C_{T-T}<E_{M-T}<E_{T-T}$, where C and E stand for corner-sharing and edge-sharing, respectively. From the data of Table (2-2), we have calculated the number of shared corners and shared edges per formula unit, M_2TO_4, for the three structures, which are shown in Table (2-4). The destabilizing

Table (2-4)

NUMBER OF SHARED POLYHEDRAL EDGES AND CORNERS PER FORMULA M_2TO_4 FOR THE THREE POLYMORPHS

	Shared Edge or Corner	α	β	γ
Energy----------→ ←----------Stability	E_{T-T}	0	0	0
	E_{M-T}	3	0	0
	C_{T-T}	0	1/2	0
	E_{M-M}	3	6(1/3)	6
	C_{M-T}	6	10(1/3)	12
	C_{M-M}	6	0	0

effects of C_{M-M} and C_{M-T} are small compared with the others and can be neglected. Thus, the α-structure is unfavorable by its 3 M-T shared edges, and the β-structure by its 1/2 T-T shared corner and 1/3 M-M shared edge. However, the destabilizing factor in the α-structure is partly compensated by its lower number of M-M shared edges. In addition, the shortening of all 6 shared edges at the L-site significantly lowers its lattice energy. In fact, the lattice energy of the α-structure is the lowest among the three structures. The destabilization of the β-structure is not compensated. In addition, charge balance in the β-structure is not maintained for some oxygen atoms (+1/3 for O(2) and -1/3 for O(1)) due to the corner-sharing of T-T sites; this violates Pauling's second rule. As a result, the lattice energy in the β-structure is the highest among the three structures. Computer calculated lattice energies in Co_2SiO_4 have confirmed that lattice energies of the three structures increase in the order $\alpha<\gamma<\beta$ (Tokonami et al., 1972).

By taking the difference of the lattice energies into account, the above phase relationships will be modified in such a way that the stability field of the α-structure expands at the expense of both the β- and the γ-structures, and the stability of the γ-structure expands at the expense of the β-structure. The qualitative relationship among the three phases is not changed. However, the stability field of the β-structure is narrowed and it may be pinched out towards high P-T region as a result of other factors, such as the crystal

field stabilization (Chapter 3), which may favor one or both of the other two structures.

In summary, we may envisage the crystal structural control of the relative stabilities of the three structures as follows: in the α-structure, the unshared octahedral edges can be stretched to reduce cation-cation repulsion and thus reduce the lattice energy. At low pressure and high temperature, the reduction of lattice energy is such that the α-structure becomes the most stable phase of the three structures. As the pressure increases and temperature decreases, the extension of unshared octahedral edges and thus the reduction of the lattice energy in the α-structure become less prominent. At some point, the high PV term outweighs the gain in lattice energy and the β- or the γ-structure becomes stable.

The physical explanation of the structural control on the relative stabilities of olivine and spinel can be pictures as follows: Hazen has hypothesized that the melting of olivine may be due to the increased ratio of octahedral to tetrahedral volume with temperature to the limit that the structure can tolerate. By analogy, the olivine→spinel transition could be due to the decrease of this volume ratio with pressure, to a value which the olivine structure can not tolerate but the spinel structure can. This ratio can be affected by other factors such as composition, bond type, degree of site distortion, etc. For example, with increasing Fe_2SiO_4 content, the bonding becomes less ionic, and the stabilizing factor of shortening shared edges in the α-

structure (Kamb, 1968) becomes less effective. This could facilitate the olivine→spinel transition by increasing the critical volume ratio of the octahedral to the tetrahedral sites. In addition, the increase of octahedral site distortion with Fe_2SiO_4 content may further facilitate the transition. Thus, we may expect the critical volume ratio to increase with Fe_2SiO_4 content. The equilibrium olivine→spinel transition pressures at room temperature are 80 kb and 26 kb for Mg_2SiO_4 and Fe_2SiO_4, respectively. A crude calculation by extrapolating (for Mg_2SiO_4) and intrapolating (for Fe_2SiO_4) the high pressure crystallographic data of olivine (Hazen, 1975) to those transition pressures gives critical volume ratios of 5.3 and 7.2 for Mg_2SiO_4 and Fe_2SiO_4, respectively. Thus, the calculation is consistent with our prediction.

Chapter 3

CRYSTAL FIELD STABILIZATION

3-1: Introduction:

In the above discussion of the crystal structural control of the olivine→spinel transition, we have neglected the contribution of crystal field stabilization. The splitting of 3d orbitals of Fe^{2+} in octahedral sites imparts a crystal field stabilization energy (CFSE) to the structure.

$$CFSE = 2((2/5)\Delta + C\delta) \qquad (3\text{-}1)$$

where Δ (or 10Dq) is the energy difference between the baricenters of e_g orbitals (d_{z2}, $d_{x^2-y^2}$) and t_{2g} orbitals (d_{xy}, d_{yz}, d_{zx}) (Figure 3-1a). C is a constant between 1/3 and 2/3, and δ is the maximum splitting of t_{2g} energy levels. The factor of 2 arises because there are two Fe^{2+} ions for each formula Fe_2SiO_4. In general, Δ increases with decreasing volume of the FeO_6 octahedra (M-sites), and to a first approximation, Δ is inversely proportional to the fifth power of the average FeO bond distance (d). Both C and δ are functions of site distortion, and the product of $2C\delta = \xi$, is the extra stabilization energy gained by the site distortion.

The crystal field splitting of the 3d orbitals not only imparts a CFSE which contributes to the lowering of the lattice energy, but also reduces the electronic configuration entropy, S_e, by removing orbital degeneracy. The latter effect has often been ignored in discussions of crystal field stabiliza-

Fig. (3-1)

Crystal field splitting of d-orbitals of Fe^{2+} in M-sites. (A) symbles, (B) crystal field splitting in the B-site of spinel, (C) crystal field splitting in the M1-site of olivine, and (D) crystal field splitting in the M-2 site of olivine. Energy splittins are proportional to those tabulated in Table (3-1) for Fe_2SiO_4.

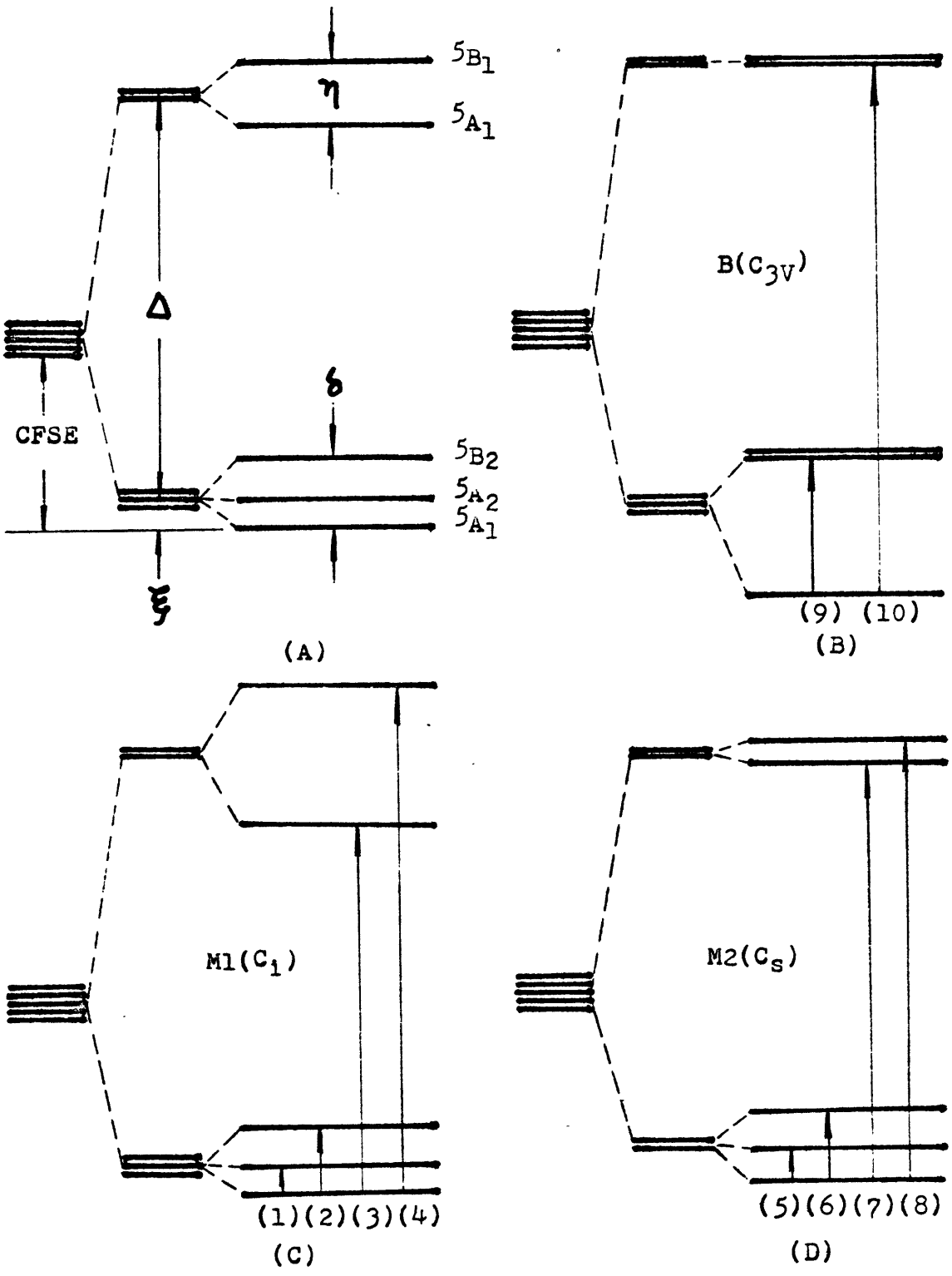
$^5B_1$
η
$^5A_1$
Δ
δ
CFSE
$^5B_2$
$^5A_2$
$^5A_1$
ξ
(A)
B(C_{3V})
(9) (10)
(B)
M1(C_i)
(1)(2)(3)(4)
(C)
M2(C_s)
(5)(6)(7)(8)
(D)

tion (Syono et al., 1971; Mao and Bell, 1972). However, the change of electronic configuration entropy tends to offset the effect of CFSE in lowering the free energy, and this cancelling effect can be especially significant at high temperature, as will be emphasized in the following discussion. For a more detailed consideration of the crystal field stabilization, we shall evaluate the two factors modifying the free energy of the system, by writing:

$$G_{CFS} = -CFSE - TS_{CFS} \quad \text{---------- (3-2)}$$

where G_{CFS} is the overall change of free energy due to the crystal field splitting, and $S_{CFS} = \Delta S_e$ is the change of entropy due to the crystal field splitting. Thus, the crystal field stabilization is very much temperature dependent.

3-2: Crystal Field Splittings:

We shall now evaluate the CFSE in the olivine and spinel structures for Fe_2SiO_4. Point group symmetries for the M1 and M2 sites in olivine and the B site in spinel are C_i, C_s, and C_{3v} respectively. Accordingly, the splitting of 3d orbitals of Fe^{2+} in these sites can be shown qualitatively as in Figure (3-1). The octahedral volumes of these three sites decrease in the order M2>M1>B (Table 2-1); thus, we may expect the crystal field splitting to increase in the same order. It should be noted that the factor C for the site distortion energy is 2/3 for the B site in spinel but less than 2/3 for the M1 and M2 sites in olivine. For convenience,

all possible electronic transitions for the sixth d electron from the ground state of Fe^{2+} are labelled by numbers in Figure (3-1). Transitions 3 and 4 for the M1 site and the average of transitions 7 and 8 for the M2 site in fayalite at 1 atm. pressure have been assigned by Burns (1970a) to be 8060, 11060, and 9290 cm^{-1}, respectively, based on measured absorption spectra in the near infrared region. Energy splittings of t_{2g} levels in fayalite have been calculated by Huggins (1974) based on Mössbauer data. He obtained values of 630 and 1400 cm^{-1} for one site, and 710 and 1500 cm^{-1} for the other site, but he was unable to assign them to individual sites. However, the difference between them is small. We shall arbitrarily assign the slightly larger energy splittings of the t_{2g} levels to the more distorted M2 site, so that the above four energy splittings correspond to transitions 1, 2, and 5, 6 respectively. These assignments will make the calculated Δ_o and CFSE consistent with the crystallographic and crystal chemical data. From the above energy splittings of 3d orbitals, the Δ_o and CFSE for fayalite at zero pressure (1 atm.) and room temperature were calculated to be 8883 and 4230 cm^{-1} for the M1 site, and 8553 and 4158 cm^{-1} for the M2 site, respectively. The higher Δ_o for the M1 site is consistent with its smaller volume relative to the M2 site. The average lengths of the Fe-O bonds (d) are 2.157 and 2.184Å (Table 2-1) for the M1 and the M2 sites, respectively. So, $\Delta_o^{M1} d_o^{M1} \sim \Delta_o^{M2} d_o^{M2} \sim 4.20 \times 10^{-35}$ cm^4, in agreement with the inverse fifth power law. Despite the difference of Δ_o between the two sites, CFSE values for

them are essentially equal (they differ by less than 2%). As a consequence, there is no site preference for Fe^{2+}, which agrees with the negligible cation ordering observed in the olivine series. The nearly complete disordering of cations in olivine is responsible for the quasi-ideal behavior of the olivine solid solution.

We have measured the absorption spectrum of a synthetic Fe_2SiO_4 spinel as shown in Figure (3-2). The absorption maximum at 11430 cm^{-1} is attributed to transition 10 in Figure 3-1. This value is only slightly larger than the value of 11100 cm^{-1} measured by Mao and Bell (1972). In order to calculate Δ_o for the B site in Fe_2SiO_4 spinel, we employ the empirical inverse fifth power law of $\Delta_o^B d_o^B \sim 4.20 \times 10^{-35}$ cm^4. Since $d_o^B = 2.137\text{Å}$ (Table 2-1), we obtain $\Delta_o^B = 9421$ cm^{-1}. Using this value and the measured transition 10, we have calculated transition 9 and the CFSE for the B site to be 3014 and 5778 cm^{-1}, respectively. The above assignments of crystal field splittings and the calculated values of Δ_o, ξ_o, and CFSE for the M1 and the M2 sites in fayalite and the B site in Fe_2SiO_4 spinel at zero pressure and room temperature are summarized in Table (3-1).

3-3: Pressure Effect:

In order to evaluate the pressure effect on Δ, we employ the first order Birch-Murnaghan equation of state:

Fig. (3-2)

Electronic absorption spectrum of a synthetic Fe_2SiO_4 spinel. Sample thickness is approximately 8 μ m. O.D. is optical density.

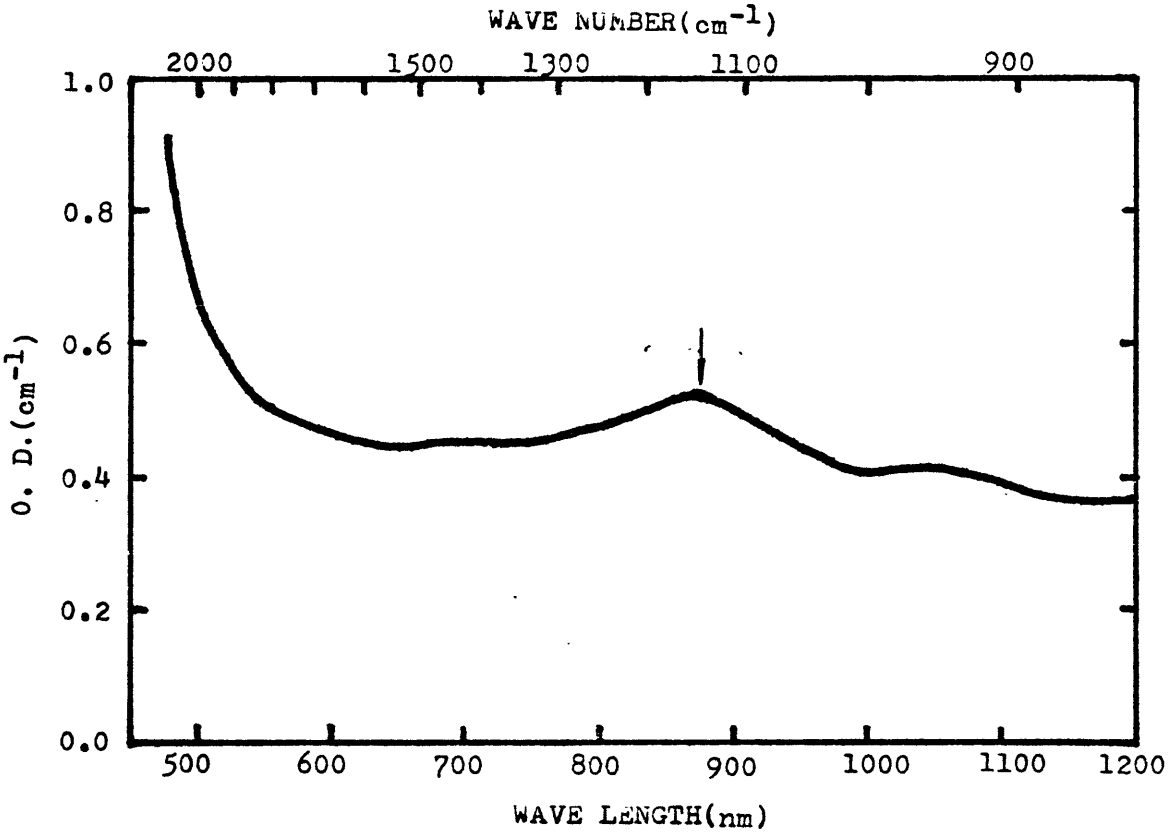
WAVE NUMBER(cm-1)
2000
1500
1300
1100
900
1.0
0.8
0.6
0.4
0.2
0.0
O. D.(cm-1)
500
600
700
800
900
1000
1100
1200
WAVE LENGTH(nm)

Table (3-1)

CRYSTAL FIELD SPLITTING ENERGIES IN M-SITES OF FAYALITE AND Fe_2SiO_4 SPINEL. (Energies in cm^{-1})

M1		M2		B	
(1)	630	(5)	710	(9)	3014
(2)	1400	(6)	1500	(10)	11430
(3)	8060	(7)	9290		
(4)	11060	(8)			
Δ	8883	Δ	8553	Δ	9421
ξ	677	ξ	737	ξ	2009
CFSE	4230	CFSE	4158	CFSE	5778

$$P = \frac{3}{2}K_o\left[\left(\frac{V_o}{V}\right)^{\frac{7}{3}} - \left(\frac{V_o}{V}\right)^{\frac{5}{3}}\right] \text{ ---------- (3-3)}$$

where K and V are the bulk modulus and volume of the M-site, respectively. The subscript "o" refers to the zero pressure value. If we neglect the shape change of the M-sites with increasing pressure, then:

$$\frac{V_o}{V} = \left(\frac{\gamma_o}{\gamma}\right)^3 = \left(\frac{\Delta}{\Delta_o}\right)^{\frac{3}{5}} \text{ ----------(3-4)}$$

Substituting eq. (3-2) into eq. (3-1), we obtain:

$$P = \frac{3}{2}K_o\left[\left(\frac{\Delta}{\Delta_o}\right)^{\frac{7}{5}} - \left(\frac{\Delta}{\Delta_o}\right)\right] \text{ ---------- (3-5)}$$

As K_o's for M-sites of fayalite and Fe_2SiO_4 spinel are not available, we used instead values for the whole mineral, namely, 1201 kb for fayalite and 2063 kb for Fe_2SiO_4 spinel (Table 5-1). Δ values as functions of pressure for the two polymorphs are calculated and shown in Figure (3-3). Note that Δ in fayalite (Δ^{fa}) increases with pressure more rapidly than that in Fe_2SiO_4 spinel (Δ^{sp}), and the former becomes larger than the latter at a pressure of approximately 190 kb. This is due to the larger compressibility for the M-site in fayalite than in Fe_2SiO_4 spinel. As M-sites may be more compressible than the whole mineral, an overestimation of K_o in the above calculation may give too low a value of Δ. However, part of the error introduced will be cancelled out because our ultimate interest is in the difference of the CFSE (ΔCFSE) between Fe_2SiO_4 spinel and fayalite.

Fig. (3-3)

Crystal field splitting parameters as functions of pressure. Note the cross over of Δ for olivine and spinel, and the decrease of ΔCFSE between them with increasing pressure.

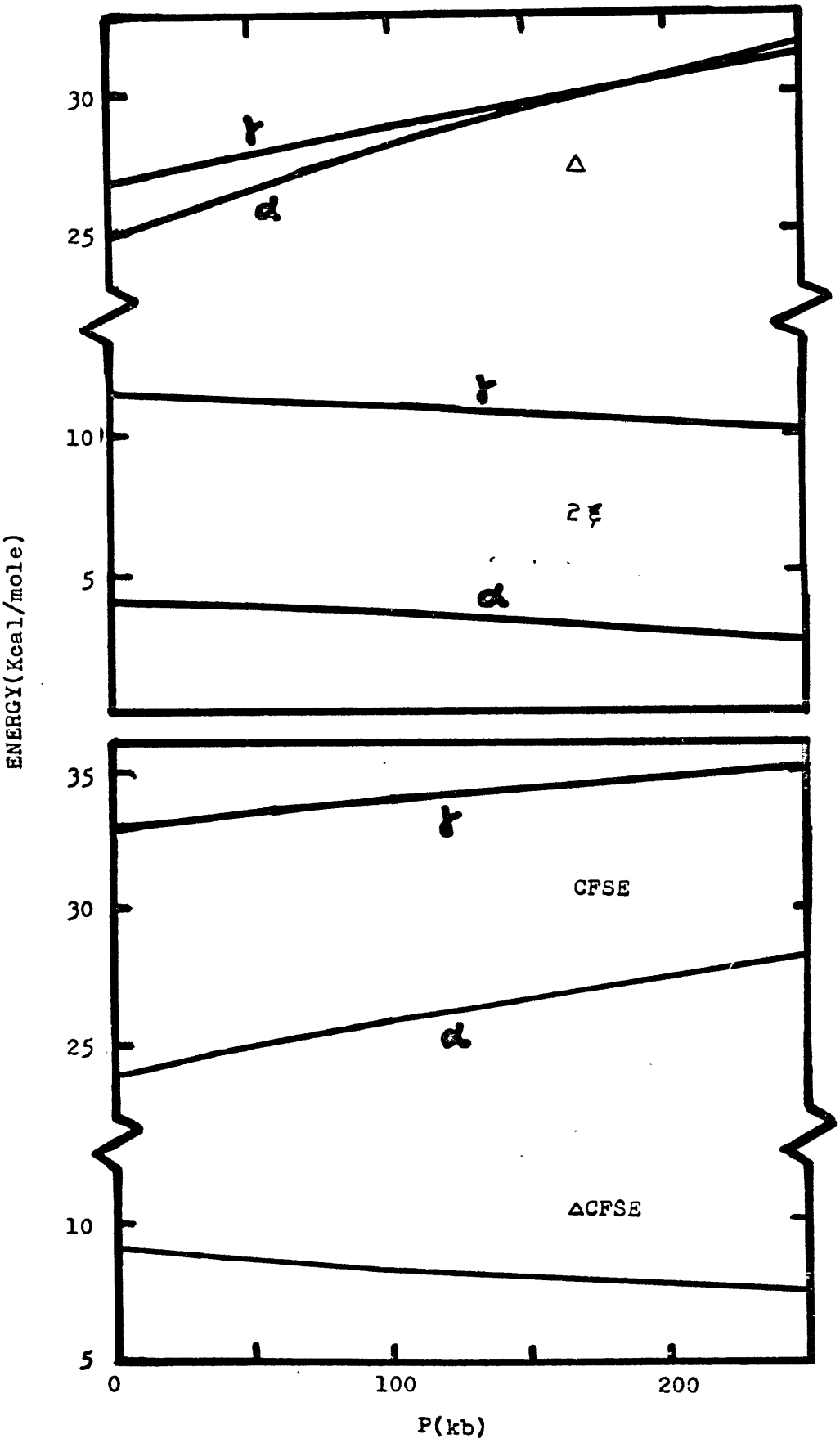
30
25
γ
α
Δ
γ
10
2ξ
5
α
35
γ
30
CFSE
25
α
10
ΔCFSE
5
0
100
200
P(kb)
ENERGY(Kcal/mole)

We shall now estimate the site distortion stabilization energy as a function of pressure. Huggins (1974) has estimated from high pressure Mössbauer data that transition energies 1, 5 and 2, 6 in fayalite (Figure 3-1) will decrease with pressure at approximate rates of 0.7 and 1.5 cm^{-1}/kb, respectively, due to the decreasing degree of site distortion with increasing pressure. For a semi-quantitative calculation, we tentatively assume the same rate of 1.5 cm^{-1}/kb for the decrease in energy of the transition 9 in Fe_2SiO_4 spinel. The site distortion stabilization energies 2ξ for the two polymorphs as functions of pressure are calculated and shown in Figure 3-3. Based on the above data for Δ and 2ξ, CFSE and ΔCFSE for the two polymorphs as functions of pressure are shown in Figure 3-3. Note that ΔCFSE decreases from 9.1 Kcal/mole at zero pressure to 7.1 Kcal/mole at 250 kb.

3-4: Temperature Effect:

We have not evaluated the effect of temperature on ΔCFSE in the above calculations. Increasing temperature will affect the CFSE in several ways. First, the volumes of M-sites in fayalite will increase (Hazen, 1975; Smyth, 1975). We may expect the same thing to occur in Fe_2SiO_4 spinel. Thus, Δ may decrease with increasing temperature. Because the thermal expansion in fayalite is larger than that in Fe_2SiO_4 spinel (Table 5-1), we expect that the former has a higher rate of decreasing Δ with increasing temperature. Secondly, heating tends to increase the degree of site dis-

tortion of M-sites in fayalite (Hazen, 1975; Smyth, 1975). This is due to the fact that, in general, thermal expansion is larger for the longer bonds than for the shorter ones. The increase of site distortion with temperature for the M1 site in fayalite is suggested by measured polarized absorption spectra as shown in Figure (3-4). The two broad peaks of the β-spectra and the two shoulders (the one at higher energy is obscured by the more intense center peak) of the γ-spectra are due to the two transitions, 3 and 4, in Figure (3-1) (Burns, 1970b, 1974). Although heating tends to broaden these two peaks, there is also a tendency for them to move apart with increasing temperature, suggesting an increase of site distortion. This observation is consistent with our previous argument (Chapter 2) that the largest thermal expansion along the c-axis (Table 2-3) tends to stretch the already elongated M1 site. As a consequence of increasing site distortion with temperature, the site distortion stabilization energy (2ξ) in fayalite will increase. In the B-site of Fe_2SiO_4 spinel, the longer octahedral edges are shared between two occupied octahedra. Thus, they are more rigid and may not have a large thermal expansion. As a result, site distortion stabilization energy in Fe_2SiO_4 spinel may not increase with temperature as much as that in fayalite. Thus, the more rapid decrease of Δ with temperature in fayalite is compensated by its larger gain in 2ξ. As a consequence, ΔCFSE between the two polymorphs may not change significantly with temperature.

Fig. (3-4)

Polarized absorption spectra of an oriented fayalite single crystal at high temperatures and a pressure approximately 10 Kb. The vertical axis is the optical density in cm^{-1}. Numbers are temperature in ^{o}C. (A) β -spectra, and (B) γ -spectra. Note the spreading out of the M-2 peaks, which indecates the increase of site distortion with increasing temperature.

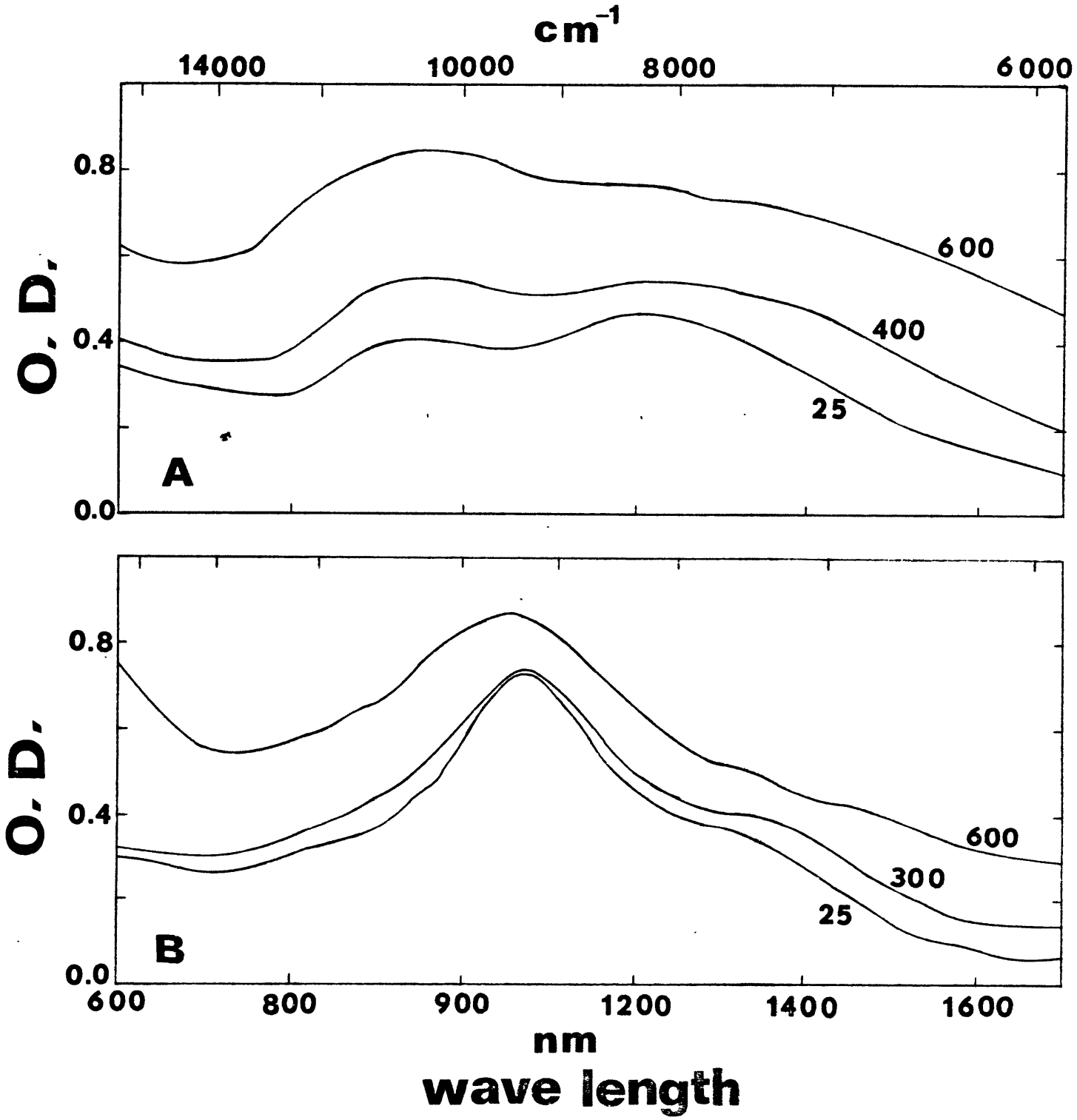
cm-1
14000
10000
8000
6000
0.8
0.4
0.0
O. D.
600
400
25
A
0.8
0.4
0.0
O. D.
600
300
25
B
600
800
900
1200
1400
1600
nm
wave length

There is still another temperature effect on the CFSE. The probability of the sixth d electron in Fe^{2+} occupying the excited state increases with temperature. This tends to decrease the CFSE, and the effect will be more pronounced in fayalite than in Fe_2SiO_4 spinel because of the smaller t_{2g} splitting in the former structure. The increased probability for the sixth d electron to occupy the excited state, mainly of the other two t_{2g} energy levels, with increasing temperature, not only decreases the CFSE, but also increases the electronic configuration entropy (S_e). The latter factor has a pronounced effect on the crystal field stabilization, as will be discussed in the next section.

3-5: Electronic Configurational Entropy:

As pointed out previously, the CFSE is but one of two components that determines the free energy lowering by the crystal field splitting. The other factor is the change of configurational entropy, S_{CFS}, due to the crystal field splitting. Before applying the crystal field, the free Fe^{2+} ion has five degenerate 3d orbitals. The probabilities of the sixth d electron and the "hole" to occupying each of these orbitals are 1/5 and 4/5, respectively. This corresponds to an electronic configurational entropy of $S_e = -2x5xR(\frac{1}{5}\ln\frac{1}{5} + \frac{4}{5}\ln\frac{4}{5})$ or about 10 cal/2mole, where the factor 2 arises from the two Fe atoms in each formula Fe_2SiO_4. In a distorted octahedral site, the degeneracy of the orbitals is eliminated, and the sixth d electron can only occupy one orbital (the

ground state). The electronic configurational entropy in this case is zero, so that the change of the electronic configurational entropy is S_{CFS} = -10 cal/mole. However, according to Boltzmann's distribution law, there is a finite probability of the sixth d electron occupying the higher energy orbitals (excited state), and this probability is proportional to exp ($-h\nu/kT$), where $h\nu$ is the energy of the transition from the ground state to the excited state. At a temperature corresponding to $kT = h\nu$, a significant fraction of the sixth d electrons will occupy the excited state. This will make a contribution to the electronic configurational entropy comparable to that of adding a degenerate orbital of the ground state. Thus, at each temperature corresponding to conditions of kT equaling the energies of transitions 1, 2, 5, 6, and 10 (Figure 3-1), the electronic configurational entropy of the particular polymorph will suddenly increase. A semi-quantitative diagram showing the increase of S_{CFS} with temperature for the two polymorphs is shown in Figure (3-5). It is noted that above a temperature of 700°C, S_{CFS} in fayalite is very high, while it is virtually zero in Fe_2SiO_4 spinel. The magnitude of ΔS_{CFS} is so large at high temperature that it is comparable to the whole entropy change of the olivine→spinel transition (Table 5-1). The rapid increase of the electronic configurational entropy with temperature in fayalite is due to the relatively smaller energy splitting of t_{2g} levels. The rapid increase of electronic configurational entropy in fayalite at 700°C and 1600°C may greatly increase the slope

Fig. (3-5)

Schematic diagram showing the rapid increase of the electronic configurational entropy with temperature in fayalite. The electronic configurational entropy in Fe_2SiO_4 spinel is almost unchanged below $2000^{o}C$.

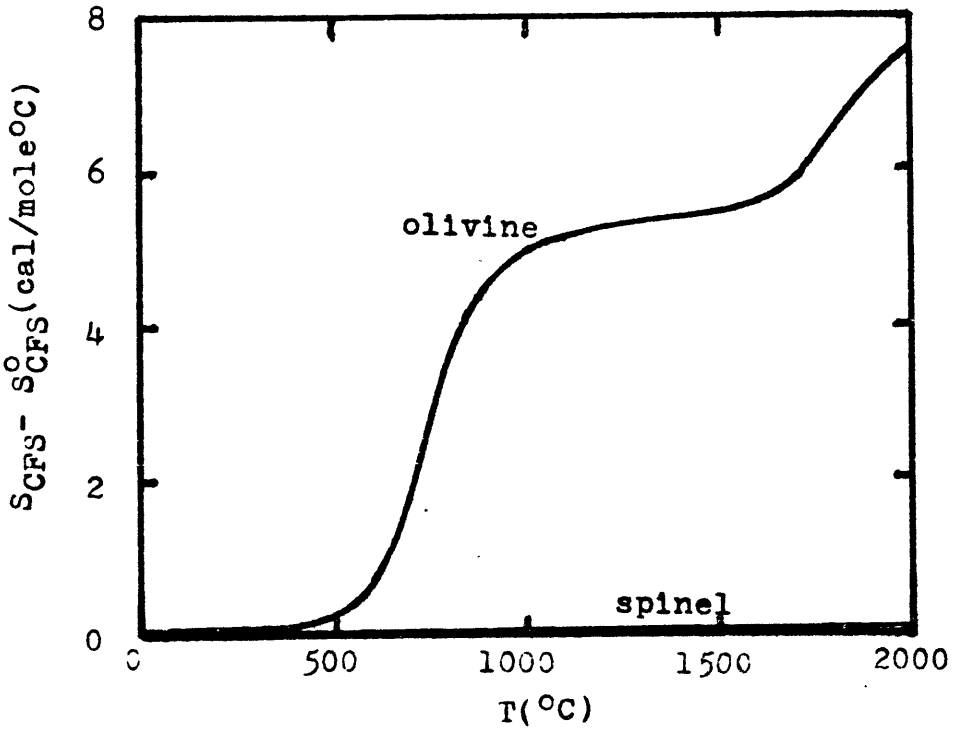
8
6
4
2
0
olivine
spinel
0
500
1000
1500
2000
T(°C)
$S_{CFS} - S^{o}_{CFS}$ (cal/mole°C)

(dP/dT) of the olivine-spinel phase boundary near these two temperatures. However, it is not known whether the olivine-spinel phase boundary in Fe_2SiO_4 has a gentle slope below 700°C, because all the experimental data have been obtained above this temperature (Akimoto and Fujisawa, 1966; Akimoto et al., 1967). It is also impossible to know whether this phase boundary has a larger slope above 1600°C, because this temperature is above the melting points of both fayalite and Fe_2SiO_4 spinel. However, Akimoto et al. (1967) observed a rapid decrease of the slope of the phase boundary between 1200°C and the triple point of α-γ-l (Figure 1-3). If the above argument is valid, this deflection of the olivine-spinel phase boundary may not be due to the change of electronic configurational entropy, but may be due to some other effect. Jackson et al. (1974) have proposed that the entropy of spinel may increase rapidly due to disordering of Fe and Si ions at high temperature, and this effect may be responsible for the decrease of the slope of the olivine-spinel phase boundary above 1200°C. However, had we assumed a smaller energy splitting of t_{2g} levels in Fe_2SiO_4 spinel, then the decrease of this slope might also be due to the increase of the electronic configurational entropy of the spinel.

3-6: Crystal Field Stabilization:

The total contribution of the crystal field splitting to the free energy decrease of the olivine→spinel transition in Fe_2SiO_4 is expressed by eq. (3-1). The calculated ΔG_{CFS} as

a function of temperature and pressure is shown in Figure (3-6). It is seen that ΔG_{CFS} increases with both temperature and pressure. The contribution of the electronic configurational entropy to ΔG_{CFS} is so important that the latter may become positive above a temperature of approximately 1600°C (Figure 3-6). Thus, although the crystal field splitting may facilitate the olivine→spinel transition at low temperature below 1600°C, it may become an additional barrier to the transition at high temperature above 1600°C. The crystal field splitting may have no effect on the olivine→spinel transition at temperatures around 1600°C.

Because the crystal field splitting contributes an amount, ΔG_{CFS} to the free energy change (ΔG) of the olivine→spinel transition, it can also affect the transition pressure and thus displace the equilibrium phase boundary. Hence, $\Delta G = \Delta G' + \Delta G_{CFS} = \Delta V \Delta P$, where $\Delta G'$ is the free energy change for the olivine→spinel transition under the hypothetical condition of no crystal field splitting, ΔV is the volume change of the transition, and ΔP is the overpressure or the pressure beyond the equilibrium phase boundary. At the transition pressure neglecting the crystal field splitting, $\Delta G' = 0$, $\Delta P = \Delta P_{CFS}$, where ΔP_{CFS} ($=P'-P_{CFS}$) is the difference of transition pressure between conditions without and with the crystal field splitting. Thus, $\Delta G_{CFS} = \Delta V \Delta P_{CFS}$, or $\Delta P_{CFS} = \Delta G_{CFS}/\Delta V$. The heavy solid line in Figure (3-7) is the experimentally determined phase boundary for the olivine→spinel transition in Fe_2SiO_4. The equation for this boundary is P(kb) = 25.5 + 0.026T(°C)

Fig. (3-6)

Schematic diagram showing ΔG_{CFS} for the olivine→spinel transition in Fe_2SiO_4 as a function of P and T. Note ΔG_{CFS} increases with temperature and may become positive above approximately 1600°C.

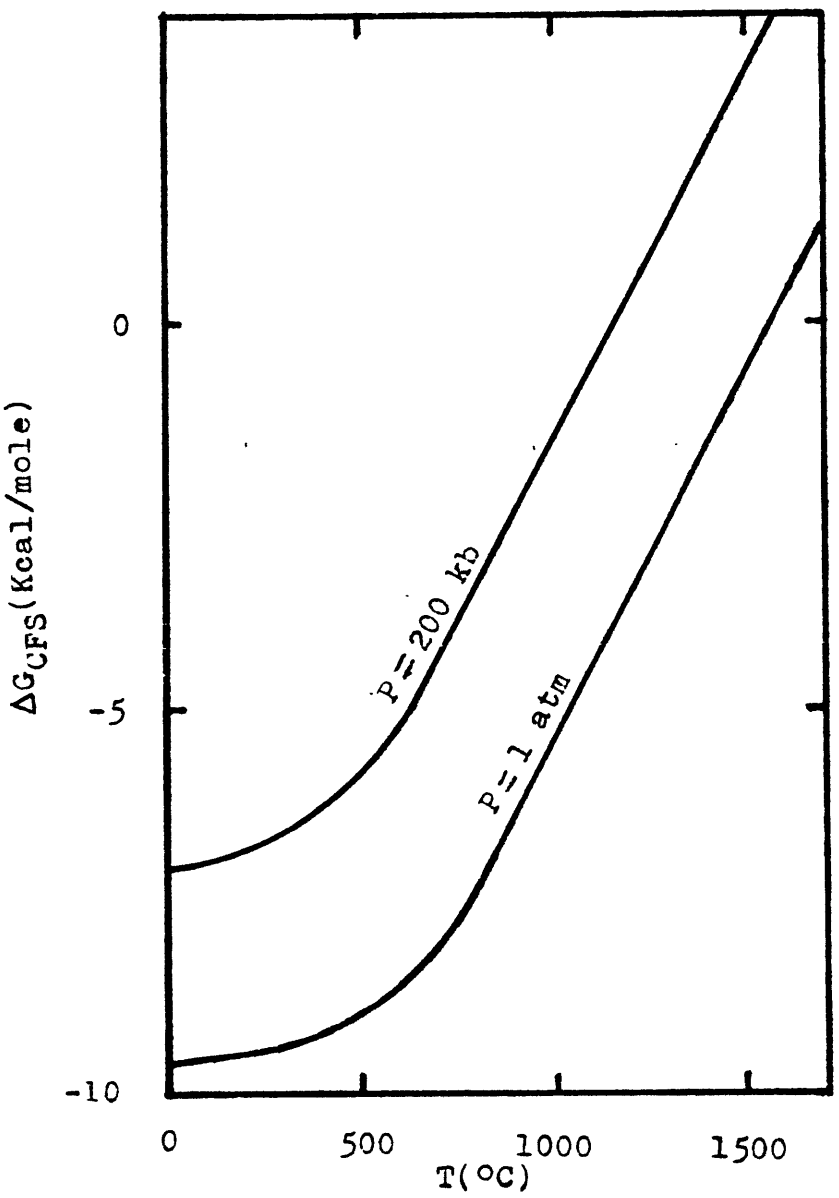
0
-5
-10
ΔG_{CFS}(Kcal/mole)
P=200 kb
P=1 atm
0
500
1000
1500
T(°C)

Fig. (3-7)

Schematic diageam showing the possible crystal field stabilization on the olivine→spinel transition in Fe_2SiO_4. Heavy solid line is the experimentally determined phase boundary(Mao et al, 1969). Dashed and dotted lines are hypothetical phase boundaries, assuming no crystal field stabilization for the transition. The former and the latter correspond to the smaller energy splitting of t_{2g} energy levels in fayalite and in Fe_2SiO_4 spinel, respectively. For reference, the olivine-spinel phase boundaries in Mg_2SiO_4 taken from Fig. (1-3) are shown in light Y-shaped lines.

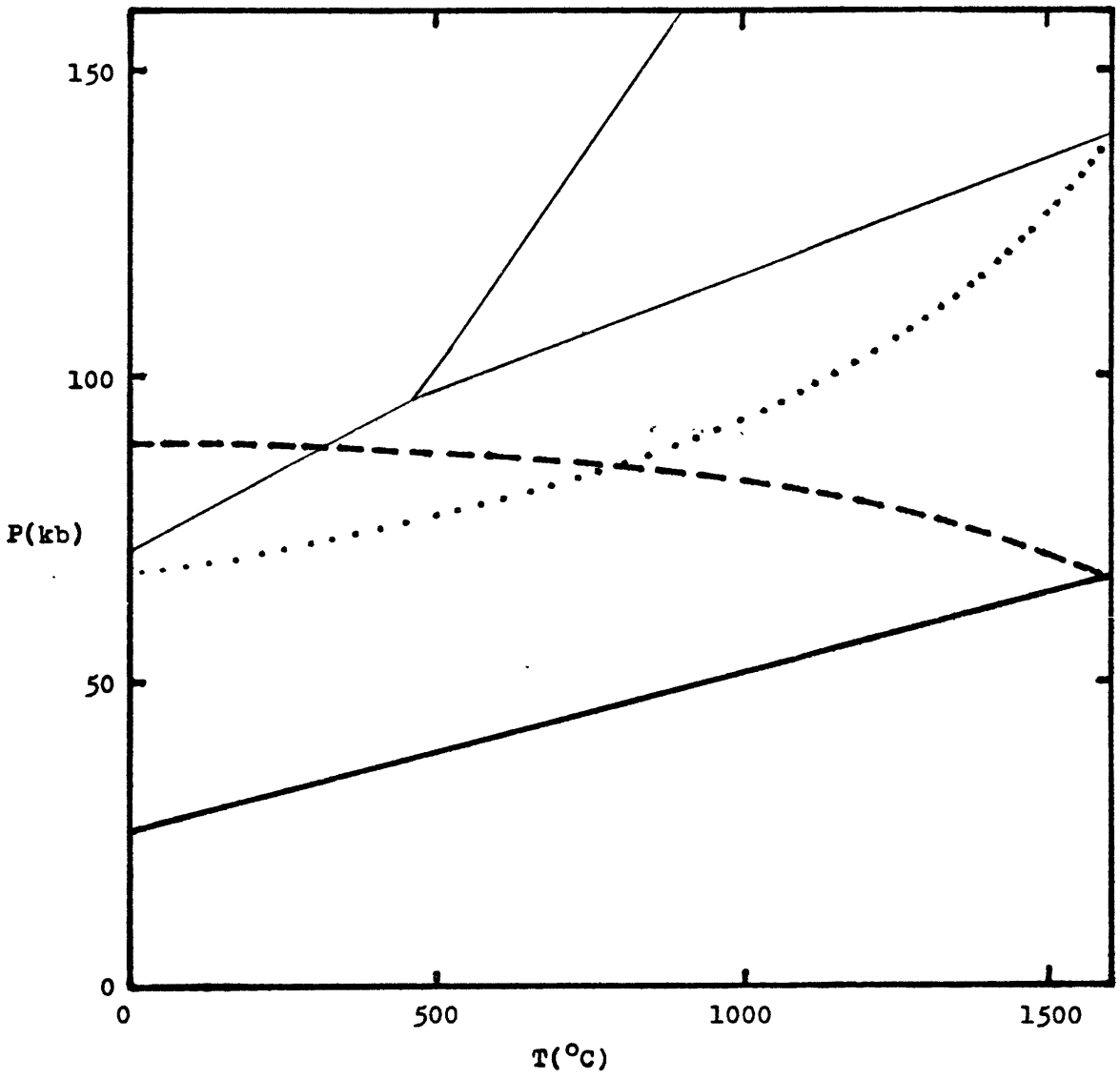
150
100
50
0
P(kb)
0
500
1000
1500
T(°C)

(Mao et al., 1969) (Table 1-1). Using the above estimated value of ΔG_{CFS}, and ΔV calculated by Birch-Murnagham equation of state (eq. 3-3) (neglecting the small temperature effect), the calculated hypothetical phase boundary for the olivine→spinel transition without crystal field splitting is shown as the dashed line in Figure (3-7). It is interesting to observe that although the crystal field splitting can stabilize the transition by approximately 89 kb at low temperature, the stabilization effect will decrease with increasing temperature. In fact, if the above argument is correct, the crystal field splitting may change the slope of the olivine-spinel phase boundary from negative to positive. However, we emphasize here that the whole argument above is based on the assumption of the amount of the splitting of the t_{2g} orbitals. Had we assumed a smaller splitting energy for the t_{2g} orbitals in spinel (transition 10 in Figure 3-1) compared to that in fayalite (transitions 1 and 5), we would reach an opposite conclusion. In this case, the change of electronic configurational entropy (ΔS_{CFS}) will also stabilize the transition as does ΔCFSE, and the phase boundary without crystal field splitting will have a higher positive slope compared to the real one, as shown by the dotted line in Figure (3-7).

Since $\Delta G = \Delta E + P\Delta V - T\Delta S$, where ΔE is the change of internal energy, at the equilibrium phase boundary of the olivine→spinel transition, $\Delta G = 0$, so the transition pressure $P = (T\Delta S - \Delta E)/\Delta V$. Syono et al. (1971) have assumed that both

ΔS and ΔV are each approximately the same for the olivine→spinel transitions of different compositions, so that the transition pressure P is proportional to ΔE. They then further assumed that ΔE is linearly proportional to the ratio of ionic radii of the octahedrally coordinated cation to the tetrahedrally coordinated cation (R_M/R_T), and predicted a linear increase of transition pressure P with the ratio R_M/R_T. They, therefore, noticed that at 1000°C, the ratio of R_M/R_T in Fe_2SiO_4 implies a transition pressure of about 150 kb, which is higher than the 120 kb for the transition in Mg_2SiO_4. The measured transition pressure in Fe_2SiO_4 is only about 50 kb. Syono et al. (1971) attributed this lowering of actual transition pressure to the effect of crystal field stabilization. However, Navrotsky (1973) has shown that although ΔV^o for the olivine→spinel transition of silicates and germanates may be approximately the same, ΔS^o can differ by a factor of more than 4 (e.g. 4.6 cal/mole°C in Fe_2SiO_4 and 1.0 cal/mole°C in Ni_2SiO_4). Thus, the assumption of Syono et al. (1971) of a linear relationship between P and R_M/R_T may not be valid. Our calculation above indicates that at 1000°C, the crystal field stabilization for the olivine→spinel transition is negligible, contrary to the prediction of Syono et al. (1971). In this case, the lower transition pressure in Fe_2SiO_4 compared to that in Mg_2SiO_4 may be due to some other cause, such as the less ionic character of bonds in the former structures (Kamb, 1968). Mao and Bell (1972) have calculated ΔP_{CFS} could be as high as 100 kb. However, their calcula-

tion may not be valid because: (1) they neglected the entropy contribution of the crystal field splitting; (2) they neglected the Jahn-Teller energy in the spinel; (3) they used the value of ΔV at the predicted transition pressure (150 kb) instead of the observed transition pressure (50 kb); and (4) they assumed identical pressure and temperature coefficients for CFSE in both fayalite and Fe_2SiO_4 spinel. The first three considerations will change the calculated value of ΔP_{CFS} by a factor of 2 or more. Thus, the question of whether the crystal field splitting can stabilize the olivine→spinel transition in Fe_2SiO_4 at high temperature is unanswered. Accurate experimental data on crystal field splitting, especially for t_{2g} levels, are needed to clarify this point.

Chapter 4

MECHANISMS

4-1: Introduction:

Although the stability fields and crystal structures of the three polymorphs, α-, β-, and γ-M_2SiO_4 have been studied in detail, mechanisms for their transitions have not been discussed. The mechanism is important because it determines the kinetics of the transition. We shall here attempt to deduce the possible mechanisms of transition from the crystal structural features of the three polymorphs.

4-2: Nucleation and Growth Model:

As described previously, all three structures (α, β, and γ) are based upon closest packing of oxygen atoms. The α-structure is based on the h.c.p., and the β- and the γ-structures are based on the c.c.p. of oxygen atoms. Thus, the α→β, and the α→γ transitions require a rearrangement of oxygen atoms, but the β→γ transition does not. The former two transitions are similar in terms of the h.c.p.→c.c.p. transition of oxygen atoms and will be discussed first.

The h.c.p.→c.c.p. transition rearranges the closest packed atomic layers from ABABAB to ABCABC, where A, B, and C denote the three distinct positions in the closest packed layer. Thus, the transition will displace 4 out of 6 atomic layers according to this order: A→C, B→A, A→B, and B→C. Therefore, two thirds of atoms need to be remobilized during

the transition, although each atom moves only about one interatomic distance and there is no long-range diffusion of atoms. The h.c.p.→c.c.p. transition requires a breaking and later reformation of first coordination bonds, and, therefore, it falls into the reconstructive transition category of Burger (1951).

Elements describing the h.c.p.→c.c.p. transition include C (hexagonal and cubic diamonds), Ca, Do, Ni, Pb, Sc, Sr, N_2 molecules, and large rare earth elements such as La, Ce, and Pr. Other minerals, besides these involved in the olivine→spinel transitions ($\alpha\rightarrow\beta$, and $\alpha\rightarrow\gamma$), whose large atoms undergo h.c.p.→c.c.p. transitions include the sphalerite-wurzite and the perovskite-ilmenite pairs. If the h.c.p.→c.c.p. transition involves only one element, such as Co, the transition may proceed rapidly by a mechanism called martensite transition and may approach the speed of sound. The martensite transition operates by sweeping off a glissile interface, which is a strain-invariant phase or strain-free plane, across the transforming phase. The transforming and the transformed phases are joined together by this glissile plane, which is called the habit plane, with a definite orientation relationship between the two structures. The martensite transition relates to the two structures on a two-dimensional plane, just as the displacive transition relates them in three-dimensional space (Roy, 1973). Buerger (1934) suggested a simple shearing mechanism for the c.c.p.→h.c.p. transition in Co. The transition is achieved by shearing of the c.c.p.

structure along the habit plane of (111) in the direction of (112). By analogy, the h.c.p.→c.c.p. transition for a pure element can be achieved by shearing of the h.c.p. structure along the habit plane of (0001) in the direction of $(10\bar{1}0)$, as depicted by Figure(4-1). The shearing occurs on every other layer parallel to the habit plane. Since the shearing requires breaking all bonds of the first coordination on the plane, this has a large activation energy and is inconsistent with the observed fast rate of transition. Thus, other mechanisms must be operative to reduce the activation energy. One possible mechanism will be the fast propagation of dislocations on the shearing plane. The propagation of a dislocation will break the bonds one by one instead of all at the same time, thus greatly reducing the activation energy.

Although the martensite mechanism can be important for the h.c.p.→c.c.p. transition in a pure element, it cannot operate in the olivine spinel→transitions ($\alpha\rightarrow\beta$ and $\alpha\rightarrow\gamma$). The reason for this is the presence of cations which hinder the simple shearing mechanism for the oxygen atoms. In addition, the distribution of cations in olivine is such that they cannot be moved to positions in a spinel phase (β or γ) by any shearing model for the h.c.p.→c.c.p. transition of oxygen atoms. The redistribution of cations in the olivine→spinel transition requires the reaction to proceed by short range diffusion corresponding to about one cation-cation distance. Although the coordination numbers for all atoms are not changed, all bonds of both cations (Mg, Fe, and Si) and oxygen atoms are

Fig. (4-1)

Simple shearing mechanism for the mutual transitions of h.c.p.-c.c.p. structures(after Buerger, 1934).

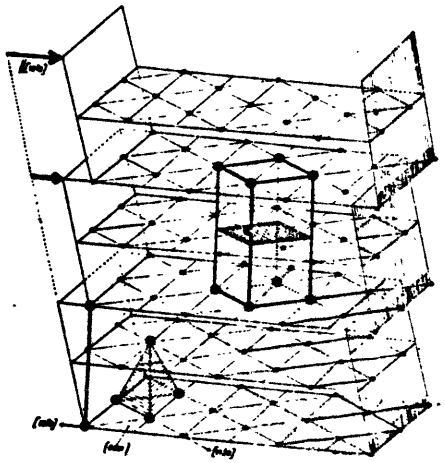

h.c.p

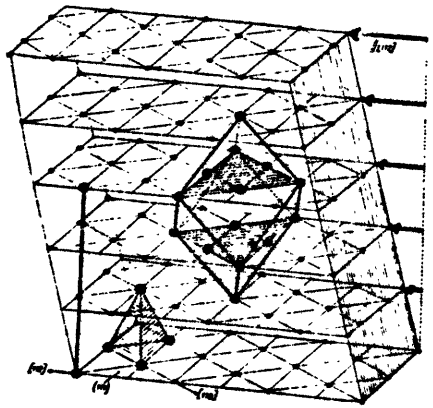

c.c.p.

required to break and reform by diffusion during the olivine→spinel transition. Thus, the transition does not conform with the martensite mechanism but can best be described by models of nucleation and growth, as proposed by Sung and Burns (1976). This nucleation and growth model has been confirmed in our kinetic experiments for the olivine→spinel transition, as will be described in Chapter 8.

The kinetics of the martensite transition are generally characterized by the following features: (1) non-quenchable, (2) athermal, i.e. the transition is not facilitated by increasing temperature, (3) reversible with negligible hysteresis, (4) the degree of transition is not time dependent at constant temperature and pressure, and (5) the transition is apt to be induced by shearing deformation. None of these characteristics of the martensite transition were observed to exist in our experiments of the olivine→spinel transition. On the contrary, our observations (Chapter 8) indicate: (1) the transition is quenchable. Both olivine and spinel can be preserved metastably for an indefinite period of time provided the temperature is lower than a critical value, (2) the transition is greatly facilitated by increasing temperature, (3) the degree of transition increases with time at constant temperature and pressure, (4) the transition may have a large hysteresis at low temperature, and (5) deformation alone will not induce the transition, although it may promote the transition rate at temperatures above a critical value. Although the olivine→spinel transition in $(Mg,Fe)_2SiO_4$ has

been measured under quasi-hydrostatic conditions, it is expected to occur under hydrostatic conditions as well. Thus, the kinetics of the olivine→spinel transition excludes martensitic mechanism and probably follows a model of nucleation and growth. In the following discussion, we will develop the model of nucleation and growth for the mechanism of the olivine→spinel transition.

The model of nucleation and growth assumes that atoms migrate independently across the interphase boundary during the transition. This contrasts with the cooperative motion of atoms in the martensite transition. Nucleation and growth are the two stages of development of the new phase. During the nucleation state, atoms cluster to form metastable nuclei of the new phase. The nuclei are metastable because surface and strain energies are created during their formation. These two energies form a barrier to nucleation. However, when the nucleus grows to reach a critical size, the lowering of the chemical-free energy begins to outweigh the energy barrier for nucleation. This starts the growth stage of the transition, and the stable super-critical sized nucleus begins to grow steadily thereafter. Based on the model of nucleation and growth, the semi-quantitative calculation for the kinetics of the olivine→spinel transition will be treated in Chapter 6.

4-3: Nucleation and Growth Mechanisms:

For the transition in an infinite perfect crystal, nuclei will form randomly within the crystal, so that homogeneous

nucleation (volume nucleation) prevails. For the transition in a real material, nuclei will form preferentially on crystal heterogeneities which have higher energies than in the perfect crystals, and heterogeneous nucleations will dominate. All nucleation mechanisms are competing processes. The relative importance of each nucleation mechanism depends on the nature and the abundance of the crystal heterogeneities, as well as the P-T conditions. Semi-quantitative calculations of the nucleation rate for the major nucleation mechanisms of the olivine→spinel transition are described in Chapter 6.

The nature of the olivine-spinel interphase boundaries (interfaces) is not known. However, the interface will be incoherent except at the very beginning of the formation of the spinel nucleus (Chapter 6). The incoherent interface is a region of closely spaced dislocations and vacancies. The growth of the nucleus is then a complicated process of advancing this interface by a combination of dislocation climb, glide, and vacancy diffusion. The activation energy of growth (Q_a), i.e. the activation energy of migrating atoms across the interface, may have a magnitude comparable to the activation energy of grain boundary diffusion. The latter usually falls within 1/2 to 2/3 of the activation energy for lattice diffusion. The activation energy of lattice diffusion for the slowest species in forsterite has been determined by Goetze and Kohlstedt (1973) to be approximately 135 Kcal/mole. Thus, Q_a may fall within the range of 68-90 Kcal/mole for the olivine→spinel transition of Mg-rich composition. The activa-

tion energy for lattice diffusion may increase with pressure because the activation volume (ΔV^*) for the activated state. However, the migration of atoms across the olivine-spinel interphase may be favored by dislocations and vacancies on the interface and need not pass through a stage of increased volume. This could imply that the activation volume for the growth of spinel is small, and thus the activation energy of growth is less pressure dependent than that for lattice diffusion.

We shall now discuss the possible mechanism of the $\beta \rightarrow \gamma$ transition. Because the oxygen packings for the two structures are identical, they may remain unchanged during the transition. Thus, the $\beta \rightarrow \gamma$ transition may proceed by cation diffusion only. This implies that the $\beta \rightarrow \gamma$ transition could be an intracrystalline process. In this respect, it resembles an order-disorder transition. In addition, as will be shown later that the $\beta \rightarrow \gamma$ transition may also result in domain structure, which is characteristic of an order-disorder transition. However, the $\beta \rightarrow \gamma$ transition differs from the order-disorder transition in two major ways. First, the diffusion of cations during the $\beta \rightarrow \gamma$ transition changes the patterns of cation distribution in the two structures, but the diffusion of cations during the order-disorder transition involves only interchange of cations of different species and leaves the pattern of the cation distribution unchanged. Second, the $\beta \rightarrow \gamma$ transition changes the cation distribution from one pattern to the other without intermediate stages, whereas on order-disorder transition is gradational and can extend over a range of intermediate stages.

As a consequence, the $\beta \rightarrow \gamma$ transition is a first order transition, while the order-disorder transition is a higher order transition.

The $\beta \rightarrow \gamma$ transition can be achieved by many paths of cation diffusion. The path with the least activation energy will be followed in a real transition. Although the patterns of cation distribution are different between the two structures, locally there are similar regions. A close examination of the two structures has revealed that they can be overlapped three-dimensionally in such a way that only one quarter of the divalent cations (Mg, Fe) and one-half of the tetravalent cations (Si) need to be redistributed for their mutual transition, as shown in Figure (4-2). According to this mechanism, the redistribution of this minor portion of cations can be accomplished by diffusion in sparsely isolated bands parallel to (010) in the β-structure or to (110) in the γ-structure (Figure 4-2). The diffusion paths for the divalent cation follows either V_M-M through one shared edge, or M-V_T-V_M through two shared faces; and the diffusion path for the tetravalent cation follows either T-V_T through one shared edge, or T-V_M-V_T through two shared faces (Figure 4-2), where M, T, V_M, and V_T denote occupied octahedra and tetrahedra, and unoccupied octahedra and tetrahedra, respectively. As the activation energy for the diffusion through a shared face will be much less than through a shared edge, we favor the paths of cation diffusion through shared faces. This mechanism leaves the maximum part of the structure unchanged and requires the mini-

Fig. (4-2)

Schematic diageam showing the possible growth mechanism for the $\beta \rightarrow \gamma$ transition. Parallelograms and triangles represent occupied octahedra and tetrahedra, respectively. Cross-hatched, open, and dotted polyhedra represent the three positions perpendicular to the diagram as shown by the legend at the bottom. Upper and lower diagrams show the β- and the γ- structures, respectively. Arrows in the β-structure indicate paths of cation diffusion which can transform the β-structure into the γ-structure. Note that the major part of the β-structure remains unchanged and the diffusion bands are restricted to certain planes during the $\beta \rightarrow \gamma$ transition.

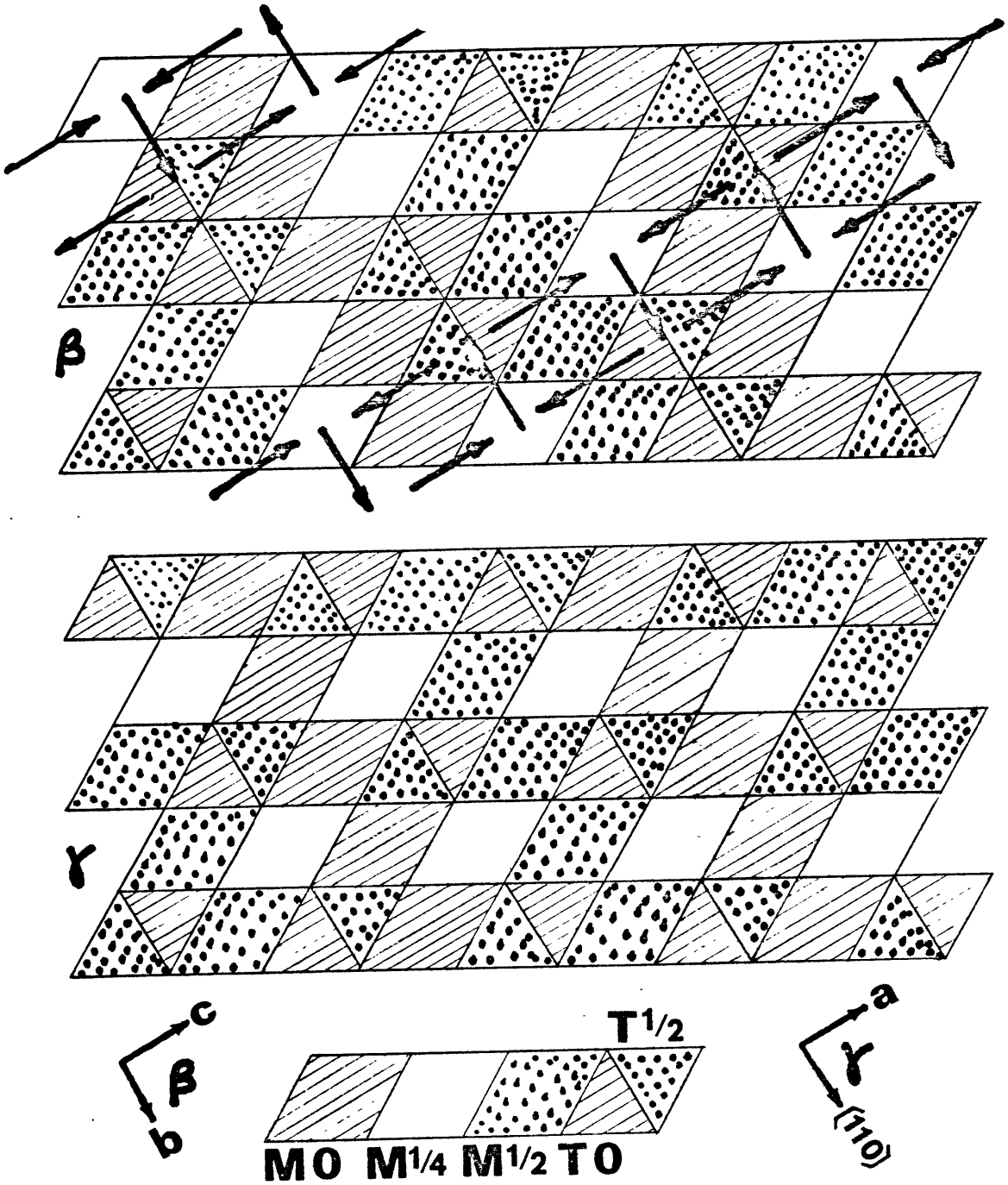
β
γ
c
β
b
T1/2
a
γ
[110]
M0 M1/4 M1/2 T0

mum amount of diffusion. Thus, it is likely to be operative in the $\beta \rightarrow \gamma$ transition. The nucleation and growth of the γ-structure are accomplished by initiating local cation diffusion and by spreading out the transformed bands. If two γ-structures developed in this way meet in phase, i.e. the repetition of the two cation patterns matchs, they merge into a single continuous phase. On the other hand, if they meet out of phase, then the two substructures will be separated by an anti-domain boundary. The verification of the presence of the domain structure in the γ-structure transformed from the β- structure awaits future studies of transmission electron microscopy (TEM).

According to our model, the activation energy of growth for the $\beta \rightarrow \gamma$ transition corresponds to that for cation diffusion in the β-structure. The activation energy of cation diffusion in the β-structure is not known; however, it may have a magnitude similar to that in the α-structure because of the similarity of oxygen closest packing between the two structures. The activation energy of cation diffusion in the β-structure may be slightly higher than that in the α-structure because of the more compact packing of the β-structure. The activation energy for divalent cation diffusion in the α-structure under pressure has been studied by Misener (1975). For the possible olivine composition in the mantle, $Fo_{0.9}$, it can be expressed by Q_a (Kcal/mole) = 58 + 0.13P(kb). As Q_a for a silicon ion will be higher than that for a divalent cation, the above expression of Q_a as a function of pressure could be the lower limit for

the activation energy of growth of the $\beta \rightarrow \gamma$ transition. It is surprising to note that the activation energy of growth for the $\beta \rightarrow \gamma$ transition could be comparable to that for the $\alpha \rightarrow \beta$ or the $\alpha \rightarrow \gamma$ transitions at low pressure estimated previously, because the former transition involves no change in the oxygen framework while the later transitions do. However, one might envisage that the breaking down of the oxygen framework would have the effect of facilitating atomic transport. Thus, the similarity of activation energies between these two types of transition may be reasonable.

Chapter 5

THERMODYNAMICS

5-1: Introduction:

The decrease in Gibbs free energy forms the fundamental driving force of phase transformations. In order to have a thorough understanding of the olivine→spinel transition under different physical conditions in the mantle, a knowledge of thermidynamic quantities, especially Gibbs free energies, of the two phases at high pressure and high temperature is essential. Although some scattered thermodynamic data for the olivine→spinel transition in the Mg_2SiO_4-Fe_2SiO_4 system, which are summarized in Table (5-1), have been reported in literatures, a systematic synthesis of such data has not been attempted. In this chapter, a complete, quantitative derivation of basic thermidynamic quantities as functions of P and T for olivine and spinel in the Mg_2SiO_4-Fe_2SiO_4 system is presented. The derivation of these thermidynamic quantities is self-consistant and values agree well with the existing experimental data. Based on the derivation, a more complete picture of the variations of the Gibbs free energies of olivine and spinel, as well as the fundamental driving forces for their mutual transitions, as functions P, T and composition has emerged. This enables one to predict thermodynamic properties of the olivine→spinel transition at physical conditions pertaining to the mantle, but beyond the current capability of laboratory equipment. To start, we shall evaluate volumes of olivine and spinel as functions of P and T.

Table (5-1)

THERMODYNAMIC PARAMETERS OF OLIVINE AND SPINEL.

	Mg_2SiO_4			Fe_2SiO_4	
	α	β	γ	α	γ
$V_{0,298}$ (cm^3/mole)	43.67[a]	40.59[b]	39.60[c]	46.29[d]	42.03[e]
$K_{0,298}$ (Kb)	1293[f]	1660[g]	2090[h]	1201[i]	2063[j]
$(\partial K/\partial P)_T$	5.09[k]	4.1[l]	4.4[m]	5.97[m]	5.5[l]
$(\partial K/\partial T)_P$ (Kb/°C)	-0.152[n]			-0.138[m]	
μ (Kb)	808[o]		1090[m]	536[m]	890[m]
$(\partial \mu/\partial P)_T$	1.82[p]			0.62[m]	
$(\partial \mu/\partial T)_P$ (Kb/°C)	-0.129[q]			-0.10[m]	
$\nu_{0,298}$	0.241[r]		0.278[r]	0.306[r]	0.311[r]
$S_{0,298}$ (cal/mole)	22.75[s]	19.80[t]	17.6[t]	34.7[s]	32.4[u]
$\Delta G^f_{0,298}$ (Kcal/mole)	-15.117[s]	-10.029[v]	-8.995[v]	-7.28[s]	-4.70[u]
$E_{0,298}$ (Kb)	2006[w]		2786[w]	1400[w]	2334[w]

References:

a) Average value of Matsui and Syono(1968)(43.68), Ringwood and Major(1970)(43.79), Fisher and Medaris(1969)(43.62), and Hazen(1975)(43.59).

Table (5-1)
(CONTINUED)

b) Average value of Ringwood and Major(1970)(40.65), Suito (1972)(40.63), and Moore and Smith(1970)(40.48).
c) Average value of Akimoto(1972)(39.62), and Ringwood and Major(1970)(39.58).
d) Average value of Akimoto(1972)(46.28), Ringwood and Major (1970)(46.39), Fisher and Medaris(1969)(46.26), and Hazen (1975)(46.23).
e) Average value of Nishizawa and Akimoto(1973)(42.03), and Ringwood and Major(1970)(42.03).
f) Average value of Kumazawa and Anderson(1969)(1286), Mizutani et al(1970)(1291), Chung(1971)(1281), Graham and Barsch(1969)(1296), and calculated from Hazen's(1975) data(1313).
g) Mizutani et al(1975).
h) Average value of Nishizawa and Akimoto(1973)(2050), Mizutani et al(1975)(2130).
i) Average value of Nishizawa and Akimoto(1973)(1320), Chung (1971)(1220), Clark(1966)(1100), and calculated from Hazen's(1975)data(1162).
j) Average value of Nishizawa and Akimoto(1973)(2050), Mao et al(1969)(2120), Chung(1973)(1960), and Mizutani et al (1970)(2120).
k) Average value of Kumazawa and Anderson(1969)(5.33), Mizutani et al(1970)(4.97), Chung(1971)(5.07), Graham and Barsch(1969)(4.97).
l) Chung(1971)
m) Chung(1973)
n) Average value of Kumazawa and Anderson(1969)(-0.150), Graham and Barsch(1969)(-0.176), and Chung(1971)(-0.131).

Table (5-1)
(CONTINUED)

0) Average value of Kumazawa and Anderson(1969)(811), Graham and Barsch(1969)(816), and Chung(1971)(797).

p) Average value of Kumazawa and Anderson(1969)(1.80), Graham and Barsch(1969)(1.82), and Chung(1971)(1.85).

q) Average value of Kumazawa and Anderson(1969)(-0.130), Graham and Barsch(1969)(-0.136), and Chung(1971)(-0.12).

r) Calculated from $\nu=(3K-2\mu)/(6K+2\mu)$.

s) Clark(1966).

t) Calculated by $S^{\beta(\gamma)}_{0,298}=S^{\alpha}_{0,298}+\Delta V^{\alpha\rightarrow\beta(\gamma)}_{0,298}(dP/dT)^{\alpha\rightarrow\beta(\gamma)}$, slopes of transitions are taken from ref. (c) of Table (1-1).

u) Mao et al(1969).

v) Calculated by $\Delta G^{f\beta(\gamma)}_{0,298}=\Delta G^{f\alpha}_{0,298}-P_{298}\Delta V^{\alpha\rightarrow\beta(\gamma)}_{0,298}$, where P_{298} is the equilibrium transition pressure at $298^{o}K$. P_{298} is taken from ref. (c) of Table (1-1).

w) Calculated from $E=(18K\mu)/(6K+2\mu)$.

5-2: Volume:

Volume as a function of pressure at constant temperature is usually calculated by the Birch-Murnaghan equation of state Birch(1947).

$$P = \frac{3}{2}(K_o)_T\left[\left(\frac{(V_o)_T}{(V_p)_T}\right)^{\frac{7}{3}} - \left(\frac{(V_o)_T}{(V_p)_T}\right)^{\frac{5}{3}}\right]\left[1+\xi\left\{\left(\frac{(V_o)_T}{(V_p)_T}\right)^{\frac{2}{3}}-1\right\}\right] \quad \text{----(5-1)}$$

where $(K_o)_T$ is the isothermal bulk modulus at zero pressure, $(V_o)_T$ and $(V_p)_T$ are isothermal volumes at zero pressure and at pressure P, respectively, and $\xi = \frac{3}{4}\left(\frac{\partial (K_o)_T}{\partial P} - 4\right)$. The first order correction factor $\xi\left\{\left(\frac{(V_o)_T}{(V_p)_T}\right)^{\frac{2}{3}}-1\right\}$ is very small for the olivine and spinel of interest, and can be neglected in most calculations. Although Eq. (5-1) is commonly used in the literature, it is not convenient to use it in the following calculations, because it does not include the volume dependence on temperature and because the volume is not explicitly expressed as a function of pressure. For our purpose, we shall adapt an approximate equation of state which allows the volume dependence on both pressure and temperature to be evaluated with fair accuracy, and which gives a convenient mathematic form to manipulate.

Since

$$d V_{P,T} = (\alpha_T)_P (V_T)_P \, dT - (\beta_P)_T (V_P)_T \, dP \quad \text{----------(5-2)}$$

where $(\alpha_T)_P$ and $(\beta_P)_T$ are the isobaric thermal expansion and the isothermal compressibility, respectively. Dividing Eq. (5-2) by $V_{P,T}$ we have:

$$d \ln V_{P,T} = (\alpha_T)_P \, dT - (\beta_P)_T \, dP \quad \text{----------(5-3)}$$

which upon integration gives:

$$V_{P,T} = V_{P_o,T_o} \exp\left\{\int_{T_o}^{T} (\alpha_T)_P \, dT - \int_{P_o}^{P} (\beta_P)_T \, dP\right\} \quad \text{-----(5-4)}$$

Let $\bar{\alpha}_P$ and $\bar{\beta}_T$ be mean values of $(\alpha_T)_P$ and $(\beta_P)_T$ at the P-T conditions of interest (up to 200 kb and 1600°C), and put P_o=0 kb and T_o=298°K. Then

$$V_{P,T} = V_{o,298}\, exp\{\bar{\alpha}_P (T-298) - \bar{\beta}_T P\} \text{ ----------(5-5)}$$

Substituting appropriate values of $\bar{\alpha}_P$ and $\bar{\beta}_T$ into Eq. (5-5), molar volumes (cm^3/mole) of olivine and spinel forms of Fe_2SiO_4 and Mg_2SiO_4 as functions of P(kb) and T(°K) can be expressed by:

$$V_{P,T}^{\alpha Fe} \doteq 46.29\, exp\{3.1\times10^{-5}(T-298) - 6.8\times10^{-4}P\} \text{ -----(5-6)}$$

$$V_{P,T}^{\gamma Fe} \doteq 42.03\, exp\{2.4\times10^{-5}(T-298) - 4.3\times10^{-4}P\} \text{ ------(5-7)}$$

$$V_{P,T}^{\alpha Mg} \doteq 43.67\, exp\{3.3\times10^{-5}(T-298) - 6.4\times10^{-4}P\} \text{ ------(5-8)}$$

$$V_{P,T}^{\gamma Mg} \doteq 39.60\, exp\{2.5\times10^{-5}(T-298) - 4.2\times10^{-4}P\} \text{ ------(5-9)}$$

where superscripts αFe, γFe, αMg and γMg denote Fe_2SiO_4 olivine, Fe_2SiO_4 spinel, Mg_2SiO_4 olivine, and Mg_2SiO_4 spinel, respectively.

Although Eqs. (5-6) to (5-9) are approximations, their predictions not differ from the high temperature crystallographic data of fayalite (Smyth, 1975) and forsterite (Hazen, 1975) by more than 0.6% at all temperatures up to 1000°C, and they also agree within 0.6% with the high pressure volumes up to 200 kb calculated by Eq. (5-1), using the data of Table (5-1). Thus, they are fairly accurate equations of state and will be used to derive other thermodynamic quantities for olivine and spinel at high pressure and temperature.

5-3: Entropy:

We shall now derive entropy functions for olivines and spinels, based on the above volume functions.

$$dS_{P,T} = \frac{(C_T)_P}{T} dT - (\alpha_T)_P V_{P,T}\, dP \text{ ----------(5-10)}$$

where $(C_T)_P$ is the heat capacity at constant pressure. Again

putting P_o=0 kb and T_o=298°K, and adopting mean values of $\bar{\alpha}_P$, $\bar{\beta}_T$, and $\bar{C}_P$, integration gives molar entropy(cal/mole °K) as a function of P(kb) and T(°K):

$$S_{P,T} = S_{0,298} - 5.70\,\bar{C}_P + \bar{C}_P T \ln T - \frac{23.9\,\bar{\alpha}_P V_{0,298}}{\bar{\beta}_T}\exp\{\bar{\alpha}_P(T-298)\}\{1-\exp(-\bar{\beta}_T P)\} \quad (5\text{-}11)$$

where $V_{0,298}$ is expressed in cm^3/mole and the factor 23.9 converts the unit kb-cm^3/mole °K into cal/mole °K. Substituting $S_{0,298}$ and $V_{0,298}$(Table 5-1) into Eq. (5-11), molar entropies for olivines and spinels are found to be:

$$S^{\alpha Fe}_{P,T} = 34.7 - 5.70\,\bar{C}_P^{\alpha Fe} + \bar{C}_P^{\alpha Fe} T \ln T - 50.44\exp\{3.1\times10^{-5}(T-298)\}\{1-\exp(-4.3\times10^{-4}P)\} \quad (5\text{-}12)$$

$$S^{\gamma Fe}_{P,T} = 32.4 - 5.70\,\bar{C}_P^{\gamma Fe} + \bar{C}_P^{\gamma Fe} T \ln T - 56.07\exp\{2.4\times10^{-5}(T-298)\}\{1-\exp(-4.3\times10^{-4}P)\} \quad (5\text{-}13)$$

$$S^{\alpha Mg}_{P,T} = 22.8 - 5.70\,\bar{C}_P^{\alpha Mg} + \bar{C}_P^{\alpha Mg} T \ln T - 53.82\exp\{3.3\times10^{-5}(T-298)\}\{1-\exp(-6.4\times10^{-4}P)\} \quad (5\text{-}14)$$

$$S^{\gamma Mg}_{P,T} = 17.6 - 5.70\,\bar{C}_P^{\gamma Mg} + \bar{C}_P^{\gamma Mg} T \ln T - 56.34\exp\{2.5\times10^{-5}(T-298)\}\{1-\exp(-4.2\times10^{-4}P)\} \quad (5\text{-}15)$$

Values of heat capacities for olivines and spinels will be evaluated in the next section.

5-4: Gibbs free energy:

Based on the above volume and entropy functions, Gibbs free energies for olivines and spinels can now be calculated. Since

$$dG = -SdT + VdP \quad (5\text{-}16)$$

Substituting Eqs. (5-5) and (5-11) into Eq. (5-16) and integrating, we express molar Gibbs free energy(cal/mole) as a function of P(kb) and T(°K) as:

$$G_{P,T} = G_{0,298} + 298(S_{0,298} - \bar{C}_P) + (6.70\,\bar{C}_P - S_{0,298})T - \bar{C}_P T \ln T + \frac{23.9}{\bar{\beta}_T} V_{0,298}\exp\{\bar{\alpha}_P(T-298)\}\{1-\exp(-\bar{\beta}_T P)\} \quad (5\text{-}17)$$

Substituting appropriate values of $\bar{\alpha}_P$ and $\bar{\beta}_T$ into Eq. (5-17), molar Gibbs functions for olivines and spinels are found to be:

$$G^{\alpha Fe}_{P,T} \doteq G^{\alpha Fe}_{0,298} + 298(S^{\alpha Fe}_{0,298} - \bar{C}_P^{\alpha Fe}) + (6.70\,\bar{C}_P^{\alpha Fe} - S^{\alpha Fe}_{0,298})T - \bar{C}_P^{\alpha Fe} T \ln T + 1.627\times10^{6}\exp\{3.1\times10^{-5}(T-298)\}\{1-\exp(-6.8\times10^{-4}P)\} \quad (5\text{-}18)$$

$$G^{\gamma Fe}_{P,T} \doteq G^{\gamma Fe}_{0,298} + 298\,(S^{\gamma Fe}_{0,298} - \bar{C}_P^{\gamma Fe}) + (6.70\,\bar{C}_P^{\gamma Fe} - S^{\gamma Fe}_{0,298})\,T - \bar{C}_P^{\gamma Fe}\,T \ln T$$
$$+ 2.336\times10^{6} \exp\{2.4\times10^{-5}(T-298)\}[1-\exp(-4.3\times10^{-4}P)] \quad ---(5\text{-}19)$$

$$G^{\alpha Mg}_{P,T} \doteq G^{\alpha Mg}_{0,298} + 298\,(S^{\alpha Mg}_{0,298} - \bar{C}_P^{\alpha Mg}) + (6.70\,\bar{C}_P^{\alpha Mg} - S^{\alpha Mg}_{0,298})\,T - \bar{C}_P^{\alpha Mg}\,T \ln T$$
$$+ 1.631\times10^{6} \exp\{3.3\times10^{-5}(T-298)\}[1-\exp(-6.4\times10^{-4}P)] \quad ---(5\text{-}20)$$

$$G^{\gamma Mg}_{P,T} \doteq G^{\gamma Mg}_{0,298} + 298\,(S^{\gamma Mg}_{0,298} - \bar{C}_P^{\gamma Mg}) + (6.70\,\bar{C}_P^{\gamma Mg} - S^{\gamma Mg}_{0,298})\,T - \bar{C}_P^{\gamma Mg}\,T \ln T$$
$$+ 2.253\times10^{6} \exp\{2.5\times10^{-5}(T-298)\}[1-\exp(-4.2\times10^{-4}P)] \quad ---(5\text{-}21)$$

Since Eqs. (5-18) to (5-21) involve approximations, their validity should be tested by experimental data. Two independent groups of data are available for this test. The first group of data are olivine-spinel phase boundaries (Table 1-1) and the second group of data are standard free energies of formation ($\Delta G^{f}_{0,298}$) and standard entropies ($S_{0,298}$) (Table 5-1). We shall calculate the latter data from the former ones through Eqs. (5-18) to (5-21) and then test the consistancy of the calculated data and the measured ones. First we shall test Gibbs functions for Fe_2SiO_4. At the olivine-spinel phase boundary, $G^{\alpha Fe}_{P,T} = G^{\gamma Fe}_{P,T}$. Thus from Eqs. (5-18) and (5-19), the olivine-spinel phase boundary can be expressed by:

$$\Delta G^{(\gamma-\alpha)Fe}_{0,298} + 298\,(\Delta S^{(\gamma-\alpha)Fe}_{0,298} - \Delta \bar{C}_P^{(\gamma-\alpha)Fe}) + (6.70\,\Delta \bar{C}_P^{(\gamma-\alpha)Fe} - \Delta S^{(\gamma-\alpha)Fe}_{0,298})\,T$$
$$- \Delta \bar{C}_P^{(\gamma-\alpha)Fe}\,T \ln T + 2.336\times10^{6} \exp\{2.4\times10^{-5}(T-298)\}[1-\exp(-4.3\times10^{-4}P)]$$
$$- 1.627\times10^{6} \exp\{3.1\times10^{-5}(T-298)\}[1-\exp(-6.8\times10^{-4}P)] \quad -----(5\text{-}23)$$

where $\Delta G^{(\gamma-\alpha)Fe}_{0,298} = G^{\gamma Fe}_{0,298} - G^{\alpha Fe}_{0,298}$, $\Delta S^{(\gamma-\alpha)Fe}_{0,298} = S^{\gamma Fe}_{0,298} - S^{\alpha Fe}_{0,298}$, and $\Delta \bar{C}_P^{(\gamma-\alpha)Fe} = \bar{C}_P^{\gamma Fe} - \bar{C}_P^{\alpha Fe}$. Each of these three constants is unknoen and needs to be determined. Eq. (5-23) defines a curved phase boundary which approximates a straight line. The olivine-spinel phase boundary in Fe_2SiO_4 has been accurately determined by Akimoto et al(1965,1967) and later revised by Mao et al(1969). It can be approximated by a straight line of equation P(kb)=18.4+0.026(^{o}K) (Table 1-1). Selecting

arbitrarily the following three points on this phase boundary: (P,T)=(26.2,298), (38.5,773), (51.5,1273), and substituting them into Eq. (5-23), we then obtain solutions to the three unknown constants by solving the simultaneous equations:

$$\Delta G^{(\gamma-\alpha)Fe}_{0,298} = G^{\gamma Fe}_{0.298} - G^{\alpha Fe}_{0,298} = 2464 \text{ cal/mole} \quad \text{----------(5-24)}$$

$$\Delta S^{(\gamma-\alpha)Fe}_{0,298} = S^{\gamma Fe}_{0,298} - S^{\alpha Fe}_{0,298} = -2.23 \text{ cal/mole } ^{o}K \quad \text{--------(5-25)}$$

$$\Delta \bar{C}_P^{(\gamma-\alpha)Fe} = \bar{C}_P^{\gamma Fe} - \bar{C}_P^{\alpha Fe} = -0.33 \text{ cal/mole } ^{o}K \quad \text{--------(5-26)}$$

From Table (5-1), measured values of $G^{\gamma Fe}_{0,298}-G^{\alpha Fe}_{0,298}$ and $S^{\gamma Fe}_{0,298}-S^{\alpha Fe}_{0,298}$ are 2580 cal/mole and -2.3 cal/mole ^{o}K, respectively. Both calculated values agree with experimental data within 5%, which is less than the uncertainty of the measurements. Eq. (5-26) has a correct sign and a resonable magnitute, there are no experimental data for comparison. Substituting Eqs. (5-24) to (5-26) into Eq. (5-23), a calculated phase boundary is obtained, which, when plotted out, is almost identical to the experimentally determined phase boundary, P=18.4+0.026T. Thus, despite the approximations used in deriving the Gibbs functions for Fe_2SiO_4, the surprisingly good agreement between them and the measured data strongly supports the validity of Eqs. (5-18) and (5-19).

A similar calculations are now employed to test the validity of the Gibbs functions for Mg_2SiO_4. At the olivine-spinel phase boundary, $G^{\alpha Mg}_{P,T}=G^{\gamma Mg}_{P,T}$. Thus from Eqs. (5-20) and (5-21), this phase boundary can be expressed by:

$$\Delta G^{(\gamma-\alpha)Mg}_{0,298} + 298(\Delta S^{(\gamma-\alpha)Mg}_{0,298} - \Delta \bar{C}_P^{(\gamma-\alpha)Mg}) + (6.70\Delta \bar{C}_P^{(\gamma-\alpha)Mg} - \Delta S^{(\gamma-\alpha)Mg}_{0,298})T$$
$$- \Delta \bar{C}_P^{(\gamma-\alpha)Mg} T \ln T + 2.253\times10^{6}\exp\{2.5\times10^{-5}(T-298)\}[1-\exp(-4.2\times10^{-4}P)]$$
$$- 1.631\times10^{6}\exp\{3.3\times10^{-5}(T-298)\}[1-\exp(-6.4\times10^{-4}P)] \quad \text{------(5-27)}$$

where $\Delta G^{(\gamma-\alpha)Mg}_{0,298}=G^{\gamma Mg}_{0,298}-G^{\alpha Mg}_{0,298}$, $\Delta S^{(\gamma-\alpha)Mg}_{0,298}=S^{\gamma Mg}_{0,298}-S^{\alpha Mg}_{0,298}$, $\Delta \bar{C}_P^{(\gamma-\alpha)Mg}=\bar{C}_P^{\gamma Mg}-\bar{C}_P^{\alpha Mg}$. Again, Eq. (5-27) defines a curved phase boundary which approximates a straight line. There is a wide discrepency for the olivine-spinel

phase boundary in Mg_2SiO_4 determined from experimental data(Table 1-1). Here we adopt the equation P(kb)=57.5+0.053T(^oK) based on screened experimental data(Sung and Burns, 1976). Again we constrain Eq. (5-27) by the following three points on this experimental phase boundary: (P,T)=(73.3,298), (98.5,773), (125,1273). Solving the appropriate simultaneous equations, we get the following values for the constants:

$$\Delta G^{(\gamma-\alpha)Mg}_{0,298} = G^{\gamma Mg}_{0,298} - G^{\alpha Mg}_{0,298} = 6442 \text{ cal/mole} \quad (5\text{-}28)$$

$$\Delta S^{(\gamma-\alpha)Mg}_{0,298} = S^{\gamma Mg}_{0,298} - S^{\alpha Mg}_{0,298} = -5.16 \text{ cal/mole } ^oK \quad (5\text{-}29)$$

$$\Delta \bar{C}_P^{(\gamma-\alpha)Mg} = C_P^{\gamma Mg} - C_P^{\alpha Mg} = -0.28 \text{ cal/mole} \quad (5\text{-}30)$$

From Table (5-1), the measured values for $G^{\gamma Mg}_{0,298} - G^{\alpha Mg}_{0,298}$ and $S^{\gamma Mg}_{0,298} - S^{\alpha Mg}_{0,298}$ are 6122 cal/mole and -5.15 cal/mole ^oK, respectively. Again Eq. (5-30) has a correct sign and resonable magnitute, although there is no experimental data for comparison. The agreement between calculated and measured values is again within 5%, which is less than the uncertainty of the measured data. Thus the derived Gibbs functions for Mg_2SiO_4(Eqs. 5-20 and 5-21) are again quantitatively consistant with the experimental data.

In order to make use of Eqs. (5-18) to (5-21), we need to have estimates of $\bar{C}_P$. According to the approximation of Debye, C_V for atoms at temperatures higher than the Debye temperature will approach a value of approximately 6 cal/ mole ^oK(3R). Debye temperatures for Mg, Fe and Si are 133, 180 and 385^oC, respectively. The Debye temperature for oxygen ions is not known, but may also be several hundred degrees centigrade. As our interest is in the olivine-spinel transition in the transition zone where the temperature is much higher than these Debye temperatures, these C_V's for olivine and spinel in the Mg_2SiO_4-Fe_2SiO_4 system are approximately

6x7=42 cal/mole ^{o}K, since there are 7 atoms per formula unit. From this value we can calculate C_P by:

$$C_P=C_V+(TV\alpha)/\beta \quad \text{----------(5-31)}$$

Thus, at 1000^{o}C $\bar{C}_P^{\gamma Fe} \sim C_P^{\alpha Fe} \doteqdot 44$ cal/mole ^{o}K. According to Eq. (5-31), $\bar{C}_P$ for olivines and spinels may increase in the order γ-$Fe_2SiO_4 \sim$ γ-$Mg_2SiO_4 < \alpha$-$Fe_2SiO_4 \sim \alpha$-Mg_2SiO_4. The difference of $\bar{C}_P$ between spinels and olivines, calculated from Eq. (5-31), is approximately 0.3 cal/mole ^{o}K. This agrees well with our early calculations (Eqs. 5-26 and 5-30) from the derived Gibbs functions. Thus, in the following calculations, we shall assume $\bar{C}_P^{\alpha Fe} \sim \bar{C}_P^{\alpha Mg} \doteqdot 44$ cal/mole ^{o}K. These data also agree with an early estimate of 1.25×10^7 erg/gm ^{o}K ($\sim$ 44 cal/mole ^{o}K) for olivine in the mantle (Jacobs, 1956).

Based on the above estimated values of the heat capacities, values of $G_{0,298}^{\gamma Fe} - G_{0,298}^{\alpha Fe} = 2580$ cal/mole, $G_{0,298}^{\gamma Mg} - G_{0,298}^{\alpha Mg} = 6122$ cal/mole, and entropies from Table (5-1), Gibbs free energies for olivines and spinels as functions of pressure and temperature were calculated based on Eqs. (5-18) to (5-21) and are shown in Fig. (5-1). The notable features of these Gibbs functions are: (1) for the same composition, the free energy of olivine increases with pressure and decreases with temperature more rapidly than does free energy of spinel. Thus, wherever the two free energy curves cross, phase transition may occur; and (2) for the same phase, the free energy of Fe_2SiO_4 increases with pressure but decreases with temperature more rapidly than that of Mg_2SiO_4.

5-5: Regular solution model:

Having evaluated the Gibbs functions for Mg_2SiO_4 and Fe_2SiO_4 endmember olivines and spinels, we shall next calculate the Gibbs

Fig. (5-1)

Gibbs free energies of olivines and spinels as functions of (A) pressure, and (B) temperature. Solid and dashed lines are for olivines and spinels, respectively. Vertical dashed lines mark the equilibrium transition pressures(A), or temperatures(B).

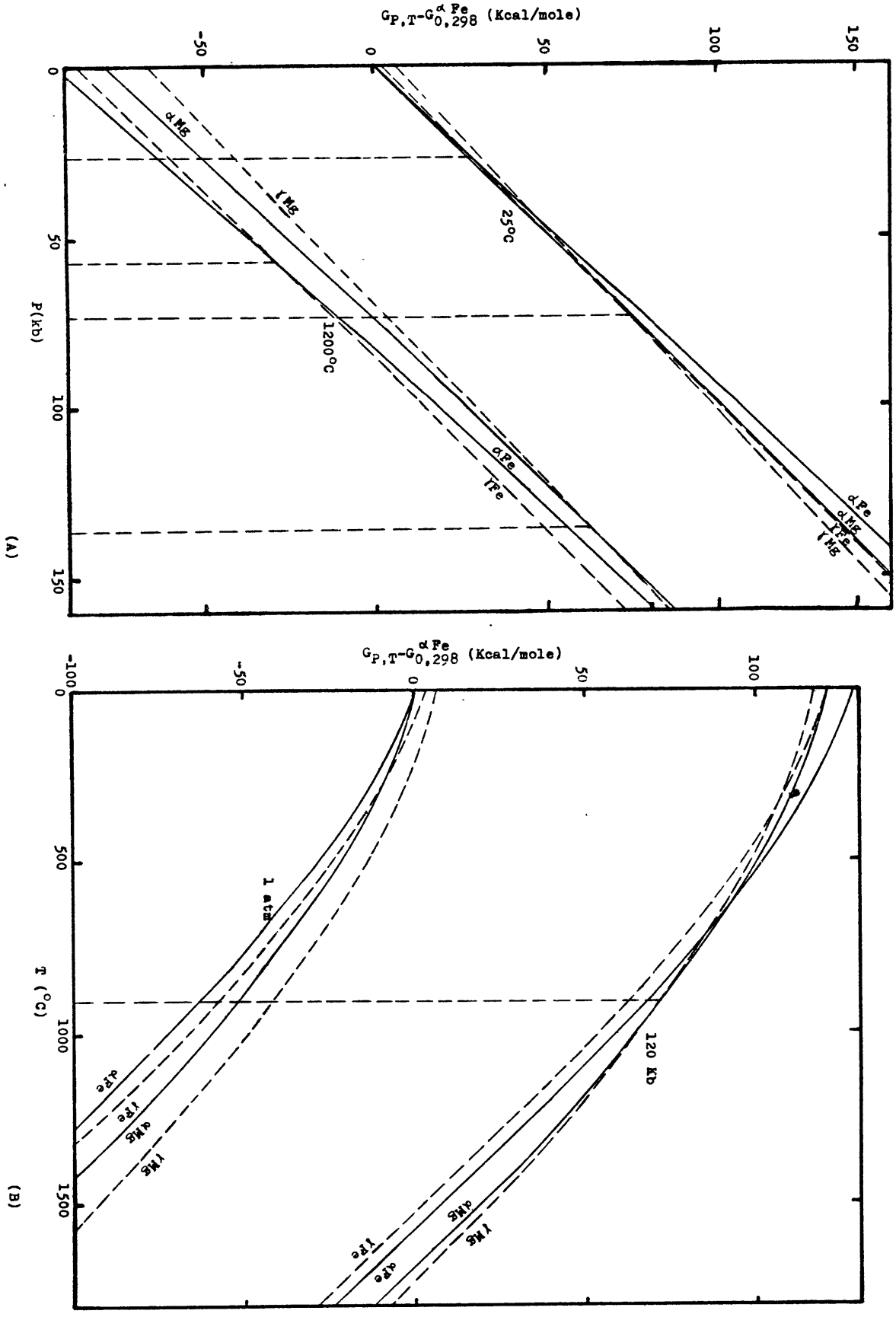
(A)
$G_{P,T}-G^{\alpha Fe}_{0,298}$ (Kcal/mole)
-50
0
50
100
150
P(kb)
0
50
100
150
αMg
γMg
25°C
1200°C
αFe
γFe
(B)
$G_{P,T}-G^{\alpha Fe}_{0,298}$ (Kcal/mole)
-100
-50
0
50
100
T (°C)
0
500
1000
1500
1 atm
120 Kb
αFe
γFe
αMg
γMg

function for intermediate compositions. In order to make this calculation possible, we shall adopt a simple solution model, such as the regular solution model, for both olivine and spinel. First, we shall calculate Gibbs functions based on the model of symmetrical regular solution(Thompson, 1967). According to this model,

$$\mu^{Fe}=G^{Fe}_{P,T}+2RT\ln X^{Fe}+W_G X^{Mg\,2} \quad \text{----------(5-32)}$$

$$\mu^{Mg}=G^{Mg}_{P,T}+2RT\ln X^{Mg}+W_G X^{Fe\,2} \quad \text{----------(5-33)}$$

where μ , R, X, and W_G are the chemical potential, the gas constant, mole fraction, and interaction energy, respectively. Superscripts Fe and Mg again are abbreviations for Fe_2SiO_4 and Mg_2SiO_4, respectively. When olivine is in equilibrium with spinel, we have

$$\mu^{Fe}_{\alpha}=\mu^{Fe}_{\gamma} \quad \text{----------(5-34)}$$

$$\mu^{Mg}_{\alpha}=\mu^{Mg}_{\gamma} \quad \text{----------(5-35)}$$

Thus, using Eqs. (5-18) through (5-21) and (5-32) through (5-35), the interaction energies, which measure the degree of non-ideality for olivine and spinel at a given pressure and temperature can be calculated from their equilibrium compositions. Using this method, we have calculated W_G^{α} and W_G^{γ} , based on isothermal sections of the Mg_2SiO_4-Fe_2SiO_4 system determined by Akimoto et al(1976)(Fig. 1-2). The results indicate that both interaction energies are positive over the whole P-T range of two-phase coexistence. However, their values are so scattered, ranging from less than 1Kcal/mole to more than 10 Kcal/mole, that they fail to show any systematic variation with pressure and temperature. Similar results have also been reported by Nishizawa and Akimoto(1973). The scattering of calculated interaction energies may originate from the inaccurate

compositions of coexisting olivine and spinel. If the two-phase region in Fig. (1-2) could be pushed further apart, especially for the low temperature isothermal section, the calculated interaction energies would show a considerably smaller degree of scattering. In this case, W_G would increase with pressure but decrease slightly with temperature. The difference of equilibrium compositions between olivine and spinel could be larger than that shown in Fig. (1-2), because of the possible kinetic problem encountered in experiments. This could be especially true for the low temperature(800°C) runs.

For a more realistic model one should adopt the asymmetric regular solution model(Thompson, 1967) for both olivine and spinel. According to this model, we have:

$$\mu^{Fe} = G^{Fe}_{P,T} + 2RT \ln X^{Fe} + [W_G^{Fe} + 2(W_G^{Mg} - W_G^{Fe})X^{Fe}]X^{Mg^2} \quad ----(5\text{-}36)$$

$$\mu^{Mg} = G^{Mg}_{P,T} + 2RT \ln X^{Mg} + [W_G^{Mg} + 2(W_G^{Fe} - W_G^{Mg})X^{Mg}]X^{Fe^2} \quad ----(5\text{-}37)$$

Because accurate equilibrium compositions of olivine and spinel at high P-T conditions are not available for our caaculation of interaction energies, the following calculations are semi-quantitative and are used to demonstrate the possible composition dependence of Gibbs free energies for olivine and spinel at high pressure and high temperature. In order to evaluate the possible magnitude for interaction energies, we choose arbitrarily the following two pairs of coexisting compositions of olivine and spinel at 1200°C from Fig. (1-2): $(X^{Fe},X^{Fe})=(0.18,0.59)$ and (0.11,0.42) at P=110 and 120 Kb, respectively. Using the above data and Eqs. (5-18) to (5-21) and (5-34) to (5-37), we obtain

the following interaction energies at an average pressure of 115 Kb and temperature of 1200°C.

$$W_G^{\alpha Fe}=5700 \text{ cal/mole} \qquad W_G^{\alpha Mg}=410 \text{ cal/mole}$$
$$W_G^{\gamma Fe}=7120 \text{ cal/mole} \qquad W_G^{\gamma Mg}=3960 \text{ cal/mole} \quad \text{----------(5-38)}$$

Interaction energies for olivine at 0 Kb(1 atm) and 1200°C are less than 1000 cal/mole(Obata et al, 1974), A tentative value of 1000 cal/mole is assumed for both interaction energies.

$$W_G^{\alpha Fe}=1000 \text{ cal/mole} \qquad W_G^{\alpha Mg}=1000 \text{ cal/mole} \quad \text{----------(5-39)}$$

Interaction energies for spinel at 0 Kb and room temperature are not known. However, they may be negligible, because both the refractive indices and the cell parameters of spinel solid solutions were found to be linear functions of composition (Akimoto and Fujisawa, 1968; Ringwood and Major, 1966, 1970). Interaction energies could be lower at hgih temperatures; thus, we tentatively assume that at 1200°C:

$$W_G^{\gamma Mg} \sim W_G^{\alpha Mg} \sim 0 \text{ cal/mole} \quad \text{----------(5-40)}$$

If we further assume linear dependence of interaction energies on pressure, we have at 1200°C:

$$W_G^{\alpha Fe}=1000+41P \quad \text{----------(5-41)}$$
$$W_G^{\alpha Mg}=1000-5P \quad \text{----------(5-42)}$$
$$W_G^{\gamma Fe}=62P \quad \text{----------(5-43)}$$
$$W_G^{\gamma Mg}=34P \quad \text{----------(5-44)}$$

Activities(a) of Fe_2SiO_4 and Mg_2SiO_4 in olivine and spinel as functions of composition and temperature can be calculated by:

$$a^{Fe}=X^{Fe}\exp\left\{\frac{X^{Mg^2}}{2RT}\left[W_G^{Fe}+2(W_G^{Mg}-W_G^{Fe})X^{Fe}\right]\right\} \quad \text{----------(5-45)}$$

$$a^{Mg}=X^{Mg}\exp\left\{\frac{X^{Fe^2}}{2RT}\left[W_G^{Mg}+2(W_G^{Fe}-W_G^{Mg})X^{Mg}\right]\right\} \quad \text{----------(5-46)}$$

Substituting Eqs. (5-41) to (5-44) into Eqs. (5-45) and (5-46),

we obtain activities of Fe_2SiO_4 and Mg_2SiO_4 in olivine and spinel at 1200°C as shown in Fig. (5-2a). According to our model, activities in spinel at a given composition increases with pressure more rapidly than they do in olivine.

Excess Gibbs free energies(G_{XS}) of olivine and spinel can be calculated by:

$$G_{XS} = (W_G^{Fe}X^{Mg} + W_G^{Mg}X^{Fe})X^{Fe}X^{Mg} \quad \text{----------(5-47)}$$

G_{XS} so calculated are all positive, and except for Mg-rich olivine, they tend to increase with pressure. Thus G_{XS} will compensate Gibbs free energy of mixing, $G_{MX} = 2RT(X^{Fe}\ln X^{Fe} + X^{Mg}\ln X^{Mg})$, and the compensation increases with pressure as shown in Fig. (5-2b). It is noted that G_{XS} for spinel increases rapidly with pressure. Thus, it seems possible that above a certain pressure(more than 200 Kb) spinel may not form a continuous solid solution but may unmix to form two solid solutions. However, at that high pressure, spinel may have transformed into the other phases begore this unmixing could occur.

It is also noted from Fig. (5-26) that at low pressures, the deviation of $G_{MX}+G_{XS}$ from the ideal solution is larger in olivine than in spinel. This has the effect of decreasing the Fe_2SiO_4 content of equilibrium compositions in olivine and spinel relative to that in ideal solutions. At high pressures, this trend is reversed. This effect of G_{XS} on equilibrium compositions can decrease or increase the Fe_2SiO_4 content in olivine and spinel up to 10%.

Gibbs free energies of olivine and spinel as functions of

Fig. (5-2)

(A) Activities of Fe_2SiO_4 (a^{Fe}) and Mg_2SiO_4 (a^{Mg}) in olivine (solid lines) and spinel (dashed lines) as functions of pressure at 1200°C. Note the more rapid increase of activities with pressure in spinel than in olivine. (B) Excess free energies (G_{XS}) in olivine (solid lines) and spinel (dashed lines) as functions of pressure at 1200°C. Note the more rapid increase of G_{XS} with pressure in spinel than in olivine.

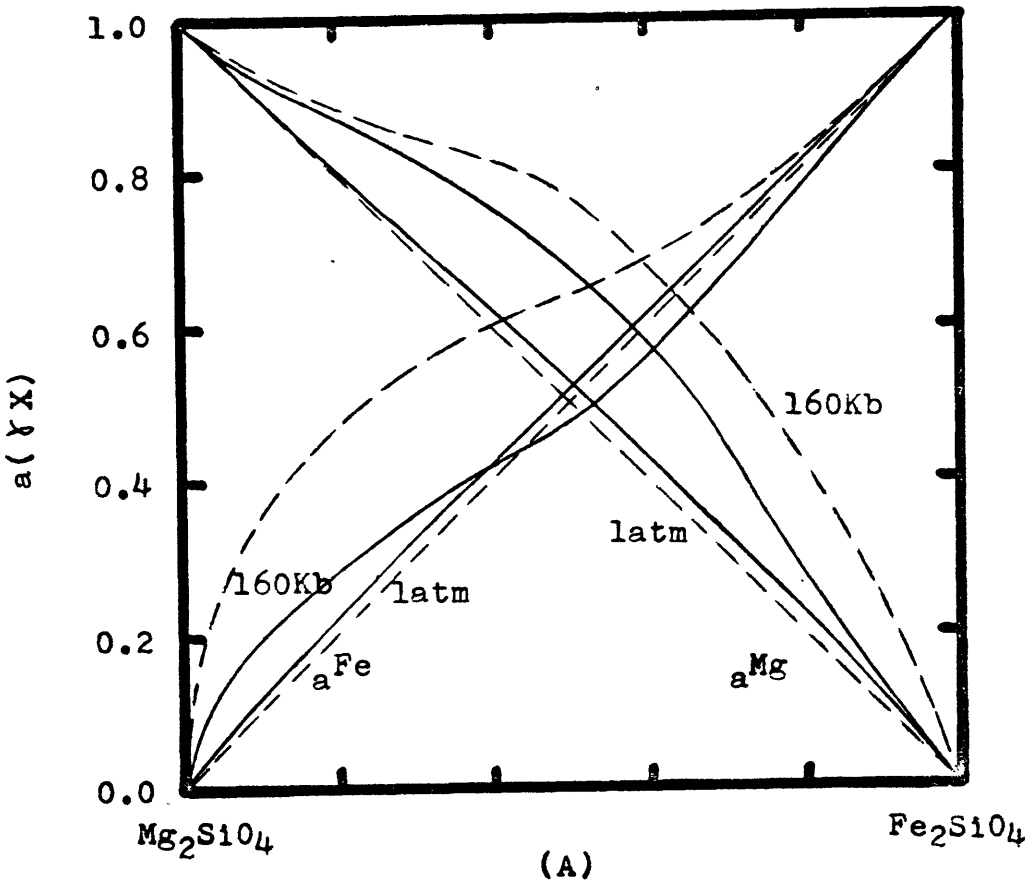
1.0
0.8
0.6
0.4
0.2
0.0
a(γ X)
160Kb
1atm
160Kb
1atm
a^{Fe}
a^{Mg}
Mg_2SiO_4
Fe_2SiO_4

(A)

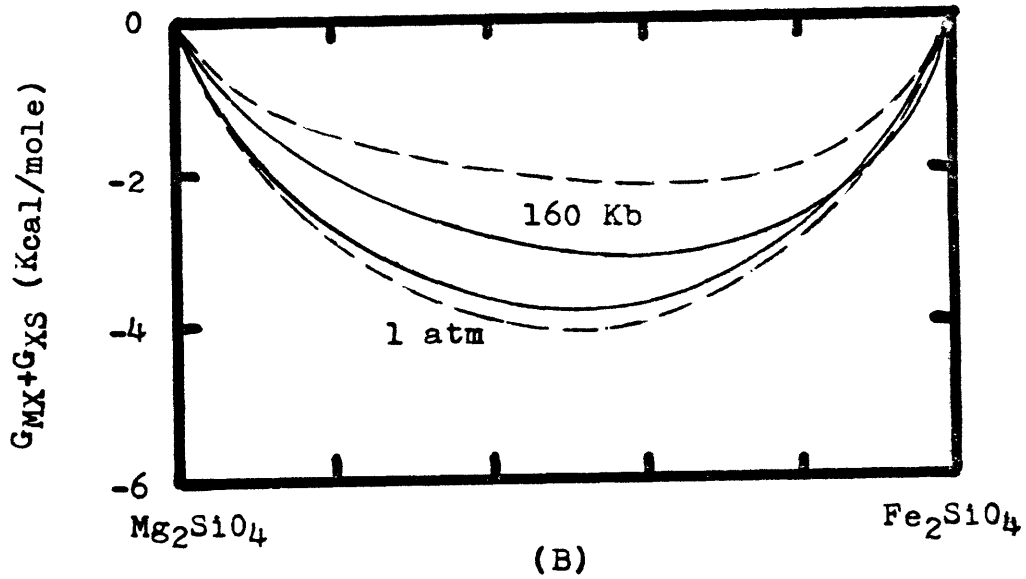
0
-2
-4
-6
$G_{MX}+G_{XS}$ (Kcal/mole)
160 Kb
1 atm
Mg_2SiO_4
Fe_2SiO_4

(B)

composition, pressure and temperature can now be calculated by:

$$G_{P,T}=X^{Fe}G^{Fe}_{P,T}+X^{Mg}G^{Mg}_{P,T}+2RT(X^{Fe}\ln X^{Fe}+X^{Mg}\ln X^{Mg})+$$
$$(W^{Fe}_{G}X^{Mg}+W^{Mg}_{G}X^{Fe})X^{Fe}X^{Mg} \quad \text{----------(5-48)}$$

Substituting Eqs. (5-18) to (5-21) and (5-41) to (5-44) into Eq. (5-48), the calculated results are shown in Fig. (5-3). Free energy curves for olivine and spinel are skewed towards the Fe_2SiO_4 endmember, since the free energy of Fe_2SiO_4 decreases with temperature more rapidly than Mg_2SiO_4. It is interesting to note that although the calculation is semi-quantitative, equilibrium compositions of coexisting olivine and spinel obtained from these free energy curves(Fig. 5-3, c and d) agree well with the experimentally determined phase diagram(Fig. 1-2).

5-6: Equilibrium transition versus massive transition:

From Fig. (5-4) we see that the free energy decrease is very small for the transition of a metastable olivine into two equilibrium phases, $\Delta G_e^{\alpha\to\gamma}=G_e^{\alpha}+G_e^{\gamma}-G_{m,}^{\alpha}$ where subscripts e and m denote equilibrium and metastable phases, respectively. In contrast to this small driving force of transformation, the activation energy is large for the equilibrium transformation, because it involves a composition change. Thus, the equilibrium transformation is a sluggish precess. On the other hand, the free energy decrease for the metastable transition

of a metastable olivine into a metastable spinel in the two phase region, $\Delta G_m^{\alpha\to\gamma}=G_m^{\gamma}-G_m^{\alpha}$, is only slightly smaller than $\Delta G_e^{\alpha\to\gamma}$. However, this metastable transition, which is formally called massive transition, does not involve a composition change and thus may have a smaller activation energy. As a result,

Fig. (5-3)

Gibbs free energies of olivine(solid lines) and spinel(dashed lines) as functions of pressure and composition at 1200^{o}C. Light solid lines are common tangent lines of Gibbs free energy curves. Verical dashed lines mark the equilibrium compositions of olivine and spinel at the particular pressure.

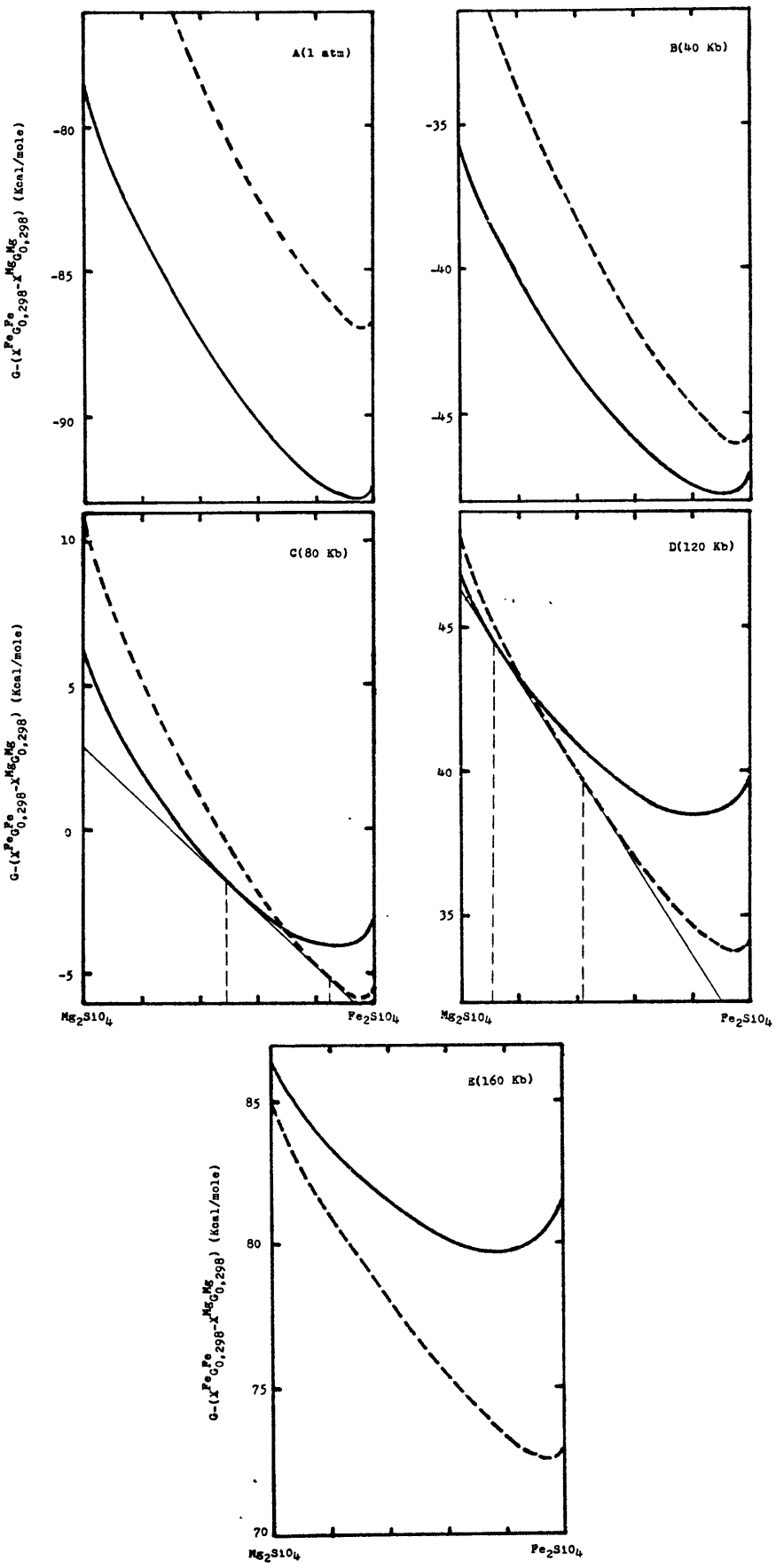
A(1 atm)
B(40 Kb)
C(80 Kb)
D(120 Kb)
E(160 Kb)
$G-(X^{Fe,Fe}_{G_{O,298}}-X^{Mg,Mg}_{G_{O,298}})$ (Kcal/mole)
$G-(X^{Fe,Fe}_{G_{O,298}}-X^{Mg,Mg}_{G_{O,298}})$ (Kcal/mole)
$G-(X^{Fe,Fe}_{G_{O,298}}-X^{Mg,Mg}_{G_{O,298}})$ (Kcal/mole)
-80
-85
-90
-35
-40
-45
10
5
0
-5
45
40
35
85
80
75
70
Mg_2SiO_4
Fe_2SiO_4
Mg_2SiO_4
Fe_2SiO_4
Mg_2SiO_4
Fe_2SiO_4

the massive transition may take place rapidly and dominate the transformation precesses. The massive transition will begin to compete with the equilibrium transformation when G_m^{α} is rising above G_m^{γ}. The composition where the massive transition begins in the two phase region can be calculated from Eq. (5-48) by putting $G_{P,T}^{\alpha}=G_{P,T}^{\gamma}$. The composition boundary which marks the beginning of the massive transition lies approximately in the middle of the two equilibrium composition boundaries of the two phase region. Beyond the two phase region and in the spinel field, the olivine→spinel transiton will occur exclusively by massive transition. The characterization of this massive transition precess, using the model of nucleation and growth, is the subject of the next chapter.

Chapter 6

KINETICS

6-1: Introduction:

The Gibbs free energy decrease, ΔG^d, is the fundamental driving force of the olivine→spinel transition. ΔG^d as a function of P, T and composition can be calculated from the Gibbs functions of olivine and spinel, derived in Chap. 5. The rate of ΔG^d decrease, i.e. the rate of penetration into teh metastability field, determines the dominant mechanism of the olivine→spinel transition, as described qualitatively below. Fig. (6-1) shows schematic the polythermal, polybaric section of the Mg_2SiO_4-Fe_2SiO_4 system(Fig. 6-1a) along a positive P-T gradient, as well as the Gibbs free energies of olivine and spinel(Fig. 6-1b,c,d) at the three different positions along the P-T gradient, as labelled by (1), (2) and (3) in Fig. (6-1a). If olivine is moved along the P-T path of (1)→(2)→(3) at an extremely slow rate, this allows enough time for compositions to change by diffusion, so that the dominant mechanism of transition will be the equilibrium transition as depicted by: $\alpha_e \rightarrow \alpha_e + \gamma_e \rightarrow \gamma_e$, where the subscript "e" denotes an equilibrium phase. With the increasing rate of penetration into the metastability field, diffusion becomes less effective and the reaction becomes $\alpha_e \rightarrow \alpha_{e'} + \gamma_{e'} \rightarrow \gamma_m + \gamma_{e'}$, where subscripts "e'" and "m" denote semi-equilibrium and massive phases, respectively. In this case, there is a finite composition range for the transformed spinel, and this composition range is reduced

Fig. (6-1)

Schematic diagram showing the polythermal, polybaric section of the Mg_2SiO_4-Fe_2SiO_4 system along a positive P-T gradient(A), and free energy diagrams at the three points, labelled (1), (2) and (3) in (A), aling the P-T gradient(B), (C) and (D). Arrows are driving forces of the olivine-spinel transition at the particular composition. OM and OP are driving forces for massive transition and equilibrium transformation, respectively.

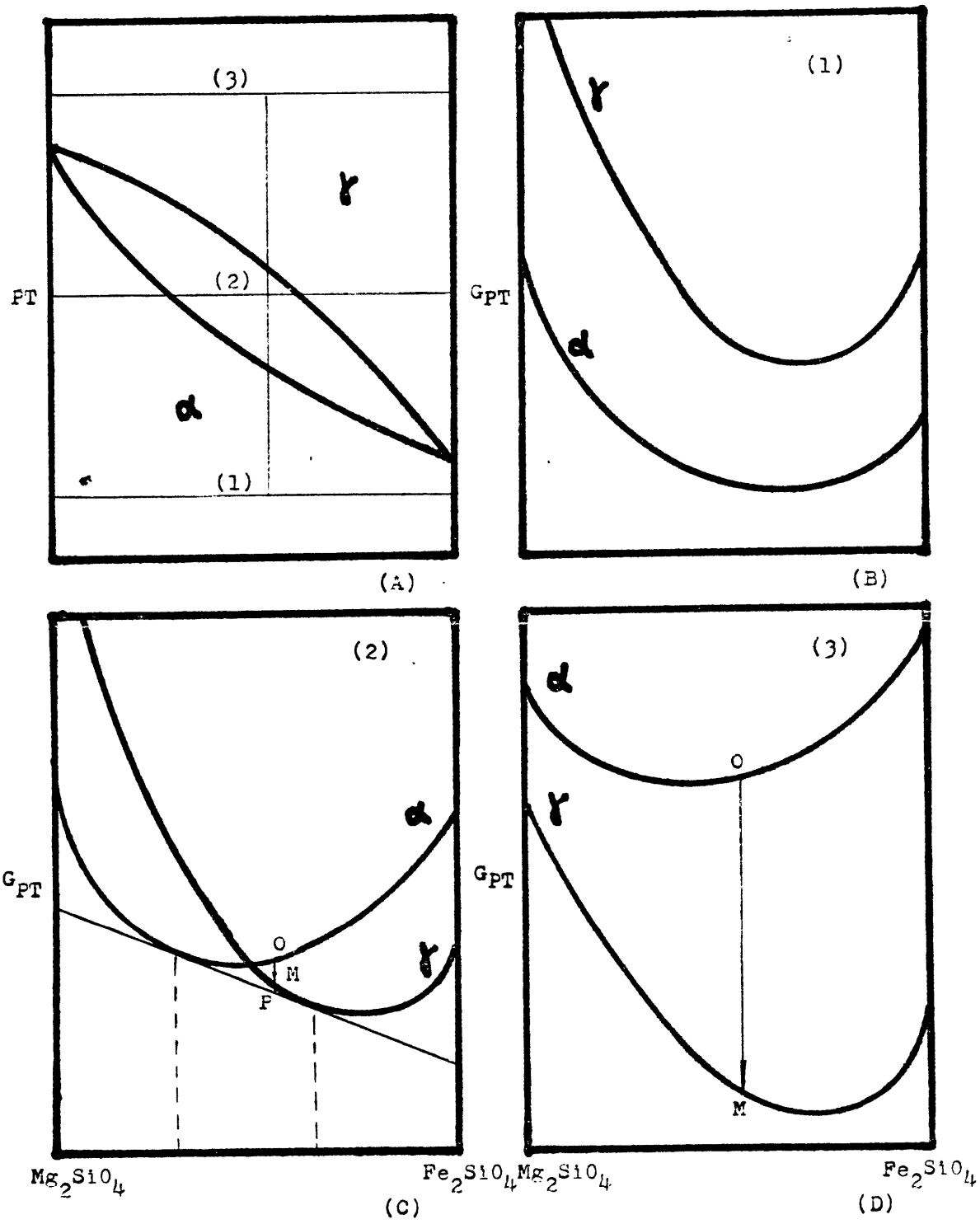
(3)
γ
PT
(2)
α
(1)
(A)
(1)
γ
G_{PT}
α
(B)
(2)
α
G_{PT}
O
M
γ
P
Mg_2SiO_4
Fe_2SiO_4
(C)
(3)
α
O
γ
G_{PT}
M
Mg_2SiO_4
Fe_2SiO_4
(D)

as the rate of penetration into the metastability field increases. As the rate of penetration into the metastability field increases further, diffusion is further suppressed and the proportion of the massive phase increases. The massive transition will eventually dominate, and the reaction becomes: $\alpha_e \rightarrow \gamma_m \rightarrow \gamma_m$. At this stage, the transition is totally isochemical. As the rate of penetration into the metastability field increases further, the massive transition can be suppressed and there is an increased proportion of untransformed olivine, as depicted by: $\alpha_e \rightarrow \alpha_u \rightarrow \gamma_m$, where the subscript "u" denotes the untransformed phase. As the rate of penetration into the metastability field increases even further, olivine may stay completely untransfoemed, and the reaction finally becomes: $\alpha_e \rightarrow \alpha_u \rightarrow \alpha_u$. If the untransformed olivine is held metastably for an extended period of time, it will transform into γ_m, provided the temperature is higher than a characteristic temperature (T_{ch}). The untransformed olivine will stay indefinitely at temperatures lower than T_{ch}. T_{ch} will decrease with increasing transition time. If the crystallography of olivine and spinel allowed a martensitic transition, the reaction $\alpha_e \rightarrow \alpha_u \rightarrow \alpha_M$, where the subscript "M" denotes the martensitic phase, would occur instantaneously at a certain degree of metastability, when the massive transition was suppressed. The martensitic transition would not be suppressed and the proportion of martensitic phase would increase with the degree of metastability. However, we have concluded in Chap. 4 that a martensitic transition does not occur in the olivine→spinel transition. Thus, a massive transition dominates the metastable transi-

tions prevailing in laboratory experiments. The massive transition may also prevail in the cold interior of some rapid plunging downgoing slabs. The semi-quantitative treatment of the kinetics of the massive olivine→spinel transition will be the major objective of theis chapter. Since there is no suitabel rate equation for a first order, high pressure phase transition in solids, we shall develop a kinetics theory applicable to the massive olivine→spinel transition. Because the massive transition involves no composition change and thus no long range diffusion, the rate-limiting step will be the migration of atome across interphase boundary. The transition precess is thus interface controlled and can best be described by the midel of nucleation and growth. We shall, therefore, derive the rate equation for the olivine→spinel transition by extending the model of nucleation and growth to be applicable at high pressure. In doing so, we shall emphasize the dependence of the rate equation on such variables as pressure, temperature, grain size, and shear stress for a given composition.

6-2: The driving force and the energy barrier:

In addition to the decrease of Gibbs free energy, ΔG^d, there are also other energy changes associated with the olivine-spinel transition. Spinel may preferentially mucleate on crystal heterogeneities and thus take advantage of the high energy assiciated with them. Typical heterogeneities which can localize spinel nuclei are grain surfaces(solid-air contact), grain boundaries(solid-solid contact), grain edges, dislications,

grain corners, and point defects. During heterogeneous nucleation, the energy of the heterogeneity, ΔE^h, will either be completely or partially released, and contribute to the nucleation. When the spinel nucleus forms, it absorbs an interfacial energy(σ) by creating a new olivine-spinel interphase boundary(interface). In addition, it may absorbs an amount of strain energy(ξ) due to the volume change accompanying the transition. Furthermore, there are always vacancies present in olivine. If the concentration of vacancies is not in equilibrium with olivine, the destruction or creation of vacancies during the olivine-spinel transition will modify the driving force of the transition. Because spinel is more compact than olivine, excess and undersaturated vacancies in olivine will have effects of decreasing and increasing the rate of the olivine→spinel transition, respectively. The equilibrium concentration of vacancies will not affect the driving force of the transition(Russel, 1976). For our approximations below, we shall neglect the disequilibrium concentration of vacancies in olivine.

The total energy change associated with the formation of a spinel nucleus can now be expressed by:

$$\Delta G_T = \Delta G^d + \Delta E^h + \sigma + \xi \quad \text{----------(6-1)}$$

the resolutiion of the total energy change into its components is for the convenience of evaluating their roles in driving the olivine-spinelt transition. It should be borne in mind that the component energies may not be independent of one another.

The first two terms in Eq. (6-1) are negative and thus they tend to be driving forces for the olivine→spinel transition. The latter two terms are positive and form energy barriers to

nucleation. In the following section, we shall examine these energy terms in more detail. Because the component energies depend on the mechanism of nucleation, as well as on the nature of the interface, we shall discuss the driving force and energy barrier in each of these important cases in the olivine→spinel transition. There are three possible competing mechanisms of nucleation for the olivine→spinel transition in the laboratory and in the mantle: homogeneous nucleation, nucleation on grain surfaces or grain boundaries, and nucleation on dislications. Other heterogeneous nucleation processes are relatively unimportant because of the low concentration of atoms on these heterogeneities(grain edge, grain corner, and point defect), although they are also energetic nucleation sites. In each of the nucleation mechanisms, we shall also discuss the effect of the interface of the driving force and the energy barrier. Two types of interfaces will be considered: coherent and incoherent. It is assumed that the characteristics of the semicoherent interface will lie in between the two extremes.

6-3: Homogeneous nucleation:

Homogeneous nucleation is the least favorable nucleation mechanism, since there is no extra energy($\Delta E^h=0$), in addition to decrease of Gibbs free energy, available to drive the nuvleation. However, because of the large number of nucleation sites, homogeneous nucleation may be a competing process for the olivine→spinel transition in favorable physical conditions. This is especially true when the olivine is highly metastable,

which makes the contribution of the heterogenity energy to the driving foece less prominent.

In the following discussion, we shall consider the olivine→spinel transition at constant pressure and temperature. In addition, all calculated parameters will be based on a possible mantle composition, $(Mg_{0.89}Fe_{0.11})_2SiO_4$ at 150 Kb and 700°C. The decrease of Gibbs free energy for and isothermal, isobaric olivine-spinel transition can be expressed by:

$$\Delta\bar{G}^d = \bar{G}^{\gamma}_{P,T} - \bar{G}^{\alpha}_{P,T} \sim \Delta\bar{V}\Delta P \sim -6.7\times10^7 \Delta P \text{ erg/cm}^3 \text{------(6-2)}$$

where the superscript "-" denotes the quantity per unit volume (cm^{-3}), and ΔP(in Kb) is the overpressure or the pressure beyond equilibrium. The fractional volume change calculated from Eqs. (5-6) to (5-9) has a value, $\Delta\bar{V} \sim -0.067$, corresponding to an average P-T condition(150 Kb and 700°C) for the olivine→spinel transition in a downgoing slab. This value of fractional volume change does not vary by more than 10% in the P-T range of interest.

The interfacial energy per unit area for the coherent interface, $\bar{\sigma}_c$,is not known, but may fall in the range of 20 to 200 erg/cm^2 for most materials(Russel, 1976). A tentative value of 100 erg/cm^2 is assumed for the olivine→spinel transition in the mantle. The interfacial energy for the semicoherent or incoherent interface, $\bar{\sigma}_i$, is composed of two terms, $\bar{\sigma}_c + \bar{\sigma}_s$. The latter arises from the structural mismatch on the interface, and according to van der Merwe(1963a,b):

$$\bar{\sigma}_s \sim \frac{\mu a}{2\pi^2}\left[1+\psi-(1+\psi^2)^{\frac{1}{2}}\right] \text{----------(6-3)}$$

where μ is the shear modulus, a is the interatomic distance, $\psi = \frac{2\pi\Delta\bar{V}}{3(1-\nu)}$, ν is Poisson's ratio. Substituting appropriate

values for the olivine→spinel transition into Eq. (6-3), a value of approximately 200 erg/cm^2 is obtained for $\bar{\sigma}_s$. Thus $\bar{\sigma}_i = \bar{\sigma}_c + \bar{\sigma}_s \sim 300$ erg/cm^2, which is also comparable to the interfacial energies of incoherent interfaces for other materials. Both $\bar{\sigma}_c$ and $\bar{\sigma}_i$ are nearly independent of pressure and temperature. The uncertainty of the above estimations of interfacial energies is believed to be within a factor of two.

The strain energy for a coherent interface, ξ_c is composed of two parts. One is the dilatational strain energy, ξ_D, which arises from the volume change of the olivine→spinel transition, and the other is the shear strain energy, ξ_S, which comes from the lattice distortion due to the volume change. Eshelby(1957) has calculated the strain energies based on a simple model. Following his method, the strain energies per unit volume for spherical nuclei of spinel in an olivine matrix can be calculated by:

$$\bar{\xi}_D \sim \frac{K^r}{2}\left(\frac{3K^r}{3K^r+4\mu^\alpha} - 1\right)^2 \Delta\bar{V}^2 \qquad \text{(6-4)}$$

$$\bar{\xi}_S \sim \frac{2\mu^\alpha}{3}\left(\frac{3K^r}{3K^r+4\mu^\alpha}\right)^2 \Delta\bar{V}^2 \qquad \text{(6-5)}$$

where μ^α and K^r are the shear modulus in olivine and the bulk modulus in spinel, respectively. In this model $\bar{\xi}_D$ and $\bar{\xi}_S$ are located within spinel and olivine, respectively. The former is independent of the shape of spinel nuclei but not the latter. From Table (5-1) we estimate that at 150 Kb and 700°C, μ^α and K^r have manitudes of 990 and 2670 Kb, respectively. This gives values of $\bar{\xi}_D \sim 0.6\times10^9$, $\bar{\xi}_S \sim 1.2\times10^9$, and $\bar{\xi}_c = \bar{\xi}_D + \bar{\xi}_S \sim 1.8\times10^9$ erg/cm^3. The magnitude of strain energies so estimated

are comparable to those of other materials. The uncertainty of this estimate may be within one order of magnitude, in the P-T range of interest.

The strain energy will not accumulate if the interface is incoherent, because it can be relieved on this interface by free running vacancies(Russel, 1976). Thus $\bar{\xi}_i = 0$.

In the following semi-quantitative calculations, we shall assume a spherical nucleus for spinel when it is small. From Eq. (6-1), and with $\Delta E^h = 0$ for homogeneous nucleation, we get:

$$\Delta G_T^H = \frac{4}{3}\pi r^3(\Delta \bar{G}^d + \bar{\xi}) + 4\pi r^2 \bar{\sigma} \quad \text{---------(6-6)}$$

where r(in cm) is the radius of the spinel nucleus. Substituting the above estimated values of $\Delta \bar{G}^d$, $\bar{\sigma}$ and $\bar{\xi}$ for the olivine-spinel transition, we obtain:

$$\Delta G_T^H(\text{erg}) \doteqdot (-2.81\times10^8\Delta P + 7.54\times10^9)r^3 + 1.26\times10^3 r^2 \quad \text{--(6-7)}$$

for a coherent interface, and

$$\Delta G_T^H(\text{erg}) \doteqdot -2.81\times10^8 \Delta P\, r^3 + 3.77\times10^3 r^2 \quad \text{------(6-8)}$$

for an incoherent interface.

The energy barrier, $\bar{\sigma} + \bar{\xi}$, for coherent and incoherent interfaces as a function of nucleus size, r, is shown in Fig. (6-2). The surface energy increases with the square, while the strain energy increases with the cube, of the size of a nucleus, the surface energy will dominate the energy barrier when the nucleus is small and the strain energy will domonate when the nucleus is large. The coherent

Fig. (6-2)

Energy barriers for coherent interface(solid line) and incoherent interface(dashed line) as functions of the size of spinel nucleus. Note that a coherent interface will be favored only when the nucleus is smaller than r=33 A, in this particular case.

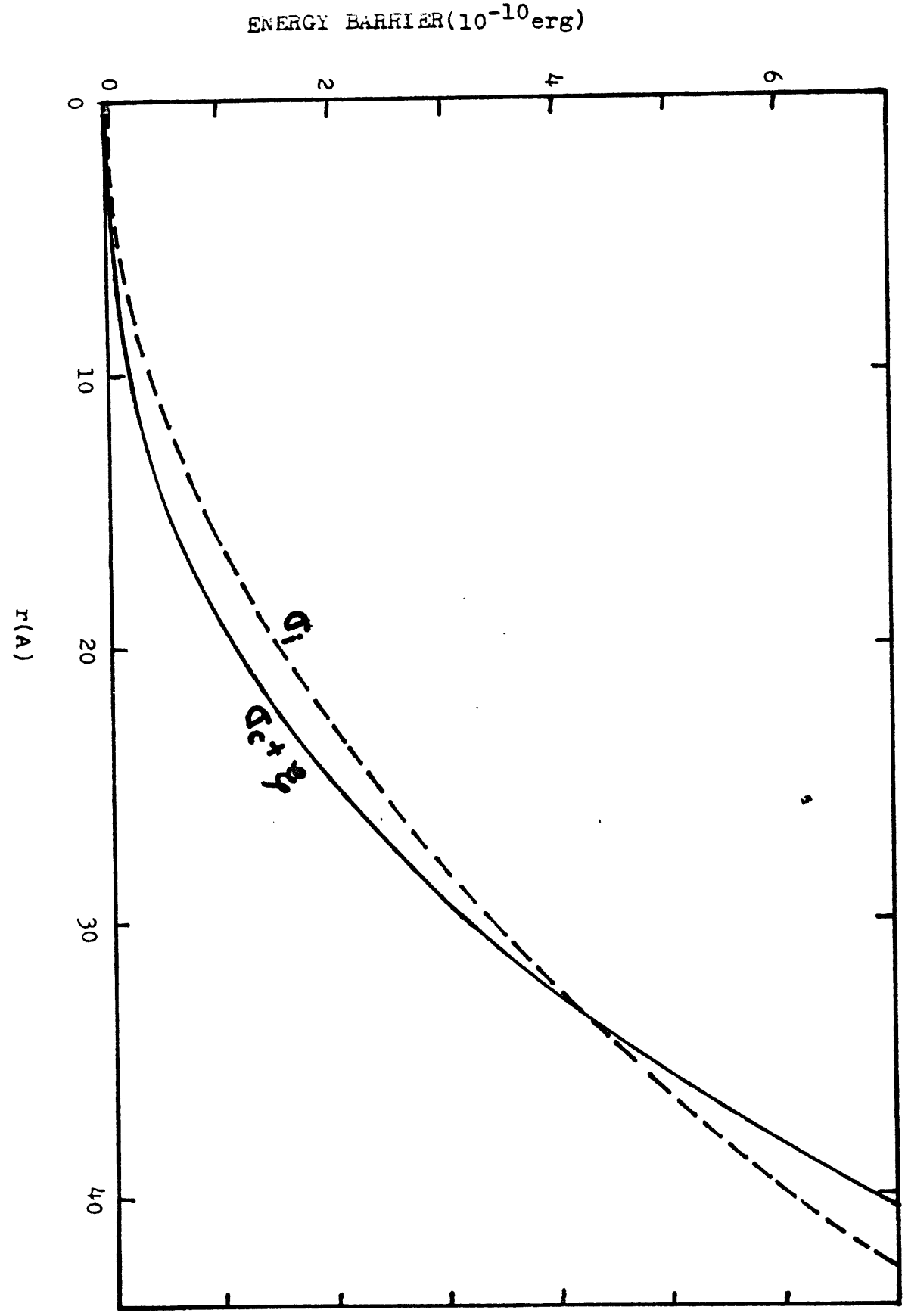
ENERGY BARRIER(10^{-10}erg)
0
2
4
6
0
10
20
30
40
r(A)
σ_i
σ_{c+p}

interface has a smaller surface energy and a much larger strain energy than the incoherent interface. This makes the energy barrier for the coherent interface smaller than that for the incoherent interface at the earliest stage of the transition. This trend is reversed when the nucleus grows beyond a certain size. As a consequence, a nucleus will have a coherent interface at a very early stage of its formation, but this interface will break up upon its growth. The size of the nucleus at which the coherent interface breaks is approximately r=33 A, as shown in Fig. (6-2).

The total energy changes for the olivine-spinel transition, as a function of the nucleus size, are calculated from Eqs. (6-7) and (6-8), as shown in Fig. (6-3). Each ΔG_T^H function traces out a dome-shaped curve with an energy maximum ΔG_T^{H*}, which forms the activation energy of nucleation. The activation energy of nucleation exists because the surface energy can be compensated by the decrease of Gibbs free energy only when the nucleus is sufficiently large. The critical-sized mucleus, r=r*, possesses the maximum energy, ΔG_T^{H*}, which separates the transition into two stages, nucleation and growth. At the nucleation stage the nucleus is subcritical, and this is the size which is metastable and easily decomposed. On the other hand, at the growth stage, the nucleus is supercritical, which is stable and can grow spontaneously.

The activation energy of nucleation and the critical

Fig. (6-3)

Total free energy changes(ΔG_T^H) as functions of the size of a spinel nucleus for homogeneous nucleation with coherent interface(H_c) and with incoherent interface(H_i). Heavy solid lines and dashed lines are energy curves at overpressures of 50 and 100 Kb, respectively. The zero energy refers to the state before transition. Note the decreasing activation energy of nucleation (ΔG_T^{H*}) and critical size(r*) of the nucleus with increasing overpressure(Δ P). Note also that a coherent interface is always favored over an incoherent interface for nucleation, when $\Delta P > 50$ Kb.

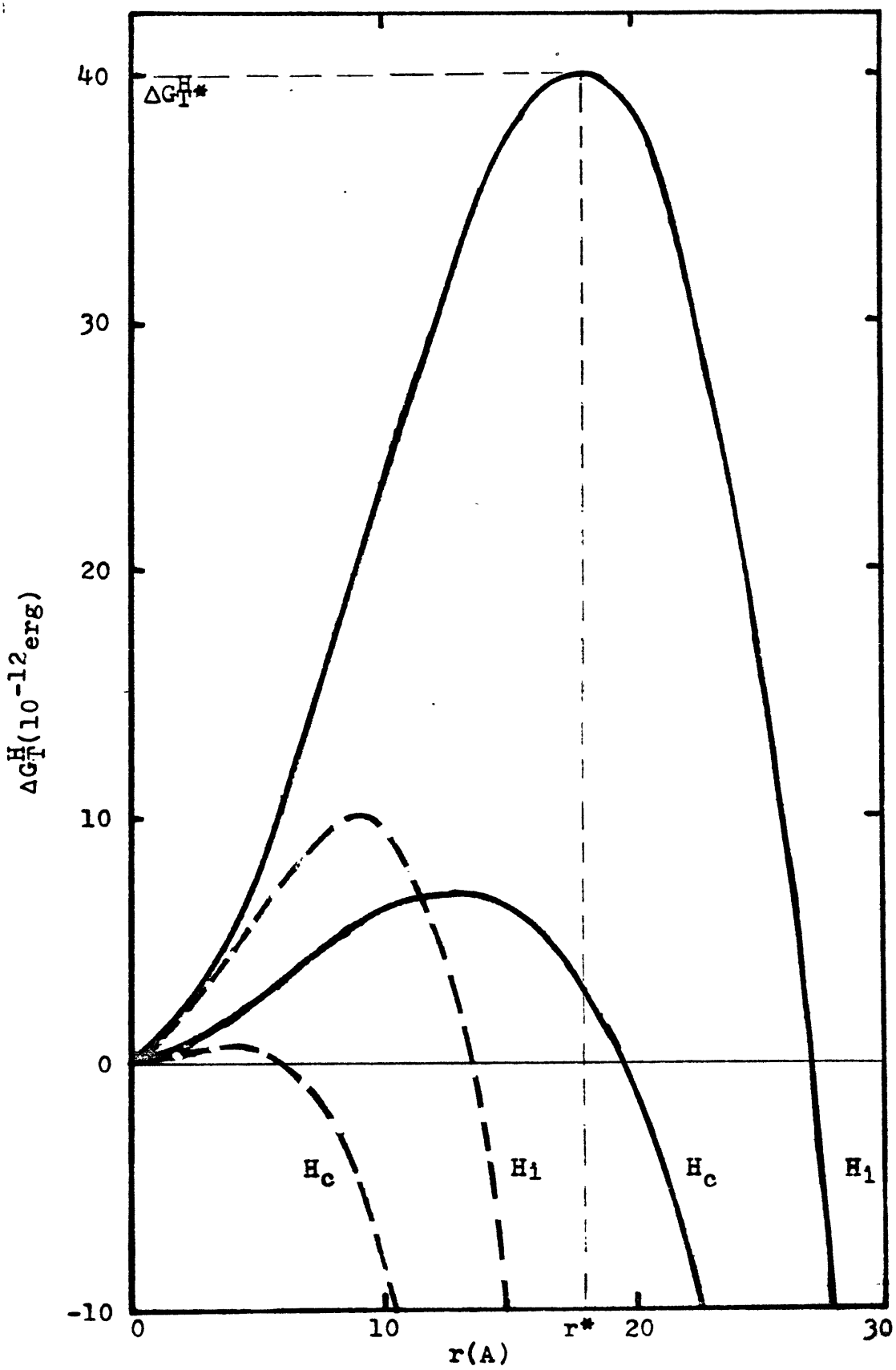
40
30
20
10
0
-10
ΔG_T^H*
$\Delta G_T^H(10^{-12}erg)$
H_c
H_i
H_c
H_1
0
10
r*
20
30
r(A)

size of the nucleus can be easily calculated as follows: at $r=r^*$, $\Delta G_T^H = \Delta G_T^{H*}$, $d\Delta G_T^H/dr=0$, and from Eq. (6-6), we obtain:

$$r^* = \frac{-2\bar{\sigma}}{\Delta\bar{G}^d + \bar{\xi}} \qquad (6\text{-}9)$$

and

$$\Delta G_T^{H*} = \frac{16\pi\bar{\sigma}^3}{3(\Delta\bar{G}^d + \bar{\xi})^2} \qquad (6\text{-}10)$$

It is readily seen that both r^* and ΔG_T^{H*} decrease as ΔP increases. For the olivine→spinel transition, r^* will be smaller than 33 A when ΔP is larger than 36 Kb. Thus the spinel nuclei will be completely coherent during the nucleation stage for homogeneous nucleation at an overpressure of more than 36 Kb. It is also important to note that for the coherent interface a minimum overpressure is required to overcome the strain energy before any nucleation can take place. Thus there will be no transition when ΔP is smaller than approximately 27 Kb, because ΔG_T^H is always positive(Eq. 6-7) and r^* approaches infinity (Eq. 6-10). This corresponds to a displacement of the olivine-spinel phase boundary by 27 Kb towards high pressure. The phase boundary will also be displaced towards lower pressure for the reversed transition. Thus, there will be a large hysteresis for the olivine→spinel transition of coherent interface. On the other hand, there is no strain energy to overcome for the incoherent interface, so that, the olivine→spinel transition will occur immediately across the equlibrium phase boundary, although the nucleation rate

could be very small due to the higher surface energy for the incoherent interface.

Both the interfacial energy, $\bar{\sigma}$, and the strain energy, $\bar{\xi}$, used above are average values. The interfacial energy is a function of the spacial position of the interface in the olivine lattice, the relative orientation between olivine and spinel latteces, and even the curvature of a spinel nucleus. The strain energy depends strongly on the spacial position of the spinel in the olivine lattice. As a consequence of the anisotropy of the interfacial and the strain energies, the spinel will not be spherical, but will assume a shape so as to minimize the total energy barrier, $\bar{\sigma} + \bar{\xi}$. Thus, r* and ΔG_T^{H*} calculated above by assuming a spherical nucleus could be overestimated and may represent limiting values for the real case. However, the interfacial energy is much less anisotropic than the strain energy. Since the former dominates the total energy barrier when the nucleus size is small, the assumption of a spherical nucleus in the nucleation stage of homogeneous nucleation may still be reasonable. The quasi-spherical nucleus will become increasingly irregular in shape upon growth and will eventually form a plate lying along "soft planes" in the olivine lattice, due to the increasing effect of the highly anisotropic strain energy.

6-4: Nucleation on grain surfaces and grain boundaries:

Nucleation on grain surfaces or grain boundaries is favored over homogeneous nucleation, because the energy associated with grain surfaces($\Delta\bar{E}^h = \Delta\bar{E}^s = -\bar{\sigma}^{\alpha\alpha}$) or grain boundaries($\Delta\bar{E}^h = \Delta\bar{E}^b = -\bar{\sigma}^{\alpha\alpha}$) may be completely or partially released to contribute to the driving force of nucleation. Nucleation on grain surfaces and grain boundaries is important, because the concentration of atoms located on grain surfaces or grain boundaries is usually very high, especially when the grain size is small. The former is the dominating nucleation mechanism for the olivine→spinel transition in a powdered sample, as has been verified experimentally and will be described in Chap. 8. The latter may be one of the major competing nucleation mechanisms in downgoing slabs, as will be shown in Chap. 9.

As was the case for homogeneous nucleation of an incoherent interface, so too the strain energy for the nucleation on grain surfaces or grain boundaries can also be relieved by free running vacancies. As shown in the previous section, the coherent interface will prevail during the nucleation stage. Thus, for the formation of a spherical nucleus of spinel on a grain surface or grain boundary with the latter located on the diametrical plane of the former:

$$G_T^{s(b)} = \frac{4}{3}\pi r^3 \Delta\bar{G}^d + \pi r^2 (4\bar{\sigma}_c^{\alpha r} + \Delta\bar{E}^{s(b)}) \text{ ----------} (6\text{-}11)$$

This gives

$$r^* = \frac{(4\bar{\sigma}_c^{\alpha r} + \Delta\bar{E}^{s(b)})}{2\Delta\bar{G}^d} = \frac{400 + \Delta\bar{E}^{s(b)}}{1.34\times10^8 \Delta P} \text{ cm} \text{ ----------} (6\text{-}12)$$

and

$$\Delta G_T^{S(b)*} = \frac{\pi(4\bar{\sigma}_c^{dr} + \Delta\bar{E}^{S(b)})^3}{12\,\Delta\bar{G}^d} = 5.83\times10^{-17}\frac{(400+\Delta\bar{E}^{S(b)})^3}{\Delta P^2}\ \text{erg} \quad (6\text{-}13)$$

The average values of the grain surface energy($\bar{\sigma}^{da}$) and the grain boundary energy($\bar{\sigma}^{dd}$) for olivine are not known. As a crude approximation the former can be calculated (Gilman, 1960; Brace and Walsh, 1962) by:

$$\sigma = \frac{\bar{E}\,a^2}{d_o\,\pi^2} \quad \text{----------} \quad (6\text{-}14)$$

where E, a and d_o are the average value of Young's modulus, the average ionic radius lying on the cleavage plane, and the spacing of cleavage planes, respectively. From Table (5-1), the following values are estimated for olivine of mantle composition at 150 Kb and 700°C: E=2470 Kb, a=1.0x10^{-8} cm(average ionic radii on oxygen atoms and divalent cations), and d_o=5.02x10^{-8} cm(half of the cell edge b, for cleavage planes of (010)). This gives $\bar{\sigma}^{da}$=500 erg/cm^2. For most material, the grain boundary energy is approximately 30% of the grain surface energy. Hence $\bar{\sigma}^{dd}$ is tentatively assumed to have a value of 150 erg/cm^2. If the grain surface energy is completely released during the nucleation, then $\Delta\bar{E}^S = -\bar{\sigma}^{da}$ =-500 erg/cm^2. This will greatly reduce r* and ΔG_T^S* and could even make them negative(Eqs. 6-12 and 6-13). However, in order to destroy the grain surface and release the surface energy, the air on the original grain surface should be driven out. Thus, there arises a new activation energy (activation energy for vacancy diffusion) which contributes

to ΔG_T^{s*}. This will make ΔG_T^{s*} and thus r* positive, although they are still less than the corresponding values for homogeneous nucleation. If the original grain surface is replaced by other crystal heterogeneities, such as a grain boundary of spinel, the contribution of $\bar{\sigma}^{aa}$ to the mucleation is much reduced. A rough calculation of the grain boundary energy of spinel, $\bar{\sigma}^{rr}$, by Eq. (6-14), gives a value of approximately 400 erg/cm^2. In this case, $\Delta\bar{E}^s=-(\bar{\sigma}^{aa}-\sigma^{rr})=-100$ erg/cm^2 which gives $\Delta G_T^{s*}\sim 6.3\times10^{-13}$ erg at an overpressure of 50 Kb. Thus ΔG_T^{s*} is approximately 10% of the corresponding value for homogeneous nucleation of coherent interface. A semi-quantitative calculation of ΔG_T^{b*} for the nucleation on grain boundaries, assuming $\Delta E^b=-150$ erg/cm^2 and $\Delta P=50$ Kb, gives $\Delta G_T^{b*}=2.4\times10^{-14}$ erg, which is equivalent to ΔG_T^{H*} for coherent interface at $\Delta P=100$ Kb. Thus, the effect of reducing the activation of nucleation on grain boundaries is equivalent to an increase of overpressure of 50 Kb, in this particular example.

Because energies on grain surfaces and grain boundaries can contribute to the driving force of nucleatiom, nuclei formed on these surfaces and boundaries will not be spherical but will extend as far as possible along these interfaces. Thus r* and $\Delta G_T^{s(b)*}$ calculated from Eqs. (6-12) and (6-13) may again be overestimated.

6-5: Nucleation on dislocations:

Just as grain surfaces or grain boundaries can catalyze nucleation, so too can dislocations which also serve as powerful nucleation sinks. Nucleation on dislocations is favored over homogeneous nucleation, because the strain energy associated with the nucleation may be partially or completely released, which contributes to the driving force. Nucleation on dislocations can be important, if the dislocation density is high. The dislocation density in Mg-rich olivine has been shown to increase rapidly with differential stress, $\sigma_1 - \sigma_3$, and thus shear stress (Goetze, 1975; Kohlstedt et al, 1976). Thus, we may expect that nucleation on dislocations can be greatly promoted by increasing the shear stress. In fact, as will be shown latter, nucleation on dislocations may become the major competing nucleation mechanism for the olivine-spinel transition in laboratory experiments and in downgoing slabs.

For a semi-quantitative evaluation of the effect of depressing the activation energy of nucleation, ΔG_T^{D*}, by a dislocation, we consider the simple geometry of nucleating a spherical spinel on a dislocation of olivine lying diametrically within the spinel (see Fig. B-1 in Appendix B). Thus from Eq. (6-1), noting that $\Delta E^h = \Delta E^D = 2r\,\Delta\bar{E}^D$, where ΔE^D is the part of strain energy of dislocation which is released during the olivine→spinel transition, we have

$$G_T^D = (4/3)\pi r^3 (\Delta G^d + \bar{\xi}) + 4\pi r^2 \bar{\sigma} + 2r\,\Delta\bar{E}^D \qquad (6\text{-}14)$$

If the dislocation can be complerely eliminated during the nucleation then all the strain energy of the dislocation will contribute to the driving foece. In this case, it can be shown (Appendix B) that $\Delta E^D \sim -2.3\times10^{-4}\ln(1.6\times10^8 r)$. Again, the strain energy ξ in Eq. (6-14) can be relaxed on an incoherent interface, and thus we obtain, for coherent interface:

$$\Delta G_T^D(\text{erg}) = (-2.81\times10^8\,\Delta P + 7.54\times10^9)r^3 + 1.26\times10^3 r^2 - 4.59\times10^{-4} r\ln(1.6\times10^8 r) \quad \text{----------(6-15)}$$

and for incoherent interface:

$$\Delta G_T^D(\text{erg}) = -2.81\times10^8\,\Delta P r^3 + 3.77\times10^3 r^2 - 4.59\times10^{-4} r\ln(1.6\times10^8 r) \quad \text{----------(6-16)}$$

We have assumed that for the coherent interface the two strain energies, ξ and ΔE^D, do not interact. In the real case the strain energy of dislocation can be used as the strain energy of nucleation, and thus the effects of the two strain energies partly cancel out. The dislocation may also persist during the nucleation of a coherent nucleus and thus ΔE^D in Eq. (6-15) may be overestimated.

ΔG_T^D as functions of r calculated from Eqs. (6-15) and (6-16) is shown in Fig. (6-4). Noted that the activation ΔG_T^{D*} for nucleation on dislocations of incoherent interfaces will exist only when the overpressure is small ($\Delta P < 5$ Kb). This applies also the the coherent interface, if we take into account the displacement of the olivine-spinel phase boundary by 26.8 Kb towards high pressure due to the presence of the strain energy ξ . There will be no activation energy for nucleation

Fig. (6-4)

Total free energy change(ΔG_T) as a function of nucleus size(r). H and D refer to homogeneous nucleation and nucleation on dislocations, respectively. Subscripts c and i refer to coherent and incoherent interfaces, respectively. Numbers in parentheses are overpressures. Note the decrease of ΔG_T^* for nucleation on dislocations, when compared to homogeneous nucleation on the same type of interface at similar ΔP.

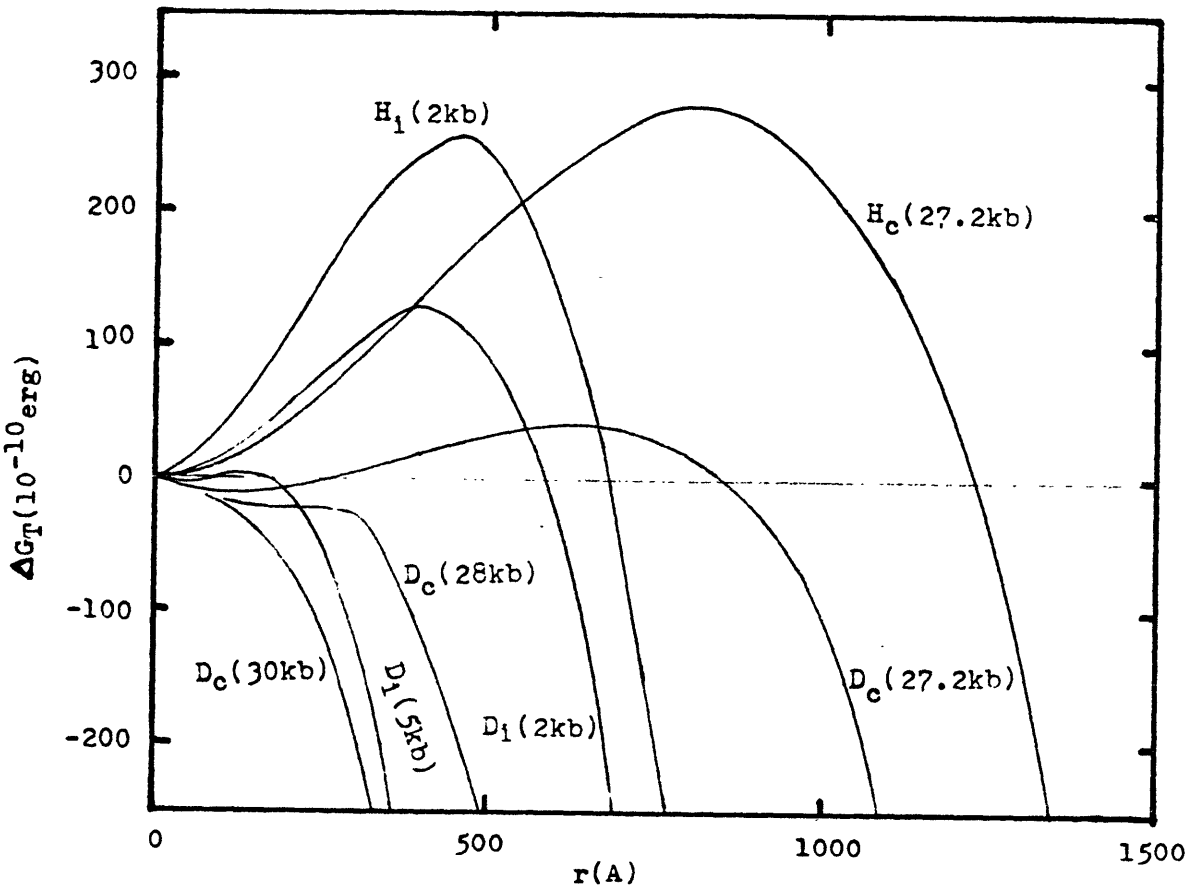
300
200
100
0
-100
-200
$\Delta G_T(10^{-10}erg)$
H_i(2kb)
H_c(27.2kb)
D_c(28kb)
D_c(30kb)
D_i(5kb)
D_i(2kb)
D_c(27.2kb)
0
500
1000
1500
r(A)

on dislocations, as soon as olivine reaches a certain small degree of metastability. Even when ΔG_T^{D*} exists at a small value of ΔP, the total free energy may still decrease at the very beginning of nucleation(Fig. 6-4). This is due to the high strain energy density in the vacinity of the dislocation core, which has a predominant effect when the nucleus is small. As the nucleus grows, the interfacial energy becomes important, and the total free energy increases. Finally, the decrease of Gibbs free energy gains control, and the total free energy drops rapidly. The existence of an energy valley at small values of r has led Cahn(1957) to propose the presence of metastable sub-critical sized nuclei during nucleation on dislocations.

In order to evaluate the effect of dislocations in reducing the activation energy of nucleation, the corresponding functions of ΔG_T^H for homogeneous nucleation are superimposed in Fig. (6-4). Thus, at a small degree of metastability of olivine, ΔG_T^* is reduced by 14% and 50% by nucleation on dislocations of coherent and incoherent interfaces, respectively, in our particular example. The ratio of $\Delta G_T^{D*}/\Delta G_T^{H*}$ will rapidly diminish with increasing degree of metastability and becomes zero when the overpressure is greater than 5 Kb.

A more quantitative discussion of nucleation on dislications was given by Gomez-Ramirez and Pound(1973), who have shown that the activation energy for nucleation on dislocations is almost independent of the shape of the nucleus.

6-6: Nucleation rates:

Having evaluated the activation energies of nucleation, we shall now attempt to calculate the nucleation rates of the major nucleation mechanisms for the olivine→spinel transition, based on classical nucleation theory. Comprehensive reviews for classic nucleation theory were given by Fine(1964), Christian(1965) and Russel(1970, 1976).

The total concentration of nuclei, C_n, and the corresponding nucleation rate, $\bar{I}$, as a function of time, t, for a particular nucleation mechanism during an isothermal and isobaric transition have the general forms shown schematically in Fig. (6-5). At the beginning of nucleation, there is an induction period at $t < \tau$, where τ is the incubation time. During this period of time, both the total concentration of nuclei and the nucleation rate increase with t. After the induction period, the total concentration of nuclei begins to intrease linearly with t and the nucleation rate reaches a steady state(becomes a constant). At some point, $t=t_s$ in Fig. (6-5), the total concentration of nuclei becomes so high that nuclei begin to contact one another or their diffusion fields overlap. The increase of total concentration of nuclei slows down, so that the nucleation rate decreases and eventually ceases. This stage is called site saturation, which means that all the available nucleation sites have been exhausted. After site saturation, the total concentration of nuclei declines, due to the growth of large nuclei at the

Fig. (6-5)

Schematic diagram showing total concentration of nuclei(C_n) and nucleation rate($\bar{I}$) as functions of transition time(t).

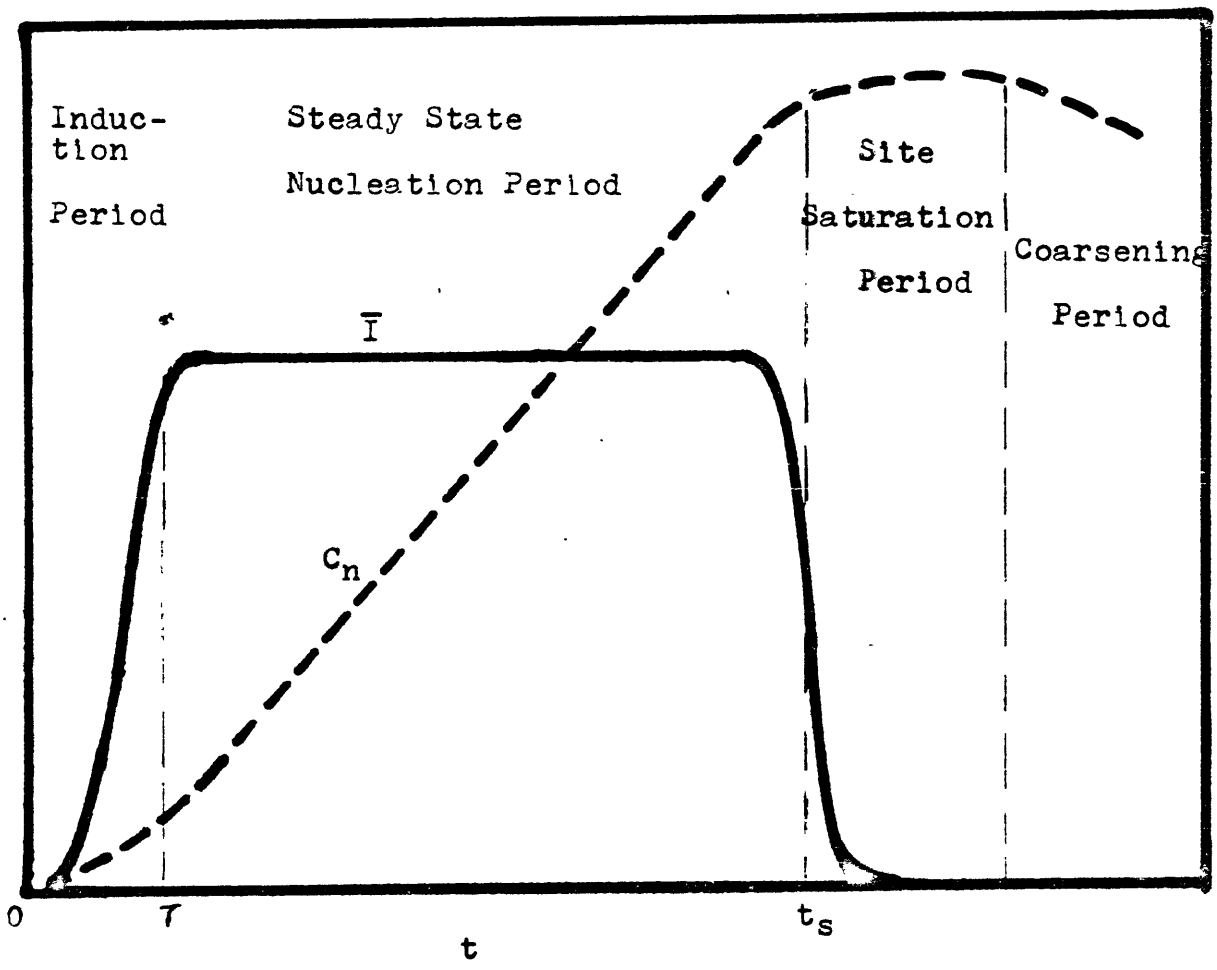
Induc-
tion
Period
Steady State
Nucleation Period
Site
Saturation
Period
Coarsening
Period
$\bar{I}$
C_n
0
τ
t_s
t

expense of the smaller ones in order to reduce the total grain boundary energy. This stage is generally referred to as particle coarsening or Ostwald ripening. As our interest is in the kinetics of the olivine-spinel transition before the process is completed, we shall ignore the last tow stages described above.

Either the induction period or steady state nucleation will dominate the transition precess, depending on the nature of the material and the physical conditions of the transition. If the transition involves a composition change and the diffusion is sluggish, the whole transition process will be covered by the induction period and steady state nucleation may never be attained before the completion of the transition. On the other hand, if the transition is isochemical and the process is interface controlled, steady state nucleation will be rapidly established and will cover the major part to the transition process. The olivine→spinel transition belongs to the latter category, and we shall expect that steady state nucleation dominates the whole transition precess. We will prove this point towards the end of this chapter.

According to classical nucleation theory, the steady state nucleation rate, $\bar{I}_s$, for an isothermal isobaric transition, can be expressed(Turnbull and Fisher, 1949) by:

$$\bar{I}_s = Z N_e^* \beta^* \qquad (6\text{-}17)$$

where Z is the Zeldovich non-equilibrium factor, which corrects the nucleation rate by taking into account the decom-

position of super-critical sized nuclei, N_e^* is the equilibrium concentration of critical sized nuclei, and β^* is the rate of adding atoms to the critical sized nucleus. The Zeldovich factor($\sim 10^{-2}$), whose reciprocal measures the width of ΔG_T as a function of the number of atoms in the nucleus approximately kT below ΔG_T^*, can be approximated by:

$$Z \sim (\Delta G_T^*/(3\pi kT))^{1/2}/n^* \text{----------} (6\text{-}18)$$

where n* is the number of atoms in the critical-sized nucleus, and k is Boltzmann's constant. The equilibrium concentration of the critical-sized nuclei can be calculated by:

$$N_e^* \sim \bar{N} \exp(-\Delta G_T^*/(kT)) \text{----------} (6\text{-}19)$$

where $\bar{N}$ is the concentration of available nucleation sites for each particular nucleation mechanism. $\bar{N}$ can be approximated by the concentrations of total atoms($\bar{N}_V$), atoms on grain surfaces($\bar{N}_S$), atoms on grain boundaries($\bar{N}_B$), and atoms on dislocations($\bar{N}_D$), for homogeneous nucleation, nucleation on grain surfaces, nucleation on grain boundaries, and nucleation on dislocations, respectively. For the isochemical transition, the rate of adding atoms to the critical-sized nucleus can be approximated by:

$$\beta^* \sim s^*(kT/h)\exp(-Q_a/(kT)) \text{----------} (6\text{-}20)$$

where s* is the number of atoms on the interface of the critical-sized nucleus, h is Planck's constant, Q_a is the activation energy of growth or the energy barrier for the migration of atoms across the interface. If the transition involves a composition change, Q_a will be the activation

energy of diffusion. Q_a is the crucial factor in determining the kinetics of the olivine→spinel transition, as will be stressed at the end of this chapter and in Chap. 9.

Combining Eqs. (6-17) to (6-20), we obtain

$$\bar{I}_s \sim \bar{N}(kT/h)(s^*/n^*)(\Delta G_T^*/(3\pi kT))^{1/2}\exp(-(\Delta G_T^*+Q_a)/(kT)) \quad \text{----------(6-21)}$$

According to Turnbull and Fisher(1949), the quantity $(s^*/n^*)(\Delta G_T^*/(3\pi kT))^{1/2}$ falls within one or two orders of magnitude for all problems of interest. Since the kinetics of the transition will not depend sensitively on the pre-exponential terms, the steady state nucleation rate can be approximated by:

$$\bar{I}_s \sim \bar{N}(kT/h)\exp(-(\Delta G_T^*+Q_a)/(kT)) \quad \text{----------(6-22)}$$

It should be noted that the total activation energy for nucleation is the sum of $\Delta G_T^*+Q_a$. The former will dominate at a small degree of metastability(samll ΔP); the latter will control the nucleation rate at a larger degree of metastability. Q_a also controls the growth rate of spinel nuclei as will be discussed in the next section.

Because oxygen ions are considerably larger than the cations in olivine, the rate-limiting step for the olivine→spinel transition is likely to be the migration of oxygen atoms across the interface. We shall then assume that the olivine→spinel transition proceeds by nucleation and growth of oxygen atoms and that the cations offer no additional resistance to this process. Based on this assumption we can

calculate semi-quantitatively the nucleation rate for each nucleation mechanism.

The available nucleation sites for himogeneous nucleation is approximated by the number of oxygen atoms in olivine, which gives

$$\bar{N}_V \sim 5.9 \times 10^{22} \text{ cm}^{-3} \quad (6\text{-}23)$$

For the olivine→spinel transition in powdered or polycrystalline samples, it is best to approximate the grain shapes by equal sized regular tetrakaidecahedra(truncated ocathdra), which are ideal polyhedra to fill up space(Christian, 1965). In this case, the area of grain surfaces or the grain boundaries per unit volume can be calculated by:

$$\bar{S}(\bar{B}) \sim 3.35/D \quad (6\text{-}24)$$

where D is the mean grain diameter. If we take the effective thickness of grain surfaces or grain boundaries to be 2b, where b is the Burguer vector, or approximately 10 A in olivine, this gives:

$$\bar{N}_{s(B)} \sim 2.0 \times 10^{16}/D \text{ cm}^{-3} \quad (6\text{-}25)$$

The grain sizes for most powdered samples used in the laboratory are smaller than 10 μ. Thus

$$\bar{N}_S \geq 2.0 \times 10^{19} \text{ cm}^{-3} \quad (6\text{-}26)$$

A reasonable grain size of olivine in the downgoing slab is 0.5 cm, which gives

$$\bar{N}_B \sim 4.0 \times 10^{16} \text{ cm}^{-3} \quad (6\text{-}27)$$

Assuming dislocations in olivine have effective diameters of 2b, this gives

$$\bar{N}_D \sim 4.6 \times 10^{8} \rho \text{ cm}^{-3} \quad (6\text{-}28)$$

where ρ is the dislocation density. The logarithm of dislocation densities in Mg-rich olivines has been shown to increase linearly with the logarithm of differential stresses(Fig. 6-6) and this linear relationship is almost independent of temperature(Goetze, 1975, Kohlstedt et al, 1976). For the olivine→spinel transition performed in the laboratory, olivine usually yields under high shear stress, characteristic of high pressure presses. This corresponds to a differential stress of more than 10 Kb, which gives dislocation densities of more than 10^{10} cm^{-2} (fig. 6-6). Thus

$$\bar{N}_D^{lab} \geq 4.6 \times 10^{18} \text{ cm}^{-3} \quad \text{----------(6-29)}$$

The maximum differential stress in the cold interior of downgoing slabs is approximately 0.5 Kb(Toksöz et al, 1973). This corresponds to a maximum differential stress of 1 Kb and a dislocation density in olivine of approximately 10^8 cm^{-2}, so

$$\bar{N}_D^{slab} \leq 4.6 \times 10^{16} \text{ cm}^{-3} \quad \text{----------(6-30)}$$

It is interesting to note that the number of available nucleation sites is comparable between nucleation on grain surfaces or grain boundaries, and nucleation on dislocations. They are approximately 10^{-6} to 10^{-4} times that for homogeneous nucleation.

The activation energy of growth, Q_a, for the olivine→spinel transition, is approximated by the activation energy for oxygen atoms to jump across the interface. This is an unknown quantity, but since it is the activation energy for the short term diffusion on the interface, it may have a magnitude comparable to the activation energy of grain boundary diffusion. For most materials in which, both activation energies

Fig. (6-6)

Experimental determined correlation between free dislocation density and applied differential stress during steady-state deformation in forsterite(after Goetze, 1975).

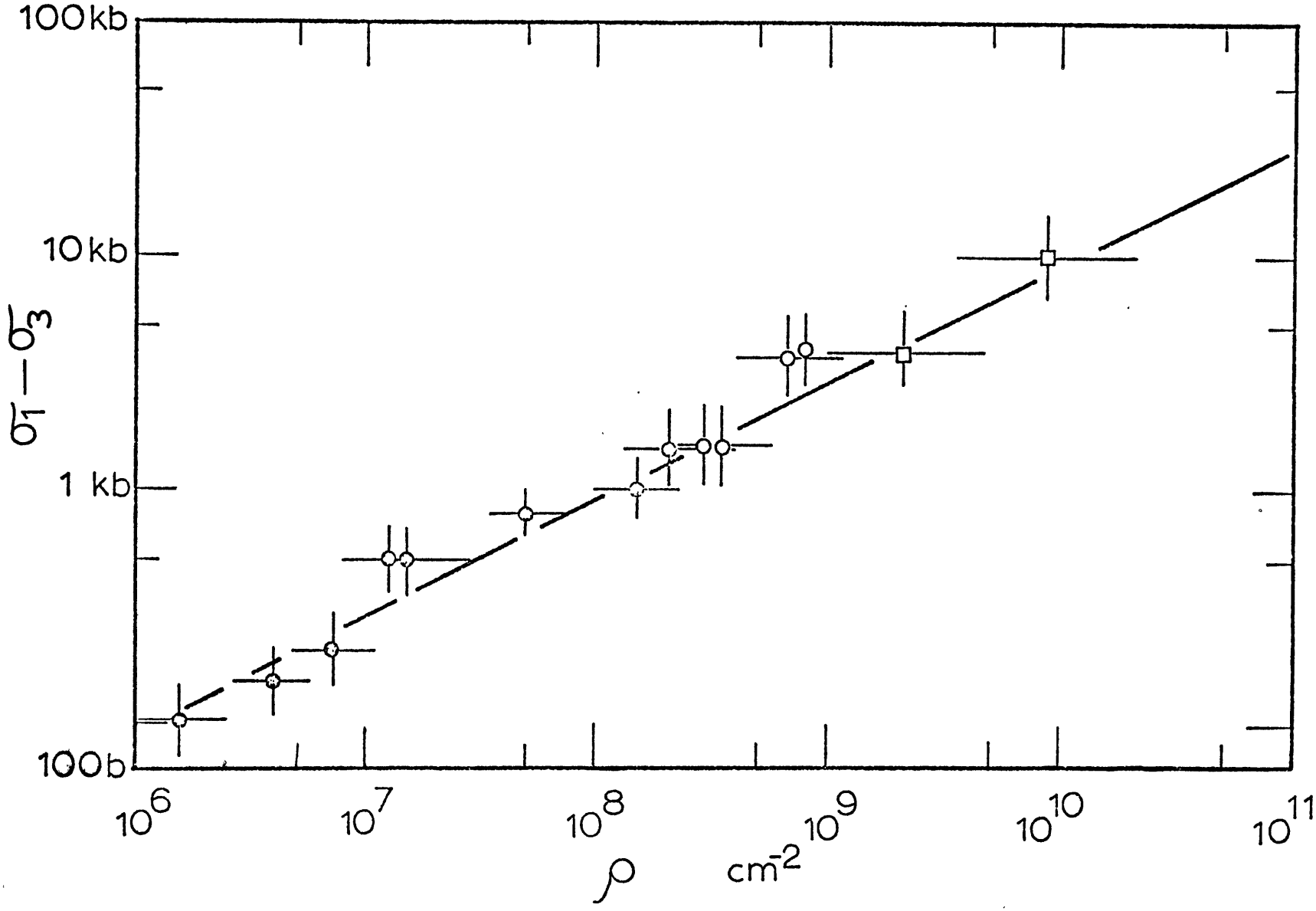
100kb
10kb
1 kb
100b
$\sigma_1 - \sigma_3$
10^6
10^7
10^8
10^9
10^{10}
10^{11}
ρ
cm^{-2}

of grain boundary diffusion and lattice diffusion have been measured, the magnitude of the former falls within the range 1/2 to 2/3 of the latter. The reduction of the activation energy of diffusion on grain boundaries is due to the presence of ample vacancies and dislocations on grain boundaries. In our semi-quantitative calculations, we shall tentatively assume $Q_a \sim (2/3)Q_D$, where Q_D is the activation energy of oxygen lattice diffusion in olivine. The activation energy of diffusion for the slowest species in forsterite has been measured by a variety of methods, and falls in the range 120 to 160 Kcal/mole (Table 6-1). The slowest diffusion species in forsterite is likely to be oxygen atoms. Thus Q_D may fall within the above range. Q_D will increase with pressure according to the following relationship:

$$Q_D = Q_D^o + P\Delta V^* \text{----------} (6\text{-}31)$$

where the superscript "o" refers to the zero pressure value. ΔV^* is the activation volume, which may fall into the range of 10 to 20 cm^3/mole(Goetze, personal communication). We shall adopt the values of Q_D^o =135 Kcal/mole(Goetze and Kohlstedt, 1973) and ΔV^*=15 cm^3/mole for our following semi-quantitative calculations. Thus

$$Q_D(\text{erg/atom}) \sim 9.4\times10^{-12} + 2.5\times10^{-14}P \text{----------} (6\text{-}32)$$

and

$$Q_a(\text{erg/atom}) \sim (2/3)Q_D \sim 6.2\times10^{-12} + 1.7\times10^{-14}P \text{----------} (6\text{-}33)$$

We also choose the univariant line($\alpha+\beta+\gamma$) of $P=72+0.033T(^oK)$ (Table 1-1) to be the olivine-spinel phase boundary and make no distinction between the β- and the γ-phases. From Eq. (6-22)

Table (6-1)

ACTIVATION ENERGY OF DIFFUSION OF THE SLOWEST SPECIES IN FORSTERITE

Q_D (Kcal/mole)	Reference
120±17 (1100-1350°C)	Carter and Avé Lallemant (1970)
154	Stocker and Ashby (1973)
130 (725-1325°C)	Post and Griggs (1973)
135±30 (1290-1450°C)	Goetze and Kohlstedt (1973)
140±30 (1200-1400°C)	Goetze and Kohlstedt (1973)
126±2 (1400-1600°C)	Kohlstedt and Goetze (1974)
125±5 (1400-1600°C)	Kohlstedt and Goetze (1974)

and the above estimated values, we can calculate the nucleation rate for each nucleation mechanism. In the case of heterogeneous nucleation, ΔG_T^* may not exist, especially at large degree of metastability. In this case, we put $\Delta G_T^*=0$. The calculated results are shown in Fig. (6-7). The most notable features of nucleation rates for different nucleation mechanisms are:

(1) The nucleation rate for each mechanism will increase initially with increasing pressure, due to the decrease of ΔG_T^*. Because ΔG_T^* is large for homogeneous nucleation, especially for homogeneous nucleation with an incoherent interface, the trend of increasing nucleation rate with pressure for homogeneous nucleation can extend to very high pressure.

(2) When ΔG_T^* becomes smaller than Q_a, the nucleation rate will decrease monotonically with increasing pressure, due to the effect of ΔV^*. For heterogeneous nucleations, ΔG_T^*'s are very small, so that their nucleation rates will decrease with increasing pressure as soon as a small degree of metastability is attained.

(3) At each temperature, heterogeneous nucleations are far more effective than homogeneous nucleation, at low pressures. Homogeneous nucleation will be competing only at pressures higher than approximately 190 Kb.

(4) Nucleation rates for the olivine→spinel transition performed in the laboratory are more than five orders of magnitude higher than that which could take place in the mantle at identical pressure and temperature.

Fig. (6-7)

Nucleation rates as functions of pressure, temperature, nucleation mechanism, grain size, and shear stress. H, S, B, and D refer to homogeneous nucleation, nucleation on grain surfaces, nucleation on grain boundaries, and nucleation on dislocations, respectively. Subscripts c and i refer to coherent and incoherent interfaces, respectively. Subscripts l and s refer to conditions of laboratory experiments and of the cold interior of downgoing slabs, respectively.

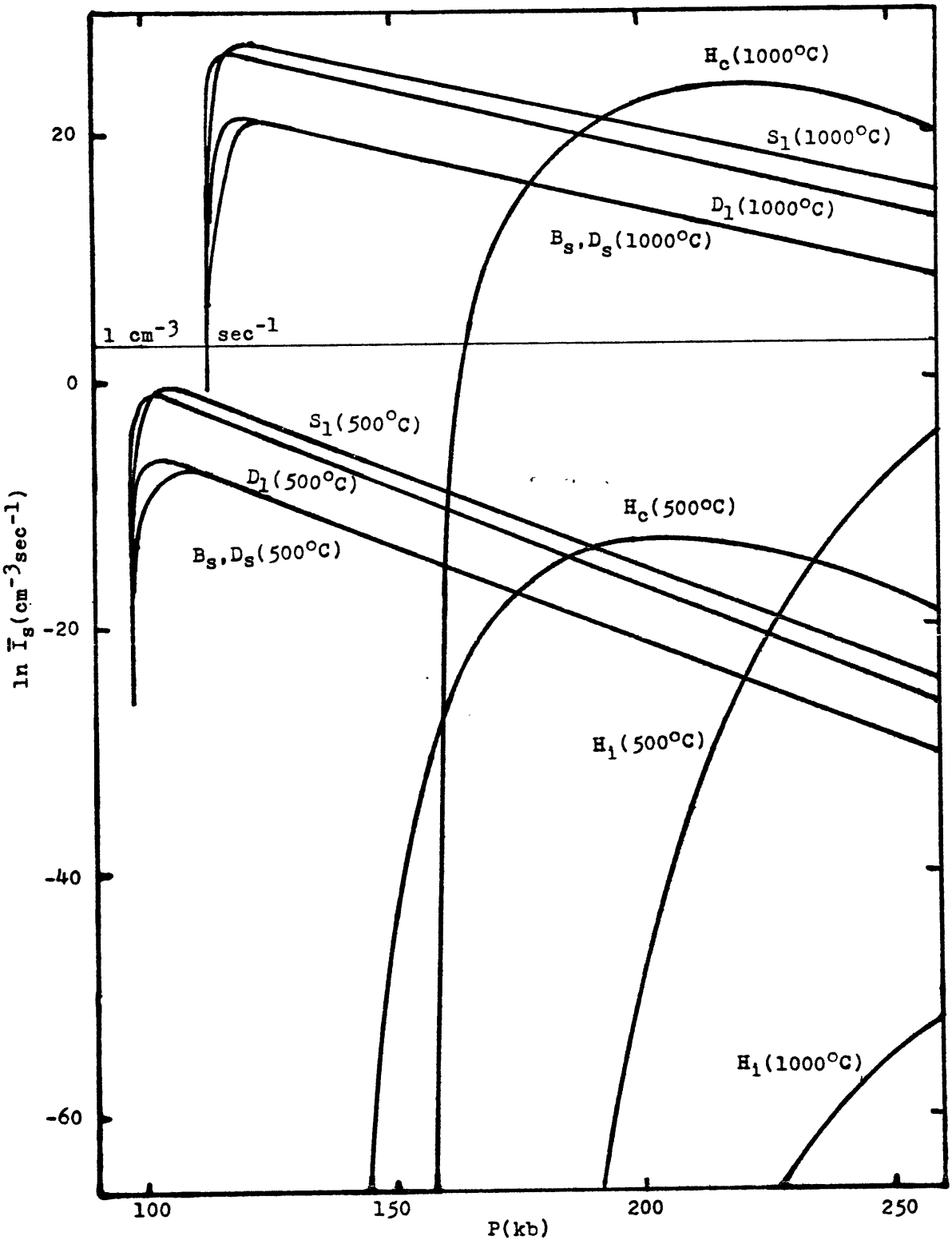
H_c(1000°C)
S_l(1000°C)
D_l(1000°C)
B_s, D_s(1000°C)
1 cm^{-3} sec^{-1}
S_l(500°C)
D_l(500°C)
B_s, D_s(500°C)
H_c(500°C)
H_l(500°C)
H_l(1000°C)
20
0
-20
-40
-60
100
150
200
250
P(kb)
ln $\bar{I}_s$(cm^{-3}sec^{-1})

(5) Nucleation on grain surfaces is more effective than nucleation on dislocations for the olivine→spinel transition performed in the laboratory. The latter may dominate only at large grain size and high shear stress. Both nucleation mechanisms may be equally important for the olivine→spinel transition in the cold interior of downgoing slabs.

(6) Nucleation rates are greatly promoted by increasing tmeperature. For example, nucleation rates at 1000°C are 10^{14} times higher than these at 500°C for the same mechanism of nucleation at the same pressure. For the transition to be observable within a reasonably short period of time, the nucleation rate should be higher than 1 cm^{-3} sec^{-1}. This nucleation rate is marked in Fig. (6-7). Note that this nucleation rate can never be attained below approximately 600°C. Thus the olivine→spinel transition may not be observed below this temperature.

6-7: Growth rate:

For an interface controlled transition at constant pressure and temperature, the growth rate may not vary with time, which is in contrast to the parabolic growth rate for diffusion controlled processes. We shall now evaluate this steady state growth rate(Y) for the olivine→spinel transition, as a function of P and T.

During the growth of a supercritical sized spinel nucleus, for each oxygen atom moving across the olivine-spinel interface there corresponds an energy change: $\Delta G_a^T=\Delta G_a^d+\Delta E_a^h+\sigma_a+\xi_a$, where

the subscript "a" denoted per atomic value. In addition, the oxygen atom has to overcome the energy barrier Q_a. The relationships among these energy terms is shown schematically in Fig. (6-8). Note that the net energy barrier for an oxygen atom to move from olivine to spinel is $Q_a+\Delta E_a^h$, whereas from spinel to olivine it is, $Q_a-\Delta G_a^d-\sigma_a-\xi_a$. For each supercritical-sized nucleus, there are S_n oxygen atoms in olivine facing a spinel nucleus, each with a jumping frequency of approximately, kT/h, Thus, the net rate of adding oxygen atoms to the spinel nucleus is:

$$S_n(kT/h)(\exp(-(Q_a+\Delta E_a^h)/(kT))-\exp(-(Q_a-\Delta G_a^d-\sigma_a-\xi_a)/(kT)))\text{--(6-34)}$$

For every increment of S_n atoms on the spinel nucleus, the latter grows by one interatomic distance δ, Thus, the growth rate can be approximated by:

$$Y\sim\delta(kT/h)\exp(-Q_a/(kT))(\exp(-\Delta E_a^h/(kT))-\exp((\Delta G_a^d+\sigma_a+\xi_a)/(kT)))$$

----------(6-35)

During the growth stage, the nucleus is sufficiently large, so that ΔE_a^h, σ_a, and possibly ξ_a becomes negligible. Thus Eq. (6-35) simplifies to

$$Y\sim\delta(kT/h)\exp(-Q_a/(kT))(1-\exp(\Delta G_a^d/(kT)))\text{----------(6-36)}$$

We shall approximate $\delta$by the average oxygen-oxygen distance of olivine and spinel, which gives

$$\delta\sim 2.54\times10^{-8}\text{ cm----------(6-37)}$$

In addition, we have

$$G_a^d\doteqdot\Delta\bar{V}\Delta P/\bar{N}_n\sim -1.1\times10^{-15}\Delta P\sim 7.6\times10^{-14}-1.1\times10^{-15}P+3.5\times10^{-17}T$$

erg/atom----------(6-38)

Fig. (6-8)

Schematic diagram showing the variation of energies during the migration of each atom from olivine(Left-hand side) to spinel(right-hand side). Note that ΔG_a^h and ΔG_a^d are released while σ_a and ξ_a are absorbed during the transition. For each atom moving across the interface, the energy path is A to B to C.

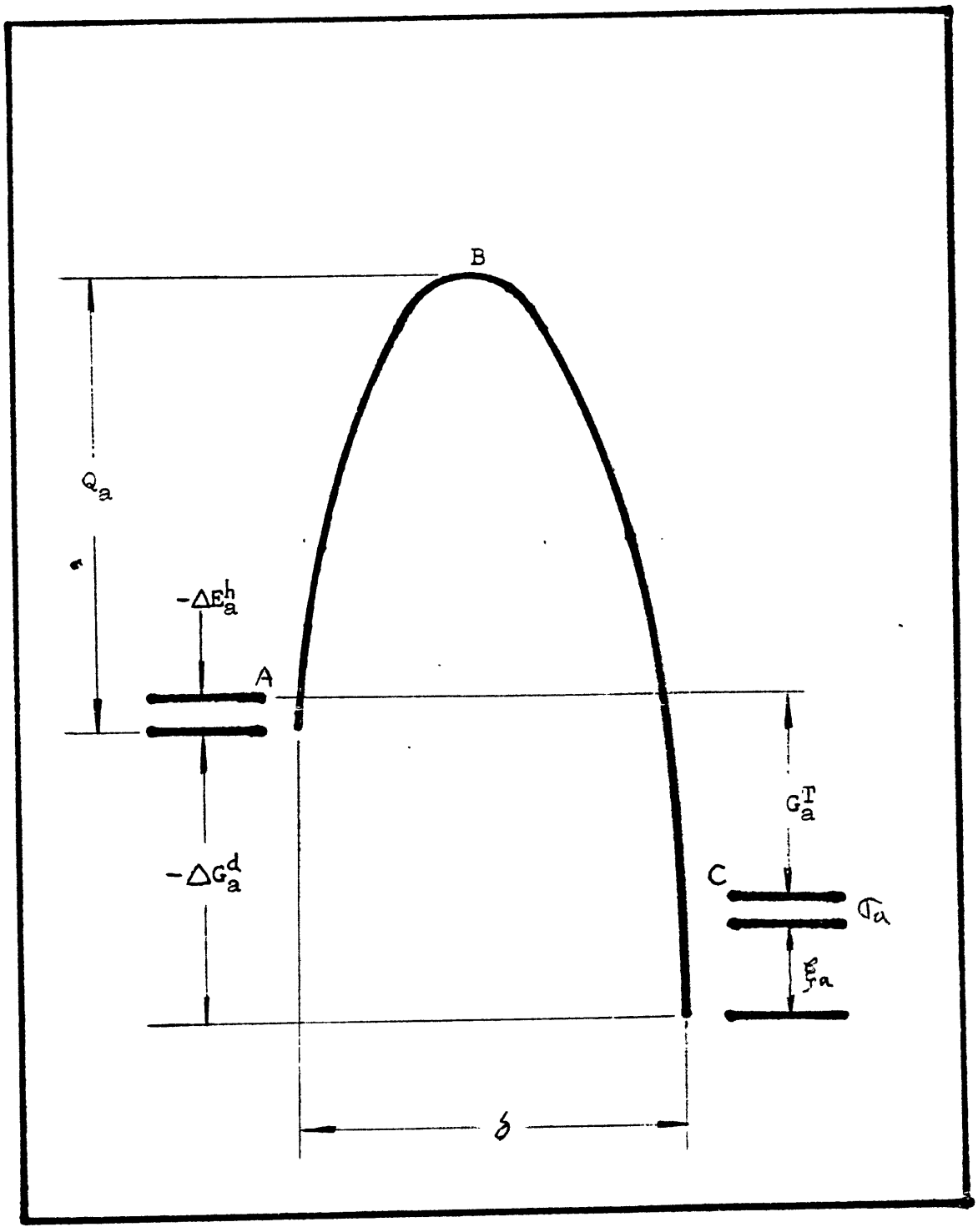
B
Q_a
$-\Delta E_a^h$
A
$-\Delta G_a^d$
G_a^T
C
G_a
G_{fa}
δ
ENERGY
REACTION COORDINATE

where $\bar{N}_n$ is the number of oxygen atoms per unit volume(cm^3) in the spinel nucleus. Thus the growth rate of spinel is:

$$Y(cm/sec) \sim 530T\exp(-(4.5\times10^4+120P)/T)(1-\exp(o.25+(550-7.7P)/T)) \quad \text{----------(6-39)}$$

Calculated growth rates of spinel as functions of P and T are shown in Fig. (6-9). They are generally similar to the nucleation rates(Fig. 6-7), thus, growth rates of spinel may increase rapidly with pressure at small degrees of metastability ($\Delta P<10$ Kb) and decrease monotonically with pressure thereafter. Trends of growth rate dependence on decreasing of temperature are the same as these for increasing pressure.

The growth rate is primarily controlled by Q_a and depends less sensitively on the pre-exponential terms in Eq. (6-36). With the magnitude of Q_a we assumed, even under most favorable conditions, the growth rate of spinel is extremely slow. For example, at 130 Kb and 1500°C, it will take one year for the spinel nucleus to grow beyond on micron. This rate is much slower than what one would expect for the olivine→spinel transition in the laboratory. Thus the value we have assumed for Q_a in the calculation may be overestimated as will be discussed in section (6-9).

6-8: Rate equations:

Kinetic equations which relate the degree of transition to the nucleation and growth rates were first derived by Johnson and Mehl(1939). A more general treatment was later given by Cahn(1956). Their kinetic equations were derived by

Fig. (6-9)

Growth rate of spinel nucleus as a function of pressure and temperature.

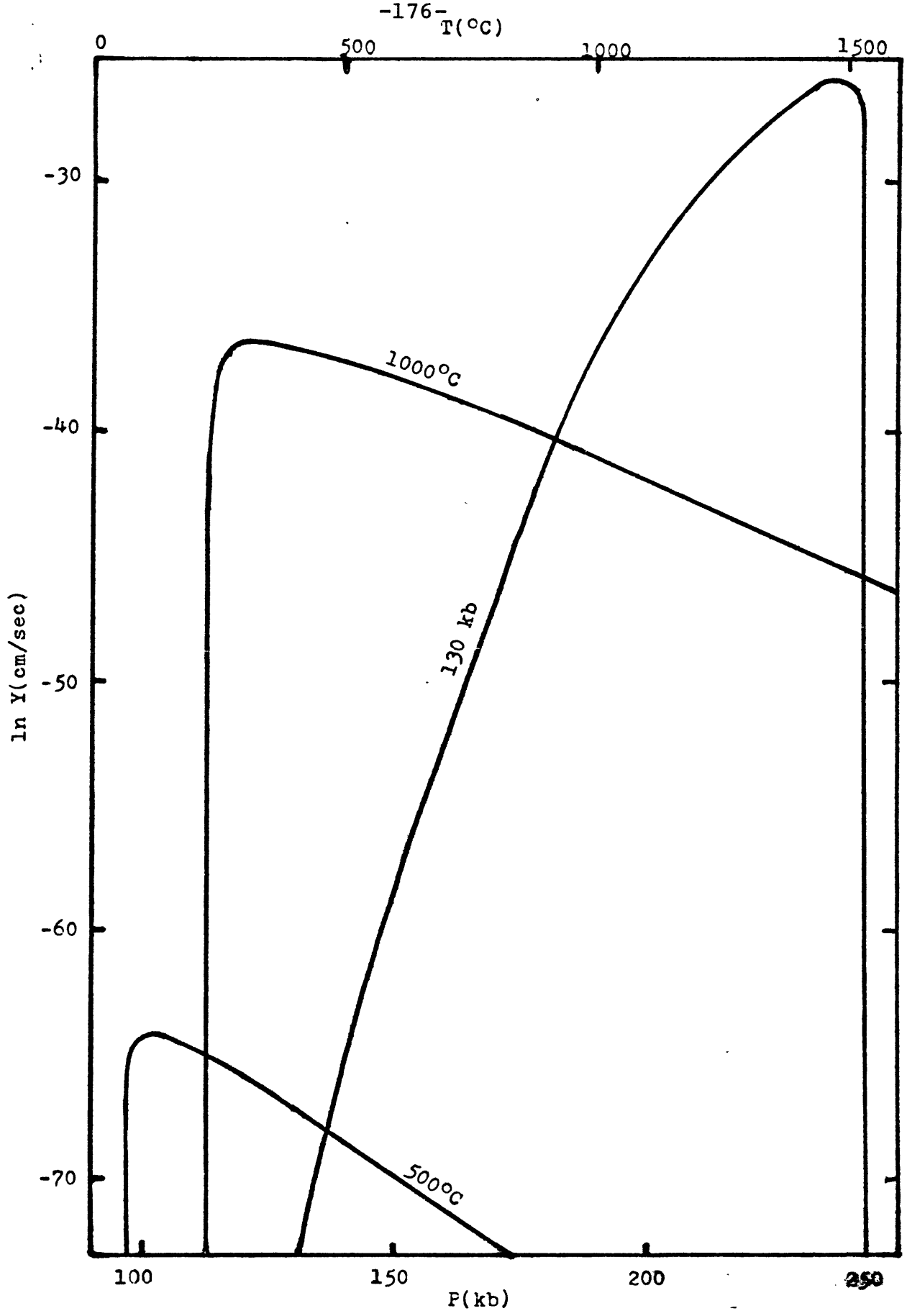
T(°C)
0
500
1000
1500
-30
-40
-50
-60
-70
ln Y(cm/sec)
1000°C
130 kb
500°C
100
150
200
250
P(kb)

using the method of phantom nuclei(nuclei are formed within the transformed region as well) and extended growth(nuclei keep growing when they hit each other), and were applicable to isothermal and isobaric transitions. Assumptions made in deriving these kinetic equations include:

(1) All grains are equal sized regular tetrakaidecahedra

(2) Grain surfaces or grain boundaries offer no resistance to the growth of nuclei, and

(3) All nuclei are spherical.

Cahn(1956) has derived kinetic equations for nucleation on grain boundaries and nucleation on grain edges. The former can also apply to nucleation on grain surfaces, and the latter, if we replace the total length of grain edges per unit volume by the dislocation density which is approximately equal to the total length of dislocation per unit volume, can also apply to nucleation on dislocations. In the latter case, the nucleation rate no longer depends on the grain size.

For an interface controlled process like the olivine-spinel transition, the nucleation and growth rates will soon reach a steady state and can be treated as constants. In this case, before site saturation occurs, i.e. before nucleation sites are exhausted on the crystal heterogeneities, kinetic equations for all the heterogeneous nucleation mechanisms we have considered have the same form as that for the homogeneous nucleation:

$$X=1-\exp(-(\pi/3)\bar{I}_s\ Y^3t^4) \qquad (6-40)$$

where X is the volume fraction of the transformed phase and t is the time of transition. If more than one nucleation mechanism is operative and none of them is site saturated. $\bar{I}_s$ in Eq. (6-40) will be the sum of the nucleation rates for them. After site saturation, the kinetic equation for nucleation on grain surfaces or grain boundaries becomes

$$X=1-\exp(-2\bar{S}Yt) \qquad (6\text{-}41)$$

and that for nucleation on dislocations becomes

$$X=1-\exp(-\pi\bar{L}Y^2t^2) \qquad (6\text{-}42)$$

where $\bar{S}$ and $\bar{L}$ are the total area of grain surfaces or grain boundaries, and the total length of dislocations per unit volume. It is noted that after site saturation, the transition will proceed by the growth of existing nuclei alone and the kinetics of the transition do not depend on the nucleation rate.

In general, the kinetic equation can be expressed by

$$X=1-\exp(-Kt^n) \qquad (6\text{-}43)$$

where n is a constant. Before site saturation, n=4 and

$$K=(\pi/3)\bar{I}_sY^3=(\pi/3)\delta\bar{N}(kT/h)^4\exp(-(\Delta G_T^*+4Q_a)/(kT))(1-\exp(\Delta G_a^d/(kT)))^3 \qquad (6\text{-}44)$$

n may be greater than 4 if the nucleation rate is increasing with time, such as occurs during the induction period(Fig. 6-6). After site saturation, n=1 for nucleation on grain surfaces or on grain boundaries, and

$$K=2\bar{S}Y=2\bar{S}\delta(kT/h)\exp(-Q_a/(kT))(1-\exp(\Delta G_a^d/(kT))) \qquad (6\text{-}45)$$

, and n=2 for nucleation on dislocations,

$$K=\pi\bar{L}Y^2=\pi\bar{L}\delta^2(kT/h)^2\exp(-2Q_a/(kT))(1-\exp(\Delta G_a^d/(kT)))^2 \qquad (6\text{-}46)$$

Eq. (6-43) can be rewritten as

$$\ln(\ln(1/(1-X)))=\ln K+n \ln t \quad \text{----------(6-47)}$$

Thus, a plot of $\ln(\ln(1/(1-X)))$ versus $\ln t$ for the experimental data of an isothermal and isobaric transition will fall on a curve with an initial slope of n=4 corresponding to the stage before site saturation. After site saturation the curve will approach a slope of n=1 for nucleation on grain surfaces or on grain boundaries, and a slope of n=2 for nucleation on dislocations. The intercepts of these slopes on the $\ln(\ln(1/(1-X)))$ coordinate give the values of $\ln K$ for each transition stage. The transition of the slope of the curve from n=4 to n=1 or 2 during site saturation is fairly abrupt, so that the whole observable range(X=0.01 to 0.99), which spans only a very brief range on the $\ln(\ln(1/(1-X)))$ coordinate, will fall on either of the straight line portions of the overall curve. We will see in the later discussion, site saturation for the olivine→spinel transition occurs at a very early stage (X<<1%)of the transition, so that its kinetics can be effectively described by either Eq. (6-45) or (6-46).

Substituting the previously estimated values for the olivine→spinel transition into Eqs. (6-44) to (6-46), we obtain the following rate equations for the isothermal and isobaric olivine→spinel transition:

(1) before site saturation:

(A) himogeneous nucleation with a coherent interface

$$K_c^H(\sec^{-4})=1.9\times10^{41}T^4\exp(-(1.2\times10^{23}/(6.6\times10^9-6.7\times10^7P+2.2\times10^6T)^2 +1.8\times10^5+490P)/T)(1-\exp(0.25+(550-7.7P)/T))^3 \quad \text{----------(6-48)}$$

(B) homogeneous nucleation with an incoherent interface

$$K_i^H(\sec^{-4})=1.9\times10^{41}T^4\exp(-(3.3\times10^{24}/(4.8\times10^9-6.7\times10^7P+2.2\times10^6T)^2+1.8\times10^5+490P)/T)(1-\exp(0.25+(550-7.7P)/T))^3 \quad (6\text{-}49)$$

(C) nucleation on grain surfaces or grain boundaries, assuming $\Delta G_T^{S(B)*}=0$

$$K^{S(B)}(\sec^{-4})=(6.5\times10^{34}/D)T^4\exp(-(1.8\times10^5+490P)/T)(1-\exp(0.25+(550-7.7P)/T))^3 \quad (6\text{-}50)$$

(D) nucleation on dislocations, assuming $\Delta G_T^{D*}=0$

$$K^D(\sec^{-4})=1.5\times10^{27}\rho T^4\exp(-(1.8\times10^5+490P)/T)(1-\exp(0.25+(550-7.7P)/T))^3 \quad (6\text{-}51)$$

(E) all nucleation mechanisms operating simultaneously

$$K^T=K^H+K^{S(B)}+K^D \quad (6\text{-}52)$$

(2) after site saturation:

(A) nucleation on grain surfaces or grain boundaries

$$K^{S(B)}(\sec^{-1})=(3.6\times10^3/D)T\exp(-(4.5\times10^4+120P)/T)(1-\exp(0.25+(550-7.7P)/T)) \quad (6\text{-}53)$$

(B) nucleation on dislocations

$$K^D(\sec^{-2})=8.8\times10^5\rho T^2\exp(-(9.0\times10^4+250P)/T)(1-\exp(0.25+(550-7.7P)/T))^2 \quad (6\text{-}54)$$

For each nucleation mechanism, if we specify X and t, the rate constant K is uniquely determined(Eq. 6-43). The P-T trace corresponding to this particular value of K defines the isograd (equal degree of transition)X at a transition time t. We have calculated the isograds of each nucleation mechanism for the olivine→spinel transition at two extreme values of t, 4.3 million years and 60 minutes. The former corresponds to the time required

to descend a downgoing slab 300 Km beyond the depth for equilibrium olivine→spinel transtion. The latter corresponds to the average time for the olivine→spinel transition performed in the laboratory. In addition we have assumed that the grain size and the dislocation density of olivine in the downgoing slab and in the laboratory are 0.5 cm, 10^8 cm^{-2}, and $5x10^{-4}$ cm, 10^{10} cm^{-2}, respectively. We also assume that site saturation for heterogeneous nucleations occurs at the very beginning of the transition. The results are shown in Fig. (6-10). The shaded bands correspond to the degree of transition between 10%(X=0.1) and 90%(X=0.9) for each nucleation mechanism. Thus olivine remains virtually untransformed on the low temperature side of the isograd band, and it is almost completely transformed on the high temperature side.

From rate equations derived(Eqs. 6-48 to 6-54) and isograds calculated(Fig. 6-12), the general characteristics of the kinetics of the olivine→spinel transition may be summarized as follows:
(1) The rate of transition is greatly promoted by increasing temperature. Thus, the isograd of the higher degree of transition always lies on the high temperature side of the isograd of the lower degree of transition.
(2) The rate of transition will initially increase, and then decrease monotonically, with pressure. The increasing rate is due to decreasing ΔG_T^* and the increasing energy barrier for the decomposition of supercritical-sized nuclei(Fig. 6-10) with increasing ΔP. The decreasing rate is due to increasing of Q_a

Fig. (6-10)

Calculated kinetic diagram for the olivine→spinel transition in a downgoing slab. Inclined straight line is the olivine-spinel phase boundary. Black bands represent the degree of transition between 10% and 90% for different nucleation mechanisms. H, B and D refer to homogeneous nucleation, nucleation on grain boundaries, and nucleation on dislocations, respectively. Subscripts c and i denote coherent and incoherent interfaces, respectively. Note that all these black bands do not extend below a temperature of approximately 700°C, suggesting that the olivine→spinel transition in the downgoing slab may be suppressed below this temperature.

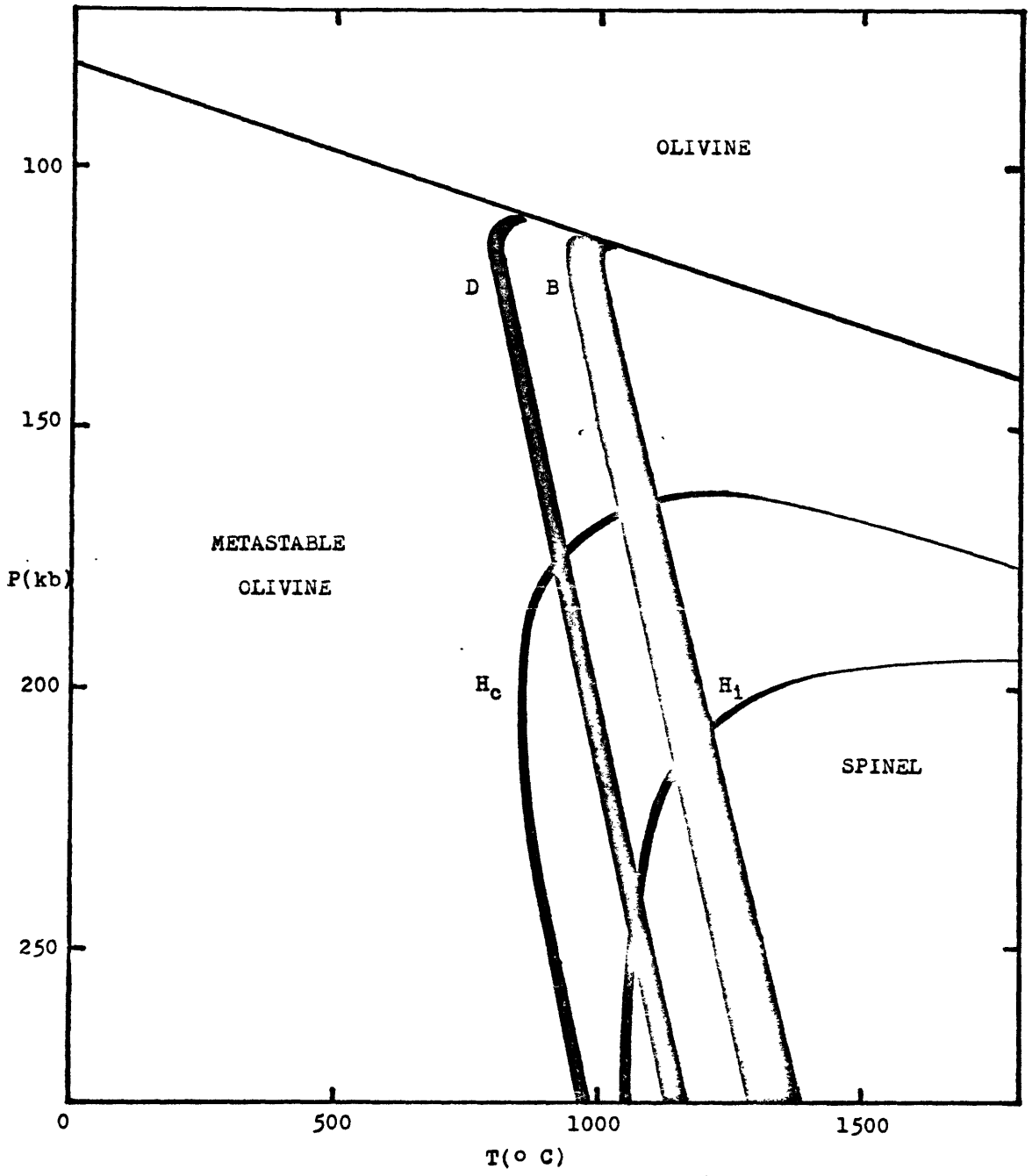
OLIVINE
D
B
METASTABLE
OLIVINE
H_c
H_i
SPINEL
100
150
200
250
P(kb)
0
500
1000
1500
T(° C)

with P.

(3) As a consequence of (1) and (2), isograds are C-shaped curves, and concave towards lower temperature. The slope of the upper(lower pressure) portion of the isograds is determined by $\bar{\sigma}$ and $\Delta\bar{V}$, and the slope of the lower(higher pressure) portion of the isograds is determined by ΔV^*.

(4) For each nucleation mechanism, there is a characteristic trmperature, T_{ch}, below which the degree of transition is negligible, say $X<0.1$. Olivine can exist metastably below T_{ch} no matter how high the overpressure.

(5) Heterogeneous nucleations will dominate the olivine→spinel transition at small over pressure. Homogeneous nucleation will compete only at very high overpressure($\Delta P>100$ Kb) and at low temperature.

(6) If grain size is sufficiently small, nucleation on grain surfaces or on grain boundaries will dominate the transition. In this case the rate of transition will be promoted by diminishing the grain size.

(7) If the dislocation density is sufficiently high, nucleation on dislocations will dominate the transition. In this case, the rate of transition can be promoted by increasing the dislocation density, that is by increasing the shear stress.

(8) Nucleation on dislocations may dominate the olivine→spinel transition in a downgoing slab, while nucleation on grain surfaces will dominate under laboratory conditions.

(9) The increase of interfacial energy, an effect more pronounced at lower temperature, will push the isograd towards higher pres-

sure, and thus, can reduce the rate of transition. Therefore, the olivine→spinel transition with an incoherent interface is slower than that with a coherent interface.

(10) Because of the presence of high strain energy, the olivine→spinel phase boundary for the transition with a coherent interface is displaced towards high pressure by an amount $\bar{\xi}/\Delta \bar{V} \sim 27$ Kb.

(11) Although nucleation on grain surfaces is faster than nucleation on grain boundaries, their rates of transition are similar(if the grain size is the same), because site saturation will occur at the very beginning of the olivine→spinel transition(see section 6-10).

(12) Isograds will move towards higher temperature with decreasing transition time. The characteristic temperature T_{ch} moves likewise. For example, by decreasing t from 4.3 m.y. to 60 min., isograds and T_{ch} will move towards higher temperature by approximately $1000^{o}C$.

(13) Isograds will move towards higher temperature with increasing Q_a. For each nucleation mechanism, the position of the isograd at a given time is primarily determined by Q_a and is less sensitive to the pre-exponential terms in the rate equation.

Because the position of the isograd and thus the rate of the olivine→spinel transition is mainly controlled by Q_a, the accuracy of our above semi-quantitative calculations depends on the accuracy of our estimation of Q_a. For example, if we have overestimated Q_a by a factor of two, the positions of all the

previously calculated isograds should be displaced towards lower temperature by approximately 300^0C. In the following section we will calculate the value of Q_a, based on some scattered experimental data in literature , and compare it with our previous theoretical estimate.

6-9: Activation energy of growth:

In the previous calculations, we have tentatively assumed that Q_a for the olivine→spinel transition is comparable to the activation energy for grain boundary diffusion of oxygen atoms in olivine. Because the latter is not known well, Q_a previously estimated may have a high uncertainty. We shall attempt here to calculate Q_a from selected experimental data in the literature and compare it with our previous estimated value.

Although the olivine→spinel transition on Mg-rich compositions has been extensively studied, most of the experiments performed used "reactive forsterite" as the starting material or mixed the charge with a mineralizer such as water and $Mg(OH)_2$. None of these experimental data list the degree of transition. Thus, they are not useful for kinetic calculations. However, there are some experimental data on the transition of pure forsterite(synthetic), done in the absence of mineralizer. Among them, there are four runs from which the proportion of transformed phase can be estimated from the description of the experimental results. These four sources include one on the $\alpha \rightarrow \gamma$ transition(Ito et al, 1974) and three on the $\alpha \rightarrow \beta$ transition(Akimoto and Ida, 1966) and are listed in Table (6-2). The

Table (6-2)

SELECTED EXPERIMENTAL DATA USED TO CALCULATE Q_a FOR THE OLIVINE→SPINEL TRANSITION IN Mg_2SiO_4

Estimated Grain Size D(μ)	P(Kb)	ΔP[a] (Kb)	T'(°C)	t (min)	Transition	Estimated Degree of Transition (X)	Calculated Q_a (10^{-12} erg/atom) S[b]	D[b]
2[c] (Finely Pulverized)	250	125	1000	55	α→γ	0.95 (Minute Residual Forsterite)	5.3	5.7
0.2[d] (Microcrystalline)	155	44	815	60	α→β[e]	0.01 (Trace Amount)	5.6	5.2
0.2[d] (Microcrystalline)	230	122	740	20	α→β[e]	0.01 (Trace Amount)	5.2	4.8
0.2[d] (Microcrystalline)	230	112	1010	60	α→β[e]	0.50 (Maximum 50% Conversion)	6.0	5.8

Notes and references:

a) Calculated from Table (1-1), ref. (c)

b) S and D refer to nucleation of grain surfaces and nucleation on dislocations, respectively.

c) Ito et al(1974)

d) Akimoto and Ida(1966)

e) Akimoto and Ida(1966) claimed that the transition was α→γ. However, later studies(Ringwood and Major, 1970; Akimoto, 1972) have revealed that the transition should be α→β.

starting material for the experiments were in the form of finely pulverized powder or microcrystalline crystalites, so nucleation on grain surfaces may have dominated the transtion. Assuming site saturation occurred at the very beginning of the transition, then Eq. (6-45) is applicable, and using the data of Table(6-2), values of Q_a for each run were calculated and are tabulated in Table (6-2). The Q_a's so calculated fall in the range of 5.2×10^{-12} to 6.0×10^{-12} erg/atom. If nucleation on dislocations dominated the transition instead, by assuming a dislocation density of 10^{10} cm^{-2} and using Eq. (6-46), Q_a is calculated to fall within the range of 4.8×10^{-12} to 5.8×10^{-12} erg/atom(Table 6-2). In both calculation models, Q_a for each run may not vary by more than 2% within the reasonable range of grain size and dislocation density assumed. Thus, all the experimental data on the olivine→spinel transition in Mg_2SiO_4 suggest a value of Q_a of approximately 5.5×10^{-12} erg/atom. It is also suggested from the above calculation that Q_a may be comparable for the $\alpha \rightarrow \gamma$ and the $\alpha \rightarrow \beta$ transitions. This agrees with our previous prediction, based on crystal structural considerations(Chap. 4). In addition, the calculated Q_a does not seem to increase with pressure. Our experimental results on the olivine→spinel transition of Fe-rich composition also suggest that Q_a may not increase with pressure as will be described in Chap. 8. This could mean that the activation volume for the olivine→spinel transition is negligible. It is speculated that the migration of oxygen atoms across the incoherent interface may take advange of the presence of ample dislocaitons and

vacancies on the interface, which would eliminate a volume increase for the activated stage. It is also suspected that the high shear stress characteristic of high pressure apparatus may facilitate the migration of oxygen atoms across the interface and thus reduce the activation volume. If this is true, Q_a for the olivine→spinel transition in downgoing slabs may be much larger than that calculated from the experimental data and may approach the value of our previous estimate. It is interesting to note that Q_a so calculated is 59% of Q_D estimated previously(Eq. 6-32), assuming that the activation volume is zero. Thus both theoretical and experimental data are consistant with a value of $Q_a \sim 5.5 \times 10^{-12}$ erg/atom, which is independent of both pressure and temperature.

Isograds of the olivine→spinel transtion for each nucleation mechanism under the two extremely different conditions in the downgoing slab and in the laboratory were recalculated based on $Q_a = 5.5 \times 10^{-12}$ erg/atom. The results are shown in Fig. (6-11). The general kinetic features are similar to these depicted in Fig. (6-10). However, because the activation volume is zero, all isograds are displaced towards lower temperature by more than 300°C. In addition, they are parallel to the pressure axis above a certain overpressure, where the ΔG_T^*'s become smaller than Q_a. The activation volume is therefore crucial in determining the kinetics of the olivine→spinel transition. The significance of its role in plate dynamics will be discussed in Chap. 9.

Fig. (6-11)

Recalculated kinetic diagram for the olivine→ spinel transition based on $Q_a=5.5\times10^{-12}$ erg/atom. Symbols are the same as in Fig. (6-10). Black and cross-hatched bands correspond to the olivine→ spinel transition in the downgoing slab and in the laboratory, respectively. Note the isograds become vertical at high pressure for laboratory conditions because of $\Delta V^*=0$ assumed in calculation.

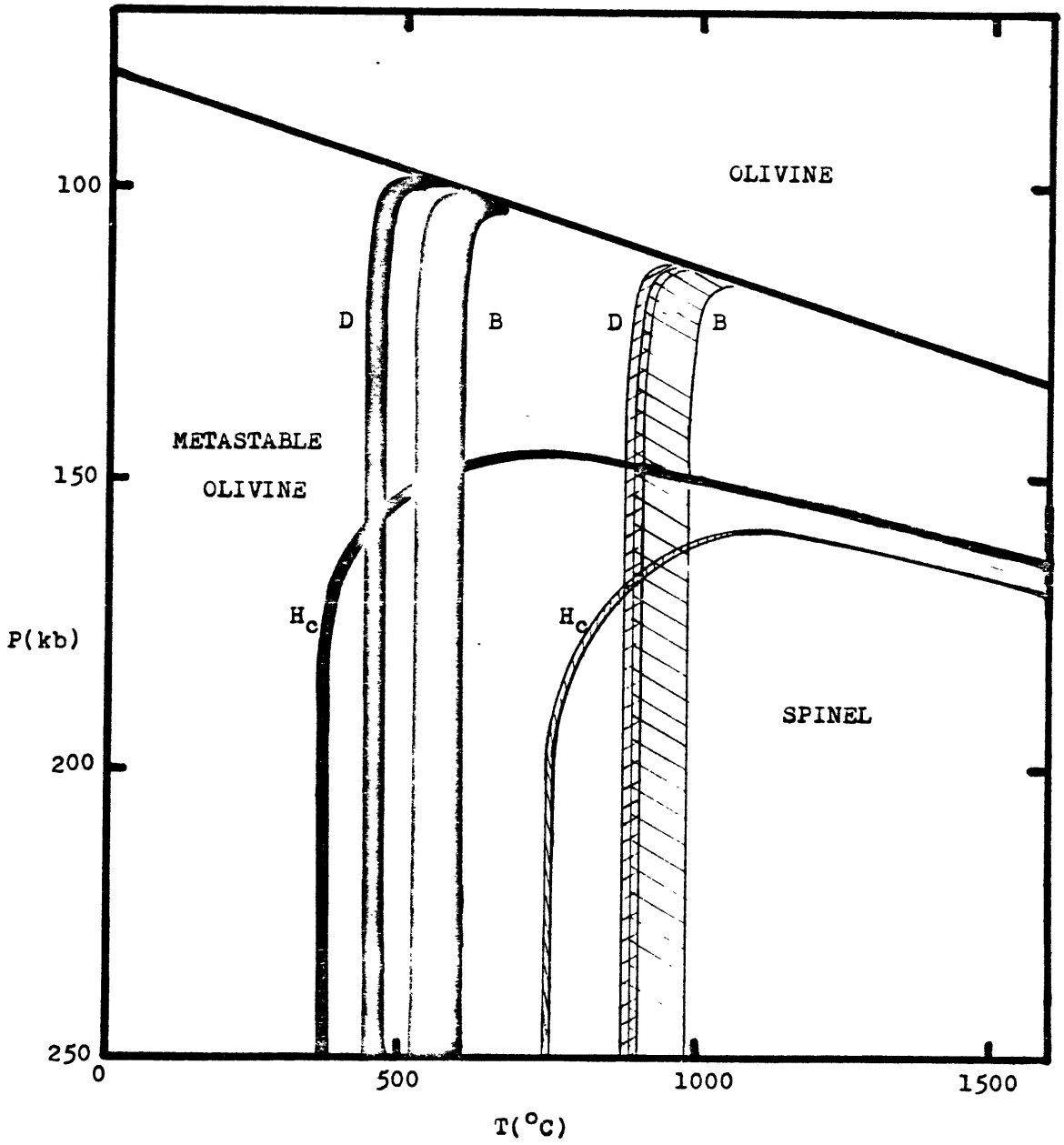
OLIVINE
100
D
B
D
B
METASTABLE
OLIVINE
150
H_c
H_c
P(kb)
SPINEL
200
250
0
500
1000
1500
T(°C)

6-10: Incubation time and site saturation time:

We have assumed in the previous calculations that a steady state nucleation rate will be established and that site saturation on crystal heterogeneities will occur at an early stage of the olivine→spinel transition. In this section we will justify these two assumptions, by showing that the incubation time, τ, and the time for site saturation on crystal heterogeneities, t_s, are indeed much shorter than the time required to attain a small degree, say 1%, of olivine→spinel transition.

The incubation time for a solid-solid transition can by expressed(Russel, 1976) by:

$$\tau \sim 1/(2Z^2\beta^*) \qquad (6\text{-}55)$$

Substituting Eqs. (6-18) and (6-20) into Eq. (6-55), we obtain

$$\tau \sim (3\pi h n^*/(s^* \Delta G_T^*)) \exp(-Q_a/kT) \qquad (6\text{-}56)$$

For a spherical nucleus

$$n^* = (4/3)\pi r^{*3} \bar{N}_V^s \qquad (6\text{-}57)$$

and

$$s^* = 4\pi r^{*2}/a^2$$

where $\bar{N}_V^s$ and a are the number of oxygen atoms per unit volume and the average oxygen-oxygen distance in the spinel nucleus. Substituting Eqs. (6-9) and (6-10) into Eq. (6-56), we obtain

$$\tau \sim (\pi h \, \overline{\sigma N}_V^{s2} a^2/(8(\Delta \bar{V} \Delta P + \bar{\xi})^2)) \exp(Q_a/(kT)) \qquad (6\text{-}59)$$

for the olivine→spinel transition. The incubation time is then primarily temperature dependent. Let $\bar{N}_V^s \sim 6.3 \times 10^{22}$ cm^{-3}, $a \sim 2.5 \times 10^{-8}$ cm and $Q_a \sim 5.5 \times 10^{-12}$ erg/atom, τ as a function of temperature for homogeneous nucleation at $\Delta P = 100$ Kb is shown in Fig. (6-12).

Fig. (6-12)

Incubation time (τ) for homogeneous nucleation as a function of temperature at an overpressure of 100 Kb. Cross-hatched band are times required to attatin 1% to 99% completion of the olivine→spinel transition, assuming the highest nucleation rate(steady state nucleation rate $\bar{I}_s$). Note τ is always smaller than the time for a small degree of transition, so that the steady state nucleation rate dominates the major transition process.

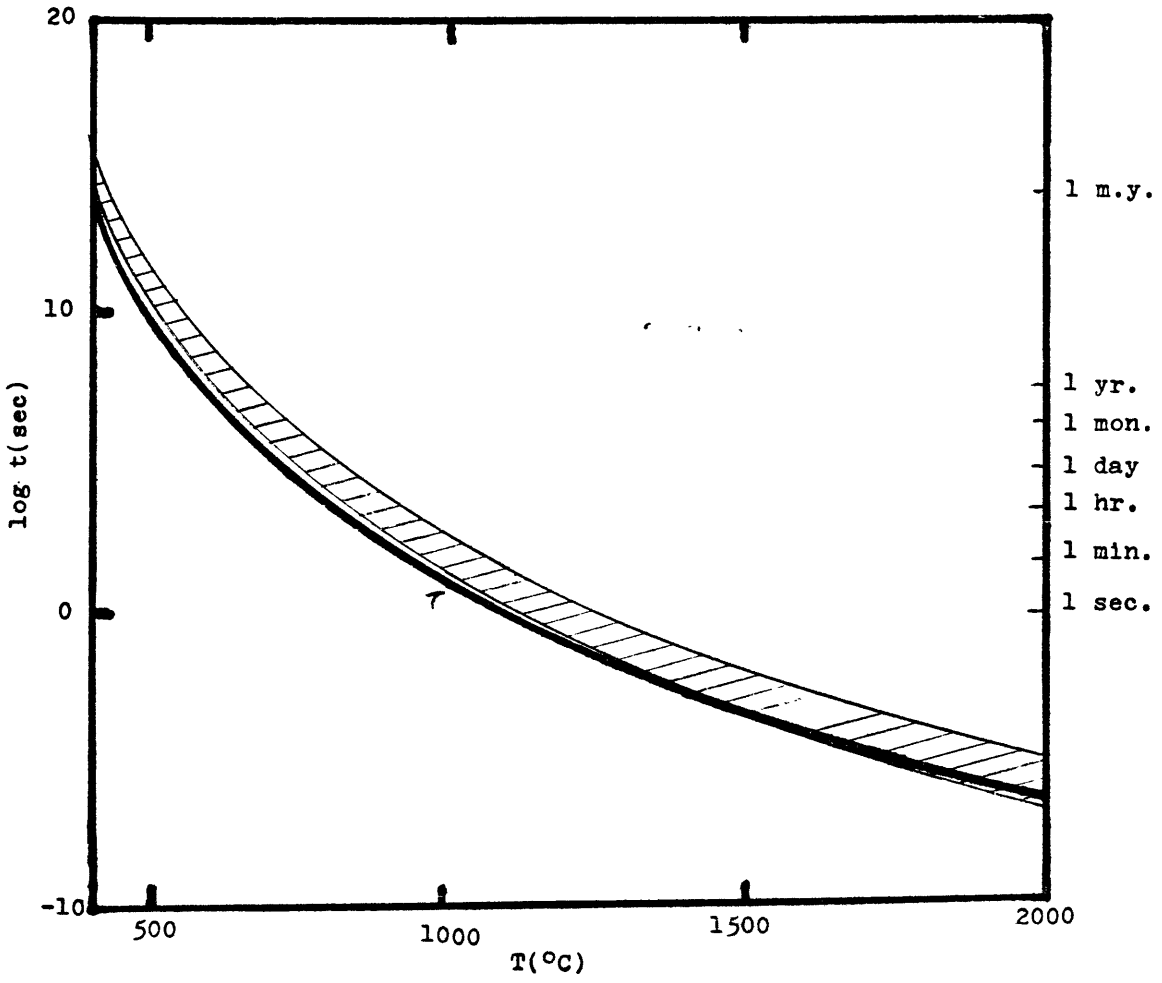
20
10
0
-10
log t(sec)
500
1000
1500
2000
T(°C)
1 m.y.
1 yr.
1 mon.
1 day
1 hr.
1 min.
1 sec.

Cross-hatched bands superimposed in the same figure are the times required to accomplish 1%($t_{0.01}$) to 99%($t_{0.99}$) of the olivine→spinel transition, assuming a steady state nucleation rate. Except in the very high region for the olivine→spinel transition with a coherent interface, τ is smaller than $t_{0.01}$. The difference between $t_{o.o1}$ and τ will increase slightly with decreasing overpressure. Thus, it is apparent that the steady state nucleation rate will be established at a very early stage of the olivine→spinel transition.

The time required for site saturation on grain surfaces or grain boundaries is (Cahn, 1956):

$$t_s^S(\text{sec}) = (\bar{I}_s^S Y^2/\bar{S})^{-1/3} \sim 3.1\times10^{-11} T^{-1} \exp(4.0\times10^4/T) \left(1-\exp(-7.7\Delta P/T)\right)^{-2/3} \quad (6\text{-}60)$$

The time required for site saturation on dislocations can be shown to be:

$$t_s^D(\text{sec}) = (\bar{I}_s^D Y/\bar{L})^{-1/2} \sim 2.2\times10^{-15} T^{-1} \exp(4.0\times10^4/T) \left(1-\exp(-7.7\Delta P/T)\right)^{-1/2} \quad (6\text{-}61)$$

Note that t_s is independent of the grain size and of the dislocation density. t_s as a function of temperature at ΔP=100 Kb for both nucleation on grain surfaces or grain boundaries, and nucleation on dislocarions is shown in Fig. (6-13). Dotted lines are $t_{0.01}$ calculated by assuming site saturation doesn't occur. t_s is much smaller than $t_{0.01}$ for both nucleation on grain surfaces or grain boundaries, and nucleation on dislocations. A similar conclusion is reached at other values of ΔP. Thus, it is reasonable to assume that site saturation occurs at

Fig. (6-13)

Saturation time(t_s) as a function of temperature at ΔP=100 Kb for nucleation on grain surfaces(A) and nucleation on dislocations(B). Dashed curves are times required to attain 1% of the olivine→spinel transition ($t_{0.01}$), calculated by assuming that site saturation does not occur. Numbers in parentheses are grain sizes (A) and dislocation densities(in cm^{-2})(B). Note t_s is smaller than $t_{o.ol}$ in all cases, suggesting that site saturation occurs at the very beginning of the olivine-spinel transition and that the major transition process is growth of the existing nuclei on the heterogeneities.

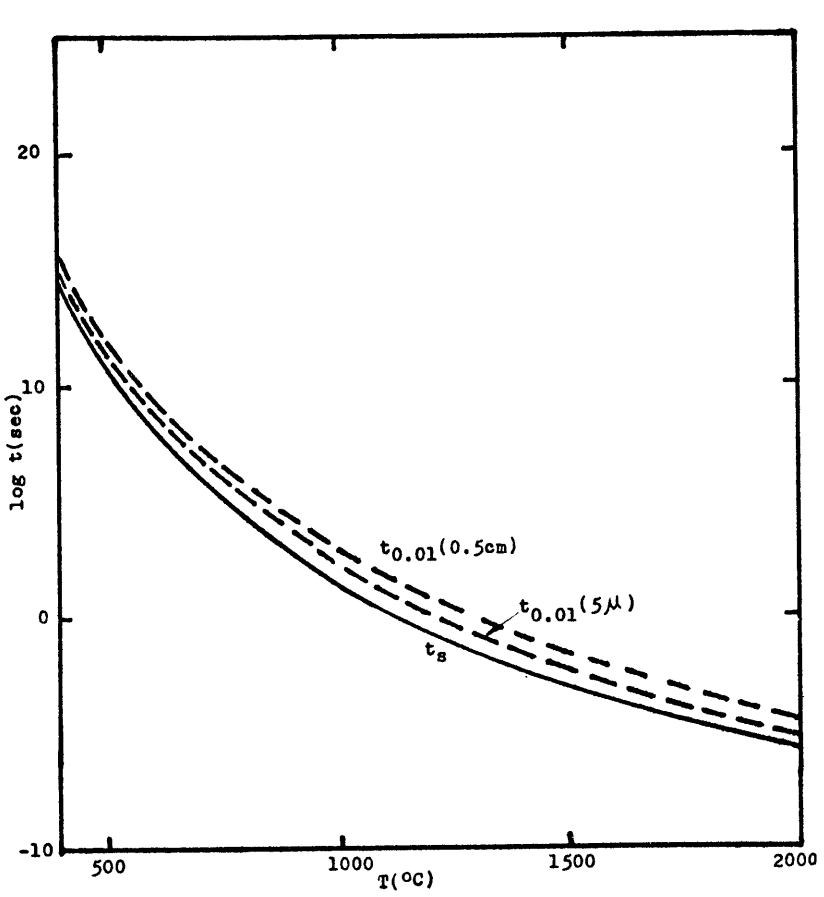
20
10
0
-10
log t(sec)
500
1000
1500
2000
T(°C)
$t_{0.01}$(0.5cm)
$t_{0.01}$(5μ)
t_s

(A)

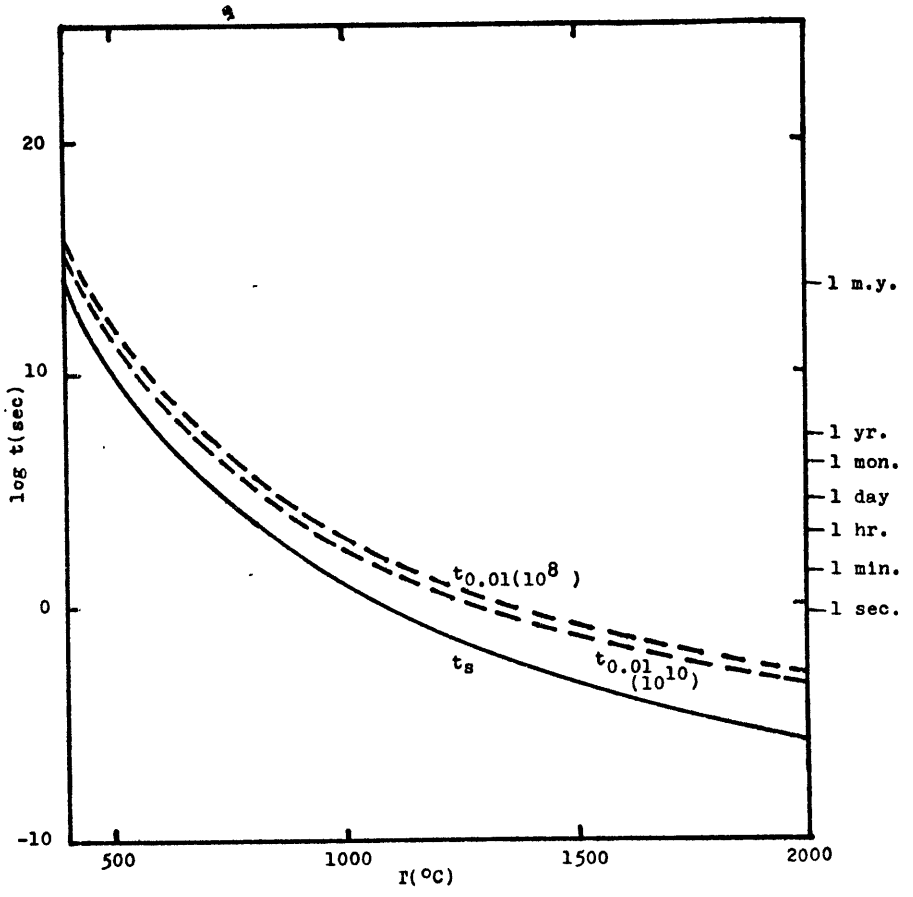
20
10
0
-10
log t(sec)
500
1000
1500
2000
T(°C)
$t_{0.01}(10^8)$
t_s
$t_{0.01}(10^{10})$
1 m.y.
1 yr.
1 mon.
1 day
1 hr.
1 min.
1 sec.

(B)

the beginning of the olivine→spinel transition for heterogeneous nucleations, and that the transition will proceed only by the growth of existing nuclei. Our experimental results on the olivine→spinel transition is also consistent with this prediction, as will be described in Chap. 8. Thus, for heterogeneous nucleations, the kinetics of the olivine→spinel transition is independent of nucleation rate. Therefore it makes no difference whether or not the nucleation rate has reached a steady state before site satuation occurs.

Chapter 7

INSTRUMENTATION

7-1: Introduction:

There are many high pressure-high temperature apparatuses which can be used to study the olivine→spinel transition. They include: piston-cylinder apparatus, Bridgeman anvil, Bell type tetrahedral press, sliding anvil press, multi-anvil split-sphere high pressure vessel, etc.. Among them the diamond anvil press (diamond cell) is unique in that it allows both visual observations and instrumental measurements to be made while the transition is taking place under high pressure and high temperature. This aspect is especially useful for our purpose of studying the kinetics of the olivine→spinel transition. In addition, the construction of the diamond anvil press is simple, so the original investment and subsequent maintenance costs are small compared to those for other types of high pressure apparatus. Thus, it has been used for the major part of our experimental studies of the olivine→spinel transition.

7-2: The Diamond Anvil Press:

The diamond anvil press we used is a new modification, derived from the original design of Bassett and Takahashi (1965), and employs a new mechanism for aligning the two diamonds and a new design of heating elements (Sung, 1976). This new diamond anvil press is capable of maintaining 300 kb and 1000°C over long periods of time. It can be mounted on a

Zeiss microscope, an x-ray generator, Cary 17 spectrophotometer, and the Mössbauer spectrometer, and thus is a versatile apparatus for research at high pressure and high temperature.

The anvils are made of 1/8 carat brilliant cut natural diamonds with the culet diameter ranging from 0.3 to 0.7 mm. For the purposes of alignment, the two anvils used have culet surfaces with different diameters, the smaller one being mounted on the lower piston. The detailed assembly of the diamond anvil press is shown in Figure (7-1). The two diamond anvils (A) are mounted on the two pistons (B, C), using a high temperature cement such as Sauereisen No. 1 paste. The upper piston (B) is driven by the gimbal (D) and guided by the cylindrical sleeve (E). The pressure is achieved by turning the screw (F) to squeeze on the spring (G), which ultimately transmits the force to the sample held between the two diamond anvils. There are holes through the center of the two pistons which allow the transmission of radiation from optical light, x-ray, or Mössbauer γ-ray sources through the sample. The hole in the upper piston is a tapered slot which allows the passage of diffracted x-rays of up to $2\theta=35°$. The x-ray source is usually monochromatized Mo K_α radiation. It is collimated to a diameter of about 100 μm by a lead dispersed glass capillary tube (H) before entering the lower diamond and impinging on the sample. The position of the collimator (H) can be adjusted by turning the three equally spaced set screws (I) on the collimator holder (J). The latter is joined to the press by thread and can easily be detached or mounted

Fig. (7-1)

Detailed assambly for the new modification of the diamond anvil press.

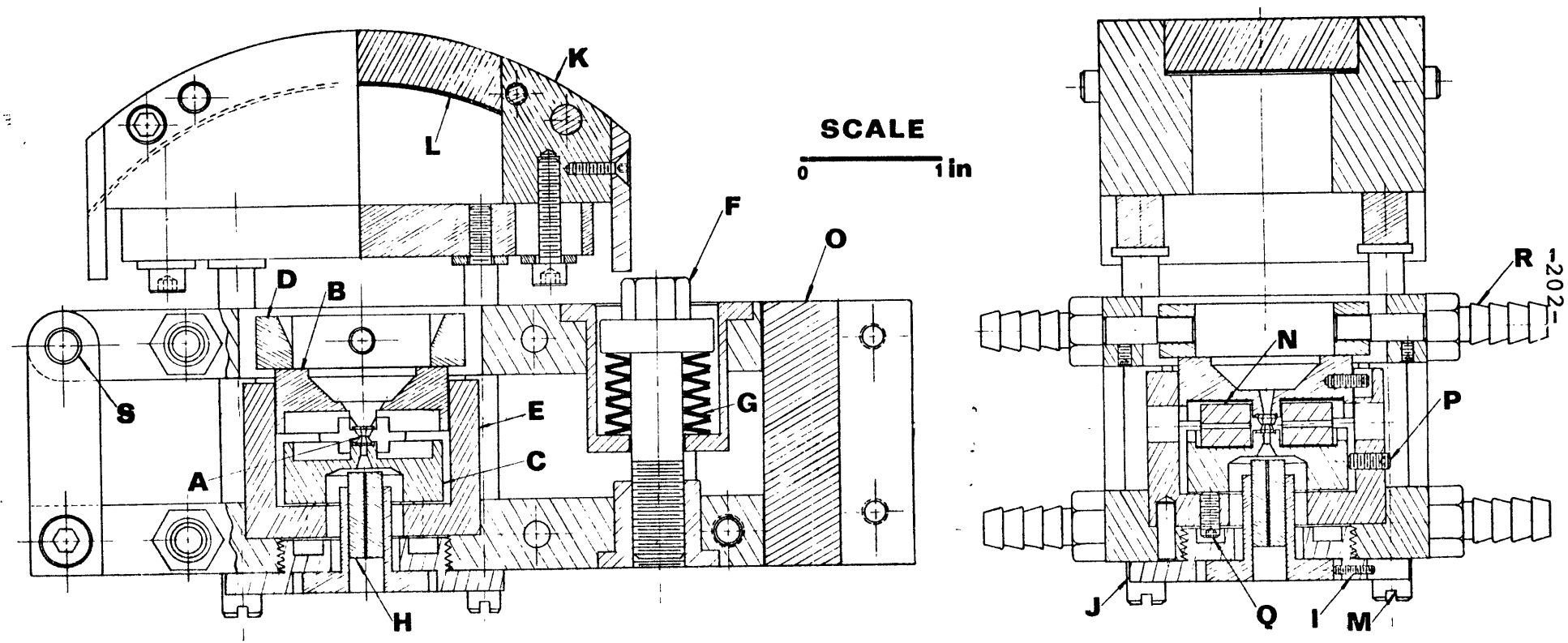
K
L
F
O
D
B
S
E
G
C
A
H
SCALE
0
1 in
R
N
P
J
Q
I
M
1202

without disturbing the original collimation. The x-ray camera (K) is a duplication of that designed by Bassett et al. (1967). The x-ray film is curved to a radius of 2.5" with its center coinciding with the sample. The camera is attached to the press by the four legs (M) and the sample-to-film distance can be adjusted before the heater (N) is placed around the two diamonds. The sample-to-film distance can be monitored by placing a platelet of NaCl outside the upper diamond. The whole press can be connected to a simple fixture (O) which fits to the track on the x-ray generator. Using NaCl as an internal standard to calibrate the pressure, the exposure time for Mo K_α radiation is about 400 hours. The exposure time can be reduced by using a smaller film radius, but this also reduces the precission of the pressure determination. Pressure can also be determined by the ruby fluorescence technique (Barnett et al., 1973). In this case, neither the x-ray collimator nor the camera is used, and they can be removed from the press.

The alignment of the two diamonds is achieved by translation and rotation of the lower diamond. Three equally spaced set screws (P) are used for the translational adjustment and the other three (Q) are used for the rotational adjustment. A similar alignment technique has been described before (Barnett et al., 1973). There are three alternative ways of arranging the six adjustment set screws as shown in Figure 7-2. The two sets of screws can both be located outside the lower piston (Figure 7-2b, c). The latter arrangement is better,

Fig. (7-2)

Three alternative ways to align the lower diamond: (A) both translational and rotational adjustment set screws are located outside the lower poston; (B) translational adjustment set screws are located outside the lower piston; and (C) rotational adjustment set screws are located outside the lower piston. Rotational adjustment set screws can also be mounted on the upper piston. The maximum pressure which can be achieved using these three alignment geometries is in the order (C)>(B)>(A).

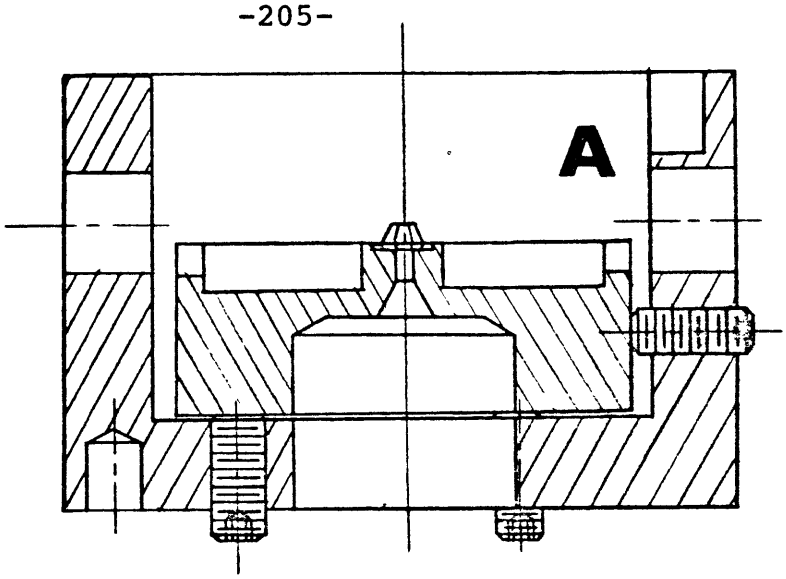
A

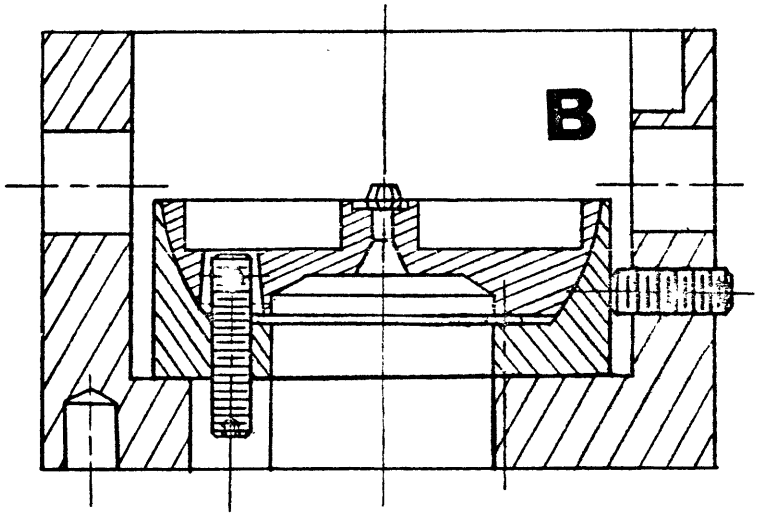
B

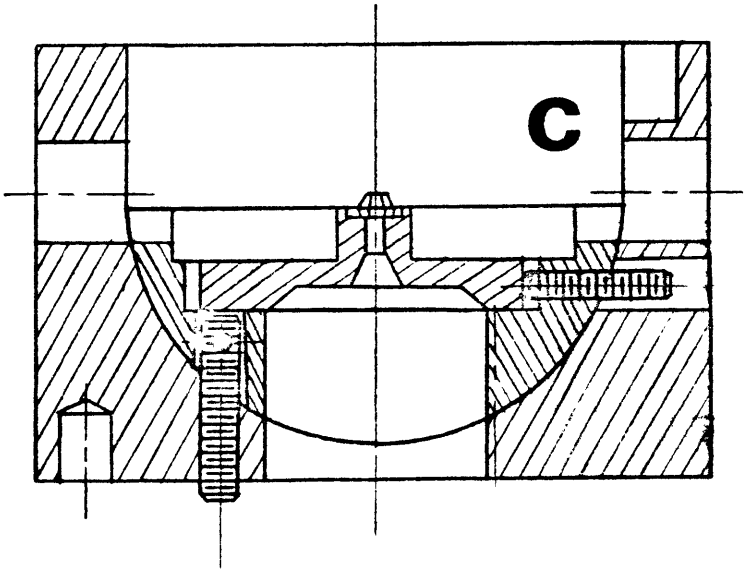
C

because the two adjustments (translational and rotational) are independent and will not interfere with each other. In addition, it can sustain higher load force and thus can be used to achieve higher pressure, even when a gasket is used. This new design makdes the alignment very easy and enables continuous adjustment under a microscope to be made. The alignment can also be performed in the middle of an experiment, without unloading the sample. A good alignment of the diamonds is indicated by the concentric phase boundaries of the sample and the centering of the isogyre cross of the uniaxially strained diamonds between crossed polars.

The heater (N) is made of a fired pyrophyllite disc wound with thermocouple wire (0.016" diameter, 3' long) of platinum-rhodium (13%). The immediate surrounding of the sample by the heater has the advantage of rapid heating, e.g. 1 minute from 400°C to 600°C, without sacrificing the effectiveness of the quenching, e.g. 1 minute from 600°C to 300°C. This kind of heater can be used for continuous heating over several months.

X-ray identification of phases is usually done on the unloaded sample. The sample is mounted on a lead dispersed glass collimator with a 100μ diameter opening. The collimator is then attached to a specially designed camera of Debye-Scherrer geometry. The camera can be loaded on the track of an x-ray generator. The source of x-ray radiation is Fe K_{α}. The radius of the film is only 0.6" so the exposure time can be less than 200 hours.

7-3: Temperature Calibration:

Heating the sample is achieved by passing the current through the Pt-Pt (Rh13%) wire within the heater. Temperature is adjusted by varying the output voltage of the variac. Two variacs are connected in series which makes the adjustment smoother. A temperature controller can be used to stabilize the heating and a recorder can be used to monitor the temperature variation. Temperature is measured by Pt-Pt (Rh13%) thermocouple wires which connect to a digital temperature indicator. There are two holes penetrating horizontally through the heater (N) (Figure 7-1, 7-3). Two thermocouples can be used simultaneously to measure temperatures inside the heater. Temperature distribution inside the heater is quite homogeneous when the two diamonds are not inserted. The horizontal and the vertical temperature gradients inside the heater can both be very large, especially at high sample temperature, when the two diamonds are closed up as shown in Figure (7-3).

Measured temperatures can be 50°C higher than the true sample temperature, even if the thermocouple head touches the diamonds. Because the diamond is a good thermal conductor (although it is a poor electrical conductor), and the sample is small and very thin (about 5 to 10 μm), the temperature gradient inside the sample is probably not large. The true sample temperature can be measured by clamping the head of an ultrafine thermocouple (0.001 wire diameter) at one edge,

Fig. (7-3)

Temperature profile across the heater at a sample temperature of 600°C. The lower figure shows the temperature distribution along the horizontal line passing through the center of the sample. Numbers are temperatures in °C. C and O mean the two diamonds are closed together and open, respectively.

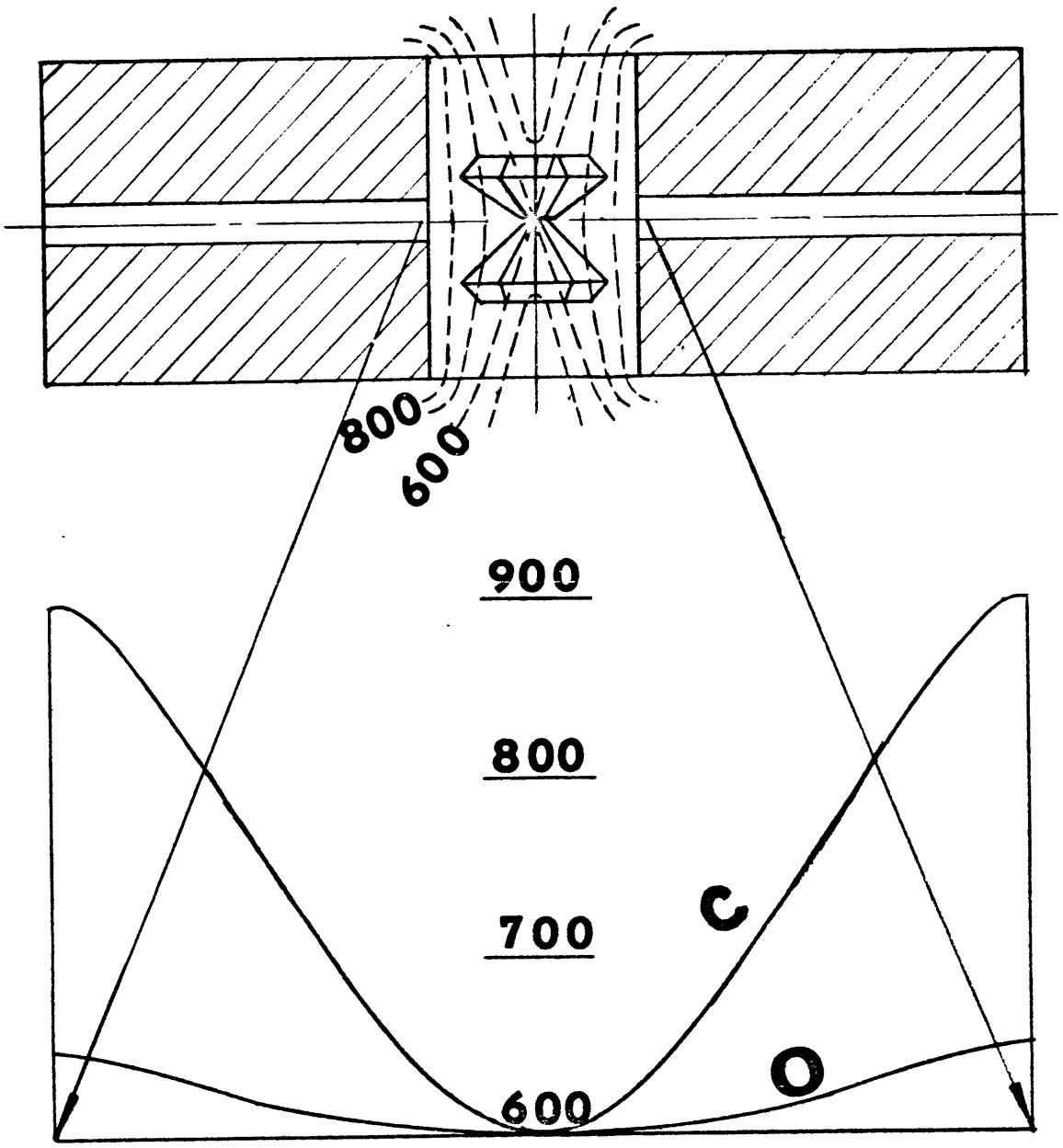
800
600
900
800
700
600
C
O

between the two diamonds. Because the pressure there is low, say below 30 kb, it will not decrease the temperature reading by more than 2%. Applying pressure tends to give a lower temperature reading, but the sample is slightly colder at the center than at the edge, so these two sources of error tend to cancel oneanother out. We believe that the maximum accuracy of temperature measurement is within $\pm$ 10°C.

The steady state power input for the heater to maintain a particular sample temperature is shown in Figure (7-4). The steady state power can be approached in a few hours of heating at low temperatures and in a few minutes at high temperatures, say above 750°C. It is reproducible if the condition of the environment (ambient temperature, contact condition between the press and the ground, etc.) remains the same. The non-steady state power for the heater is higher and lower than the steady state power during heating and cooling, respectively, and the difference will increase with the rate of heating or cooling. Both the pistons (B, C) and the cylindrical sleeve (E) are made of inconel metal. If Corning machinable glass is inserted in each of the pistons, the steady state power can be reduced up to 20% at a sample temperature of about 600°C.

7-4: Pressure Calibration:

For a stress tensor $\begin{pmatrix} \sigma_1 & 0 & 0 \\ 0 & \sigma_2 & 0 \\ 0 & 0 & \sigma_3 \end{pmatrix}$, where σ_1, σ_2, and σ_3 are the three principal stresses with the convention $\sigma_1 \geq \sigma_2 \geq \sigma_3$, the pressure is defined by $P = 1/3(\sigma_1+\sigma_2+\sigma_3)$. The stress tensor

Fig. (7-4)

Electrical power input(W) and current(I) versus sample temperature at thermal equilibrium. W and I will be higher and lower during heating and cooling, respectively.

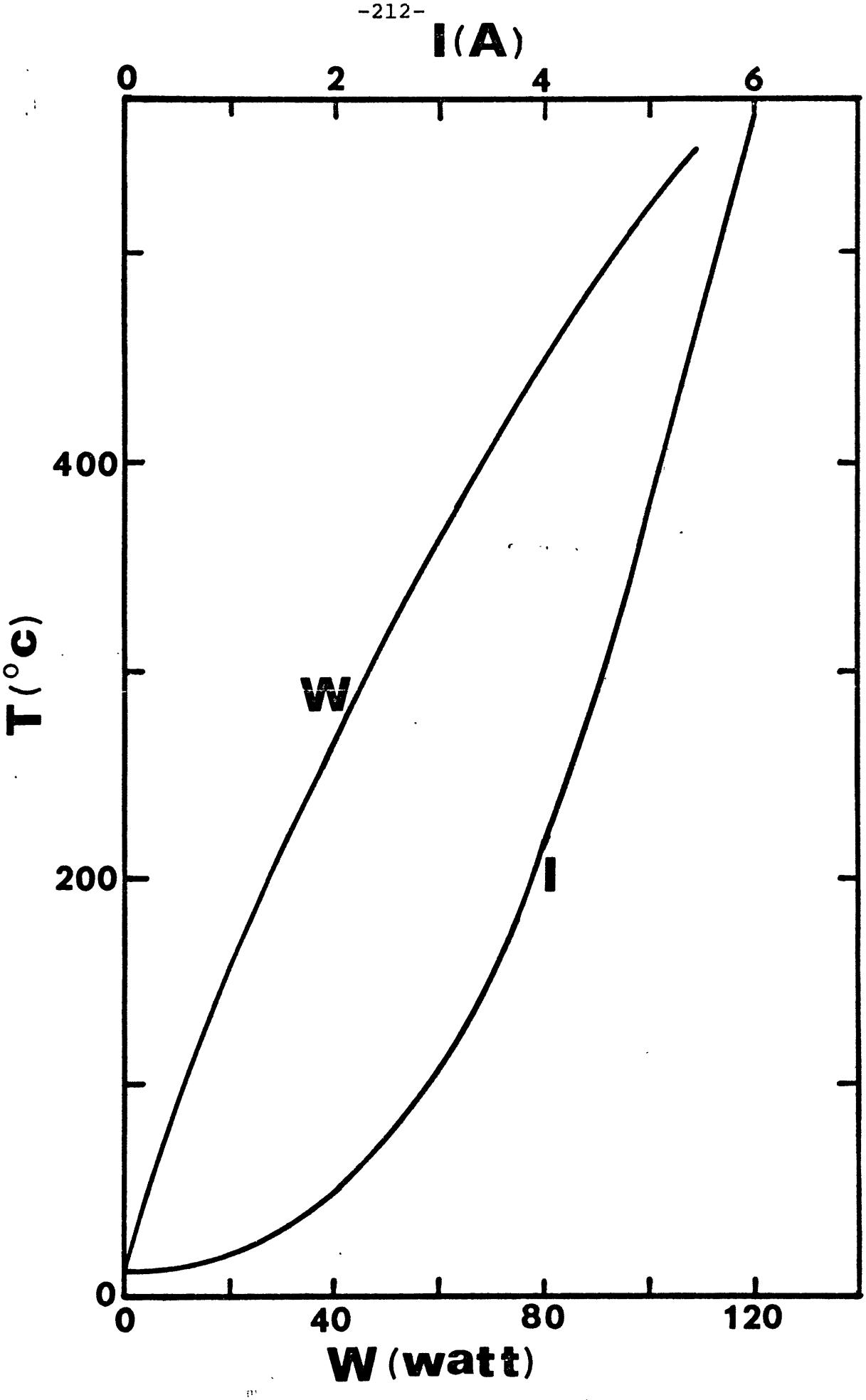
I(A)
0
2
4
6
400
200
0
T(°C)
W
I
0
40
80
120
W (watt)

can then be split into a spherical (hydrostatic) and a deviator (shear) component:

$$\begin{pmatrix} \sigma_1 & 0 & 0 \\ 0 & \sigma_2 & 0 \\ 0 & 0 & \sigma_3 \end{pmatrix} = \begin{pmatrix} P & 0 & 0 \\ 0 & P & 0 \\ 0 & 0 & P \end{pmatrix} + \begin{pmatrix} \sigma_1-P & 0 & 0 \\ 0 & \sigma_2-P & 0 \\ 0 & 0 & \sigma_3-P \end{pmatrix} \qquad (7\text{-}1)$$

For a material yields under non-hydrostatic stress, $\sigma_1-\sigma_3$ will be limited by the yield shear strength(τ) of the material. τ will increase almost linearly with pressure(Riecker and Seifert, 1964a,b) until it reaches a maximum value(τ^*). After that and thus $\sigma_1-\sigma_3$ remains constant for further increase of pressure. For experimets performed using the diamond anvil press, the pressure is so high, so

$\sigma_1-\sigma_3 = \tau^*$. At room temperature, τ^* is approximately 1 kb for NaCl (Ruoff, 1976) and 20 kb for olivine (Goethe, personal communication). τ^* will decrease with temperature, and at 600°C it is negligible in NaCl and is approximately 16 kb in olivine. Thus, for the sample mixed with abundant NaCl (>60 volume %), the pressure is quasi-hydrostatic. For the sample of pure olivine, $\sigma_1-\sigma_3$ is 20 kb or less, depending on the temperature. In the latter case, the pressure is anisotropic, meaning the pressure is dependent on the orientation relative to the anvil surfaces.

There exists another complication of pressure distribution, if the sample is composed of more than one material. The difference of compressibilities between them will result in higher pressure in the harder (less compressible) material relative to the soft one. This phenomenon is known as stress

concentration (pressure enhancement, pressure intensification, pressure inhomogeneity) (Corll et al., 1965; Corll, 1967; Jamieson and Olinger, 1971; Sato et al , 1973; Nelson and Ruoff, 1976a, b). For MgO mixed with NaCl, the pressure in MgO has been found to be 1.35 times the pressure in NaCl (Sato et al., 1973). The bulk modulus of MgO (1599 kb, Anderson and Andreath, 1966) is more than 20% higher than that of olivine (Table 5-1); thus, we may expect a smaller stress concentration factor in olivine when mixed with NaCl.

Pressure distributions across the diamond anvil have been measured by Lipincott and Duecker (1964) and by Piermarini et al. (1973). Pressure distributions are generally dome-shaped, with the maximum pressure located at the center of the anvil surface. The pressure gradient is minimal at the center region of the sample. The pressure gradient will increase with the nominal pressure (mean pressure) and will be larger for a thicker and harder sample. The pressure gradient will decrease with increasing temperature. It can also be greatly reduced by gasketing the sample. The center pressure may not always be the highest in the sample. It can be lower than that in the intermediate region if the pressure is applied and reduced cyclically, or if the sample is insufficient to sustain an equilibrium thickness. When the sample undergoes the phase transition, the center pressure can also be greatly reduced due to the volume contraction associated with the phase transition.

There are at least three methods which can be used to

measure the pressure (the average pressure in the center region) of the sample between the diamond anvils. One method is to use the fixed points of phase transitions to calibrate the force (the length of spring G in Figure 7-1) required to achieve a certain pressure and later to use the calibrated force to estimate the pressure in the sample. The second method is to use NaCl as an internal standard (Bassett et al., 1967; Decker, 1971). The pressure can be continuously monitored by the variation of cell edge of NaCl mixed with the sample at high pressure. The third method is to use the peak positions of the sharp fluorescent lines (R1 and R2) of ruby mixed with the sample. The peak positions of R-lines have been shown to shift linearly with pressure (Forman et al., 1972; Barnett et al., 1973). In this thesis, we adopted the second method for the pressure calibration. Finely pulverized olivine is intimately mixed with abundant NaCl (approximately 60 volume %) and x-rayed at high pressure. The x-ray source is Mo K_{α} and the exposure time is approximately 400 hours. The pressure is calculated from the cell edge of NaCl determined by d-spacings of (200) and (220). The correction for the variation of sample-to-film distance follows, in general, the procedures described by Ming (1974) (Appendix C). It is believed that the accuracy of pressure determination is $\pm$ 4 kb. Because the pressure decreases during the olivine→spinel transition, the pressure so determined represents only the transient pressure. As will be described in Chapter 8, NaCl tends to

catalyze the olivine→spinel transition, so the majority of the experiments were conducted using pure olivine alone as starting material. In this case, the pressure is estimated from the spring length (G in Figure 7-1), which has been calibrated against an NaCl internal standard. Pressure estimated in this way may have an uncertainty of ± 20 kb.

7-5: Experimental Difficulties:

The diamond anvil press has the merit of compact size. It is also this feature which makes the handling of the sample difficult. The sample volume is extremely small (approximately 10^{-12} cm^3 for an anvil diameter of 0.5 mm without gasketing), so it cannot be measured using ordinary methods. However, it is still large enough for observation under a microscope and can be measured using specially designed equipment. Successful measurements in the diamond anvil press include optical spectroscopy (Lippincott et al., 1960; Abu-Eid, 1974), Mössbauer spectroscopy (Huggins et al., 1975), x-ray diffraction (Piermarini and Weir, 1962; Bassett et al., 1967), yield strength (Kinsland, 1974), conductivity (Mao, 1973), and others.

Most experimental difficulties come from the heating of the sample. For example, rapid heating may cause sample extrusion and may also disturb the alignment. However, these problems usually occur in the first cycle of heating and may not be encountered for later heating cycles.

When the diamond is heated above 600°C for a long period

of time (several days or longer), its surface becomes frosted due to slow burning in air. The oxidation of the diamond can be avoided by putting the whole press inside a box and purging with nitrogen or argon gas. Heating above 800°C may cause other problems, especially if the rate of heating is high. The anvil surface may become undulated due to the unevenness of the thermal expansion. This may cause pressure release on the sample. Prolonged heating may also reduce the pressure by reducing the elastic constant of the spring (G). This problem is overcome by circulating cooling water through the hose fitting (R). In this case, the spring end and the hinge end (S) of the press remain cold during the heating of the sample.

Heating above 800°C involves another difficulty. The thermocouple wire is so fine that contamination becomes serious above this temperature. In this case, an indirect temperature scale can be used. The steady state power is first calibrated to the temperature measured by a coarse thermocouple. The head of the thermocouple is clamped between the two anvils without the sample. When the sample is loaded, the temperature is estimated from the power input. If all other conditions are kept the same, the uncertainty of the indirect temperature measurement may be as low as $\pm$ 5%.

Chapter 8

EXPERIMENTAL RESULTS

8-1: Introduction:

In this chapter, we present experimental results on the kinetics of the olivine→spinel transition in the Mg_2SiO_4-Fe_2SiO_4 system, performed at constant P and T. In addition to P and T, we measured the effects of NaCl and water on the rate of the olivine→spinel transition. The experiments were designed to constrain the possible range of the kinetics of the olivine→spinel transition for a given composition and under specific physical conditions, and as far as possible, to test the kinetic theories developed in Chapter 6. Because Q_a is critical to determining the position of the isograds in the kinetic diagram (Figure 6-10, 6-11), one of the major goals of the experiments was to determine Q_a. As we were interested in the kinetics of the olivine→spinel transition under very metastable conditions, most of the experiments performed were at high overpressures ($\Delta P>50$ kb). Under these conditions, the activation energy of nucleation , ΔG_T^*, is negligible compared to the activation energy of growth Q_a. In addition, the correction factor $(1-\exp(-\Delta G_a/kT))$ for the growth rate (eq. 6-36) approaches unity (Figure 8-1). Thus, the kinetics of the olivine→spinel transition are mainly controlled by Q_a, which is insensitive to pressure change. Therefore, temperature will be the only key factor determining the kinetics of the olivine→spinel transition for a given composition and grain size. The olivine→

Fig. (8-1)

Dimensionless factors controlling the kinetics of the olivine→spinel transition, as functions of ΔP for Mg-rich composition at 700°C. Unlabelled curves are $\exp(-\Delta G^*_T/(kT))$. Solid, dashed and dotted curves are for heterogeneous nucleation, homogeneous nucleation of coherent interface and homogeneous nucleation of incoherent interface, respectively. For heterogeneous nucleation, Q_a will govern the rate of transition beyond a small degree of metastability(ΔP>5 Kb).

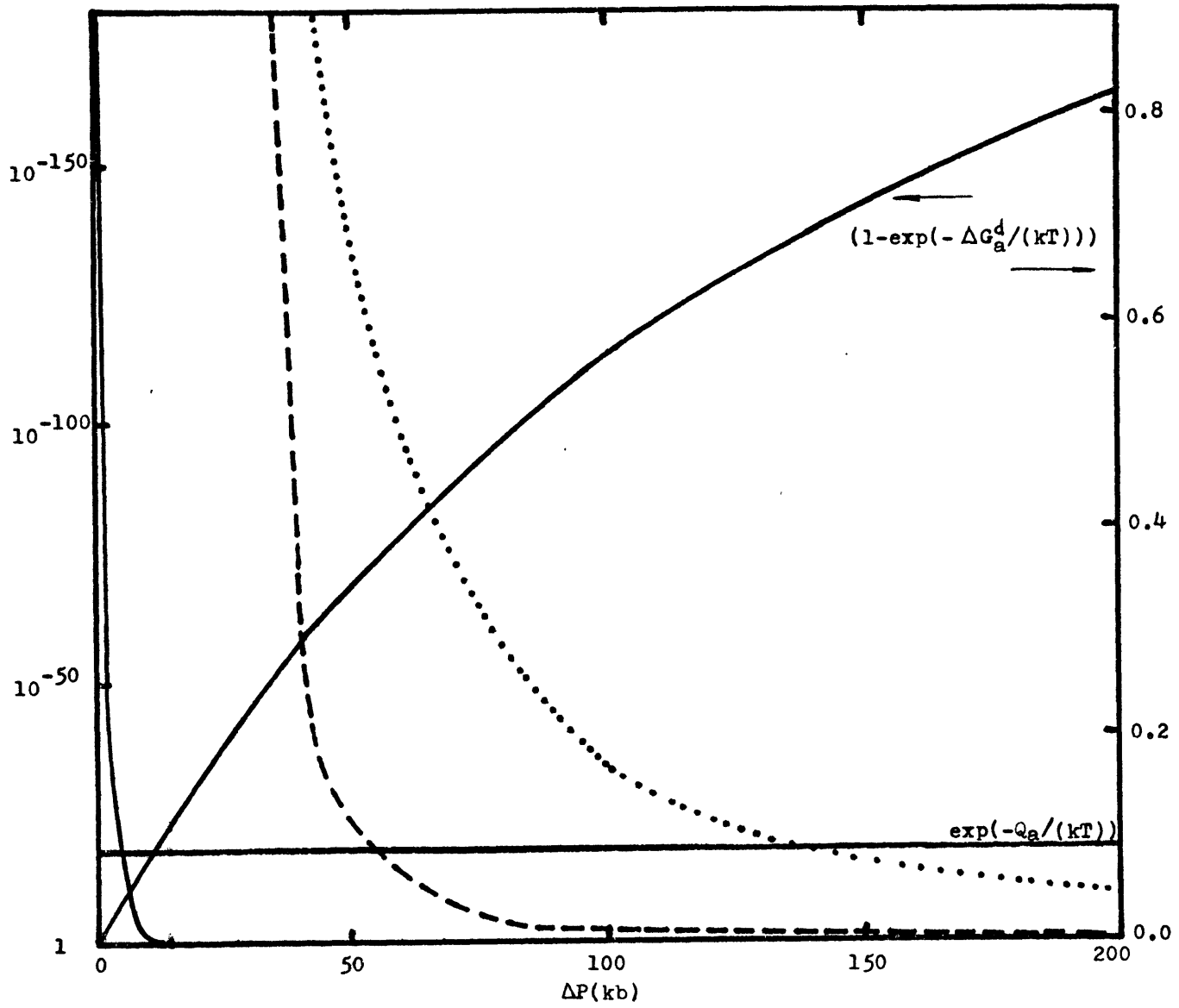
10^{-150}
10^{-100}
10^{-50}
1
0
50
100
150
200
ΔP(kb)
0.8
0.6
0.4
0.2
0.0
$(1-\exp(-\Delta G_a^d/(kT)))$
$\exp(-Q_a/(kT))$

spinel transition for different compositions was studied isothermally and isobarically at temperatures up to 800°C. For all runs above 700°C, a nitrogen atmosphere was used to prevent oxidation of the diamonds, and cooling water was circulated to maintain the stiffness of the compressional spring, and thus the pressure.

8-2: Starting Material:

Samples used for experiments were generously provided by Mr. B.M. Watson (synthetic fayalite powder), Drs. H.K. Mao (synthetic olivine powder of intermediate compositions prepared by Dr. N.F.H. Bright), and Prof. R.G. Burns (natural olivine powder of intermediate compositions and natural fayalite single crystals). All of the synthetic olivines have been identified by x-ray diffraction (Watson, personal communication; Bright, unpublished) and no foreign phases were detected. However, there are trace amounts (<1%) of opaque minerals (iron and magnetite) in natural olivine of Fe-rich compositions, which can be observed under the microscope. The presence of this trace amount of foreign material did not interfere with our kinetic experiments because spinel did not nucleate preferentially around these materials. Natural olivines used for this study are the same as those used for the spectroscopic measurements of Burns (1970a, b). The exact compositions and sources of these samples are described in his papers.

The numbering of our experimental runs incorporates the following information arranged in order: The press used (A, B,

C, or D), the number of the diamond pair, the sample number for the particular press and diamond pair, the heating cycle (0 refers to the stage before the first heating cycle), and the heater number. An example is A310-5. The samples are described by the following information arranged in order: The initial of the donor's last name (W, M, or B), the mole percentage of Fe_2SiO_4, powder (P) or single crystal (S), dry (D), or wet (W), and the extra phase added (H for halite). An example is W100PDH.

8-3: Transition kinetics in Fe_2SiO_4:

Samples of synthetic fayalite powder (W100PD) were used in this study. The grain size was, in general, between 2 and 5μ. When fayalite is subject to a pressure of more than 100 kb, it becomes black due to the shifting of the absorption edge into the visible region (Mao and Bell, 1972). As temperature increases, the region of intermediate pressure becomes more transparent and the region of high pressure (usually at the center) becomes even darker. When the sample is heated above 500°C for a few minutes, spinel begins to nucleate along the grain surfaces of fayalite particles. The spinel nuclei formed scatter light and are thus eye-catching, so that a degree of transition as small as $\chi \sim 0.001$ can be detected under the microscope. The nucleation of spinel is manifested by the sudden emergence of a brown-colored region at the center of the sample. The color of the nucleated region will become increasingly dark until the nucleation sites are saturated.

After that, the color does not change with further heating, and the transition is proceeding by the growth of the existing nuclei. With the higher power magnification under the microscope, one can see that the spinel bands surrounding the fayalite particles in the unloaded samples becomes increasingly thick with increasing temperature or with increasing time of heating. The growth of spinel is difficult to observe when the sample is held between the two anvils unless the thickness of spinel bands is so great that they merge together. In this case, a red homogeneous region of pure spinel can be observed easily through the diamond. The red color of the spinel is due to red light emitted from the heater at high temperature; the true color of spinel is pale green, as shown by the quenched sample. The spinel is easily identified under a microscope by its distinct color and its isotropic nature. A typical experimental run (C220-10) is shown in Figure (8-2). When the sample was heated to 500°C for 100 minutes, site saturation was almost complete (Figure 8-2a). Note that the boundary of the nucleated region is very sharp. At 600°C for 10 minutes, spinel begins to merge (Figure 8-2b). The merged region of pure spinel gradually spread out with further heating (Figure 8-2c). The unloaded sample is shown in Figure 8-2d); greenish spinel bands can be clearly seen surrounding the residual fayalite particles.

When the nucleation starts, the nucleated region will spread out very rapidly at the beginning and then advance very slowly with further heating, even over several months.

Fig. (8-2)

Typical runs of the olivine→spinel transition in Fe_2SiO_4(W100PD). (A) to (D), Run C220-10, (A) at 500°C for 101 minutes, X<1%, site saturation just occurred; (B) at 600°C for 11 minutes, X∿2%, pure spinel region begins to develope at the center; (C) at 600°C for 1090 minutes, X∿80%, pure spinel region has expanded outwards. Photographs of (A), (B), (C) were taken at high temperatures. The circular black region at the lower-right corner is the head of the thermocouple. (D) Unloaded sample of Run C220-10, note the residual grains of fayalite and the spinel bands surrounding them. The degree of transition at the center region has been determined by X-ray diffraction to be 83%. The degree of transition is less outwards from this region. (E) Unloaded sample after heating to approximately 800°C for 20 minutes. Note the straight edges of the olivine-spinel boundary. (F) Same sample under crossed polars. Note the extinction of the spinel and the lineated olivine grains perpendicular to the straight edges. Samples are approximately 500μ across.

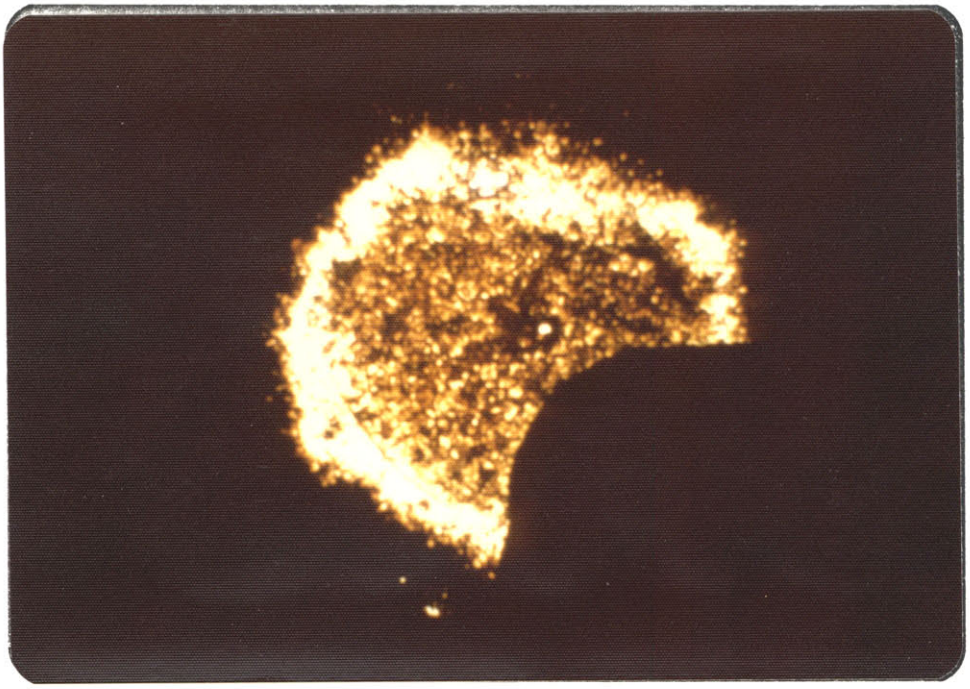

(A)

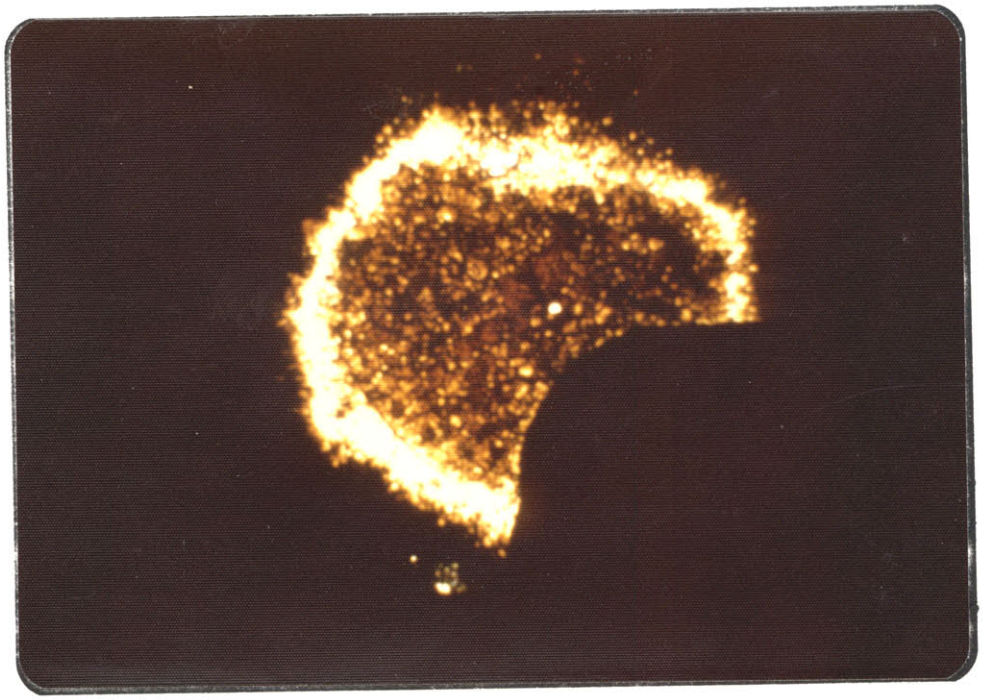

(B)

(C)

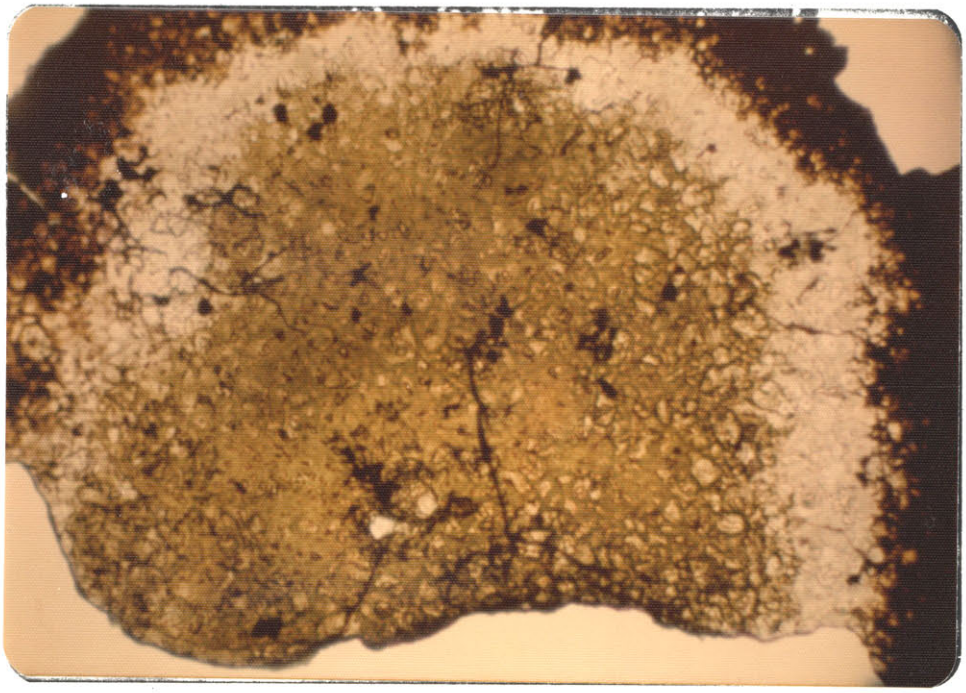

(D)

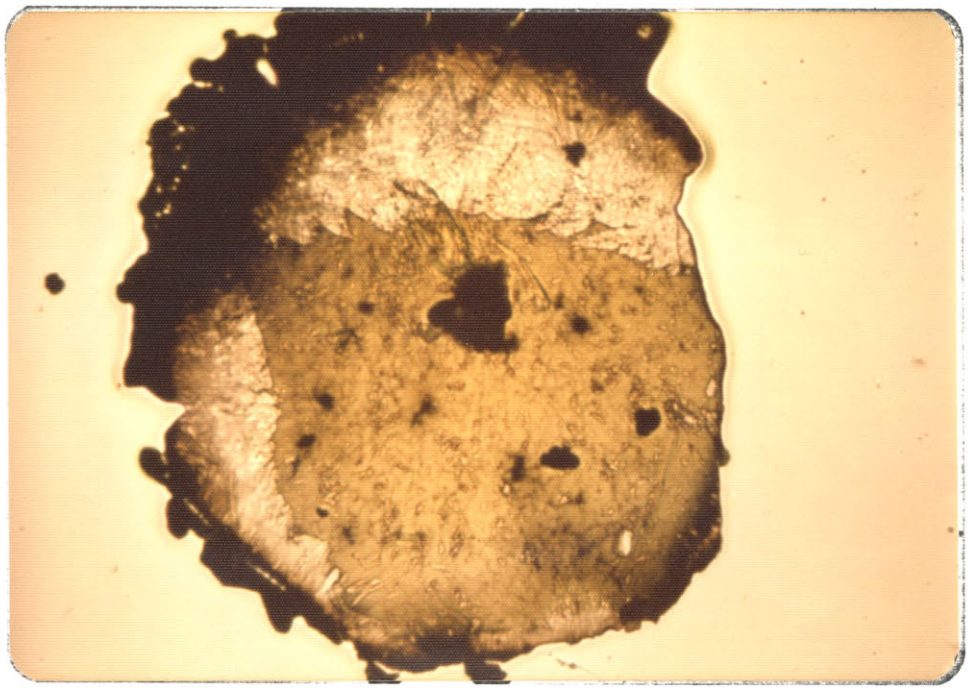

(E)

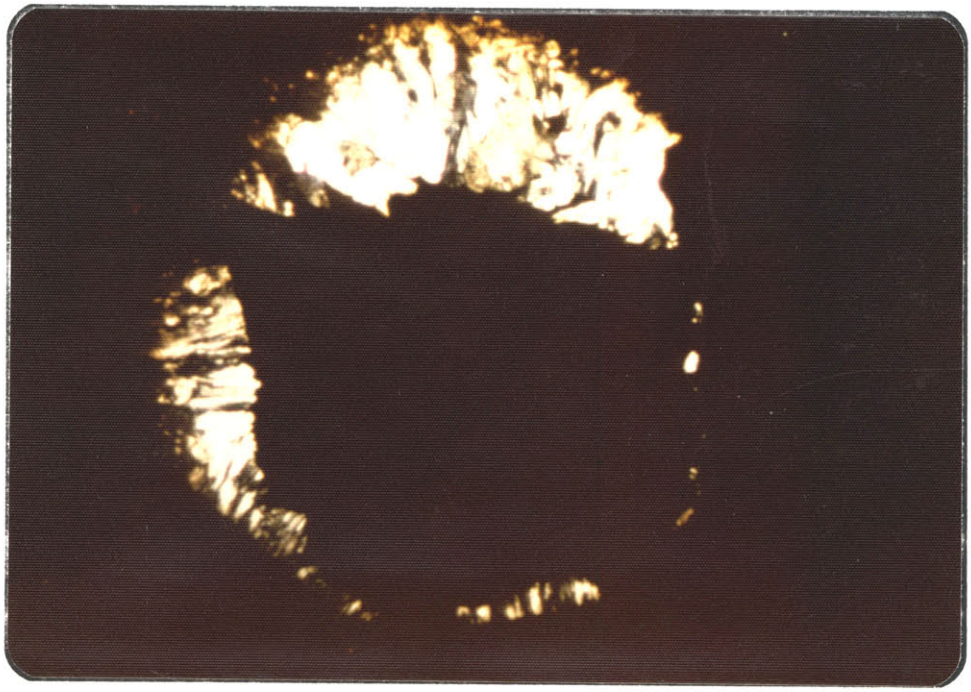

(F)

this phenomenon is illustrated schematically by Figure (8-3). The vertical line X-Y, in Figure (8-3a), represents the P-T condition of the sample held between the two diamond anvils. With increased heating time, the isograd will move in the low temperature direction as indicated by t_1, t_2, t_3, and t_4 in Figure (8-3d). As soon as the isograd sweeps across the vertical line, the proportion of spinel corresponding to the particular isograd will form. The sudden spreading out of the nucleated region suggests a nearly vertical isograd beyond a certain overpressure. This may further imply a zero or even negative activation volume, which agrees with our previous speculation (Chapter 6). With a further increase of heating time, the nucleated region will expand only very slightly (Figure 8-3b), although the degree of transition in the center region keeps increasing.

When the temperature is raised above 700°C, the growth rate of spinel is so fast that the merged pure spinel region will sweep across the whole transformed region within an hour or so. In addition, the transformed region will shrink in such a way that it becomes diamond-shaped with straight edges (Figure 8-2e, f). The shrinkage of the spinel region occurs because of the positive slope of the phase boundary (Figure 8-3), but the nature of the straight edges of the spinel region is not known. A similar phenomenon was also observed for the transformation of olivine into oxides (magnesiowüstite and stishovite), at yet higher pressure and temperature. In this case, oxides and spinel form concentric parallelograms with

Fig. (8-3)

Schematic diagram showing the rapid spreading out of the rransforming region and the slow expansion of this region thereafter. P. B. is the olivine-spinel phase boundary. t_1, t_2, t_3, t_4 are isograds of transition with increasing time. XY in (A) is the P-T condition of XY in (B). The latter is the projection of the half sample held between the two anvils. Dotted lines connect points of the same pressure. At time t_1, no transition occurs. At time t_2, transition begins at the very center of the sample. At time t_3, which is only slightly longer than t_2, the transforming region has rapidly expanded to that bounded by the inner circle in (B). At much longer time t_4, the transforming region expands only slightly, from the inner circle to the outer circle in (B). After that it will not expand further. If temperature increases, the transformed region will shrink because of the positive slope of the olivine-spinel phase boundary.

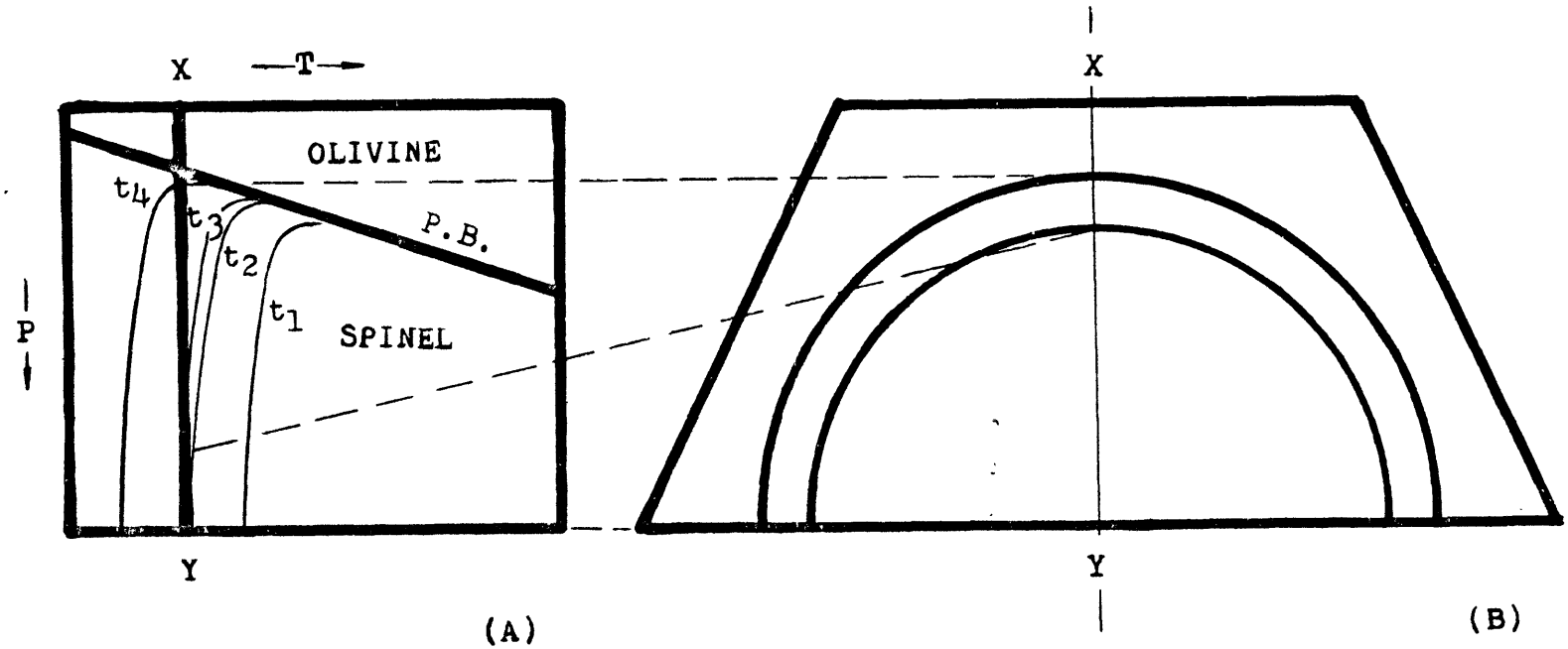
X
—T—
OLIVINE
P.B.
t_4
t_3
t_2
t_1
SPINEL
P
Y
(A)
X
Y
(B)

parallel straight edges (Ming, personal communication). When the spinel region shrinks, it leaves behind a region of spinel transformed back to olivine. The retransformed olivine is not distributed randomly but forms lineated bands perpendicular to the straight edge of the retreated spinel boundary (Figure 8-2e, f). It is suspected that this lineation may align olivine in a direction such as to minimize the strain energy. The measured absorption spectrum of the spinel transformed olivine suggested that its a-axis (γ-polarization) may lie parallel to the direction of high pressure gradient. However, because the sample was very thin, the quality of the measured spectrum was not good enough to draw a definite conclusion.

The x-ray pattern of the unloaded pure spinel (Figure 8-2e, f) is shown in Figure (8-4a). Intensities of the diffracted peaks were obtained by scanning of the x-ray film with a double beam recording microdensitometer. Both measured d-spacings and relative intensities of the pure spinel are listed in Table (8-1), along with the calculated values. The agreement between measured and calculated data is good, although measured d-spacings tend to be systematically lower than the calculated values with decreasing 2θ. This is due to the eccentricity of the sample when mounted on the x-ray camera. All the spinel peaks are present, and there is only one weak extra line which has been identified as lead (111, I = 100%). The lead was used as an additional collimator which lay immediately beneath the sample.

In order to measure the degree of transition, we tried

Fig. (8-4)

X-ray diffraction pattern obtained by scanning the film with a microdensitometer. (A) pure Fe_2SiO_4 spinel, the sample is shown in Fig. (8-2)e, (B) pure Fe_2SiO_4 spinel and pure fayalite of the same thickness put side by side with the former facing the X-ray source. Only fayalite peaks are labelled in (B). The latter X-ray pattern has been used as the standard of X=0.5 for calculation of the degree of transition for other runs.

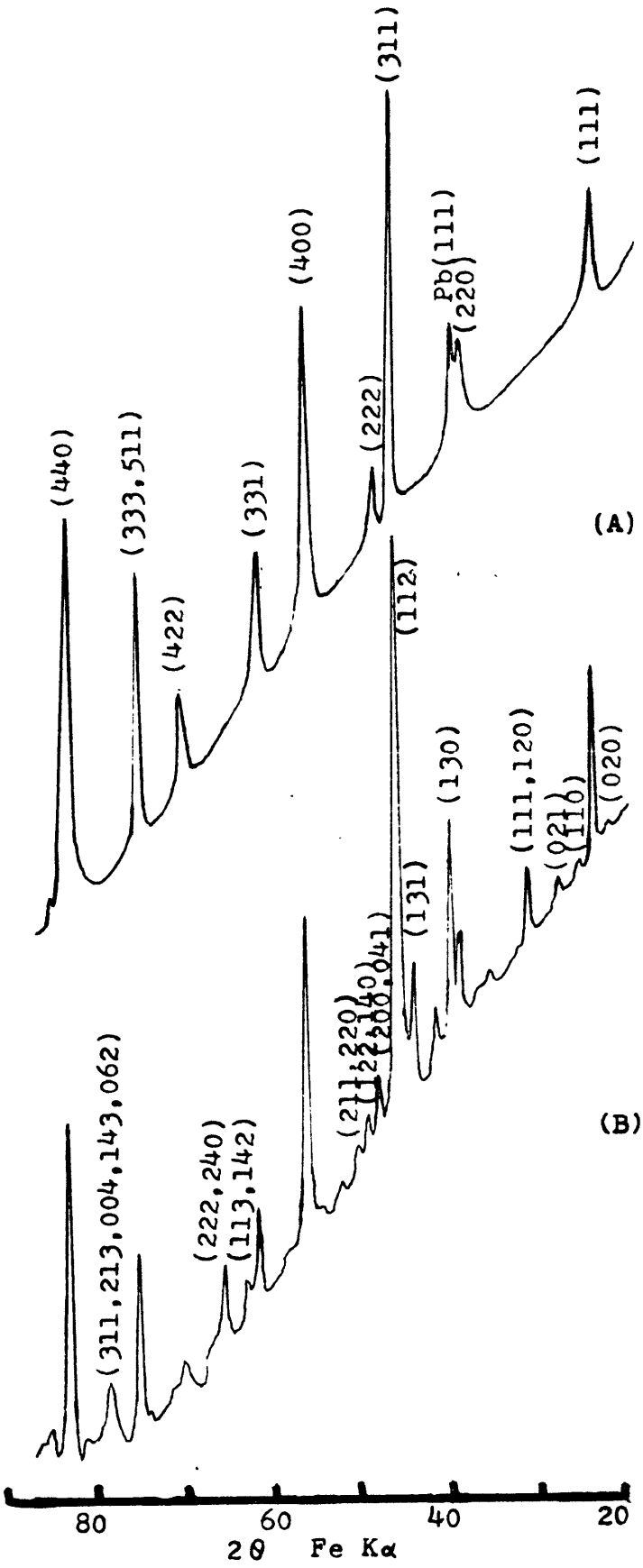
(440)
(333,511)
(422)
(331)
(400)
(222)
(311)
Pb(111)
(220)
(111)
(A)
(112)
(130)
(131)
(111,120)
(021)
(020)
(311,213,004,143,062)
(222,240)
(113,142)
(B)
80
60
40
20
2θ Fe Kα

Table (8-1)

X-RAY DIFFRACTION DATA OF γ-Fe_2SiO_4

(hkl)	$d^a_{calc.}$	$d^b_{Obs.}$	$I^c_{calc.}$	$I^d_{obs.}$	$I^e_{obs.}$
(111)	4.754	4.705	36	25	30
(220)	2.911	2.895	9	21	9
Pb(111)		2.827			
(311)	2.483	2.463	100	100	100
(222)	2.377	2.364	11	8	18
(400)	2.059	2.054	52	44	70
(331)	1.889	1.883	14	14	16
(422)	1.681	1.678	4	5	10
$(^{333}_{511})$	1.585	1.587	26	21	58
(440)	1.456	1.460	49	38	90

Note:

a) Calculated d-spacing based on a=8.234(Table 2-1)

b) Observed d-spacing in this work

c) Calculated relative intensities(Ito et al, 1974)

d) Observed relative intensities(Ito et al, 1974)

e) Observed relative intensities in this work

several methods, which included optical spectroscopy, Mössbauer spectroscopy, and conductivity measurements. The first method failed because of the high background noise of the spectra for the powdered sample. The second method failed because the peaks for Fe^{2+} in olivine and spinel are too close to be useful as quantitative indicators. The third method also failed because the resistance of olivine at high pressure and temperature becomes so low that its measurement is beyond the capability of our equipment. A fourth method was adopted to measure the degree of transition. In this case, the proportion of olivine and spinel was calculated from the relative intensities of x-ray peaks of the unloaded sample. In order to be quantitative, we needed to prepare a standard of known proportion of the two phases. This is almost impossible with the tiny amount of sample synthesized in the diamond anvil press. Instead of mixing olivine and spinel, we prepared a 50:50 standard by putting a pure olivine and a pure spinel side by side. Both samples were prepared at the same pressure and had the same thickness. The x-ray pattern of this prepared standard is shown in Figure (8-4b). It was observed that the spinel peaks were far more intense than the olivine peaks. Based on this standard, we have calculated the proportion of the two phases in several unloaded samples synthesized under different P-T conditions. The measured proportions agree with the visual estimation made by examining the unloaded samples under a polarizing microscope at high magnification.

Based on the degree of transition measured for the unloaded sample and visually estimated from successive photographs taken in the middle of the transition, we can obtain the degree of transition as a function of time at different P-T conditions. The results indicate that a plot of ln [ln(1/(1-X)] versus ln t plot for each run often results in a straight line (with some scattering) with unit slope. This strongly suggests that the kinetics of the olivine→spinel transition follow the rate equation for early site saturation on grain surfaces (eq. 6-45), and that the reaction is taking place by growth of existing nuclei only. This agrees with our previous theoretical calculations (Chapter 6) and is consistent with our experimental observations described earlier (Figure 8-2).

Experimental data on the kinetics of the olivine→spinel transition in Fe_2SiO_4 are summarized in Table (8-2). Only the degrees of transition for the unloaded sample are listed in the table. The results are also plotted in Figure (8-5). Although there is some scatter, the data are self-consistent, and, based on them, it is possible to draw isotherms of transition from 400°C to 700°C. In general, the kinetics of the olivine→spinel transition in Fe_2SiO_4 can be described as follows: (1) below 400°C, the transition may not occur within one year; (2) at 500°C, the transition will start in an hour and be completed in several months; (3) at 600°C, the transition will start in several minutes and be completed in several days; and (4) at 700°C, the transition will start in several seconds and be completed in a few hours. The grain sizes and

Table (8-2)

EXPERIMENTAL RESULTS ON THE OLIVINE→SPINEL TRANSITION IN Fe_2SiO_4 (W100PD) (Grain size, 2-5μ)

Run Number	P_B (Kb)	T' (^oC)	t(min.)	X
A330-5	120±20	400±20	>300000	~0
A310-5	100±20	450±20	3780	0.05*±0.02
C210-10	120±20	450±20	206	<0.01(0.005?)
D350-9	150±30	500±30	86400	>0.9
A320-5	100±20	550±10	60	0.15*±0.05
D210-9	160±30	550±20	4025	0.27*±0.05
D220-9	160±30	550±20	11520	0.8±0.1
C250-10	120±20	560±20	310	0.09*±0.02
C220-10	100±20	600±20	1090	0.83*±0.05
C240-10	120±20	600±10	60	0.10±0.05
B360-11	150±30	670±30	150	0.6±0.2
B370-11	160±30	670±30	1853	>0.95
B340-11	130±20	700±30	1253	>0.95
B350-11	140±20	700±30	30	0.7±0.1
C230-10	120±20	750±30	30	0.8±0.1

* Spinel proportion determined by X-ray diffraction

Fig. (8-5)

Experimental results on the kinetics of the olivine→spinel transition in pure Fe_2SiO_4(W100PD). Numbers are temperatures in ^{o}C. Coarse vertical lines are experimental data taken from Table (8-2). Solid lines are isotherms of transition drawn based on these plotted data. All isotherms have unit slopes which correspond to the kinetics of transition after site saturation. Data labelled A1 and A2 are estimated based on data of Akimoto and Fujisawa (1965) and Akimoto et al(1966), respectively. Dashed lines are isotherms of transition for Ni_2SiO_4 calculated from the experimental data of Kashahara and Tsukahara(1971).

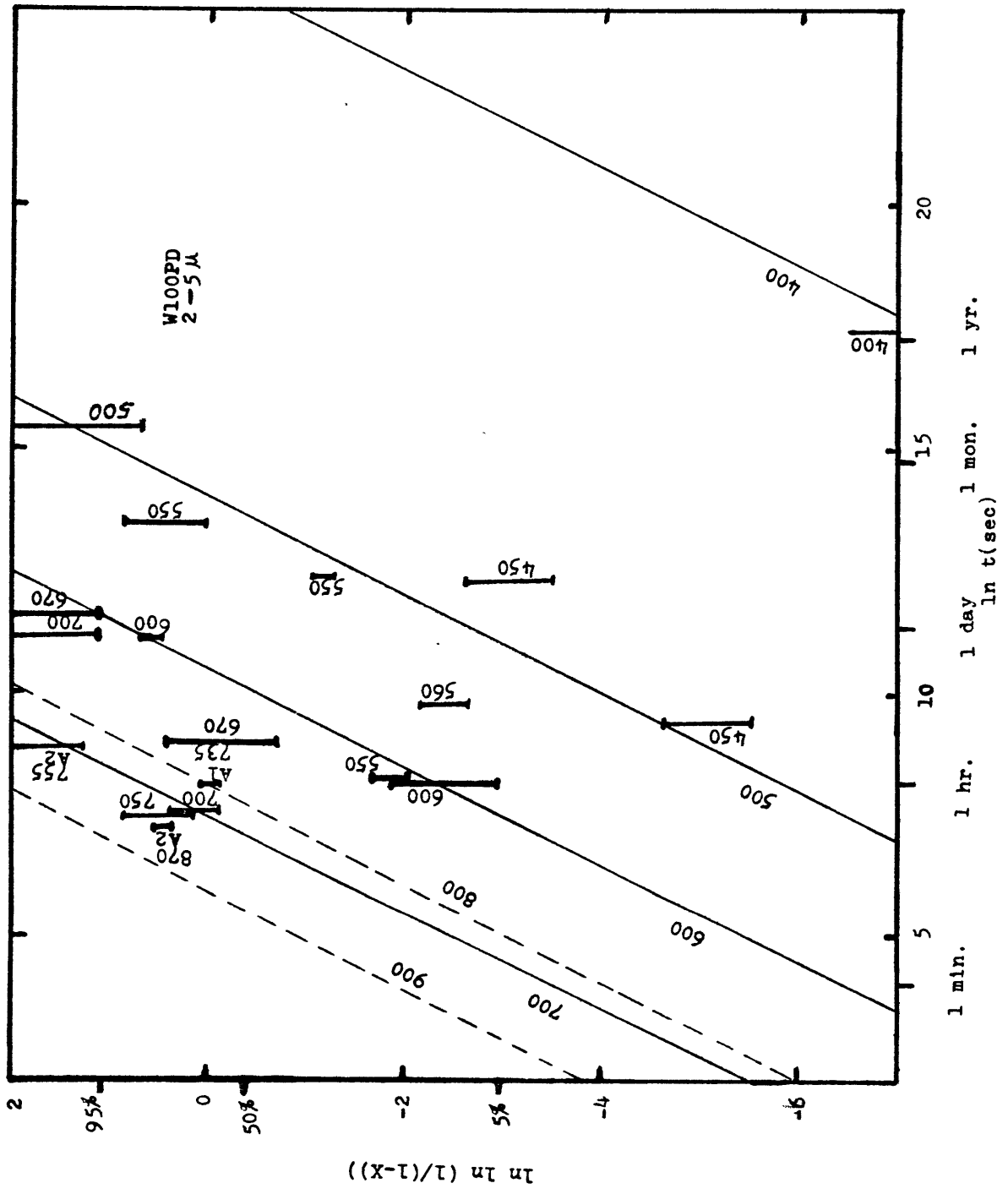
W100PD
2-5 μ
400
500
550
450
560
600
670
700
750
820
800
900
A1
A2
235
1 min.
1 hr.
1 day
1 mon.
1 yr.
ln t(sec)
5
10
15
20
95%
50%
5%
2
0
-2
-4
-6
ln ln (1/(1-X))

shear stresses for samples used in laboratory experiments do not vary greatly, so Figure (8-5) describes, in general, the kinetics of the olivine→spinel transition in Fe_2SiO_4 under laboratory conditions. Rates calculated from experimental data from another laboratory (Akimoto and Fujisawa, 1965; Akimoto et al., 1966) are also plotted on Figure (8-5). They agree, in general, with our kinetic data.

The only other experimental data on the kinetics of the olivine→spinel transition were performed on Ni_2SiO_4 by Kasahara and Tsukahara (1971). However, they used a kinetic equation of the form

$$\frac{d\chi}{dt} = K(1-\chi)^p$$

where K is the rate constant and p is a constant (the order of reaction). Although this equation is adequate for describing chemical reactions, especially those involving fluids, it does not apply to a first-order solid-solid transition. The inadequacy of this equation for the olivine→spinel transition is reflected in the extremely wide scattering of the value p calculated from their experimental data. However, their experiments seem to agree with Eq. (6-45), suggesting that the olivine→spinel transition in their experiments could also proceed by growth of existing nuclei. The results based on their experimental data were superimposed in Figure (8-5) (dotted lines). It is observed that the kinetics of the olivine→spinel transition in Ni_2SiO_4 at 800°C are comparable to those in Fe_2SiO_4 at 700°C. It is not obvious whether the slower

transition rate in Ni_2SiO_4 is intrinsic or due to different sample conditions. However, Kasahara and Tsukahara (1971) did mention that the reaction rates in their experiments were considerably higher when they used a finer-grained starting material. Thus, if their experimental data shown in Figure (8-5) were obtained from a starting material of grain size larger than say, 10μ, there is a possibility that the kinetics of the olivine→spinel transition for Ni_2SiO_4 and for Fe_2SiO_4 are comparable.

8-4: Transition kinetics in Fe_2SiO_4 and NaCl mixture:

NaCl has been widely used as an internal pressure sensor and also as a pressure medium. Its effect on the kinetics of the olivine→spinel transition will now be discussed.

The starting material (W100PDH) was a mixture of NaCl (halite, 60% by volume) and fayalite (W100PD) powders. The average grain size was between 1 and 2μ. A typical run (A230-5) is shown in Figure (8-6). As in pure fayalite, when the temperature was raised, the center region became darker and the other region became more transparent (Figure 8-6b). This could be due to the increased pressure gradient, as will be discussed in §8-5. When the sample was heated up to 550°C for a few minutes, site saturation occurred. Because the sample was diluted by more transparent NaCl, the nucleated region was not as dark as that for pure Fe_2SiO_4, and further transition by growth made the nucleation region darker, in contrast to the observations with pure Fe_2SiO_4 (Figure 8-2). The transition

Fig. (8-6)

The kinetics of the olivine→spinel transition in an Fe_2SiO_4 and NaCl mixture for run A230-5 at 550°C. (A) Before heating, (B) after heating for 1.5 minute, X∿2%. Note the darkening center region. (c) after 5 minutes, x∿ 10%. Note the spreading out of the nucleation region. (D) After 10 minutes, X∿30%. Note the formation of an oxidation rim where oxygen can penetrate. (E) After 15 minutes, X ∿50%, (F) after 20 minutes, X∿0.6. All photographs were taken at the sample temperature of 550°C. Samples are approximately 500 μ across.

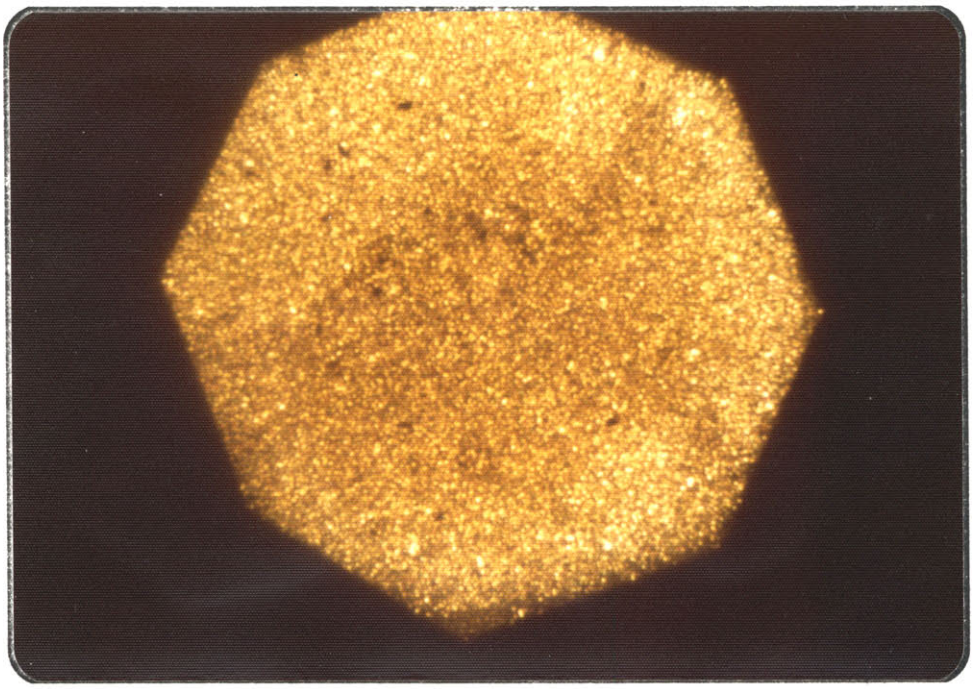

(A)

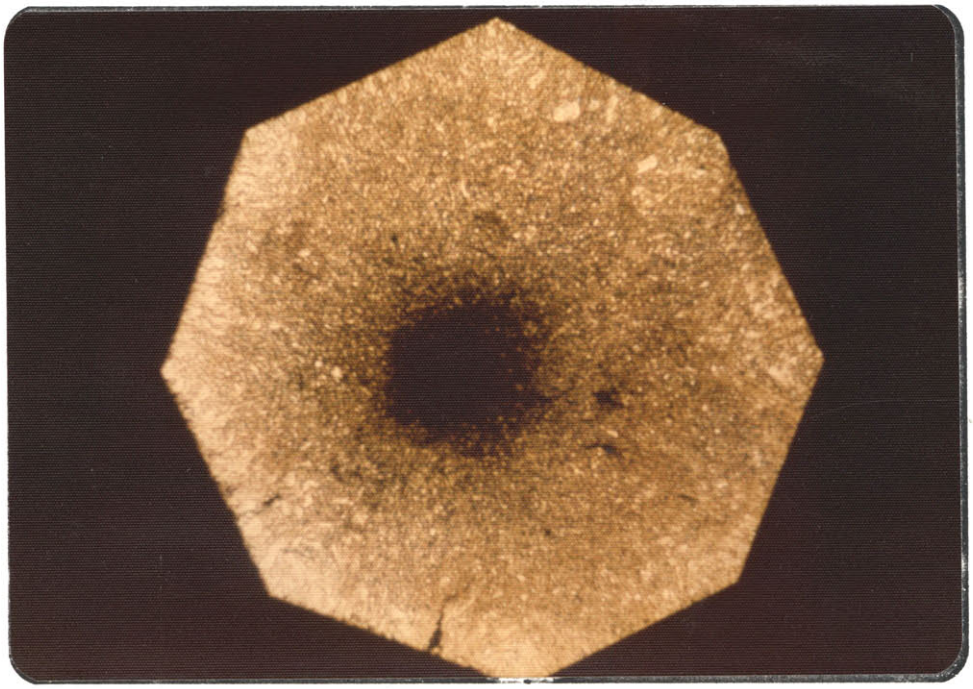

(B)

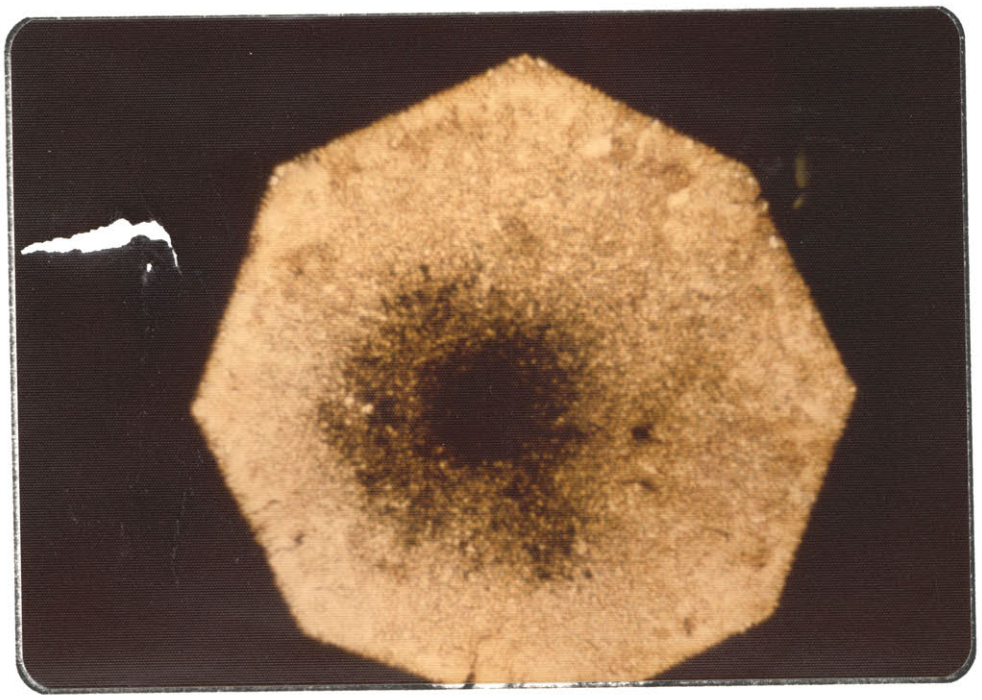

(C)

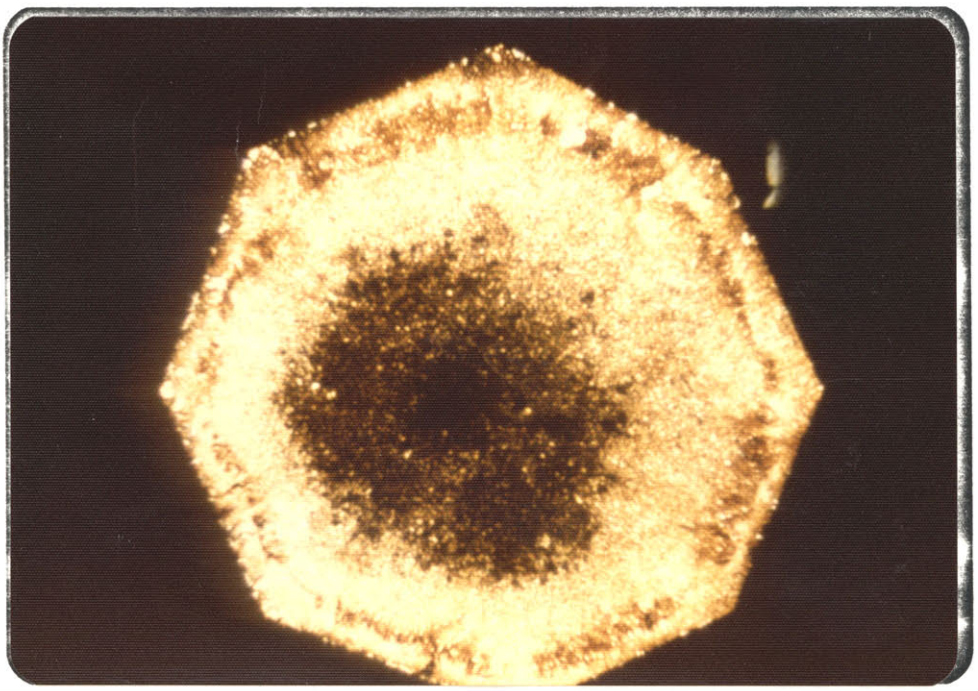

(D)

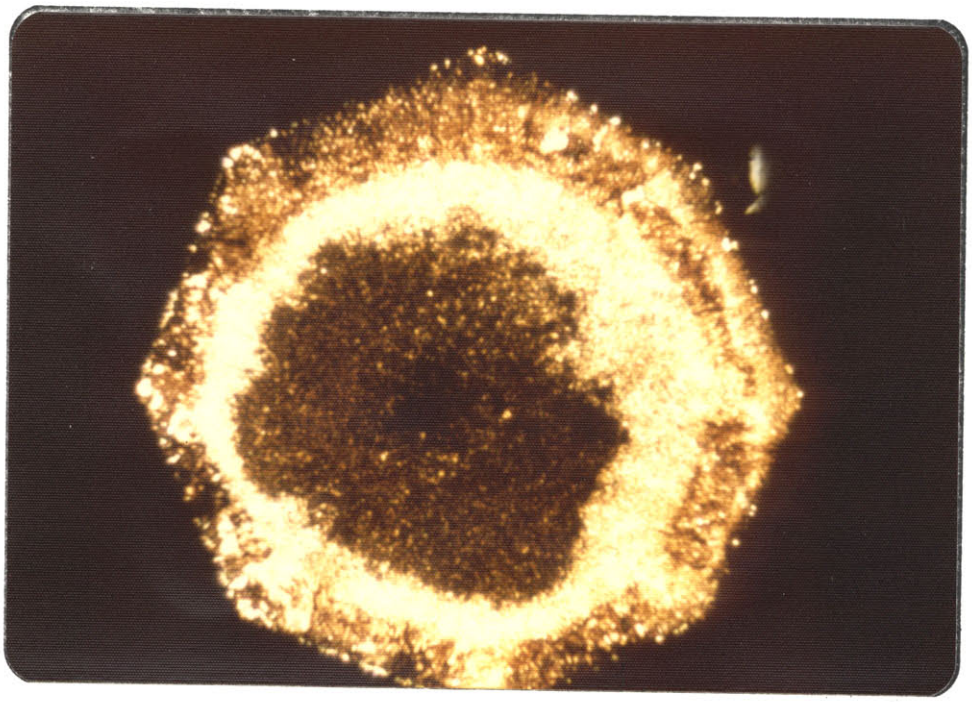

(E)

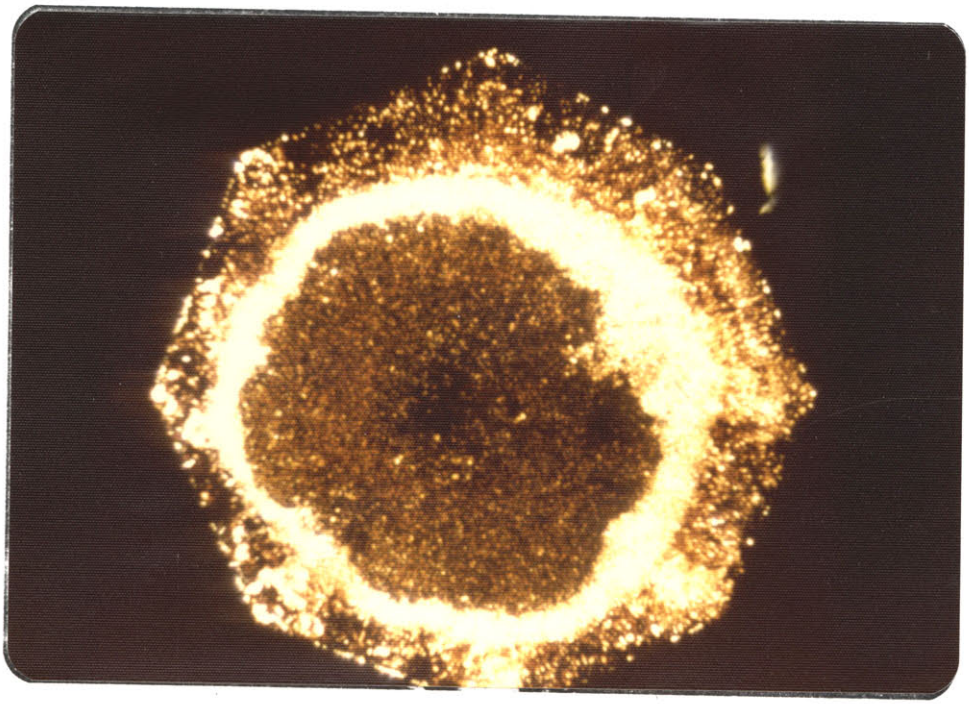

(F)

region was again spread out from the center region where the pressure was maximum. This further implies that Q_a may decrease with increasing pressure, and ΔV^* may be zero or negative. The ln [ln(1/(1-X))] versus ln t plots based on estimated X for some samples suggested slopes greater than unity (1-3). It is not obvious whether this reflects different mechanisms of nucleation or is due to the uncertainties of visually estimated X. Experiments were carried out at temperatures between 300°C and 550°C. Higher temperature may cause flowing of NaCl. Experimental results are summarized in Table (8-3). Again, only degrees of transition for unloaded samples are listed. The results are also plotted in Figure (8-7). Plotted data appear to be self-consistent and isotherms (between 300°C and 600°C) of transition with tentative unit slopes (dashed lines) can be drawn based on these data. Superimposed on the same diagram are isotherms of transition (solid lines) for pure Fe_2SiO_4 taken from Figure (8-5). It is interesting to note that the transition rate in Fe_2SiO_4 can be greatly increased by mixing with NaCl. For example, the transition rate for the sample with NaCl at 400°C is greater than that for the sample without NaCl at 500°C. Although the grain size in the former sample (1-2μ) is smaller than in the latter (2-5μ), this cannot explain such a large difference in transition rate. In addition, shear stress in the sample with NaCl (<5 kb) is much smaller than in the pure Fe_2SiO_4 (>10 kb). This tends to cancel out the effect of smaller grain size on the transition rate. Thus,

Table (8-3)

EXPERIMENTAL RESULTS ON THE OLIVINE→SPINEL TRANSITION IN MIXTURES WITH NaCl(W100PDH)(Grain size, 1-2μ)

Run Number	P_B(Kb)	T'(^oC)	t(min.)	X	P_A(Kb)	Run Number
A120-1	147±5	300±10	10	0	181±5	A121-1
B151-3	150±30	330±10	405	0	182±5	B152-3
			19015	<0.01*	144±5	B153-3
A210-5	100±20	360±10	4010	0.5±0.1	71±5	A215-5
B140-3	150±30	370±10	2625	0.10±0.05	93±5	B141-3
			4070	0.2±0.1		B142-3
A220-5	120±20	420±10	410	0.4±0.1	83±5	A221-5
B130-3	100±20	420±10	100	0.2±0.1	98±5	B132-3
A240-5	150±30	445±10	210	0.35*±0.05	92±5	A241-5
B120-3	120±20	450±10	120	0.3±0.1		B121-3
A230-5	150±30	550±10	21	0.6±0.1	86±5	A231-5

* Proportion of spinel determaied by X-ray diffraction

Fig. (8-7)

Experimental results on the kinetics of the olivine→spinel transition in the mixture(W100PDH) of Fe_2SiO_4 and NaCl. Numbers are temperatures in ^{o}C. Vertical coarse lines are experimental data taken from Table(8-3). Dashed lines are isotherms of transition based on these plotted data. Solid lines are isotherms of transition for W100PD (Fig. 8-5). All isotherms have unit slopes. Note that the transition rates in the mixtures are considerably higher than those in pure Fe_2SiO_4. This is partly due to the smaller grain size used in the former samples and partly due to the catalyzing effect of NaCl on the olivine-spinel transition.

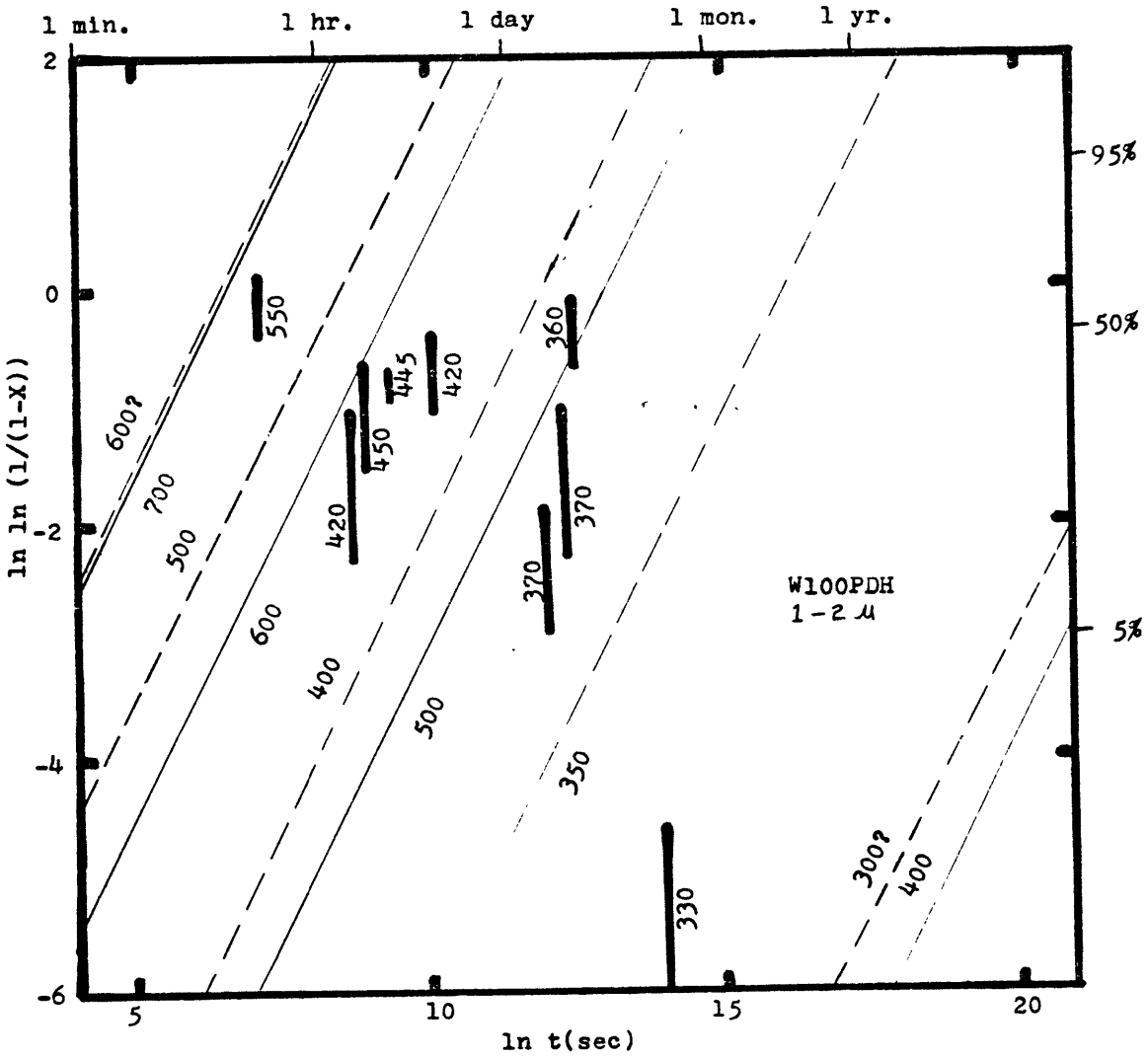
1 min.
1 hr.
1 day
1 mon.
1 yr.
2
0
-2
-4
-6
ln ln (1/(1-X))
5
10
15
20
ln t(sec)
95%
50%
5%
600?
700
500
600
400
500
350
300?
400
550
420
450
445
420
360
370
370
330
W100PDH
1-2 μ

we believe that the high transition rates in samples with NaCl are due to a catalyzing effect of NaCl, although the mechanism of catalysis is not understood.

It is noted from Figure (8-6) that the sample was oxidized inwards by the penetration of oxygen into the low pressure outer rim during the heating. The oxidation did not occur in the high pressure region. A comparison of the kinetics of oxidation around the outer rim and the olivine→spinel transition at the center region at different temperatures has revealed that the former was faster than the latter at low temperatures (<500°C), but the reverse was true at high temperatures. Thus, the activation energy for the olivine→spinel transition may be larger than that for the oxidation. The oxidation rate can also be increased by repeatedly heating and quenching the sample.

8-5: A Note on Pressure Distribution:

We have measured the center pressure (P_C) at room temperature before and after the olivine→spinel transition in different samples with NaCl by x-ray diffraction. A careful examination of the pressure before transition (P_B) and after transition (P_A) for different samples (Table 8-3) has revealed that P_C may increase with heating before the transition takes place and then decrease with the increasing degree of the olivine→spinel transition. The initial increase of P_C could be due to the extrusion of sample outside the anvils. The increase of P_C with heating is consistent with the observation that the

center region became darker and the outer region became brighter (Figure 8-6b). The decrease of P_C with increasing degree of the olivine→spinel transition is due to the volume contraction of the transition. The possible pressure distribution across the sample during the heating cycle is shown in Figure (8-8). This change of pressure distribution was constructed based on the following information for the run A210-5: (1) estimated P_B based on the calibrated spring length, (2) measured P_A after heating (360°C, 4010 min.), (3) pressure at the olivine-spinel boundary, assuming equilibrium, (4) low pressure (<5 kb) region at the outer rim where oxidation occurred, (5) estimated total load which is assumed to be constant throughout the heating cycle. This estimation of the variation of pressure distribution is still tentative, and a thorough study of pressure distribution is still tentative, and a thorough study of pressure distribution as a function of temperature and degree of transition based on the method of ruby fluorescence is needed to prove or disprove the above speculation.

Because P_C as measured by x-ray diffraction is exclusively the value at room temperature, there are no data on the variation of P_C with temperature. We have x-rayed run A241-5 at 300°C for more than 500 hours in order to obtain P_C at elevated temperature. The increase of sample-to-film distance due to thermal expansion of the press was minimized by circulation of cooling water during the period of x-ray diffraction. The result indicated that P_C=92±5 kb at room temperature increased to 112+5 kb at 300°C. This represents 20% increase of P_C. If

Fig. (8-8)

Proposed variation of pressure distribution across the sample for run A210-5 during the heating cycle. (A) Before heating, (B) after heating and before the olivine→spinel transition, and (C) after the olivine→spinel transition ($X \sim 0,5$). Note the center pressure was increased and then decreased during the heating cycle. The center pressure in each stage may increase at high temperature.

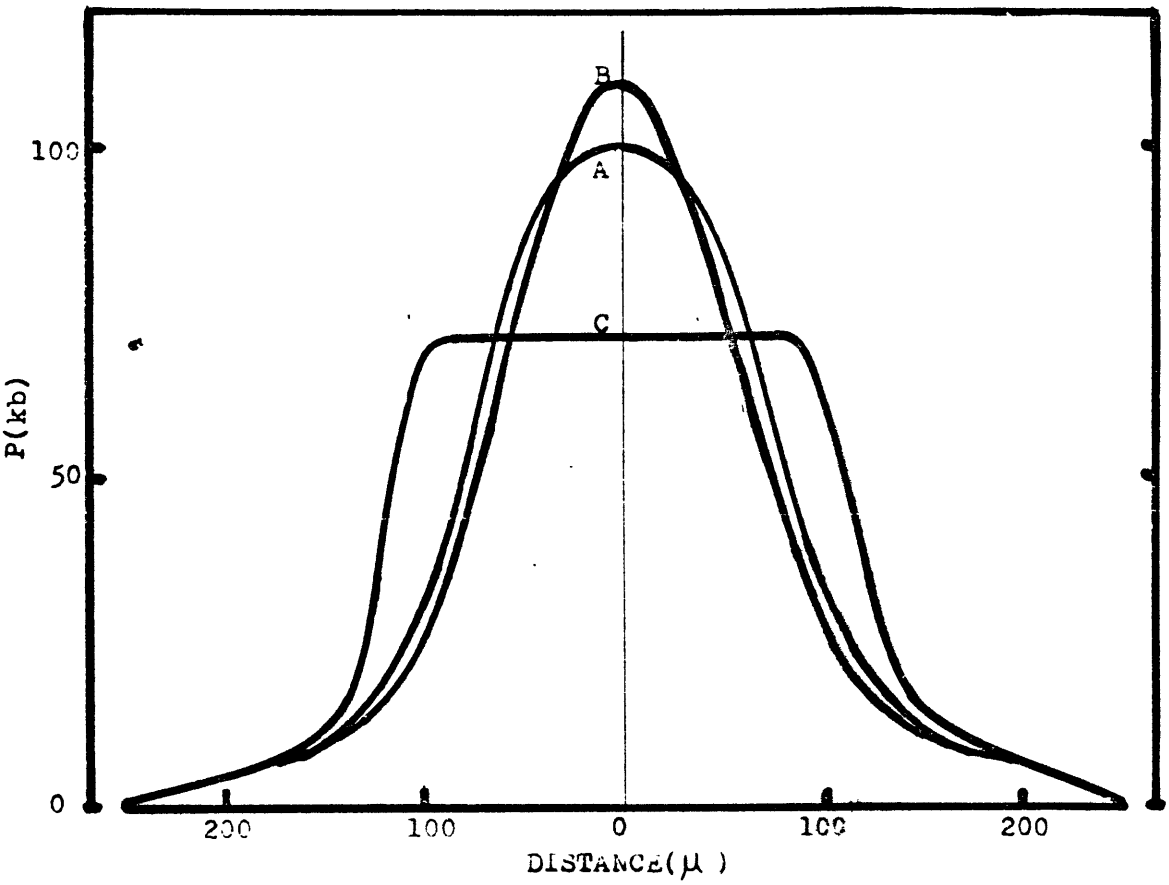
B
A
C
100
50
0
P(kb)
200
100
0
100
200
DISTANCE(μ)

this measurement is correct, then pressure gradients shown in Figure (8-8) will increase at high temperature. It may also suggest that pressures measured at room temperatures for high temperature reactions are significantly underestimated.

8-6: The Effect of Water:

Water has long been known to be capable of promoting reactions of various kinds. It has also been used as a mineralizer to reduce hysteresis in determinations of a phase boundary. However, this study is the first attempt to measure quantitatively the effect of water on the rate of the olivine→spinel transition.

The starting material was a water-saturated paste of fayalite powder (W100PW) with the grain size between 2 and 5μ. Interstitial water was locked in the sample under high pressure. When the temperature rose, water in the low pressure region began to migrate outside the anvils. At temperatures above 400°C, water at high pressure might also migrate outwards. However, before this could happen, even below 300°C, the nucleation region developed and swept across the region of metastable olivine. This happened in the dry sample only when the temperature was higher than 500°C. For the wet sample, at 500°C, the growth rate of spinel was so fast that the merged pure spinel region began to form within a minute (Figure 8-9a), and it could expand to cover almost the whole region of the metastable olivine in 10 minutes (Figure 8-9c). Further prolonged heating could only expand the spinel region slightly.

Fig. (8-9)

Kinetics of the olivine→spinel transition in water saturated Fe_2SiO_4 (W100PW) for run B610-11 at 500°C. (A) After 1 minute, X∿0.5. Note the spreading out of the merged pure spinel region. (B) After 3 minutes, X∿0.9, (C) after 10 minutes, X∿1.0, (d) after 1303 minutes. Note the expansion of the pure spinel region with prolonged heating. Field of view is approximately 400 μ across.

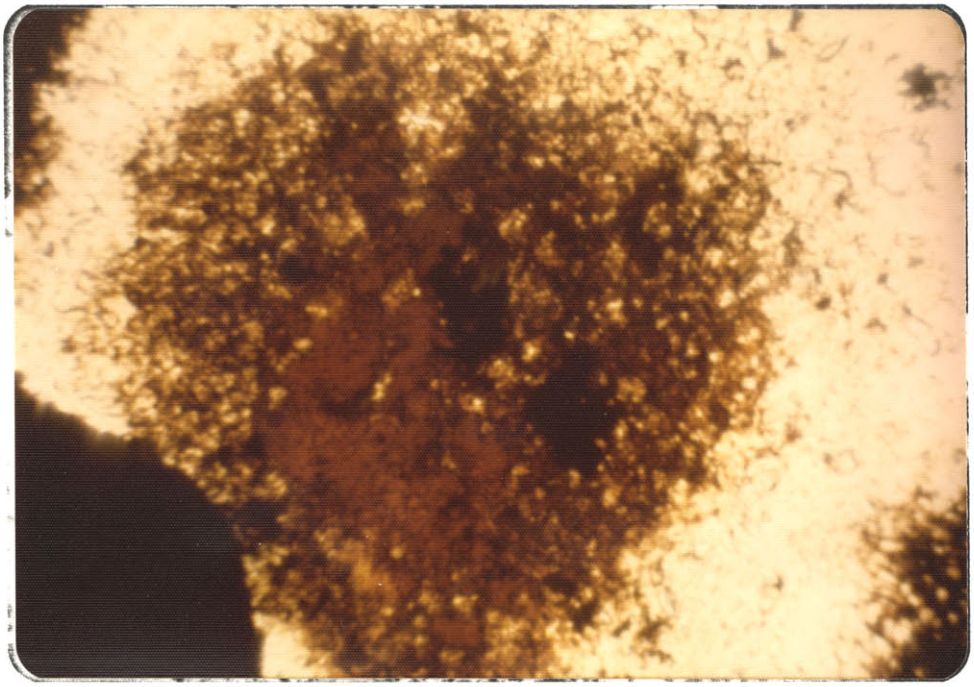

(A)

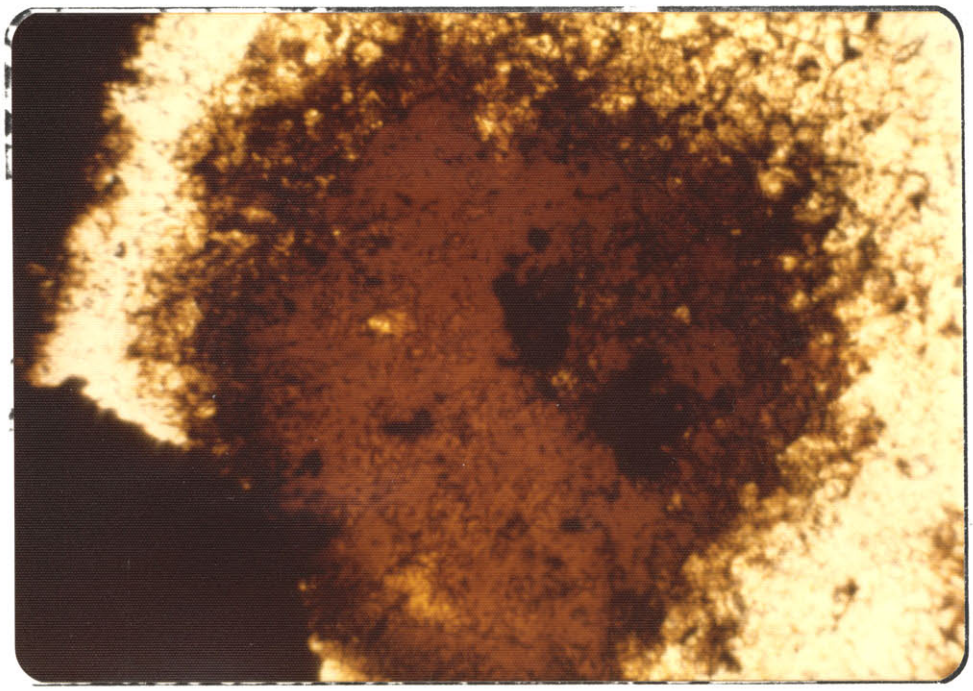

(B)

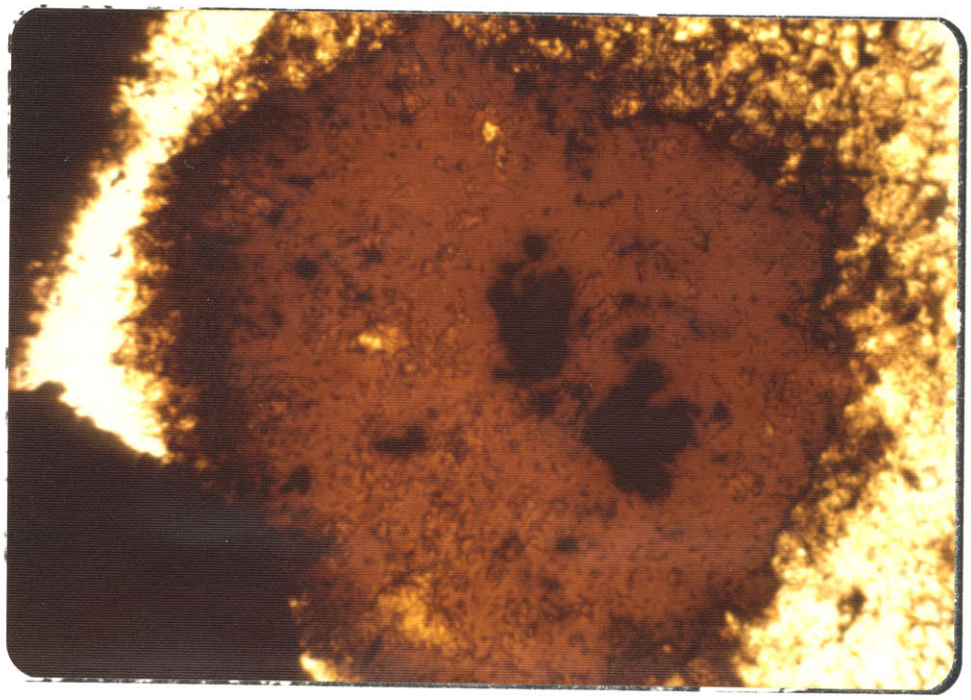

(C)

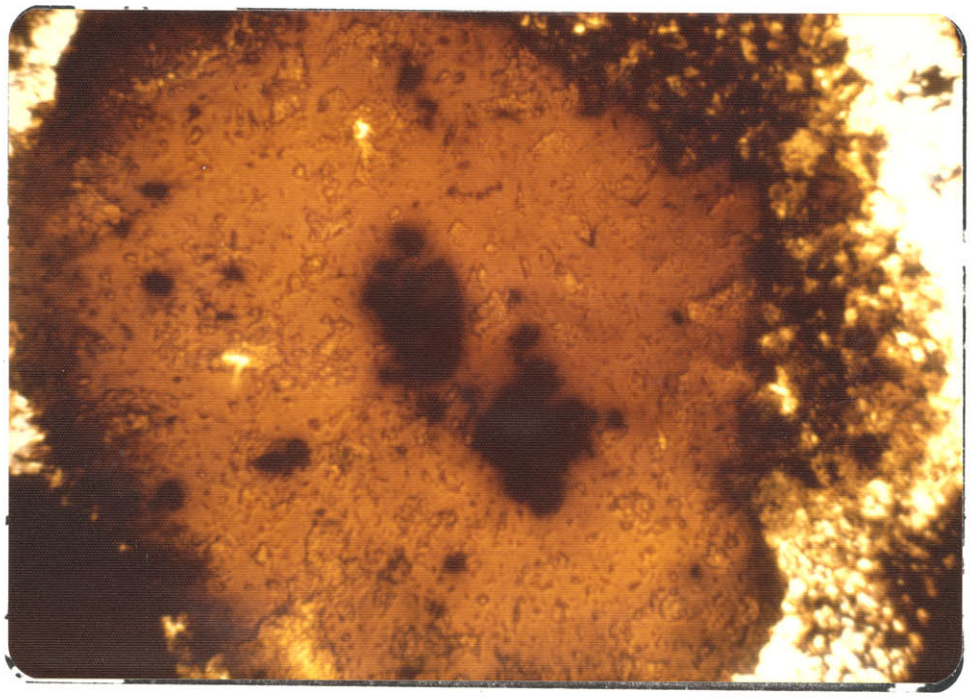

(D)

In some cases, the spinel region also shrank and left behind lineated olivine, which extended heating at 500°C. This never happened for the dry sample below 700°C.

The ln [ln(1/(1-X))] versus the ln t plot based on estimated X for wet samples again suggested unit slopes. Typical experimental results are listed in Table (8-4) and plotted in Figure (8-10). The data are again self-consistent and isotherms of transition (300°C-500°C) (dashed lines) can be drawn. Superimposed on the diagram are isotherms of transition (solid lines) for the dry sample (W100PD) taken from Figure (8-5). It is found that water increases the transition rate more than does a temperature increase of 200°C in dry samples. Water then is a more effective catalyst for the olivine→spinel transition than NaCl. However, the experimental data shown in Table (8-4) and Figure (8-10) are for samples saturated with water. The transition rate will be intermediate between that for water saturated samples and dry samples, if the sample is not saturated with water. In some of our experiments, water evaporated before the sample was held between the two anvils. In this case, the transition rates observed were the same as those for dry samples.

8-7: Transition Kinetics in Single Crystals:

In this section we present some experimental data on the kinetics of the olivine→spinel transition in single crystals. The starting material was a thin section (approximate thickness 12μ) of natural fayalite (B96SD). Its composition can be

Table (8-4)

EXPERIMENTAL RESULTS ON THE KINETICS OF THE OLIVINE→ SPINEL TRANSITION IN WET SAMPLES(W100PW)(Grain size, 2-5μ)

Run Number	P_B(Kb)	T'(^oC)	t(min.)	X
B420-11	160±30	380±20	1010	0.8±0.1
B510-11	150±30	300±10	10	<0.01
		400±10	9.44	0.9±0.1
B430-11	150±30	400±10	300	0.85±0.05
B410-11	150±30	400±10	5	0.05±0.02
		500±20	1	>0.9
B610-11	150±30	500±20	1	0.6±0.1
			3	0.9±0.1
			60	>0.99
D320-9	180±40	500±20	572	1.0

Fig. (8-10)

Experimental results on the kinetics of the olivine→spinel transition in water saturated Fe_2SiO_4 (W100PW). Numbers are temperatures in ^{o}C. coarse vertical lines are experimental data taken from Table (8-4). Dashed lines are isotherms of transition based on these plotted data. Solid lines are isotherms of transition for W100PD (Fig. 8-5). All isotherms have unit slopes. Note that the transition rates were greatly increased by water.

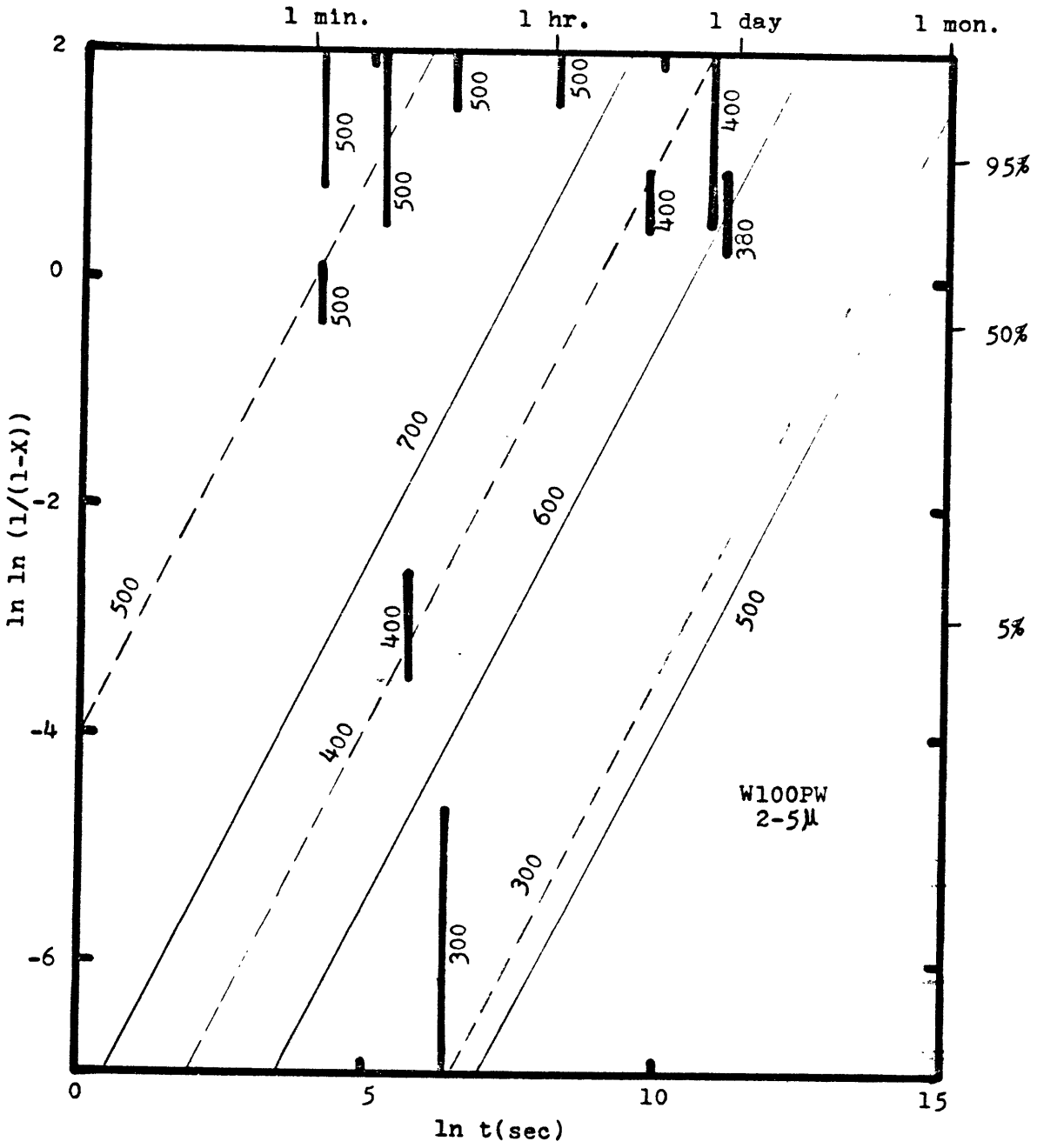
1 min.
1 hr.
1 day
1 mon.
95%
50%
5%
ln ln (1/(1-X))
ln t(sec)
W100PW
2-5μ
500
700
600
400
300
380

expressed by $(Fe_{0.961}Mn_{0.03}Mg_{0.005}Ca_{0.004})_2SiO_4$. The thin section was oriented perpendicular to the c-axis (001). Traces of closely spaced (010) cleavage planes on the sample could be observed under a microscope. A fragment of sample was dug out of the slide and washed with acetone for a few minutes. The sample was then transferred to the diamond anvil and subjected to high pressure. The sample was deformed but the crystal continuity was maintained. When the temperature was raised above 500°C, nucleation began within a few minutes. The nuclei tended to form preferentially along cleavage planes, although some of them also formed within the homogeneous region of the crystal (Figure 8-11a). It is interesting to note that nucleation often develops along the annular region (Figure 8-11a) instead of spreading out from the center. This strange phenomenon occurred in powdered samples also, but was very infrequent and was usually associated with samples whose pressure was recycled. There are three possible causes of the annular transformed region. They are low pressure at the center region, low temperature at the center region, and high Q_a at the center region. The third possibility requires a large positive ΔV^*, which seems to contradict to our previous observations on powdered samples. However, it is still not obvious whether the growth mechanism in single crystals could be different from that in powdered samples. If the growth mechanism is different, then the third possibility cannot be ruled out. The second possibility is unlikely because this requires the temperature at the center region to be substantially lower (possibly by

Fig. (8-11)

Typical runs of the olivine→spinel transition in single crystals of fayalite(B96SD). Samples were oriented perpendicular to the c-axis. Cleavage direction is parallel to the a-axis. All photographs shown are unloaded samples after heating at 600°C. (A) After heating for 50 minutes for Run C331-10. Note the clustering of spinel nuclei along cleavages and that the nucleation occurred only in the annular region. (B) Same sample under crossed polars. Note the extinction of the spinel. (C) After heating for 84 minutes for Run C321-10. Note spinel began to grow inwards. (D) After heating for 1036 minutes for Run C341-10. Note spinel grew much faster along the cleavage direction. Field of view is approximately 400 μ across.

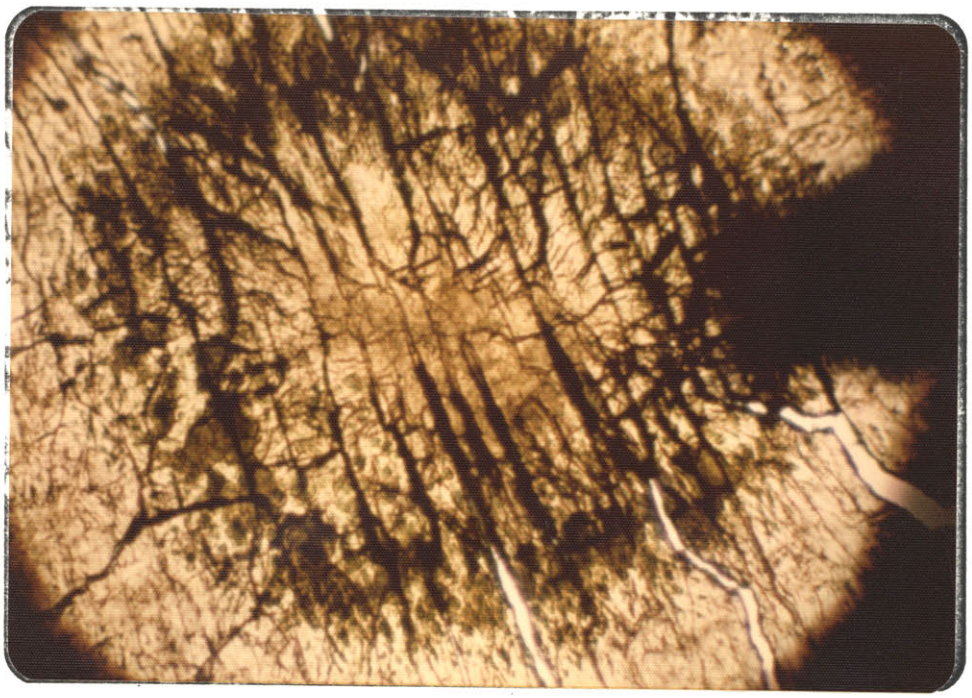

(A)

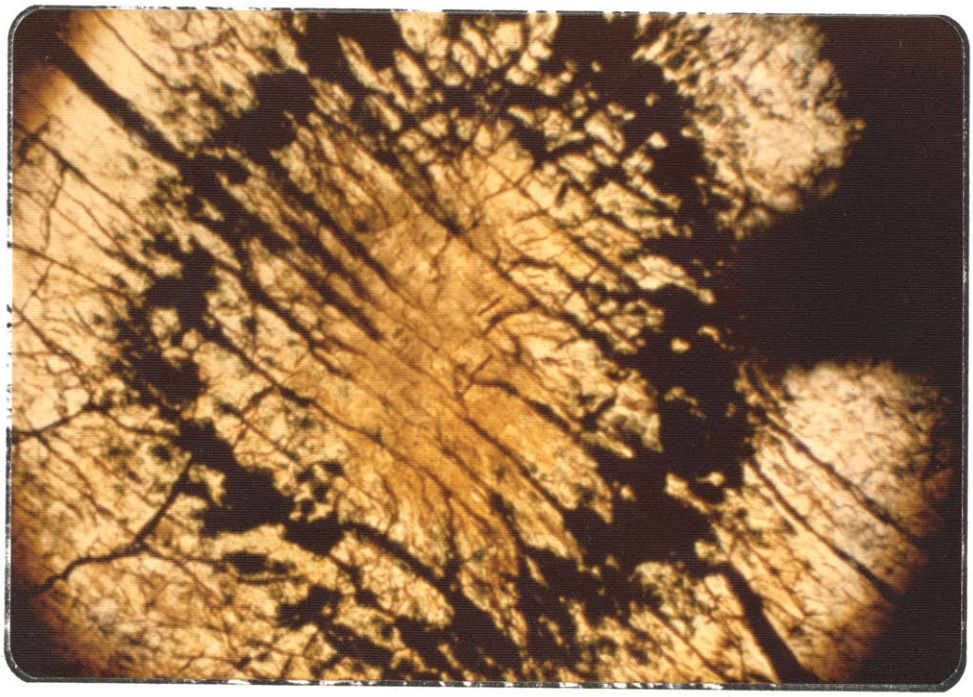

(B)

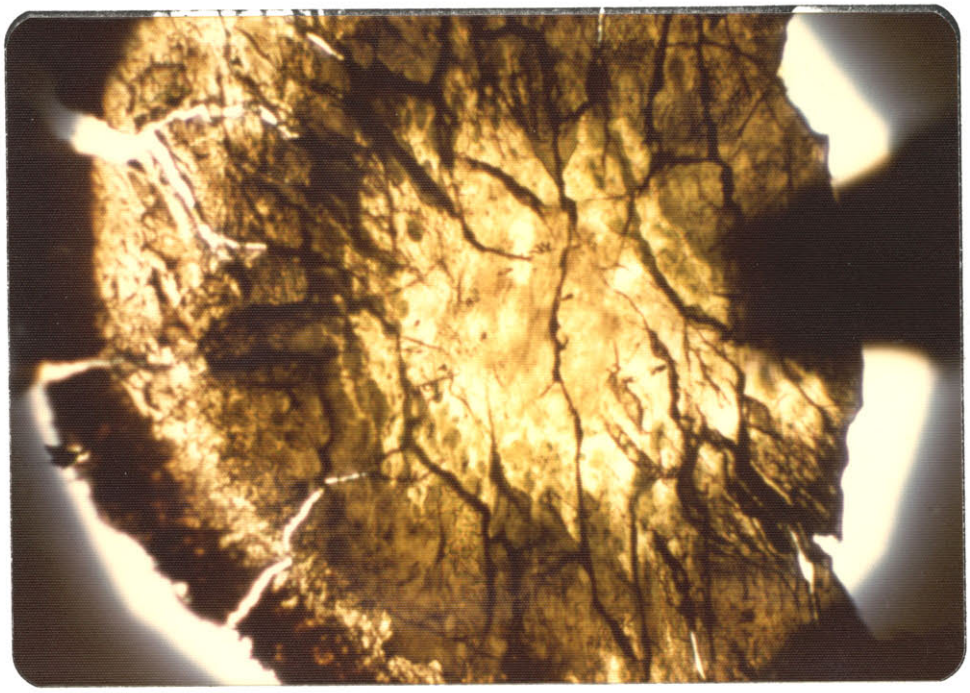

(C)

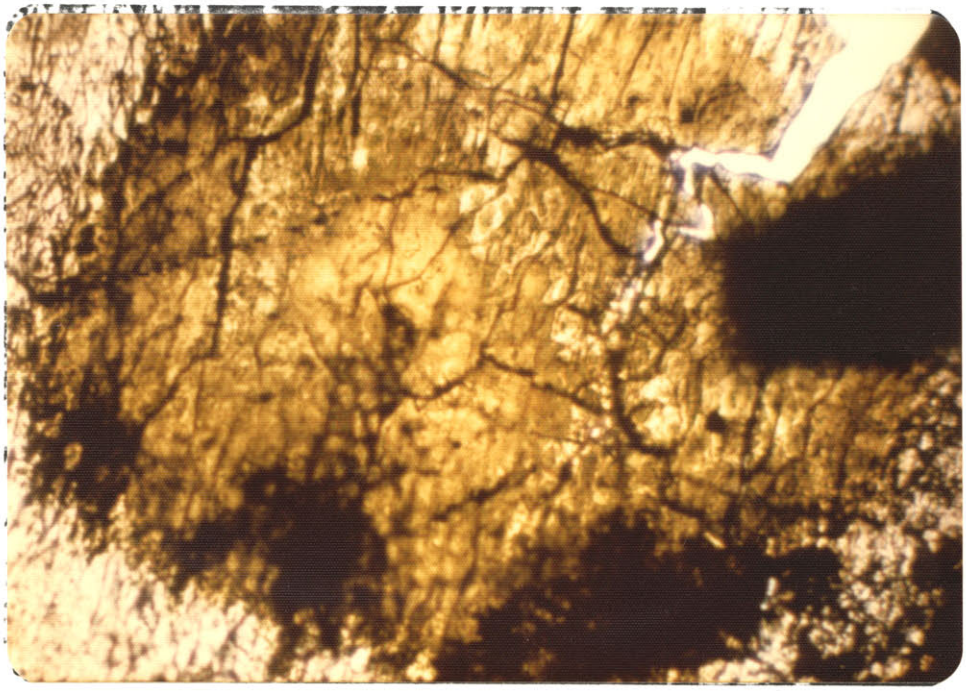

(D)

more than 50°C) than that at the nucleated annular region. In addition, some samples heated by defocussed laser beam (work done at the University of Rochester) also show the transformed annular rings. In this case, temperature at the center region should be higher than that in the annular region. The first possibility seems to be most likely. It is consistent with the observation that transformed annular rings often formed in those samples with annular dark regions present before heating. The dark region marks the position of the highest pressure. The above speculation of lower pressure in the center region than in the transformed annular region must wait to be confirmed by future investigations using the ruby fluorescence technique.

Nuclei also grew very rapidly in the annular region, so a homogeneous ring of pure spinel was soon formed (Figure 8-11b). After that, the spinel would grow inwards but at a much slower rate (Figure 8-11c). The growth rate was anisotropic. It was faster in the direction parallel to the a-axis (the cleavage direction) than parallel to the b-axis.

Experimental results for B96SD are summarized in Table (8-5). The listed X was the estimated proportion of spinel (under crossed polars) within the annular region. We realize that X so estimated may not be comparable to that reported previously for powdered samples. The experimental results are also plotted in Figure (8-12). The experimental data show a larger scattering than that for powdered samples. Superimposed in Figure (8-12) are again isotherms of transition for W100PD. The average rate of transition in single crystals seems to be similar to that

Table (8-5)

EXPERIMENTAL RESULTS ON THE KINETICS OF THE OLIVINE→ SPINEL TRANSITION IN ORIENTED SINGLE CRYSTAL(B96SD)

Run Number	P_B(Kb)	T'(^oC)	t(min.)	X
C310-10	150±30	500±20	81	0.4±0.1
C320-10	110±20	600±30	84	0.5±0.1
C330-10	140±20	600±30	50	0.15±0.05
C340-10	160±30	600±30	1036	0.6±0.1
C350-10	150±30	600±30	227	0.2±0.1
C360-10	120±20	600±30	4045	0.5±0.1

Fig. (8-12)

Experimental results on the kinetics of the olivine→spinel transition in oriented single crystals of fayalite (B96SD). Numbers are temperatures in ^{o}C. Coarse vertical lines are experimental data taken from Table (8-5). Solid lines are isotherms of transition for W100PD.

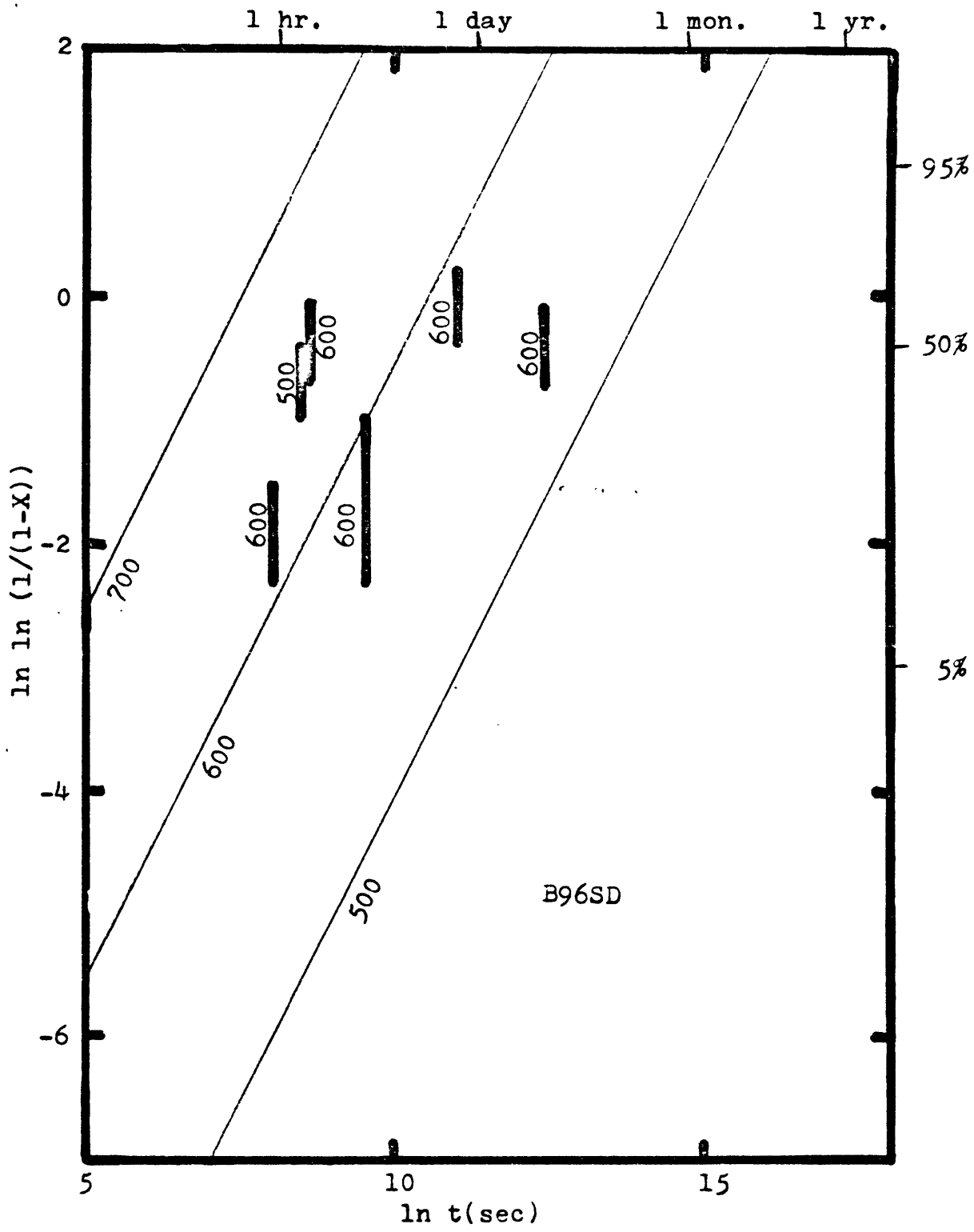
1 hr.
1 day
1 mon.
1 yr.
2
0
-2
-4
-6
95%
50%
5%
ln ln (1/(1-X))
200
600
500
B96SD
5
10
15
ln t(sec)

in Fe_2SiO_4 powders. The transition rate in the annular region will be even higher than that in Fe_2SiO_4 powders. It is not obvious whether this is due to the presence of foreign elements (Mn, Ca) or due to the possible presence of residual cementing material (balsam) in the sample.

8-8: Transition Kinetics in Intermediate Compositions:

In this section, we present experimental results on the kinetics of the olivine→spinel transition in intermediate compositions. Both synthetic and natural samples of compositions down to 40% Fe_2SiO_4 were used as starting materials. The experiments were performed over a range of temperatures between 500°C and 800°C. Unloaded samples for two typical runs are shown in Figure (8-13). At temperatures above 800°C, the recrystallization of olivine became rapid and in a few runs of more Mg-rich composition, olivine had completely recrystallized before it could transform into spinel.

The experimental results for the olivine→spinel transition in intermediate compositions are summarized in Table (8-6) and plotted in Figure (8-14). Superimposed in Figure 8-14 are isotherms (solid lines) for W100PD. Although each datum has a considerable uncertainty in the estimated degree of transition, there is a clear trend of decreasing transition rate with increasing Mg_2SiO_4 (Fo) component, and this trend is followed by both natural and synthetic samples. For example, to attain, say 5% transition, at 800°C, it may take several seconds, several hours, and a few weeks for compositions of

Fig. (8-13)

Unloaded samples for two typical runs of the olivine→spinel transition in intermediate compositions, (A) Run B171-11(M80PD) after heating at 600°C for 22835 minutes. X∿0.05. (B) Run B761-11(B49PD), after heating at 800°C for 1045 minutes. X∿o.1. Samples are approximately 400 μ (A) and 300 μ (B) across.

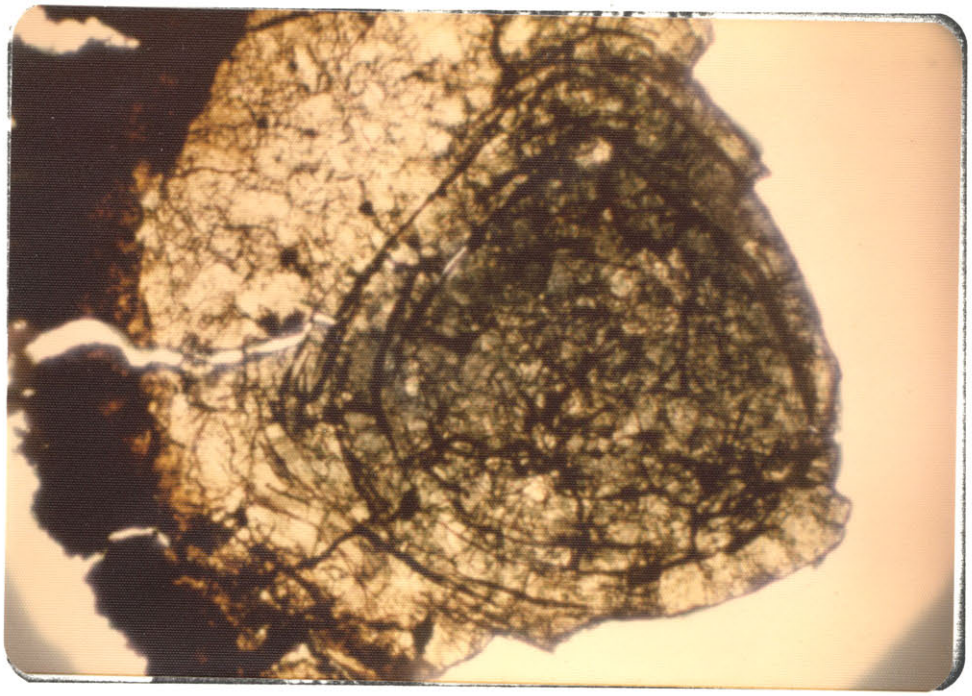

(A)

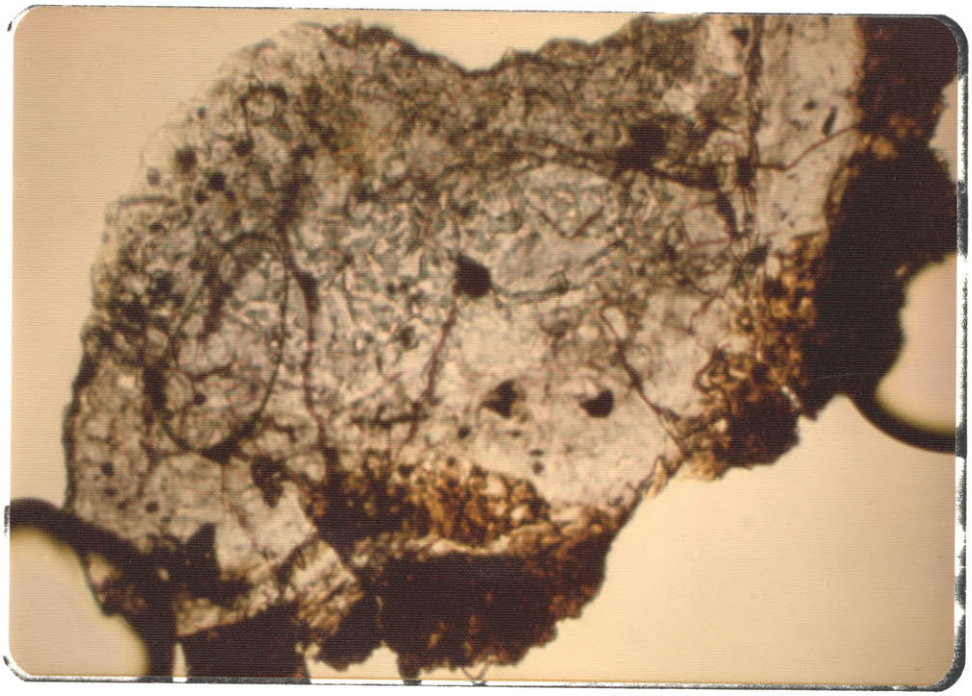

(B)

Table (8-6)

EXPERIMENTAL RESULTS ON THE KINETICS OF THE OLIVINE →SPINEL TRANSITION IN INTERMEDIATE COMPOSITIONS

Sample	D(μ)	Run No.	P_B(Kb)	T'(°C)	t(min.)	X
B97PD	15-25	C370-10	120±20	610±20	2552	>0.99
		C380-10	140±20	610±20	1126	>0.95
M80PD	15-25	B160-3	140±20	500±20	36955	<<0.01(0.001?)
		B170-11	130±20	600±20	22835	0.05±0.02
		D230-9	110±20	600±20	37800	0.05±0.03
		B180-11	120±20	690±30	1281	0.05±0.02
B78PD	15-25	D240-9	130±20	600±10	8455	<<0.01(0.001?)
		B730-11	130±20	700±30	1168	0.05±0.02
M70PD	20-30	B330-11	130±20	650±50	1115	<<0.01(0.001?)
		B620-11	190±30	680±30	101	<<0.01(0.001?)
		B310-11	130±20	700±30	30	<<0.01(0.001?)
		B320-11	200±40	700±30	30	<<0.01(0.001?)
		B520-11	170±30	700±20	35	<0.01(0.005?)
		B530-11	210±40	700±30	150	0.01±0.005
		B540-11	230±40	700±20	10	0.01±0.005
		B710-11	210±40	700±20	5280	0.07±0.02
		B720-11	220±40	700±20	21	<0.01(0.005?)
		B740-11	200±40	800±40	15	0.05±0.02
M60PD	5-15	B750-11	200±40	800±40	100	0.1±0.05
B49PD	10-15	B760-11	210±40	800±40	1045	0.1±0.05
		B770-11	210±40	800±40	1350	0.1±0.05
B39PD	20-30	B830-10	210±40	750±40	3840	<<0.01(0.001?)
		B780-11	180±30	800±40	3600	0.015±0.005

Fig. (8-14)

Experimental results on the kinetics of the olivine→spinel transition in samples of intermediate compositions. Numbers are temperatures in ^{o}C. Vertical lines are experimental data from Table (8-6). Isotherms of transition are for W100PD(Fig. 8-5). Data labelled by A are estimated from experimental results of Akimoto and Fujisawa(1968). Datum of I0PD is estimated from the experimental result of Ito et al(1974) for the olivine→spinel transition in pure Mg_2SiO_4. Note the decrease of the transition rate with increasing Mg_2SiO_4 content.

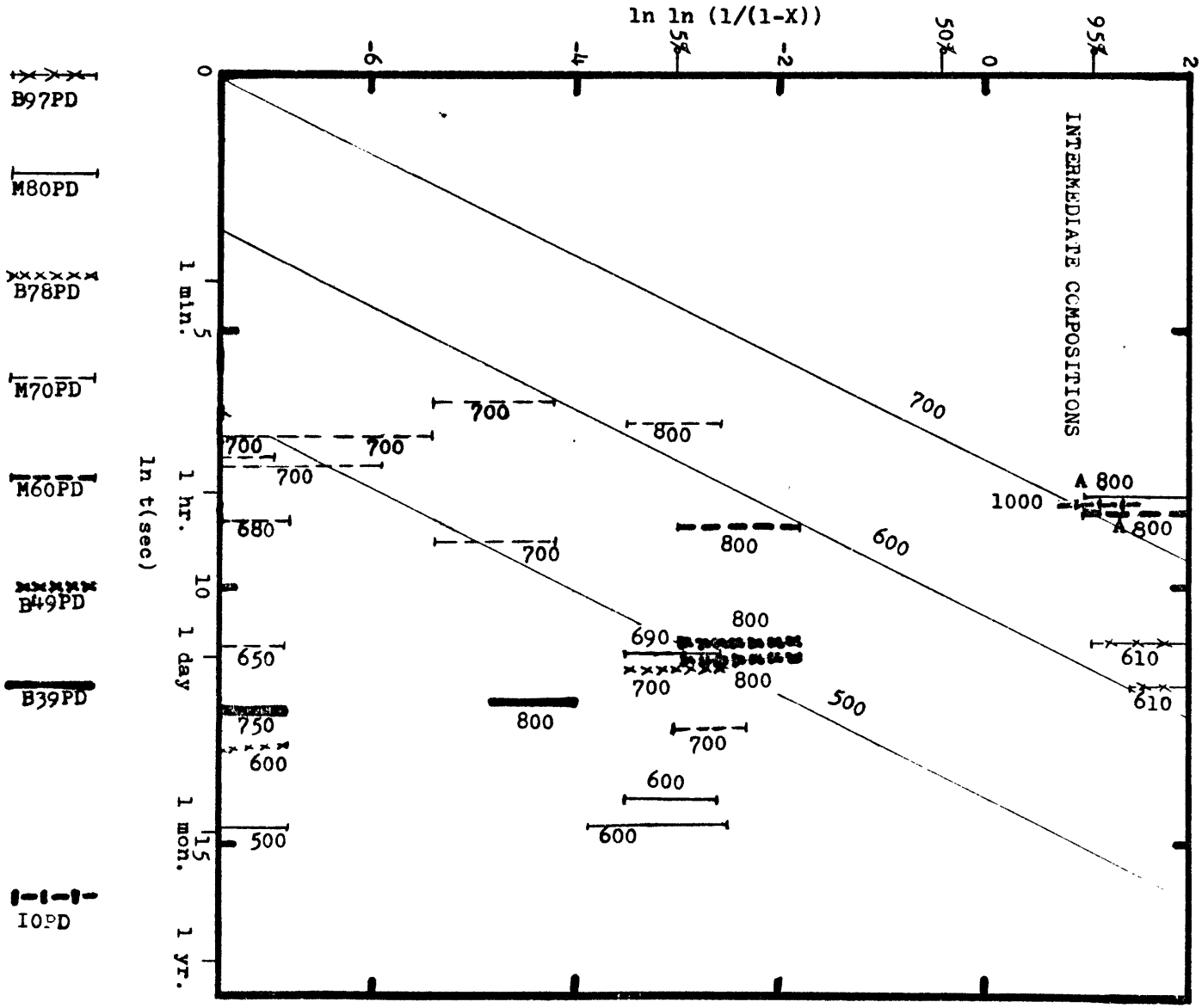
ln ln (1/(1-X))
-6
-4
-2
0
2
5%
50%
95%
INTERMEDIATE COMPOSITIONS
ln t(sec)
0
1 min.
5
1 hr.
10
1 day
15
1 mon.
1 yr.
B97PD
M80PD
B78PD
M70PD
M60PD
B49PD
B39PD
IOPD
700
800
1000
600
500
A 800
690
680
650
750
610

Fo_0 (Fe_2SiO_4), Fo_{30}, and Fo_{60}, respectively. Also plotted in Figure (8-14) are some data reported in the literature. The degree of transition for these data are estimated from the description of the experimental results. It is noted that their transition rates were significantly higher than we would expect from our results. Part of these discrepancies may be due to the difference of grain sizes of the starting material. Akimoto and Fujisawa (1968) used microcrystalline samples, while Ito et al. (1974) used finely pulverized powders. Their grain sizes should be less than 5μ. The grain sizes we used were in the vicinity of 20μ. However, the difference of grain size alone may not be sufficient to account for such a wide discrepancy in transition rates. The high pressure apparatusses they used are tetrahedral press (Akimoto and Fujisawa, 1968) and split sphere press (Ito et al., 1974). Therefore, the shear stresses in their samples could be less than in ours, but this difference could only increase the transition rates in our samples relative to theirs. We believe that discrepancies between their data and our results are due to the temperature measurement. Akimoto and Fujisawa (1968), and possibly Ito et al. (1974), also measured the temperature by putting Pt-Pt (Rh13%) thermocouples at the center of the sample under high pressure. Temperatures measured in this way could be lower than the true sample temperature by 10% at a pressure of 100 kb (Ito et al., 1971). Accordingly, their reported temperatures may be significantly underestimated. If both effects, the difference of grain sizes and temperature measurement, are

taken into account, their data may agree with our results.

8-9: Q_a Calculated Directly from the Measured Growth Rates:

We have repeatedly emphasized that the kinetics of the olivine→spinel transition under very metastable conditions (large ΔP) are governed by Q_a. Q_a can be calculated from the kinetic data obtained above. However, if it is so calculated, it will incorporate uncertainties of grain size and degree of transition estimated. The experimental technique we adopted has allowed us to calculate the growth rate of spinel from the measured thickness of the spinel band (2λ) between olivine grains by photographing magnified unloaded samples. Measured 2λ appeared to increase linearly with time at constant temperature so the growth rate was constant in each run. This is consistent with our assumption made earlier that the olivine→spinel transition is an interface-controlled process.

Measured growth rates (Y) and calculated Q_a based on eq. (6-36) for different compositions are listed in Table (8-7). 2λ measured for each run is the most probable value. Spinel seems to grow more rapidly at the higher pressure region which again suggests a negative value of ΔV^*. The calculated Q_a appears to be independent of temperature. It is noted from Table (8-7) that Q_a was reduced by approximately 30% for samples saturated with water. Q_a values for dry samples of different compositions are plotted in Figure (8-15). The uncertainty of the calculated Q_a is estimated to be $\pm 0.2 \times 10^{-12}$ erg, as indicated by error

Table (8-7)

MEASURED GROWTH RATE(Y) OF SPINEL AND CALCULATED ACTIVATION ENERGY OF GROWTH(Q_a) FOR THE OLIVINE→SPINEL TRANSITION IN DIFFERENT COMPOSITIONS

Sample	Run No.	T'(^oC)	t(min.)	2λ(μ)	Y(A/sec)	Q_a(10^{-12}erg)
W100PD	C221-10	600	1090	1.6	0.12	4.0
	D211-9	550	4025	0.5	0.010	4.0
W100PW	B411-11	500	0.75	2.5	280	2.7
	B511-11	400	500	2.5	0.42	2.8
M80PD	B171-11	600	22835	0.5	0.0018	4.5
	B181-11	700	1281	1.0	0.065	4.5
M70PD	B711-11	700	5280	1.0	0.016	4.7
M60PD	B751-11	800	100	1.2	1.0	4.6
B49PD	B761-11	800	1045	1.0	0.08	5.0
	B771-11	800	1350	1.0	0.06	5.0

Fig. (8-15)

Activation energy of growth(Q_a) of spinel as a function of composition. Q_a was calculated directly from the measured growth rate of spinel during the olivine→spinel transition. Note the linear increase of Q_a with Mg_2SiO_4 content. Open circles at Mg-rich compositions are extrapolated values of Q_a.

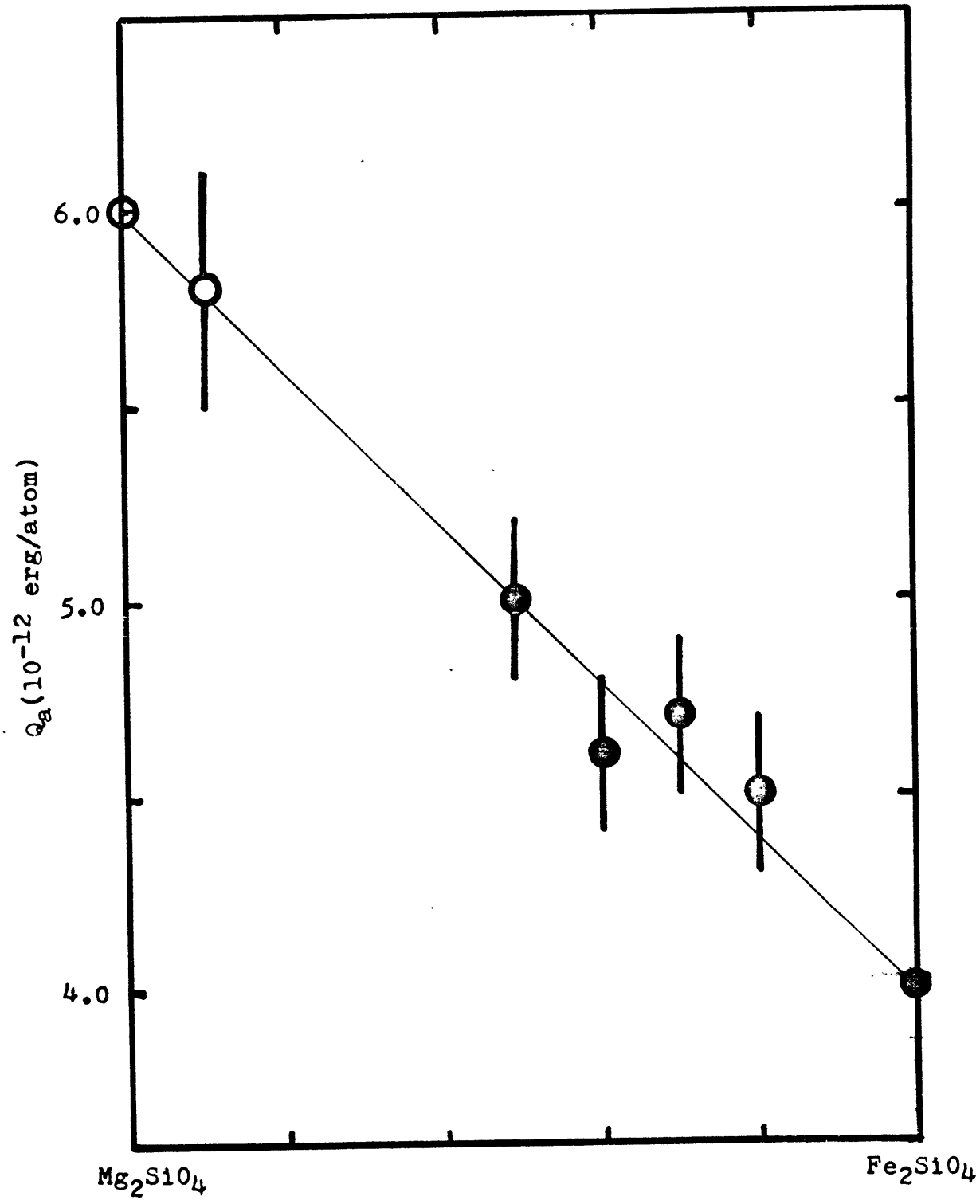
6.0
5.0
4.0
Q_a (10^{-12} erg/atom)
Mg_2SiO_4
Fe_2SiO_4

bars. It is interesting to note that Q_a seems to increase linearly with mole fraction of Fo. An extrapolation of Q_a to Mg_2SiO_4 gives a value of 6.0×10^{-12} erg which is approximately 10% higher than that calculated from the experimental data of Ito et al. (1974) (Table 6-2). However, as mentioned earlier, their temperature could be significantly underestimated. If this is taken into account, for example, if the true sample temperature was 15% higher than they reported (1000°C), Q_a would have been 6.0×10^{-12} erg, which is identical to our extrapolated value.

One of the major objectives of this chapter has been to determine Q_a for the olivine→spinel transition for compositions close to the mantle composition (Fo_{89}). From Figure (8-15) we obtain a value of $Q_a = 5.8 \times 10^{-12}$ erg. We believe that this value has an uncertainty of $\pm 0.3 \times 10^{-12}$ erg. We will use this value to constrain the kinetics of the olivine→spinel transition in the mantle, as will be described in the next chapter.

Chapter 9

GEOPHYSICAL IMPLICATIONS

9-1: Introduction:

The olivine→spinel transition under oceanic and continental plates will result in rapid rises of seismic velocities, density, electrical conductivity, and possibly temperature gradient in the upper transition zone. In addition to these static effects, the olivine→spinel transition in the downgoing slab may also have dynamic effects. It has been inferred to be a source of deep focus earthquakes and a driving mechanism for plate motion (Turcotte and Schubert, 1971; Ringwood, 1972, 1973;; Schubert, 1976). However the exact role of the olivine→spinel transtition in the downgoing slab depends on its kinetics of transition. In this chapter we shall briefly evaluate the possible role of the olivine→spinel transition in plate dynamics, based on the newly acquired data for its kinetics of transition. A more thorough discussion on the possible dynamic effects of the olivine→spinel transition in the downgoing slab can be found elsewhere(Sung and Burns, 1976 a, b) and in Appendix D.

9-2: Kinetics of the olivine-spinel transition in the mantle:

We have derived the rate equations (Eqs. 6-48 to 6-54) for the olivine→spinel transition applicable to the mantle conditions in Chap. 6, and determined the key factor, Q_a, for the olivine→spinel transition in Mg-rich composition, based on the extrapolated experimental data in Chap. 8. From these we can calculate possible positions of isograds pertaining to mantle conditions

for each nucleation mechanism. From both theoretical considerations and experimental results, it is suggested that only three possible nucleation mechanisms govern the olivine→spinel transition in the mantle. They are nucleation on dislocations, nucleation on grain boundaries and homogeneous nucleation with coherent interface. The last nucleation mechanism may be important only under certain restricted physical conditions(large grain size, low shear stress, low temperature and high overpressure). Nucleation on dislocaions has not yet been observed experimentally but is suspected to be important from theoretical considerations.

We shall now determine the possible range of isograd positions for the olivine→spinel transition in the downgoing slab. The time for the olivine→spinel transition will be the time after olivine becomes metastable. A plunging velocity of 10 cm/yr assumed for a downgoing slab with a dip angle of 45^{o} corresponds to a vertical descent velicity of 7 cm/yr and a rate of increasing pressure of approximately 8.5×10^{-13} Kb/sec. In most models of calculation the geotherm for the cold interior of the downgoing slab cuts the equilibrium phase boundary at a pressure of approximately 100 Kb. Substituting $Q_a=5.8\times10^{-12}$ erg/atom and $P=100+8.5\times10^{-13}t$ into Eqs. (6-43) to (6-46), we obtain isograds for the three major nucleation mechanisms of the olivine→spinel transition in the downgoing slab, as shown in Fig. (9-1). The grain size (D) and dislocation density (ρ) assumed in calculation are 0.5 cm and 10^{8} cm^{-2}, respectively. Isograds so calculated are for an isothermal and an isobaric transition, and for a transition time which increases with depth. Isograds for polythermal

Fig. (9-1)

Possible range of isograds for the olivine→spinel transition in the mantle. Each isograd band for a particular nucleation mechanism marks the region where the transition is 10%(X=0.1) to 90%(X=0.9) complete. H, D and B denote homogeneous nucleation with coherent interface, nucleation on dislocations and nucleation on grain boundaries, respectively. Blackened bands were calculated based on experimental results for powdered samples($Q_a=5.8\times10^{-12}$ erg and $\Delta V^*=0$). Shaded bands assumed an activation volume of 10 cm^3/mole. Isograd bands for the real transition in the mantle may lie in between these two extremes. Mixed phases for equilibrium transitions are $\alpha+\gamma$, $\alpha+\beta+\gamma$, and $\alpha+\beta$ at low($<700^oC$), intermediate($700-1600^oC$) and high($>1600^oC$) temperature respectively. Coarse curves are geotherms at the coldest part of the downgoing slab according to different models of calculation. OT(Oxburgh and Turcotte, 1970), TS(Turcotte and Schubert, 1973), M(McKenzie, 1970), TMJ(Toksöz, Minear, and Julian, 1971), G(Griggs, 1972).

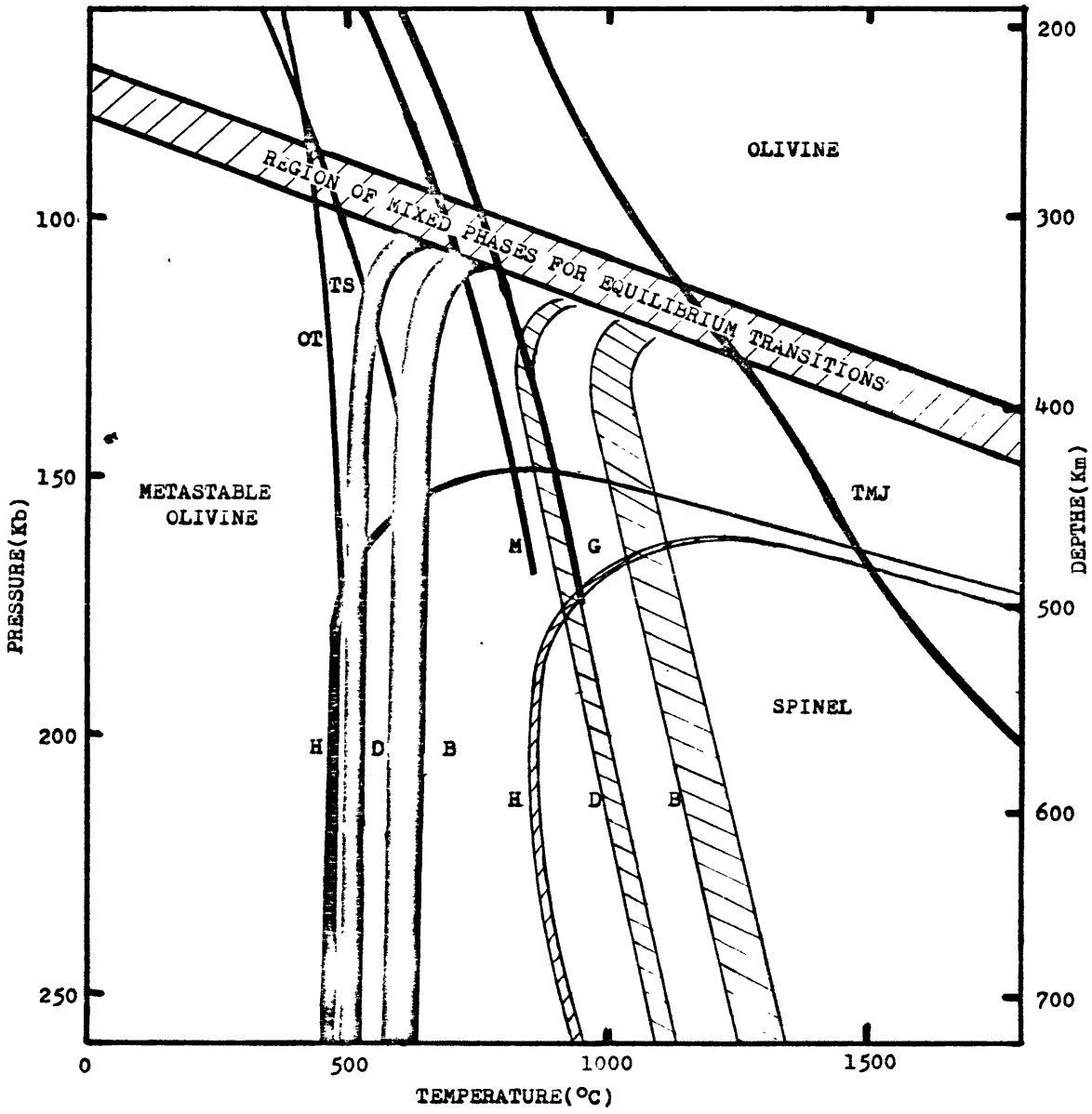
OLIVINE
REGION OF MIXED PHASES FOR EQUILIBRIUM TRANSITIONS
TS
OT
METASTABLE
OLIVINE
TMJ
M
G
SPINEL
H
D
B
H
D
B
100
150
200
250
200
300
400
500
600
700
0
500
1000
1500
PRESSURE(Kb)
DEPTHE(Km)
TEMPERATURE(°C)

and polybaric transition will lie on the high temperature side of the above calculated isograds. However, the difference of positions between these two types of isograds is small($<10^{o}C$), except at the region of small overpressure, where the transition rate is slow.

We shall now asses the possible uncertainty of the positions of the isograds calculated above. The positions of the isograds are determined by many variables; among them D, ρ and Q_a are the most critical. σ and ξ are important only for homogeneous nucleation which can not compete with heterogeneous nucleations in most of the cases. By varying D and ρ by one order of magnitude, the positions of the isograds for nucleation on grain boundaries and nucleation on dislocations calculated above will be displaced by 40 and $15^{0}C$, respectively. Since D and ρ may be underestimated and overestimated, respectively, in our calculation for the olivine→spinel transition in the downgoing slab, the positions of the above calculated isograds may represent the limit on the lower temperature side. We have estimated in Chap. 6 that the uncertainty of Q_a determined is 5%($\pm 0.3 \times 10^{-12}$ erg/atom). This will result in an uncertainty of approximately $\pm 40^{o}C$ for the positions of all isograds shown in Fig. (9-1). In the above calculations, we have assumed that the slowest species of atoms moving across the interface is oxygen. Because the parameters of oxygen atoms enter the pre-exponential term of the rate equation, which has small effect on the position of isograds, the positions of isograds calculated above may not be displaced by more than $40^{o}C$, if silicon were assumed to be the

slowest species.

It should be emphasized that isograds shown in Fig. (9-1) were calculated based on an experimentally determined Q_a, which does not increase with pressure. The small grain size and high shear stress peculiar to the laboratory experiments may be responsible for the apparent zero or negative ΔV^* observed. If this is the case, then the olivine→spinel transition for large grain sizes and low shear stresses in the downgoing slab may have a positive value of ΔV^*. As a consequence of positive ΔV^*, the isograds calculated above will be significantly displaced towards higher temperature and may approach those we have calculated in Chap. 6(Fig. 6-10), which are also shown by shaded bands in Fig. (9-1).

We have demonstrated in Chap. 6 that the presence of abundant water(>5%) can greatly increase the rate of the olivine→ spinel transtion . The water content in the downgoing slab is minor($\sim$0.1%) and is possibly concentrated in the top layers of the downgoing slab. As the slab descends, water may be gradually driven out due to the inctresing pressure and temperature. In addition, it may be extracted preferentially into the partial melt which ascends to produce andesitic magma. Thus, we do not expect a significant amount of water to catalize the olivine→ spinel transition, although it is still possible that a locally water enriched pocket may exist at a great depth in the downgoing slab. The effect of other silicates, such as pyroxene and garnet, on the rate of the olivine→spinel transition is not known. However,

since these silicates do not contain mobile elements essential to promote the reaction rate, they may not affect the kinetics of the olivine→spinel transition.

9-3: Distortion of the olivine-spinel boundary across the slab:

In the early discussions of the olivine→spinel transition in the downgoing slab, the transition was always tacitly assumed to be completed as soon as the equilibrium phase boundary was crossed. As a consequence, the olivine-spinel boundary was distorted upwards because of the lower temperature at the center of the downgoing slab(Ringwood, 1972, 1973; Turcotte and Schubert, 1971, 1973; Schubert et al, 1976; Toksöz et al, 1973). Based on theoretical calculations, Sung and Burns(1976a, b) (Appendix D) have pointed out the possibility that suppression of the olivine→spinel transition occurs at the cold interior of a rapidly plunging slab. In this case the olivine-spinel boundary will be distorted downwards, instead of upwards. This possibility will now be re-examined based on the newly acquired kinetic data.

Superimposed in Fig. (9-1) are geotherms of the coldest parts of downgoing slabs according to different models of calculation. If geotherm TMJ(Toksöz, Minear, and Julian, 1971) is followed, the olivine→spinel transition will occur close to equilibrium, so the olivine-spinel boundary will be distorted upwards as shown in Fig. (9-2b). If geotherms G(Griggs, 1972) or M(McKenzie, 1970) are followed, the olivine→spinel transition may still occur close to equilibrium, and the olivine-spinel boundary will be distorted upwards. Because temperatures at the coldest part of the slab are lower, the elevation of the

Fig. (9-2)

Proposed evolution of the profile of the olivine-spinel boundary(X=0.1-0.9) across a downgoing slab and its effects on plate dynamics. The plunging velocity increases from (B) to (F). Forces acting on the cold interior are:F_p, downwards pushing force due to the cold contraction of the slab; F_o, force due to the didtortion of the olivinr-spinel boundary; F_s, force due to the distortion of the spinel-oxides boundary; F_c, downwards force transmitted from the advected plate; F_r, upwards resistance force due to the viscous drag of the plunging slab. Note the inversion of F_o from downwards to upwards when the plunging velocity exceeds a certain critical value(between (C) and (D)), and its effects on the stress distribution in the downgoing slab. Note also that the alignment and distribution of T and P-axes of intermediate and deep earthquakes may be controlled by the evolution of the profile of the olivine-spinel boundary.

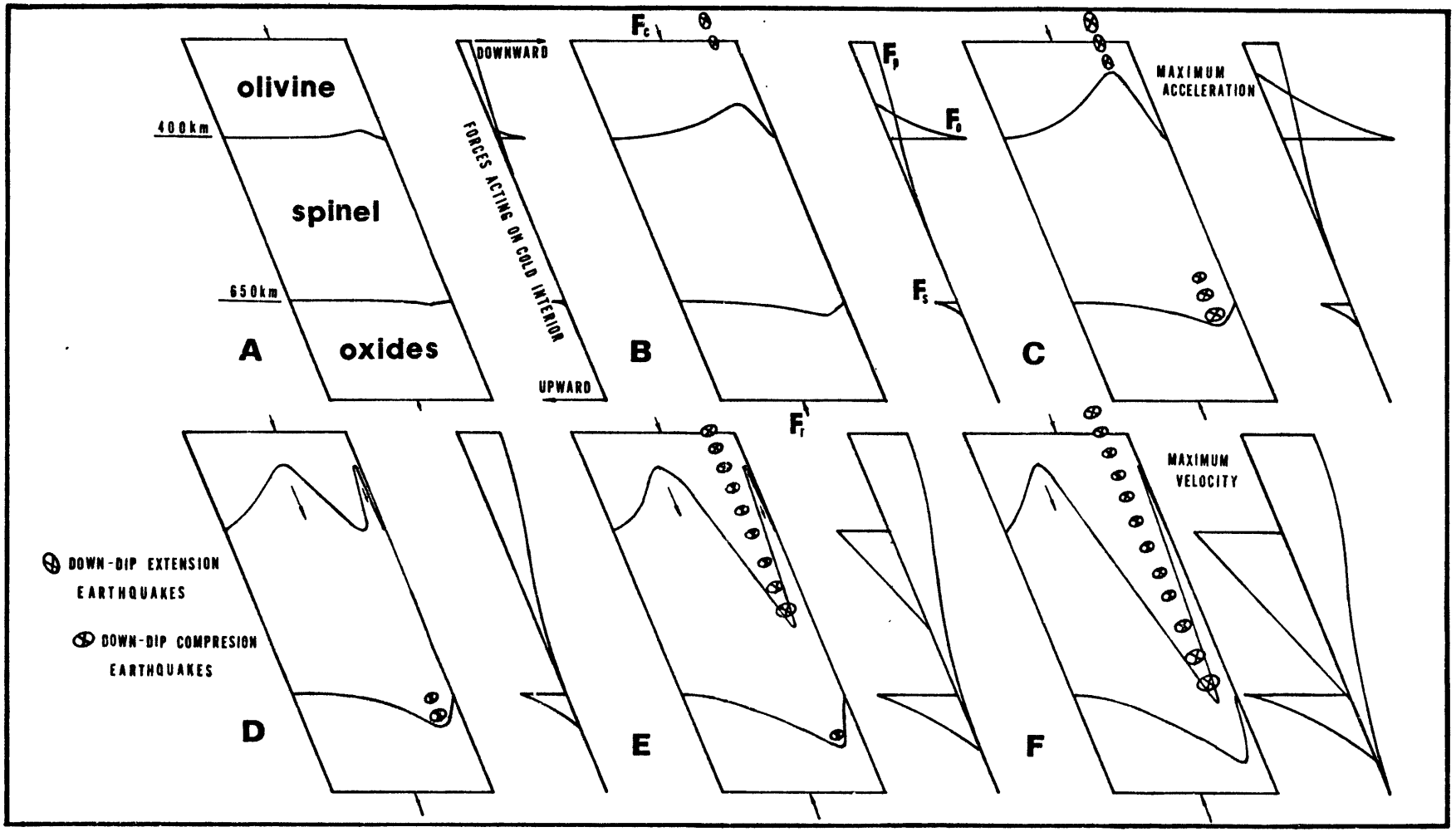
olivine
400km
spinel
650km
oxides
A
DOWNWARD
FORCES ACTING ON COLD INTERIOR
UPWARD
B
F_c
F_p
F_o
F_s
F_r
C
MAXIMUM ACCELERATION
MAXIMUM VELOCITY
DOWN-DIP EXTENSION EARTHQUAKES
DOWN-DIP COMPRESION EARTHQUAKES
D
E
F

olivine-spinel boundary will be larger as shown in Fig. (9-2c). If geotherm TS(Turcotte and Schubert, 1973) is followed, the major part of the olivine→spinel transition will not occur at the equilibrium transition pressure but will be depressed down to the depth where the geotherm cross the isograd X=0.1. The olivine-spinel boundary defined by X=0.1 to 0.9 will begin to distort downwards as shown in Fig. (9-2d). If geotherm OT (Oxburgh and Turcotte, 1970) is followed, the major part of the olivine→spinel transition will be suppressed to depths greater than 500 Km, and the olivine-spinel boundary will be depressed further as shown in Fig. (9-2e). If temperature at the cold interior of the slab could be even lower or isograds of the olivine→spinel transition could be displaced towards higher temperature(e.g. if ΔV^* is positive), the major part of olivine will exist metastably even down to the lower mantle(Fig. 9-2f), where it might decompose directly into oxides or transform into the other post-spinel phase.

It is clearly seen that the shape of the olivine-spinel boundary across the slab is determined by the relative positions of the geotherm at the cold interior of the slab and the isograds of the olivine→spinel transition. With the wide discrepancies among different models for the geotherm for the cold interior of a downgoing slab(Fig. 9-1), it is impossible to draw a definite conclusion about the shape of the olivine-spinel boundary across the slab. The geotherm of the cold interior of a downgoing slab depends on many variables; among them the plunging velocity is

the most critical. The temperature at the center of the slab will be lower if the plunging velicity is higher. Thus, with increasing plunging velocity, we may expect the olivine-spinel boundary at the center of the slab to rise until a critical plunging velocity is reached. Beyond that, the olivine-spinel boundary will suddenly be depressed. The variation of the shape of the olivine-spinel boundary with increasing plunging velicity is depicted schematically in Fig. (9-2 from b to f). It is not obvious at this stage whether or not the maximum plunging velocity of downgoing slabs exceeds the critical value such that the temperature at the cold interior of the slab is low enough to depress the olivine→spinel boundary.

Kogan(1975) has measured a gravity anomaly across the Kuril-Kamchatka Arc. He found a signuficantly lower anomaly than that required for a rising olivine-spinel boundary towards the plunging direction of the plate. He attributed this to a shallowly (180 Km) subducted slab and a compensation of less dense material under the marginal sea. However, this low gravity anomaly may also be due to the downwards distorted olivine-spinel boundary in a deeply subducted slab. The deeply subducted slab is also consistant with the deeply distributed earthquakes in this region.

Recently Solomon and Paw U(1975) have measured travel time residuals for P-wave emitting and propagating through the entire length of the slab from deep earthquakes in the Tonga Island Arc. They found negative residuals for earthquakes located shallower than approximately 300 Km. They attributed this to the

elevation of the olivine-spinel boundary of approximately 100 Km, which implys a temperature difference of approximately 1000°C between the margins and the cold center of the downgoing slab. This large temperature difference and high elevation of the olivine-spinel boundary will exert a downwards body force of several kilobars on the downgoing slab. Such a large downward force needs to be compensated in order to explain the small intraplate stresses measured(Solomon et al, 1975). If negative travel time residuals in the Tonga Arc are due to the elevation of the olivine-spinel boundary, then either temperatures in the cold interior of the slab for geotherms OT and TS are underestimated, or isograds of the olivine→spinel transition should be displaced towards the lower temperature(e.g. by the catalizing effect of water). On the other hand, if negative travel time residuals are due to some other effect, e.g. dehydration or the basalt→eclogite transformation, and the temperature at the cold interior of the slab is low enough to suppress the olivine→spinel transition, then the large downwards body force due to the cold contraction of the slab and the phase change(dehydration or basalt→eclogite transformation) can be balanced by the upwards buoyant force due to the penetration of olivine into the more dense spinel(Fig. 9-2e,f). In this case, the small intraplate stresses can be explained.

9-4: Stress distribution in downgoing slabs:

There are suggestions that a downgoing slab sinks under its own weights(Forsyth and Uyeda, 1976; Ringwood, 1972. 1973; Isacks and Molnar, 1971). Forces acting on the downgoing slab are

believed to be one order of magnitude higher than those acting on the ridge or on the bottom of the plate. Among forces acting on the downgoing slab, the downwards body force due to the cold contraction of the slab is the major force(a few kilobars for rapid plunging slabs). Body force due to the distortion of the olivine-spinel boundary is also significant (Turcotte and Schubert, 1971; Schubert et al, 1976) and may have a magnitude of one third of that for the cold contraction of the slab. As shown in Fig. (9-2), if the olivine-spinel boundary is distorted upwards, the downwards body force due to the elevation of the denser spinel tends to drive the slab (Fig. 9-2b, c). As a consequence, the slab above the olivine-spinel boundary receives a "pulling force"(less compression) and the slab beneath it is subject to a pushing force. This will align the minimum and the maximum principal stresses along the coldest part of the slab above and beneath the olivine-spinel boundary, respectively. On the other hand, if the olivine-spinel boundary is distorted downwards, the upwards buoyant force due to the penetration of less dense olivine into spinel will exert a compressive force to the cold interior of the slab above the olivine-spinel boundary(Fig. 9-2e,f). If the downwards distortion of the olivine-spinel boundary is significant, the entire length of the slab may be under compression and the maximum principal stress will be aligned throughout the cold interior of the slab.

Non-shallow(intermediate and deep) earthquakes have been shown to localize within a narrow(10 to 20 Km)seismic zone in

the coldest part of downgoing slabs, where the rock may still be brittle(Engdahl, 1973; Toksöz et al, 1973, Wyss, 1973). From a world wide survey of focal nechanism solutions for non-shallow earthquakes in downgoing slabs, Isacks and Molnar(1971) have shown that usually either the compressional axes(P-axes) or the tensional axes(T-sxes) are parallel to the seismic zone. The distribution of these two types of earthquakes, down-dip compression and down-dip extension, along the downgoing slab fall, in general, into three groups: (1) earthquakes of down-dip extension which occur down to 300 Km depth only; (2) earthquakes of down-dip extension which occur above 300 Km and earthquakes of down-dip compression which occur below 400 Km. There is a clear aseismic region separating these two seismic zones; and (3) earthquakes of down-dip compression which occur all the way down to about 700 Km depth. These three groups of earthquake distribution can be explained by the stress distribution controlled by the shape of distortion of the olivine-spinel boundary(Fig. 9-2), as described above. Thus the rise of the olivine-spinel boundary may align T-axes and P-axes of earthquakes above and below the olivine-spinel boundary, respectively, and the depression of the olivine-spinel boundary may align P-axes of all earthquakes throughout the entire length of the downgoing slab.

We have proposed above that the variation of the shape of the olivine-spinel boundary may be important in determining the stress distribution in downgoing slabs. The former depends

on the temperature at the cold interior of the downgoing slab and is determined mainly by the plunging velocity of the slab. We then propose the following scheme for the evolution of the olivine-spinel boundary in the downgoing slab. The developement of a new downgoing slab should begin with a very slow plunging velocity. As the plunging velocity increases temperature becomes lower at the center of the slab so that forces due to cold contraction and the rise of the olivine-spinel boundary increase. This tends to accelerate the downgoing slab, which further increases the downwards driving forces. At some critical plunging velocity(between Fig. 9-2 c and d) peculiar to each individual slab, the olivine-spinel boundary at the cold center of the slab may suddenly be depressed. The upwards buoyant force so created will soon balance the downward driving forces and the plunging velocity of the downgoing slab reaches a steady state(terminal velocity). The time to reach the terminal velocity may be short compared to geological time, so almost all downgoing slabs are plunging with terminal velocities. It is also possible that most or all downgoing slabs have insufficient terminal velocities to depress the olivine-spinel boundary, although the difference of temperatures at the cold interior of a downgoing slab for upward(Fig. 9-2c) and downward(Fig. 9-2d) distortions of the olivine-spinel boundary is not large. In this case, the olivine-spinel boundary will always be distorted upwards.

9-5: Deep earthquake genesis:

High pressure phase changes as possible sources for deep

earthquakes have long been speculated(Bridgeman, 1945; Evison, 1963; Benioff, 1963). If this is possible, the olivine→spinel transition will be the most likely candidate as the source for deep earthquakes, because it is the most intensive($\Delta V/V \sim 0.07$) and extensive(approximately 60% of the rock) transition occurring where deep earthquakes are located. One of the necessary requirements for the olivine→spinel transition to generate deep earthquakes is the ability for olivine to penetrate deeply into the spinel stability field. This leads to storage of implosive chemical energy which can suddenly be released, upon transition. Such a requirement can not be fulfilled if geotherm TMJ or possible M or G is followed(Fig. 9-1), because the olivine→spinel transition will occur close to equilibrium. The transition rate will then be limited by the rate of over-pressure accumulation, which is determined by the plunging velocity of the downgoing slab. Under such a condition, the olivine→spinel transition can not generate deep earthquakes. On the other hand, if geotherms OT or TS(Fig. 9-1) are followed, olivine can remain untransformed and penetrate deeply into the lower transition zone. Even if water is present and isograds of transition shift towards the lower temperature, local pockets of dry olivine may escape the equilibrium transition and be carried down to a great depth, where olivine transforms implosively into spinel. When this happens heat will duddenly be evolved and pressure will suddenly drop. Because isograds for the very metastable olivine→spinel transition are nearly parallel

to the pressure axis(Fig. 9-1), sizeable pressure drop(>50 Kb) can be tolerated without stopping the transition. If the volume for the implosive transition is large, shear stresses in the surrounding rock will be greatly enhanced. If the rock is brittle, shear rupture may occur, which may result in deep earthquakes of double-couple origin. On the other hand, if the rock is ductile, creep rate will be greatly promoted. This may result in shear melting(Griggs and Baker, 1969) and also produce earthquakes of dislocation type. Once shear rupture occurs, local shear stresses drops, but shear stresses at higher levels are enhanced. Earthquakes can then propagate upwards. According to this model of deep earthquake genesis, a series of deep earthquakes can be triggered by the metastable olivine→spinel transition, but only the first one may show the precursor of the hypocentral volume change. At least two large deep earthquakes have been identified to possess this precursor of hypocentral volume change(Gilbert and Dziewonski, 1975). If the olivine→spinel transition is not extensive enough to trigger an immediate shear rupture, the earthquake may occur a long time period after. In this case, the precursor of volume change may not even be detected. Thus the lack of a volume change component in a deep earthquake does not exclude the possibility of its being induced by the olivine→spinel transition.

The above model of generating deep earthquakes by the metastable olivine→spinel transition appears to be attractive. However, it requires T-axes of deep earthquakes to be directed towards the region of the implosion, As the highly metastable

olivine→spinel transition can only occur at the cold center of the downgoing slab, where deep earthquakes are located. We may then expect T-axes of deep earthquakes to align in the seismic zone. This contradicts the observation that for the majority of deep earthquakes, P-axes are aligned in the seismic zone (Isacks and Molnar, 1971)(Fig. 9-2). Such observations may eliminate the olivine→spinel transition as the major cause of deep earthquakes, although it may still be responsible for the genesis of some deep earthquakes.

Chapter 10

PROPOSED FUTURE WORK

This thesis is part of a long term project to study the kinetics of the olivine→spinel transition and its geophysical implications. We have developed the kinetics theory, designed equipment, obtained basic experimental results, and hypothesized geophysical consequences for the olivine→spinel transition. This forms the foundation for future research in this field. We shall now propose future work, which can refine the data we obtained and may lead to new discoveries in the characteristics of the olivine→spinel transition. We describe very briefly some work we are planning to do in the future.

(1) Perform more experiments on the olivine→spinel transition to cover a wider range of grain sizes and compositions for both synthetic and natural samples.

(2) Evaluate the effect of shear stress on the rate of the olivine→spinel transition by gasketing the sample. This will reduce both the pressure gradient and the shear stress in the sample. If possible, we plan to study the kinetics of the transition by using other equipment of low shear stress and compare the results.

(3) Study the interfacial characteristics of the olivine-spinel boundary by scanning electron microscopy(SEM) and transmission electron microscopy(TEM). The unloaded sample can be ion-thined or etched before being put under the electron microscope.

(4) Measure high temperature Mössbauer absorption spectra of spinel to determine the possibility of increasing entropy at high temperature by disordering divalent and tetravalent cations. These will settle the problem of whether or not the slope of spinel-oxides(or other postspinel phases) transformation can be positive at high temperature. The same Mössbauer data can be used to calculate the t_{2g} orbital splitting in spinel.

(5) Measure high P-T optical absorption spectra of both olivine and spinel. These will determine the crystal field stabilization of the olivine→spinel transition, as a function of P and T.

(6) Measure electrical conductivities of olivine and spinel at high P-T conditions. These can constrain the possible geotherms in the mantle.

(7) Measure the pressure distribution across the sample as a function of P, T and X, by using the technique of ruby fluorescence. It is very important to know whether the pressure at the center is lower than in the transformed annular region in single crystals. If this is not the case, then $\Delta V^* > 0$ and isograds calculated in Fig. (9-1) should be significantly displaced towards higher temperature. This will have major geophysical consequences.

APPENDIX A

PARTIAL LIST OF SYMBOLS AND UNITS (UNLESS OTHERWISE SPECIFIED) USED IN THIS THESIS

Symbols	Unit	Explanation
a		activity
C_n	cm^{-3}	total concentration of nuclei
CFSE	Kcal $mole^{-1}$	crystal field stabilization energy
C_p	cal $mole^{-1}$ $^oC^{-1}$	heat capacity at constant pressure
C_v	cal $mole^{-1}$ $^oC^{-1}$	heat capacity at constant volume
E	Kb	Young's modulus
ΔE^h	erg	energy of heterogeneity
G_{CFS}	Kcal $mole^{-1}$	free energy change due to crystal field splitting
ΔG^d	erg	Gibbs free energy change
ΔG^f	Kcal $mole^{-1}$	free energy of formation
ΔG_T	erg	total free energy change during the transition
G_{MX}	Kcal $mole^{-1}$	free energy of mixing
G_{XS}	Kcal $mole^{-1}$	excess free energy of mixing
$\bar{I}_s$	cm^{-3} sec^{-1}	steady state nucleation rate
K	Kb	bulk modulus
$\bar{L}$	cm^{-2}	total length of dislocation per unit volume
n^*		number of atoms in the critical-sized nucleus
$\bar{N}$	cm^{-3}	number of atoms per unit volume
N_e^*	cm^{-3}	equilibrium concentration of critical-sized nuclei
P	Kb	pressure
P'	Kb	hypothetical transition pressure assuming without crystal field splitting for Fe^{2+}
ΔP	Kb	overpressure
Q_a	erg $atom^{-1}$	activation energy of growth
Q_D	erg $atom^{-1}$	activation energy for lattice diffusion

APPENDIX A
(CONTINUED)

r	cm	radius of nucleus
r^*	cm	radius of critical-sized nucleus
S	cal $mole^{-1}$ ^oC	entropy
S_e	cal $mole^{-1}$ ^oC	electronic configurational entropy
S_{CFS}	cal $mole^{-1}$ ^oC	entropy change due to crystal field splitting
S_n		number of atoms on the surface of the nucleus
T	^oK	temperature
T'	^oC	temperature
t	sec	time
t_s	sec	time for site saturation
U	Kcal $mole^{-1}$	lattice energy
V	cm^3 $mole^{-1}$	molar volume
ΔV^*	cm^3 $mole^{-1}$	activation volume
W_G	cal $mole^{-1}$	interaction energy
X		degree(volume fraction) of transition
		mole fraction
Y	cm sec^{-1}	growth rate
Z		Zeldovich non-equilibrium factor
α_P	$^oK^{-1}$	isobaric thermal expansion coefficient
β_T	Kb^{-1}	isothermal compressibility
β^*	sec^{-1}	rate of adding atoms to the critical-sized nucleus
Δ	cm^{-1}	crystal field splitting energy
δ	cm	thickness of interface
	cm^{-1}	maximum splitting of t_{2g} energy levels
ξ	erg	strain energy of transition
	Kcal $mole^{-1}$	site distortion stabilization energy
σ	erg cm^{-2}	surface energy
$\sigma_1-\sigma_3$	Kb	differencial stress
ρ	cm^{-2}	dislocation density
ν		Poisson's ratio
τ	sec	incubation time
μ	Kcal $mole^{-1}$	chemical potential
	Kb	shear modulus

APPENDIX B

STRAIN ENERGY RELEASED DURING NUCLEATION ON DISLOCATION

Strain energy released(ΔE^D) during the formation of a spherical spinel nucleus on a straight dislocation in olivine is estimated as follows: Assuming the dislocation was lying diametrically in the spinel nucleus(Fig. B-1) and the dislocation within the spinel nucleus was completely eliminated so the strain energy of the dislocation inside the spherical nucleus was released to contribute to the nucleation, then the released strain energy per unit length is

$$\Delta\bar{E}^D \sim -(\bar{E}_o^D \ln(R/R_o)+\bar{E}_o^D)=-\bar{E}_o^D\ (\ln(R/R_o)+1) \quad \text{----------(B-1)}$$

where R_o is the core redius of the dislocation and $\bar{E}_o^D$ is the core energy per unit length. The total strain energy within the spherical nucleus of radius r is

$$\Delta E^D \sim -2\int_0^r \bar{E}_o^D(\ln(R/R_o)+1)dx \quad \text{----------(B-2)}$$

Knowing the relationship of $R^2+x^2=r^2$ and integrating Eq. (B-2), we obtain

$$\Delta E^D=-2\bar{E}_o^D\ r(\ln(2r/R_o)) \quad \text{----------(B-3)}$$

According to Hirth and Lothe(1968), $\bar{E}_o^D$ can be approximated by the misfit energy in the dislocation core, so

$$\Delta E_0^D \sim \mu b^2/(4\pi(1-\nu)) \quad \text{----------(B-4)}$$

for edge dislocation, and

$$\Delta\bar{E}_o^D \sim (\mu b^2)/(4\pi) \quad \text{----------(B-5)}$$

for screw dislocation. $R_o \sim b/4$ for non-metals(Hirth and Lothe, 1968). For Mg-rich olivine $b \sim 5A$ and both edge and screw

Fig. (B-1)

Simplified geometry for the nucleation of a spherical spinel nucleus on the dislocation of olivine.

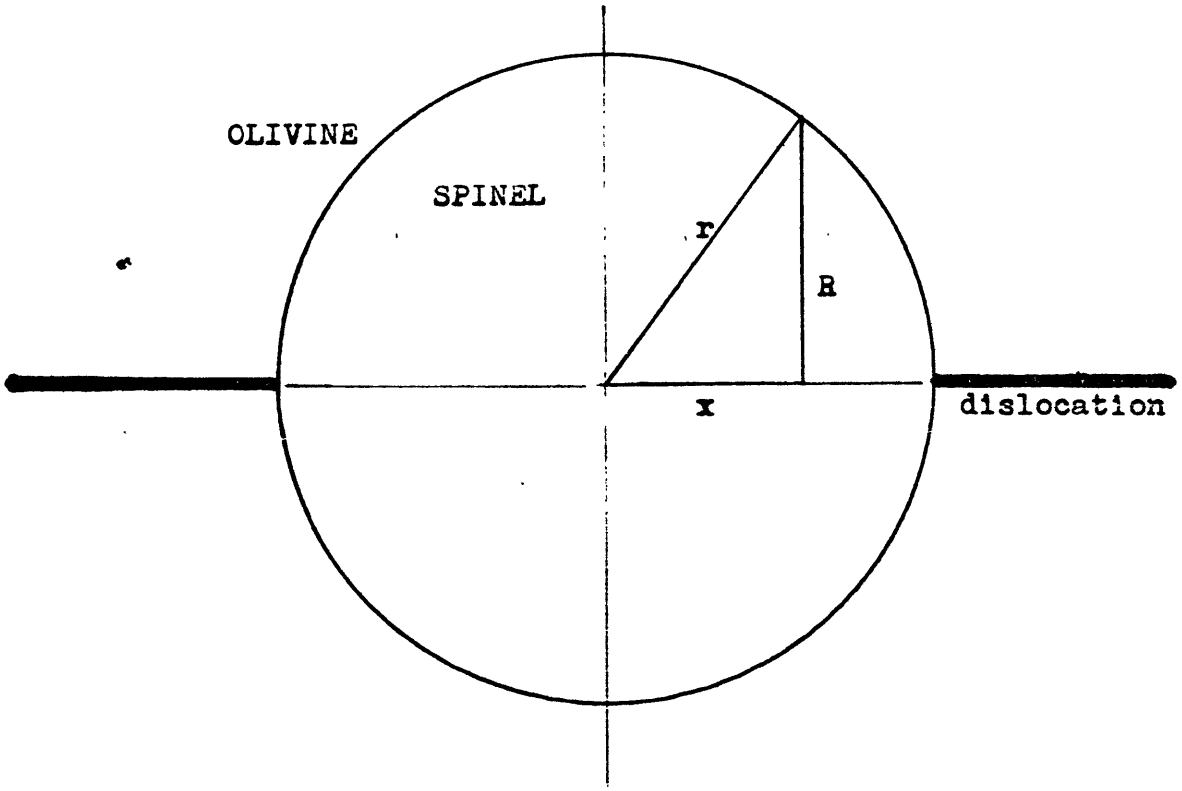
OLIVINE
SPINEL
r
R
x
dislocation

dislocations are approximately equally abundant(Goetze, personal communications), so with reasonable values of μ and ν(Table 5-1), one obtains

$$\Delta E^{D}(\text{erg}) \sim -4.6\times10^{4}\ r\ \ln(1.6\times10^{8} r) \qquad \text{(B-6)}$$

where r is in unit cm.

APPENDIX C

PRESSURE CALIBRATION AND CORRECTION

Pressure of the sample was monitored by an NaCl internal standard using the same technique as described by Ming(1974). No correction was made to compensate for the effect of pressure concentration. Sample and NaCl powders were intimately mixed and subjected to high pressure. A thin flake of NaCl powder was placed in contact with the outside surface of the upper diamond anvil, facing the film. It was used to monitor the deviation of the sample from the center of the film circle. Geometrical relationships among the film(AB), external NaCl flake(N), sample and NaCl mixture(S), and the center of the film circle(O) are shown in Fig. (C-1), in which the deviations of N from O towards the film(Fig. C-1A) and away from the film(Fig. C-1B) are differentiated. The latter represents a large deviation between S and O, and was not encountered in our measurement.

Let s=BC=measured distance on the film for a particular diffraction of the external NaCl flake at N

s'=AB=measured distance on the film for the same diffraction of NaCl under high pressure at S

2θ=diffraction angle of NaCl flake at N

2θ=diffraction angle of NaCl under high pressure at S

d=NS=thickness of the upper diamond

x=NO=deviation of NaCl flake from the center of the film circle

Fig. (C-1)

Geometry for the X-ray diffraction under high pressure (not to scale). AB, part of the film; N, external NaCl flake; S, sample and NaCl mixture; 0, center of the film circle; 2θ, diffraction angle of external NaCl flake; $2\theta'$, diffraction angle of NaCl under high pressure.

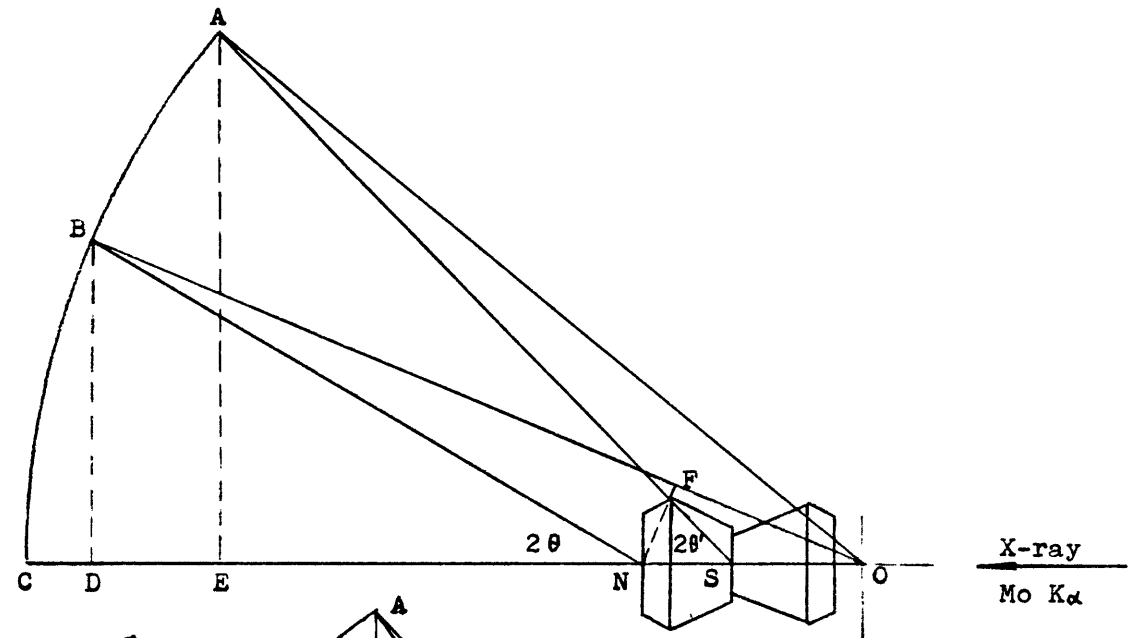

(A)

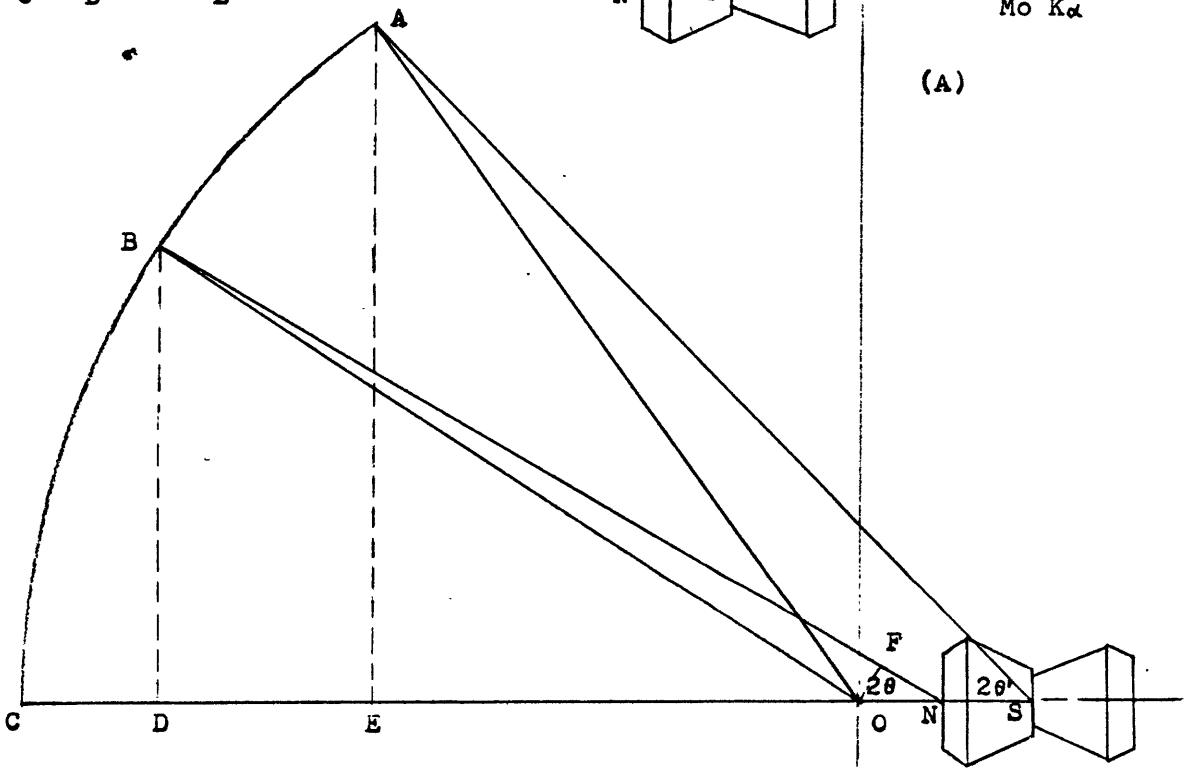

(B)

R=OA=OB=OC=radius of the film circle

If the deviation of SO was entirely due to the eccentricity of the sample, then the following correction for 2θ' applied:

Case A(Fig. C-1A), CN<R, 2θ>(s/R)

$BD=BN\sin 2\theta$

$NF=BN\sin(2\theta-(s/R))$

$\Delta BDO \sim \Delta NFO$

$x=(NF)R/(BD)=(\sin(2\theta-(s/R)))R/(\sin 2\theta)$ --------(C-1)

$AE=R\sin(s'/R)$

$ES=R\cos(s'/R)-x+d$

$2\theta'=\tan^{-1}((AE)/(ES))=\tan^{-1}((R\sin(s'/R))/(R\cos(s'/R)-x+d))$

---------- (C-2)

Case B(Fig. C-1B), CN>R, 2θ<(s/R)

$BD=R\sin(s/R)$

$OF=R\sin(s/R-2\theta)$

$BN=R\cos(s/R-2\theta)+OF\cot 2\theta$

$\Delta BDN \sim \Delta OFN$

$x=(OF)(BN)/(BD)=\sin(s/R-2\theta)R(\cos(s/R-2\theta)+\sin(s/R-2\theta)\cot 2\theta)$

$/\sin(s/R)$ ---------- (C-3)

$AE=R\sin(s'/R)$

$ES=R\cos(s'/R)+x+d$

$2\theta'=\tan^{-1}(AE)/(ES)=\tan^{-1}(R\sin(s'/R)/(R\cos(s'/R)+x+d))$

---------- (C-4)

2θ' for a given diffraction(usually (200) or (220)) was then calculated from measured s, s' and d(Eqs. C-1 to C-4). d-spacing and thus fractional volume reduction, ΔV/V, for NaCl under high pressure were then calculated. ΔV/V as a function

of pressure and temperature for NaCl has been tabulated by Decker(1971), from which the pressure was obtained.

The above correction for pressure assumed the deviation between SO was entirely due to the eccentricity of the sample. The film shrinkage might also result in apparent deviation of SO. If there was no eccentricity of the sample and the film shrinkage was the sole cause of the deviation of SO, then the following correction applied: For case A

$$2\theta'=s'/(R-x+d) \qquad \text{(C-5)}$$

and, for case B

$$2\theta'=s''/(R+x+d) \qquad \text{(C-6)}$$

The difference between calculated pressures based on Eqs. (C-2) or (C-4), and (C-5) or (C-6) was well within the uncertainty(±5 Kb) for the pressure calibration adopted in this thesis.

APPENDIX D

RELEVANT PUBLICATIONS

(1) Kinetics of high pressure phase transformations in the mantle: possible significance on deep earthquake generation

(2) Kinetics of high pressure phase transformations: implications to the evolution of the olivine-spinel transition in the downgoing lithosphere and its consequences on the dynamics of the mantle

(3) Kinetics of the olivine-spinel transition: implication to deep earthquake genesis

(4) New modifications of the diamond anvil press: a versatile apparatus for research at high pressure and high temperature

REFERENCES

Abu-Eid, R.M., 1974, Electronic absorption spectra and phase transformations of minerals at pressures up to 200 Kb, unpublished Ph. D thesis, M.I.T.

Ahrens, T.J., 1972, The mineralogic distribution of iron in the upper mantle, Phys. Earth Planet. Inter., 5, 267-281.

Ahrens, T.J., and Schubert, G., 1975a, Gabbro-eclogite traction rate and its geophysical signigicance, Rev. Geophys. Space Phys., 13, 383-400.

Ahrens, T.J., and Schubert, G., 1975b, Rapid formation of eclogite in a slightly wet mantle, Earth Planet. Sci. Lett., 27, 90-94.

Ahrens, T.J., and Syono, Y., 1967, Calculated mineral reactions in the earth's mantle, J. Geophys. Res., 72, 4181-4188.

Akimoto, S., 1972, The system MgO-FeO-SiO_2 at high pressures and temperatures-phase equilibria and elastic preperties, Tectonophysics, 13, 161-187.

Akimoto, S., and Fujisawa, H., 1965, Demonstration of the electrical conductivity jump produced by the olivine-spinel transition, J. Geophys. Res., 70, 443-449.

Akimoto, S., and Fujisawa, H., 1966, Olivine-spinel transition in the system Mg_2SiO_4-Fe_2SiO_4 at 800°C, Earth Planet. Sci. Lett., 1, 237-240.

Akimoto, S., and Fujisawa, H., 1968, Olivine-spinel solid solution equilibria in the system Mg_2SiO_4-Fe_2SiO_4, J. Geophys. Res., 73, 1467-1479.

Akimoto, S., and Ida, Y., 1966, High pressure synthesis of Mg_2SiO_4 spinel, Earth Planet. Sci. Lett., 1, 358-359.

Akimoto, S., Komoda, E., and Kushire, I., 1967, Effect of pressure on the melting of olivine and spinel polymorph of Fe_2Si0_4, J. Geophys. Res, 72, 679-686.

Akimoto, S., Fujisawa, H., and Katsura, T., 1965, The olivine-spinel transition in Fe_2Si0_4 and Ni_2Si0_4, J. Geophys. res. , 70, 1969-1977.

Akimoto, S., Akaogi, M., Kawada, K., and Nishizawa, 0., 1976, Mineralogic distribution of iron in the upper half of the transition zone in the earth's mantle, in press.

Anderson, D.L., 1967, Phase changes in the upper mantle, Science, 157, 1165-1173.

Anderson, O.1., and Andreatch, P.J., 1966, J. Am. Ceram. Soc., 49, 404-409.

Anderson, O.L., Schreiber, E., Liebermann, R.C., and Soga, N., 1968, Some elastic constant data on minerals relevant to geophysics, Rev. Geophys., 6, 491-524.

Archambeau, C.B., Flinn, E.A., and Lambert, D.G., 1969, Fine structure of the upper mantle, J. Geophys. Res., 74, 5825-5866.

Azaroff, L.V., 1961, Role of crystal structure in diffusion. I. Diffusion paths in closest-packed crystals, J. Appl. Phys., 32, 1658-1662.

Azaroff, L.V., 1961, Role of crystal structure in diffusion. II. Activation energies for diffusion in closest-packed structures, J. Appl. Phys., 32, 1663-1665.

Barnett, J.D., Block, S., and Piermarini, G.J., 1973, An optical fluorescence system for quantitative pressure measurement in the diamond-anvil cell, Rev. Sci. Instrum., 44, 1-9.

Bassett, W.A., and Takahashi, T., 1965, Silver iodide polymorphs, Am. Mineral., 50, 1576-1594.

Bassett, W.A., Takahashi, T., and Stook, P.w., 1967, X-ray diffraction and optical observations on crystalline solids up to 300 Kb, Rev. Sci. Instrum., 38, 37-42.

Baur, W.H., 1971, Geometric refinement of the crystal structure of β-Mg_2SiO_4, Nature, Phys. Sci., 233, 135-137.

Baur, W.H., 1972, Computer-simulated crystal structures of observed and hypothetical Mg_2SiO_4 polymorphs of low and high density, Am. Mineral., 57, 709-731.

Benioff, H., 1963, Source wave forms of three earthquakes, Bull. Seism. Soc. Amer., 53, 893-903.

Bernal, J.D., 1936, Discussion, Observatory, 59, 268.

Birch, F., 1939, The variation of seismic velicities within a simplified earth model in accordance with the theory of finite strain, Bull. Seism. Soc. Am., 29, 463-479.

Birch, F, 1947, Finite elastic strain of cubic crystals, Phys. Rev., 71, 809-824.

Birch, F., 1952, Elasticity and constitution of the earth's interior, J. Geophys. Res., 57, 227-286.

Birle, J.D., Gibbs, G.V., Moore, P.B., and Smith, J.V.,1968, Crystal structures of natural olicines, Am. Mineral., 53, 807-824.

Bowen, N.L., and Anderson, O., 1914, The binary system MgO-SiO_2, Amer. J. Sci., 37, 487-500.

Boyd, F.R., and England, J.L., 1960, The fayalite-Fe_2SiO_4 spinel transition, Yr. Book, Carnegie Inst. Wash., 48-49.

Brace, W.F., and Walsh, J.B., 1962, Some direct measurements of the surface energy of quartz and orthoclase, Am. Mineral., 47, 1111-1122.

Bradley, R.S., Grace, J.D., and Munro, D.C., 1963, The electrical conductivity of some organic and inorganic solids under pressure, 2, ferrous orthosilicate and spinel Fe_2SiO_4, in Physics and Chemistry of High Pressure, Society of Chemical Industry, London, 143-149.

Bridgman, P.W., 1945, Polymorphic transitions and geological phenomena, Amer. J. Sci., 243A, 90-97.

Buening, D.K., and Buseck, P.R., 1973, Fe-Mg lattice diffusion in olivine, J. Geophys. Res., 78, 6852-6862.

Buerger, M.J., 1934, Physica, 1, 561

Buerger, M.J., 1951, Crystallographic aspects of phase transformation, in Phase Transformations in Solids, Smoluchowski, et al, eds., John Wiley, New York, 183-209.

Bundy, F.P., 1961, Effect of pressure on emf of thermocouples, J. Appl. Phys., 32, 483-488.

Burns, R.G., 1970a, Crystal field spectra and evidence of cation ordering in olicine minerals, Am. Mineral., 55, 1608-1632.

Burns, R.G., 1970b, Mineralogical Application of Crystal Field theory, Cambridge University Press, England.

Burns, R.G., 1974, The polarized spectra of iron in silicates olivine. A discussion of neglected contributions from Fe^{2+} ions in M(1) sites, Am. Mineral., 59, 625-629.

Burns, R.G., and Sung, C.-M., 1975, Abstr., Kinetics of the olivine→spinel transition in downgoing lithosphere: Implications to deep earthquake genesis, EOS, Trans. Amer. Geophys. Union, 56, 453-454.

Cahn, J.W., 1956, The kinetics of grain boundary nucleated reactions, Acta Met., 4, 449-459.

Cahn, J.W., 1957, Nucleation on dislocations, Acta Met., 5, , 169-172.

Carter, N.L., and Ave' Lallemant, H.G., 1970, High temperature flow of dunite and peridotite, Geol. Soc. Amer. Bull., 81, 2181-2202.

Christian, J.W., 1965, The Theory of Phase Transformations in Metals and Alloys, Pergamon Press, Oxford, London.

Chung, D.H., 1971, Elasticity and equations of state of olivines in the Mg_2SiO_4-Fe_2SiO_4 system, Geophys. J. R. Astr. Soc., 25, 511-538.

Chung, D.H., 1973, On the equations of state of high-pressure solid phases, Earth Planet. Sci. Lett., 18, 125-132.

Calark, Jr., S.P., 1966, Handbook of Physical Constants, Geol. Soc. Am. Mem. 97.

Corll, J.A., 1967, Experimental verification of pressure enhancement by encapsulation, J. Appl. Phys., 38, 2708.

Corll, J.A., and Warren, W.E., 1965, Theoretical approach to enhanced pressure apparatus design, J. Appl. Phys., 36, 3655-3659.

Dachille, F. and Roy, R., 1960, High pressure studies of the system Mg_2SiO_4-Fe_2SiO_4 with special reference to the olivine-spinel transition, Am. J. Sci., 258, 225-246.

Dechille, F., and Roy, R., 1961, Influence of displacive-shearing stresses on the kinetics of reconstructive transformations effected by pressure in the range 1-100,000 bars, in Reactivity of Solids, Boer, J.H., ed., Elsevier Publ. Co., 502-511.

Davis, B.L., and Adams, L.H., 1965, Kinetics of the calcite-aragonite transformation, J. Geophys. Res., 70, 433-441.

Davis, B.T.H., and England, J.L., 1964, The melting of forsterite up to 50 Kb, J. Geophys. Res., 69, 1113-1116.

Decker, D.L., Bassett, W.A., Merrill, L., Hall, H.T., and Barnett, J.D., 1972, High pressure calibration: A critical review, J. Phys. Chem. Ref. Data, 1, 773-835.

Dempsey, M.J., and Strens, R.G.J., 1976, Modelling crystal structures, in press.

Dennis, J.G., and Walker, C.T., 1965, Earthquakes resulting from metastable phase transitions, Tectonophysics, 2, 401-407.

Dziewonski, A.M., and Gilbert, F., 1974, Temporal variation of the seismic moment tensor and the evidence of precursive compression for two deep earthquakes, Nature, 247, 185-188.

Decker, D.L., 1971, High pressure equation of state for NaCl, KCl, and CsCl, J. Appl. Phys., 42, 3239-3244.

Engdahl, E.R., 1973, Relocation of intermedeate depth earthquakes in the central Aleutians by seismic ray tracing, Nature, 245, 23-25.

Eshelby, J.D., 1957, The determination of the elast field of an ellipsoidal inclusion, and related problems, Proc.

Roy. Soc. London, A241, 376-396.

Evison, F., 1963, Earthquakes and faults, Bull. Seism. Soc. Amer., 53, 873-891.

Evison, F., 1967, On the occurence of volume change at the earthquake source, Bull. Seism. Soc. Amer., 57, 9-25.

Fine, M.E., 1964, Introduction to Phase Transformations in Condensed Systems, MacMillan, New York.

Fisher, G.W., and Medaris, Jr., L.G., 1969, Cell dimensions and X-ray determinative curve for synthetic Mg-Fe olivines, Am. Miner., 54, 741-753.

Forman, R.A., Piermarini, G.J., Barnett, J.D., and Block, S., 1972, Science, 176, 284-285.

Forsyth, D.W., and Uyeda, S., 1976, On the relative importance of driving forces of plate motion, Geophys. J. Roy. Astro. Soc., in press.

Gilbert, F., and Dziewonski, A.M., 1975, An application of normal mode theory to the retrieval of structural parameters and source mechanisms from seismic spectra, Phil. Trans. Roy. Soc. London, A278, 187-269.

Gilman, J.J., 1960, Direct measurement of the surface energies of crystal, J. Appl. Phys., 31, 2208-2218.

Goetze, C., 1975, Sheared lherzolites: from the point of view of rock mechanics, Geology,3, 172-173.

Goetze, C., and Brace, W.F., 1972, Laboratory observations of high-temperature rheology, Tectonophysics, 13, 583-600.

Goetze, C., and Kohlstedt, D.L., 1973, Laboratory study of dislocation climb and diffusion in olivine, J. Geophys. Res., 78, 5961-5971.

Goldschmidt, V.M., 1931, Zur Kristallchemie des Germaniums, Nachr. Akad. Wiss. Göttingen Math. Physik. Kl. 1, No.2, 184-190.

Gomez-Ramirez, R., and Pound, G.M., 1973, Nucleation of a second solid phase along dislocations, Metal. Transac., 4, 1563-1569.

Graham, E.K., and Barsch, G.R., 1969, Elastic constants of single-crystal forsterite as a function of temperature and pressure, J. Geophys. Res. 74, 5949-5960.

Griggs, D.T., 1972, The sinking lithosphere and the focal mechanism of deep earthquakes, in The Nature of The Solid Earth, Robertson, E.C., ed., McGraw-Hill, N.Y., 361-384.

Griggs, D.T., and Baker, D.W., 1969, The origin of deep focus earthquakes, in Properties of Matter under Unusual Conditions, Mark, H., and Fernbach, S., eds., Wiley, N.Y., 23-41.

Hazen, R.M., 1975, Effect of temperature and pressure on the crystal physics of olivine, Ph. D. Thesis, Harvard University.

Helmberger, D., and Wiggins, R.A., 1971, Upper mantle structure of Mid-western United States, J. Geophys. Res., 76, 3229-3245.

Heur, A.H., and Nord, Jr., G.L., 1976, Polymorphic phase transitions in minerals, in press.

Hirth, J.P., and Lothe, J., 1968, Theory of Dislocations, McGraw-Hill, New York.

Horton, M.D., 1974, Temperature correlation at high pressures, High Temp-High Pres., 6, 537-539.

Huggins, F.E., 1974, Mössbauer studies of iron minerals under pressures of up to 200 kilobars, unpublished Ph. D. thesis, M.I.T..

Huggins, F.E., Mao, H.-K., and Virgo, D., 1975, Mössbauer studies at high pressure using the diamond anvil cell, Yr. Book, Carnegie Inst. Wash., 405-410.

Isacks, B., and Molnar, P., 1971, Distribution of stresses in the descending lithosphere from a global survey of focal mechanism solutions of mantle earthquakes, Rev. Geophys. Space Phys., 9, 103-174.

Isacks, B., Oliver, J., and Sykes, L., 1968, Seismology and the new global tectonics, J. Geophys. Res., 73, 5855-5899.

Ito, K., Endo, S., and Kawai, N., 1971, Olivine-spinel transformation in a natural forsterite, Phys. Earth Planet. Inter., 4, 425-428.

Ito, E., Matsui, Y., Suito, K., and Kawai, N., 1974, Synthesis of γ-Mg_2SiO_4, Phys. Earth Planet. Inter., 8, 342-344.

Jackson, I.N.S., Liebermann, R.C., and Ringwood, A.E., 1974, Disproportionation of spinels to mexed oxides: significance of cation concentration and implications for the mantle, Earth Planet. Sci. Lett., 24, 203-208.

Jacobs, J.A., 1956, The earth's interior,in Handbuch der Physik, Geophysik I, Flügge, S., ed., Springer-Verlag, Berlin, 47, 364-406.

Jamieson, J.C., and Olinger, B., 1971, Pressure inhomogeneity; a possible source of error in using internal standards for pressure gages, in Proceed. of the Sym. on the Accurate Characterization of the High-Pressure Environment, Lloyd, E.C., ed., Nat. Bur. Stand., spec. pub., 326, 321-323.

Jamieson, J.C., Lawson, A.W., and Nachtrib, N.D., 1959, Rev. Sci. Instrum., 30, 1016.

Jeffereys, H., 1937, On the materials and density of the earth's crust, Monthly Notices Roy., Astron. Soc. Geophys. Suppl., 4, 50-61.

Johnson, L., 1967, Array measurements of P velocities in the upper mantle, J. Geophys. Res., 72, 6309-6325.

Johnson, W.A., and Mehl, R.F., 1939, Trans. Amer. Inst. Min. Met. Eng., 135, 416-442.

Kamb, B., 1968, Structural basis of the olivine-spinel stability relation, Am. Mineral., 53, 1439-1455.

Kanamori, H., 1967, Upper mantle structure from apparent velicities of P-waves recorded at Wakayama micro-earthquake observatory, Bull. Earthq. Res. Inst. Tokyo University, 45, 657-678.

Kasahara, J., and Tsukahara, H., 1971, Experimental measurements of reaction rate at the phase of nickel olivine to nickel spinel, J. Phys. Earth, 19, 79-88.

Kasahara, J., Ohno, I., and Iida, K., 1971, Generation of elastic shocks accompanied with a phase change on NH_4F, J. Phys. Earth, 19, 47-58.

Kawai, N., Endo, S., and Ito, K., 1970, Split sphere high pressure vessel and phase equilibrium relation in the system Mg_2SiO_4-Fe_2SiO_4. Phys. Earth Planet. Inter.,3, 182-185.

Kinsland, G.L., 1974, Yield strength under confining pressures to 300 Kb in the diamond anvil cell, Ph. D. thesis, University of Rochester.

Kirby, S.H., and Raleigh, C.B., 1973, Mechanisms of high-temperature, solid-state flow in minerals and ceramics and their bearing on the creep behavior of the mantle, Tectonophysics, 19, 165-194.

Knopoff, L., and Randall, M.J., 1970, The compensated linear-vector dipole, a possible mechanism for deep earthquakes, J. Geophys. Res., 75, 4957-4963.

Kogan, M.G., 1975, Gravity field of the Kuril-Kamchatka Arc and its relation to the thermal regime of the lothosphere, J. Geophys. Res., 80, 1381-1390.

Kohlstedt, D.L., and Goetze, C., 1974, Low-stress high-temperature creep in olivine single crystals, J. Geophys. Res., 79, 2045-2051.

Kohlstedt, D.L., Goetze, C., and Durham, W.B., 1976, Experimental defoemation of single crystal olivine with application to flow in the mantle, in Petrophysics: The Physics and Chemistry of Minerals and Rocks, Runcorn, S.K., ed., John Wiley and Sons, Ltd., London, in press.

Kumazawa, M., and Anderson, O.L., 1969, Elastic moduli, pressure derivatives, and temperature derivatives of single crystal olivine and single crystal forsterite, J. Geophys. Res., 74, 5961-5972.

Kumazawa, M., Sawamoto, J., Ohtani, E., and Masaki, K., 1974, Post-spinel phases of forsterite and evolution of the earth's mantle, Nature, 247, 356-358.

Lippincott, E.R., and Duecker, H.C., 1964, Pressure distribution measurements in fixed-anvil high pressure cells, Science, 144, 1119-1121.

Lippincott, E.R., Weir, C.E., van Valkenburg, A., and Bunting, E.N., 1960, Spectrochem. Acta, 16, 59.

Mao, H.K., and Bell, P.M., 1972a, Optical and Electrical behavior of olivine and spinel(Fe_2SiO_4) at high pressure, Yr. Book, Carnegie Inst. Wash., 520-524.

Mao, H.K., and Bell, P.M., 1972b, Crystal-field stabilization of the olivine-spinel transition, Yr. Book, Carnegie Inst. Wash., 527-528.

Mao, H.K., Takahashi, T., Bassett, W.A., Weaver, J.S., and Akimoto, S., 1969, Effect of pressure and temperature on the molar volumes of wüstite and of three $(Fe,Mg)_2SiO_4$ spinel solid solutions, J. Geophys. Res., 74, 1061-1069.

Massalski, T.B., 1970, Massive transformations, in Phase Transformations, Aaronson, H.I., ed., 443-486.

McKenzie, D.P., 1970, Temperature and potential temperature beneath island arcs, Tectonophysics, 10, 357-366.

Mendiguren, J.A., 1972, Speculations on phase changes in the earth's interior, unpublished manuscript.

Minear, J.W., and Toksöz, M.N., 1970a, Thermal regime of a downgoing slab and new global tectonics, J. Geophys. Res., 75, 1397-1419.

Minear, J.W., and Toksöz, M.N., 1970b, Thermal regime of a downgoing slab, Tectonophysics, 10, 367-390.

Ming, L.C., 1974, High pressure phases in the system of FeO-MgO-SiO_2 and their geophysical implications, Ph. D thesis, University of Rochester.

Ming, L.C., and Bassett, W.A., 1974, Laser heating in the diamond anvil press up to 2000°C sustained and 3000°C pulsed at pressures up to 260 kilobars, Rev. Sci. Instrum., 45, 1115-1118.

Ming, L.C., and Bassett, W.A., 1975, The post-spinel phases in the Mg_2SiO_4-Fe_2SiO_4 system, Science, 187, 66-68.

Misener, D.J., 1975, Cation diffusion in olivine to 1400°C and 35 Kbars, in Geochemical Transport and Kinetics, Hofmann, A.W. et al, ed., 117-128.

Mizukami, S., Ohtani, A., and Kawai, N., 1975, High-pressure X-ray diffraction studies on β-and γ-Mg_2SiO_4, Phys. Earth Planet. Inter., 8, 177-182.

Mizutami, H., Hamano, Y., Ida, Y., and Akimoto, S., 1970, Compressional vave velicities in fayalite, Fe_2SiO_4-spinel and coesite, J. Geophys. Res., 75, 2741-2747.

Moor, P.B., and Smith, J.V., 1969, High pressure modification of Mg_2SiO_4: crystal structure and crystallochemical and geophysical implications, Nature, 221, 653-655.

Moor, P.B., and Smith, J.V., 1970, Crystal structure of β-Mg_2SiO_4: crystal-chemical and geophysical implications, Phys. Earth Planet. Inter., 3, 166-177.

Morimoto, N., Tokonami, M., Watanabe, M., and Koto, K., 1974, Crystal structures of three polymorphs of Co_2SiO_4, Am. Mineral., 59, 475-485.

Myers, M.B., Dechille, F., and Roy, R., 1963, Pressure multiplication effect in opposed-anvil configurations, Rev. Sci. Instrum., 34, 401-402.

Navrotsky, A., 1971, Thermodynamics of formation of the silicates and germanates of some divalent transition metals and of magnesium, J. Inorg. Nucl. Chem., 33, 4035-4050.

Navrotsky, A., 1973, Enthalpy of the olivine-spinel transition in magnesium orthogermanate and the thermodynamics of olivine-spinel-phenacite stability relations,393-398.

Nelson, Jr., D.A., and Ruoff, A.L., 1976a, Non-linear theory of plastic flow and stress concentrations around rigid spherical inclusions, in press.

Nelson,Jr., D.A., and Ruoff, A.L., 1976b, Stress anisotropy and concentration effects in high pressure measurements, in press.

Nishizawa, O., and Akimoto, S., 1973, Partition of magnesium and iron between olivine and spinel, and between pyroxene and spinel, Contr. Mineral. Petrol., 41, 217-230.

Obata, M., Banno, S., and Mori, T., 1974, The iron-magnesium partitioning between naturally occuring coexisting olivine and Xa-rich clinopyroxene: an application of the simple mixture model to olivine solid solution, Bull. Soc. fr. Mineral. Cristallogr., 97, 101-107.

O'Hara, M.J., 1970, Upper mantle composition inferred from laboratory experiments and observation of volcanic products, Phys. Earth Planet. Inter., 3, 236-245.

Oxburgh, E.R., and Turcotte, D.L., Thermal structure of island arcs, 1970, Geol. Soc. Am. Bull., 81, 1665-1688.

Piermarini, G.J., and Weir, C.E., 1962, Adiamond cell for X-ray diffraction studies at high pressures, J. Res. Nat. Bur. Stand., 66A, 325-331.

Piermarini, G.J., Block, S., and Barnett, J.D., 1973, Hydrostatic limits in liquids and solids to 100 Kbar, J. Appl. Phys., 44, 5377-5382.

Post, R.L., and Griggs, D.T., 1973, The earth's mantle: evidence on non-Newtonian flow, Science, 181, 1242-1244.

Randall, M.J., 1964a, On the mechanisms of earthquakes, Bull. Seism. Soc. Amer., 54, 1283-1289.

Randall, M.J., 1964b, Seismic energy generated by a sudden volume change, Bull. Seism. Soc. Amer., 54, 1291-1298.

Randall, M.J., and Knopoff, L., 1970, The mechanism at the focus of deep earthquakes, J. Geophys. Res., 75, 4965-4976.

Reid, H.F., 1910, The mechanism of earthquakes, the California earthquake of April 18, 1906, Report of the State Earthquake Commission, 2, Carnegie Inst. Wash..

Riecker, R.E., and Seifert, K.E., 1964a, Shear deformation of upper-mantle mineral analogs: Test to 50 kilovars at 27°C, J. Geophys. Res., 69, 3901-3911.

Riecker, R.E., and Seifert, K.E., 1964b, Olivine shear strength at high pressures and room temperature, Bull. Geol. Soc. Am., 75, 571-573.

Ringwood, A.E., 1958, The constitution of the mantle II: further data on the olivine-spinel transition, Geochim. Cosmochim. Acta, 15, 18-29.

Ringwood, A.E., 1970, Phase transformations and the constitution of the mantle, Phys. Earth Planet. Inter., 3, 109-155.

Ringwood, A,E,, 1972, Phase transformations and mantle dynamics, Earth Planet. Sci. Lett., 14, 233-241.

Ringwood, A.E., 1973, Phase transformations and their bearing on the dynamics of the mantle, Fortschr. Miner., 50, 113-139.

Ringwood, A.E., and Major, A., 1966, Some high-pressure transformations: synthesis of Mg_2SiO_4-Fe_2SiO_4 solid solutions, Earth Planet. Sci. Lett., 1, 241-245.

Ringwood, A.E., and Major, A., 1970, The system Mg_2SiO_4-Fe_2SiO_4 at high pressures and temperatures, Phys. Earth Planet. Int., 3, 89-108.

Ritsema, A.R., 1970, The mechanism of mantle earthquakes in relation to phase transformation process, Phys. Earth Planet. Int., 3, 503-510.

Roy, R., 1973, A syncretist classification of phase transitions, in Phase Transitions, Herrisch, H.K., et al, eds., Pergamon Press, New York.

Runciman, W.A., Sengupta, D., and Gourley, T., 1973, The polarized spectra of iron in silicates, II. Olivine, Am. Mineral., 58, 451-456.

Runciman, W.A., Sengupta, D., and Gourley, T., 1974, The polarized spectra of iron in silicates, II. Olivine: a reply, Am. Mineral., 59, 630-631.

Ruoff, A.L., 1976, Stress anisotropy in opposed anvil high pressure cells, in press.

Russel, K.C., 1970, Nucleation in solids, in Phase Transformations, Aaronson, H.I., ed., 219-268.

Russel, K.C., 1976, Nucleation in solids, manuscript submitted.

Sammis, C.G., and Dein, J.L., 1974, On the possibility of transformational superplasticity in the earth's mantle, J. Geophys. Res., 79, 2961-2965.

Sato, Y., Akimoto, S., and Inoue, K., 1973, Pressure intensification in the composite material, High Temp.-High Pres., 5, 289-297.

Schreiber, E., and Anderson, O.L., 1967, Pressure derivatives of the sound velocities of polycrystalline forsterite with 6 per cent porocity, J. Geophys. Res., 72, 762-764, and correction p. 3751.

Schubert, G.D., Yuen, A., and Turcotte, L., 1976, Role of phase changes in a dynamic mantle, Geophys. J. Roy. Astr. Soc., in press.

Smith, A.T., and Toksöz, M.N., 1972, Stress distribution beneath island arcs, Geophys. J. Roy. Astr. Soc., 29, 298-318.

Smith, J.R., 1975, High temperature crystal chemistry of fayalite, Am. Mineral., 60, 1092-1097.

Smith, J.R., and Hazen, R.M., 1973, The crystal structures of forsterite and hortonolite at several temperatures up to 900°C, Am. Mineral., 58, 588-593.

Soga, N., and Anderson, O.L., 1967, High temperature elasticity and expansivity of forsterite and steatite, J. Am. Ceram. Soc., 50, 239-242.

Solomon, S.C., and Paw U, K.T., 1975, Elevation of the olivine-spinel transition in subducted lithosphere:seismic evidence, Phys. Earth Planet. Inter., 11, 97-108.

Solomon, S.C., Sleep, N.H., and Richardson, R.M., 1975, On the forces driving plate tectonics: Inferences from absolute plate velocities and intraplate stress, Geophys. J. Roy. Astr. Soc., 42, 769-801.

Stocker, R.L., and Ashby, M.F., 1973, On the rheology of the upper mantle, Rev. Geophys. Space Phys., 11, 391-426.

Suito, K., 1972, Phase transformations of pure Mg_2SiO_4 into a spinel structure under high pressure and temperatures, J. Physl Earth, 20, 225-243.

Sung, C.M., 1974, The kinetics of high pressure phase transformations in the mantle: possible significance on deep earthquake generation, Proc. Geol. Soc. China, 17, 67-84.

Sung, C.M., 1975, Abstr., Role of the olivine→spinel transition in p;ate dynamics, EOS, Trans. Am. Geophys. Union, 56, 454.

Sung, C.M., 1976, New modification of the diamond anvil press: a versatile apparatus for research at high pressure and high temperature, Rev. Sci. Instrum., in press.

Sung, C.M., and Burns, R.G., 1976a, Kinetics of high pressure phase transformations: Implications to the evolution of the olivine→spinel transition in the downgoing lithosphere and its consequences on the dynamics of the mantle, Tectonophysics, 31, 1-32.

Sung, C.M., and Burns, R.G., 1976b, Kinetics of the olivine→ spinel transition: Implications to deep earthquake genesis, Earth Planet. Sci. Lett., in press.

Sung, C.M., and Burns, R.G., 1976c, mechanism of the olivine→ spinel transition, EOS, Trans. Am. Geophys. Union, 57, 323.

Syono, Y., Tokonami, M., and Matsui, Y., 1971, Crystal field effect on the olivine-spinel transformation, Phys. Earth Planet. Inter., 4, 347-352.

Thompson, Jr., J.B., 1967, Thermodynamic properties of simple solutions, in Research in Geochemistry, V2, Abelson, P.H., ed., John Wiley & Sons, Inc., New York, 340-361.

Tokonami, M., Morimoto, N., Akimoto, S., Syono, Y., and Takeda, H., 1972, Stability relations between olivine, spinel and modified spinel, Earth Planet. Sce. Lett., 14, 65-69.

Toksöz, M.N., Harkrider, D., and Ben-Menaheem, A., 1965, Determination of source parameters by amplitude equalization of seismic waves, 2., J. Geophys. Res., 70, 907-929.

Toksöz, M.N., Minear, J.W., and Julian, B.R., 1971, Temperature field and geophysical effects of a downgoing slab, J. Geophys. Res., 76, 1113-1138.

Toksöz, M.N., Sleep, N.H., and Smith, A.T., 1973, Evolution of the downgoing lithosphere and the mechanism of deep focus earthquakes, Geophys. J. Roy. Astr. Soc., 35, 285-310.

Towle, L.C., and Riecker, R.E., 1966, J. Geophys. Res., 71, 2609-2617.

Tsukahara, H., 1974, Evaluation of effects of partial pressure of H_2O on power law creep for ultrabasic rocks, J. Phys. Earth, 343-358.

Turcotte, D.L., and Schubert, G., 1971, Structure of the olivine-spinel phase boundary in the descending lithosphere, J. Geophys. Res., 76, 7980-7987.

Turcotte, D.L., and Schubert, G., 1973, Frictional heating of the descending lithosphere, J. Geophys. Res., 78, 5876-5886.

Turnbull, D., and Fisher, C.J., 1949, J. Chem. Phys., 17, 71.

Van der Merwe, J.H., 1963a, J. Appl. Phys., 34, 117.

Van der Merwe, J.H., 1963b, J. Appl. Phys., 34, 123.

Weaver, J.S., Takahashi, T., and Bassett, W.A., 1971, Calculation of the P-V relation for sodium chlorite up to 300 Kb at 25°C, Nat. Bur. Stand., Spec. Pub., 326, 189-199.

Weir, C.E., Lippincott, E.R., van Valkenburg, A., and Bunting, E.N., 1959, Infrared studies in the 1-15 micron region to 30,000 atmospheres, J. Res. Nat. Bur. Stand., A63, 55-62.

Wentorf, R.H., 1959, Olivine-spinel transformation, Nature, 183, 1617.

Whatley, L.S., Lippincott, E.R., van Valkenburg, A., and Weir, C.E., 1964, Optical studies at high pressures, Science, 144, 968-976.

Whitcomb, J.H., and Anderson, D.L., 1970, Reflection of P'P' seismic waves from discontinuities in the mantle, J. Geophys. Res., 75, 5713-5728.

Wood, B.J., and Strens, R.G., 1972, Calculation of crystal field splittings in distorted coordination polyhedra: spectra and thermodynamic properties of minerals, Mineral. Mag., 38, 907-917.

Wyss, M., 1973, The thickness of deep seismic zone, Nature, 242, 255-256.

Yagi, T., Marumo, F., and Akimoto, S., 1974, Crystal structures of spinel polymorphs of Fe_2SiO_4 and Ni_2SiO_4, 59, 486-490.

VITAE

The author was born on June 21, 1947, in Fukien, China. He attended Taipei Institute of Technology from 1961 to 1966, with a major in metallurgical engineering. Upon graduation, he served as a reserve officer(ROTC) in the Chinese Armed Forces in 1967, and as a high school teacher in 1968. He also worked as a metallurgical engineer for Taiwan Alumium Corporation for a short period of time, before he attended National Taiwan University in late 1968. During his stay at N.T.U.(1968-1972), he received a scholarship from the Ministry of Economics for four years. He also worked as a mechanical design engineer for General Instrument of Taiwan during the same period of time. After receiving an B. S. degree in geology in 1972, he began his graduate studies at Massachusetts Institute of Technology, where he has been engaged in a series of active research projects (Deep Sea Drilling Project, Lunar Project, Manganese Nodule Project, Kinetics Project). He received full financial support (research assistantship) during his stay at M.I.T.. On completing this Ph. D. thesis, he will continue his research work at M.I.T. as a postdoctoral research associate.

The author married Hsu-Yin Wang in May, 1972, and they have a baby boy, David, six months old.

PUBLICATIONS OF CHIEN-MIN SUNG

Published papers:

1) 1974, with Thompson, G., Bryan, W.B., and Frey, F.A., Petrology and geochemistry of basalts and related rocks from Site 214, 215, 216, DSDP LEG 22, Indian Ocean, in Initial Reports of the Deep Sea Drilling Project, V22, von der Borch, C., et al, eds, U. S. Government Printing Office, Wash., 459-468.

2) 1974, with Frey, F.A., Geochemical results for basalts from Site 253 and 254, in Initial Reports of the Deep Sea Drilling Project, V26, U. S. Government Printing Office, Wash., 576-582.

3) 1974, Kinetics of high pressure phase transformations in the mantle: possible significance on deep earthquake generation, Proc. Geol. Soc. China, 17, 67-84.

4) 1974, with Abu-Eid, R.M., and Burns, R.G., Ti^{3+}/Ti^{4+} ratios in lunar pyroxenes: implications to depths of origin of mare basalt magma, Proc. Fifth Lunar Sci. Conf., Geochim. Cosmochim. Acta Suppl., 5, V1, 717-726.

5) 1976, with Burns, R.G., Kinetics of the olivine→spinel transition: Implications to deep earthquake genesis, Earth Planet. Sci. Lett., in press.

6) 1976, with Burns, R.G., Kinetics of high pressure phase transformations: implications to the evolution of the olivine→spinel transition in the downgoing lithosphere and its consequences on the dynamics of the mantle, Tectonophysics, 31, 1-32.

7) 1976, New Modification of the diamond anvil press: a versatile apparatus for research at high pressure and high temperature, Rev. Sci. Instrum., in press.

Published abstracts:

1) 1974, with Abu-Eid, R.M., and Burns, R.G., A search for trivalent titanium in Apollo 17 pyroxenes, Fifth Lunar Sci. Conf., Part II, Lunar Sci. Inst. Pub., 758-760.

2) 1975, with Burns, R.G., Abu-Eid, R.M., and Vaughan, D.J., Electronic absorption spectroscopy as a petrologic probe of lunar materials, Sixth Lunar Sce. Conf., Part II, Lunar Sci. Inst. Pub., 115-117.

3) 1975, with Burns, R.G., Kinetics of the olivine→spinel transition in downgoing lithospheres: implications to deep earthquake genesis, EOS, Trans. Amer. Geophys. Union, 56, 453-454.

4) 1975, Role of the olivine→spinel transition in plate dynamics, EOS, Trans. Amer. Geophys. Union, 56, 454.

5) 1975, with Burns, R.G., Burns, V.M., and Sung, W., Crystal chemistry, crystal structure and nomenclature of minerals in manganese nodules, Manganese Nodule Project(NSF/IDOE) meeting, Battelle-Seattle Research Center, Seatle, March.

6) 1975, with Burns, R.G., Schwartz, K., Sung, W., and Burns, V.M., Chemical stratigraphic mapping of manganese nodules by electron microprobe: evidence of late stage Ni and Cu enrichments in nodules from the NE Equatorial Pacific, Geol. Soc. Amer., 7, 1014-1015.

7) 1976, with Burns, R.G., Mechanism of the olivine→spinel transition, EOS, Trans. Am. Geophys. Union, 57, 323.

KINETICS OF THE OLIVINE→SPINEL TRANSITION: IMPLICATIONS TO DEEP FOCUS EARTHQUAKE GENESIS

by

Chien-Min Sung and Roger G. Burns

Department of Earth and Planetary Sciences
Massachusetts Institute of Technology
Cambridge, Massachusetts 02139

[Manuscript submitted to:
Earth and Planetary Science Letters]

Submitted February 13, 1976

Olivine, the dominant mineral in the upper mantle, is generally believed to undergo a series of pressure-induced phase changes in the earth's interior. Along geotherms under normal tectonic provinces, oceanic and continental, the transformation of Mg-rich olivine (α-phase) to the denser spinel structure (γ-phase) proceeds through the intermediate "modified spinel" or β-phase (Fig. 1a). This series of phase changes has been correlated with seismic discontinuities in the transition zone separating the upper mantle from the lower mantle [1, 2,3]. However, the stability field of the β-phase greatly expands with temperature [4]. It may wedge out at lower temperatures so that within the cold interior of a downgoing plate along a subduction zone, olivine may transform directly into the spinel structure (Fig. 1b). This transition has been inferred [5,6] to be one of the major driving mechanisms in plate tectonics and to be a possible source of deep-focus earthquakes. We here assess this possibility and propose that the kinetics of the olivine→spinel transition governs the earthquake distribution throughout a subducted lithospheric plate.

The olivine→spinel transition taking place in the spinel stability field (Fig. 1b) in the downgoing slab is an isochemical, massive transformation. As such, it is an interface-controlled process and is best described by a model of nucleation and growth [7]. This model predicts an increasing degree (X) and rate (K) of transition with time (t) and temperature (T), respectively, according to the equation:

$$X = 1 - \exp(-Kt^n) \qquad (1)$$

in which the rate function K is dependent on pressure (P) and grain size (d) as well as temperature and shear stress; X is the volume fraction of transformed phase, and n is a constant depending on the

mechanism of nucleation. When the nucleation rate ($\bar{I}$) reaches a steady state, the kinetics equation for homogeneous (volume) nucleation becomes:

$$X = 1 - \exp[-(\pi/3)\bar{I}Y^3t^4] \tag{2}$$

where Y is the growth rate of spherical nucleii. Using the appropriate I's, this equation is also applicable to heterogeneous nucleation before site saturation [8], that is, before nucleation sites are exhausted on crystal imperfections (grain boundaries, edges, defects, etc.). After site saturation, the kinetics equation for nucleation on a surface becomes [8]

$$X = 1 - \exp(-2\bar{S}Yt) \tag{3}$$

where $\bar{S}$ is the surface area per unit volume. For nucleation on linear features (dislocations, grain edges), the kinetics equation after site saturation is [8]:

$$X = 1 - \exp(-\pi\bar{L}Y^2t^2) \tag{4}$$

where $\bar{L}$ is the length of the linear feature per unit volume. The steady-state nucleation rate may be approximated by:

$$\bar{I} = \bar{N}(k/h)T[\exp\{-(\Delta G_T^* + Q_a)/(kT)\}] \tag{5}$$

where $\bar{N}$ is the number of nucleation sites per unit volume, k is Boltzmann's constant, h is Planck's constant, ΔG_T^* is the activation energy of nucleation, and Q_a is the activation energy either of growth or for the migration of atoms across the interphase boundary. For homogeneous nucleation of a spherical nucleus,

$$\Delta G_T^* = (16\pi/3)\ \bar{\sigma}^3/(\bar{\varepsilon} + \bar{G}_v)^2 \tag{6}$$

where $\bar{\sigma}$ is the surface energy per unit volume, $\bar{\varepsilon}$ is the strain energy per unit volume, and $\Delta\bar{G}_v$ is the free energy change per unit volume.

The growth rate may be approximated by:

$$Y = \lambda(k/h)T[\exp(-Q_a/(kT))(1-\exp(\Delta\bar{G}_v/NkT)] \quad (7)$$

where λ is the thickness of the interphase boundary.

Since oxygen ions are considerably larger than the cations, the rate-determining step for the olivine→spinel transition will be the migration of oxygen atoms across the interphase boundary. To simplify the calculations, the olivine→spinel transition is assumed to proceed through the nucleation and growth of oxygen atoms. In addition, we have estimated the following values: $\bar{N} = 6.1\times10^{22}$ (oxygen atoms)cm^{-3}; $\bar{\sigma}$ = 200 erg cm^{-2} and 600 erg cm^{-2} for coherent and incoherent interphase boundaries, respectively; $\bar{\varepsilon} = 1.8\times10^{9}$ erg cm^{-3} and 6.0×10^{8} erg cm^{-3} for coherent and incoherent interphase boundaries, respectively; $\bar{S} = 6.7$ cm^{2} cm^{-3} for the grain size d=0.5 cm; $\lambda = 2.5\times10^{-8}$ cm; and $\Delta\bar{G}_v = 6.3\times10^{7}$ ΔP erg cm^{-3}, where ΔP is the overpressure or the pressure beyond equilibrium. We have assumed the phase boundary of the olivine→spinel transition in the mantle to be P(kb) = 72+0.033T(°K), which is consistent with an earlier estimate [9]. Thus, $\Delta\bar{G}_v = 4.5\times10^{9} - 6.3\times10^{7}P(kb) + 2.1\times10^{6}T$ (°K) erg cm^{-3}. The estimated values for the parameters above appear to be reasonable for conditions in the transition zone and have negligible P-T coefficients. The activation energy Q_a for the migration of oxygen atoms across the interphase boundary is not known, but probably has a magnitude comparable to that for grain boundary diffusion of oxygen atoms. The latter quantity is approximately half that of the activation energy for lattice diffusion. The activation energy of oxygen lattice diffusion in forsterite has been estimated [10] to be 135 kcal/mole or 9.4×10^{-12} erg/atom. Assuming the activation volume of oxygen lattice diffusion to be 15cm^3/mole, then $Q_a = 4.7\times10^{-12}$

$+ 1.3\times10^{-14}P(kb)$ erg/atom. This value is used later to evaluate the kinetic behavior of the olivine→spinel transition.

Three possible competing mechanisms of nucleation for the olivine→spinel transition in the mantle must be considered. They are homogeneous nucleation, nucleation on grain surfaces, and nucleation on dislocations. Nucleation on dislocations demonstrates the effect of shear stress on the kinetics of transition. A value of differential stress $\sigma_1-\sigma_3 = 0.5$ kb is assumed in the downgoing slab. This corresponds to a dislocation density of about $2\times10^{7}cm^{-2}$ [11]. Thus, $\bar{L} = 2\times10^{7}$ cm cm^{-3}. For both nucleation on grain surfaces and nucleation on dislocations, we have assumed that site saturation occurs at a small degree of transformation and that the major part of the transformation is due to the growth of existing nuclei on heterogeneities. Using equations (2)-(7) and the estimated values for the parameters listed above, the following expressions have been calculated for the olivine→spinel transition at constant P and T:

(A) Homogeneous nucleation with incoherent interphase boundaries,

$$K(sec^{-4}) = 2.0\times10^{41}T^{4}\exp[-\{(2.3\times10^{25})/(5.1\times10^{9} - 6.3\times10^{7}P + 2.1\times10^{6}T)^{2} + 1.4\times10^{5} + 3.6\times10^{2}P\}/T] \cdot [1-\exp((533 - 7.4P + 0.25T)/T)]^{3} \quad (8)$$

(B) Homogeneous nucleation with coherent interphase boundaries,

$$K(sec^{-4}) = 2.0\times10^{41}T^{4}\exp[-\{(9.6\times10^{23})/(6.3\times10^{9} - 6.3\times10^{7}P + 2.1\times10^{6}T)^{2} + 1.4\times10^{5} + 3.6\times10^{2}P\}/T] \cdot [1-\exp((533 - 7.4P + 0.25T)/T)]^{3} \quad (9)$$

(C) Nucleation on grain surfaces,

$$K(sec^{-1}) = 7.2\times10^{3}T\exp[-(3.4\times10^{4} + 89P)/T][1-\exp\{(533 - 7.4P + 0.25T)/T\}] \quad (10)$$

(D) Nucleation on dislocations,

$$K(sec^{-2}) = 1.8x10^{13}T^2 exp[(-6.8x10^4 + 1.8x10^2 P)/T][1-exp\{(533 - 7.4P + 0.25T)/T\}]^2 \quad (11)$$

In each of these equations, P and T are expressed in kb and °K, respectively.

Assuming a plunging speed of 10 cm/year for a downgoing slab with dip angle of 45°, this corresponds to a vertical descent speed of 7 cm/year and a rate of increasing pressure of approximately 8.5 $x10^{-13}$kb/sec. The geotherm in the cold interior of a downgoing slab cuts the olivine-spinel phase boundary at approximately 100 kb. For a given X and t in equation (1), in which n=4, 1, and 2, for homogeneous nucleation, nucleation on grain surfaces and nucleation on dislocations, respectively, there is a corresponding rate function K for each mechanism of nucleation. Substituting K and P = $100+8.5x10^{-13}$t into the corresponding equations (8) to (11), the isograd (constant X) as a function of P and T for each mechanism of nucleation may be calculated. The results are shown in Figure 2. We have ignored the presence of the β-phase in the high temperature region in Figure 2 because our main interest is the kinetics of the olivine→spinel transition in the low-temperature region. The most notable feature in Figure 2 is that the dominant mechanism for the olivine→spinel transition is heterogeneous nucleation. Homogeneous nucleation will be a competing mechanism only at low temperature and very high pressure. On the low temperature side of the isograd X=0.1, there is a negligible degree of olivine→spinel transition. Since the isograd X=0.1 for the fastest mechanism of nucleation does not extend below a temperature of about 600°C, it follows that the

olivine→spinel transition is suppressed below this temperature no matter how high the overpressure. Three possible geotherms for the cold interior of the downgoing slab are superimposed on Fig. 2. If geotherm X [12] is followed, the olivine→spinel transition will be suppressed even down to the lower mantle, where olivine may decompose directly into oxides. On the other hand, if geotherms Y [13] or Z [14] are followed, the olivine→spinel transition will proceed close to equilibrium. The shapes of the olivine-spinel phase boundary between X=0.1 and 0.9 across the downgoing slab for the three types of geotherm are shown schematically in Fig. 3. The phase boundary will be distorted downwards if geotherm X is followed (Fig. 3a). Because the low density olivine phase penetrates deeply into the high density spinel region, the slab will receive an upward buoyant force which counteracts the downward driving force for the downgoing slab. On the other hand, the phase boundary will be distorted upwards if geotherms Y or Z are followed (Fig. 3b, c). The rising of the dense spinel phase will contribute to the driving force for the downgoing slab.

Non-shallow earthquakes have been shown to be localized in cold interiors of downgoing slabs [15,16]. If the olivine-spinel phase boundary is distorted downwards, the downgoing slab will be under compression throughout its length. This would align the compression axes (P-axes) of non-shallow earthquakes parallel to the seismic zone (Figure 3a). On the other hand, if the olivine-spinel phase boundary is distorted upwards, the upper and lower parts of the slab will be under tension and compression, respectively. This will align the tension axes (T-axes) and the P-axes of non-shallow earthquakes

in the upper and lower parts of the downgoing slab, respectively (Figure 3b, c). Both types of earthquake distribution have been observed in downgoing slabs [17], suggesting that geotherms of the cold interiors of downgoing slabs may span the whole range between X and Z shown in Figure 2.

The possibility of generating deep focus earthquakes by a catastrophic olivine→spinel transition is discussed in detail elsewhere [18]. A necessary condition for this possibility is the deep penetration of olivine into the spinel field. This condition can be fulfilled if geotherm X if followed. There are two different mechanisms for generating deep focus earthquakes from implosion during the olivine→spinel transition. The sudden contraction of the transition may either elastically deform or induce shear failure in the surrounding rock and result in deep focus earthquakes. In the former mechanism, the radiation pattern of the earthquakes will show monopolar rarefaction. This type of radiation pattern has not in fact been observed. Almost all the focal solutions of deep earthquakes are consistant with a double couple or shear dislocation origin. This excludes uniform implosions as the cause of deep focus earthquakes. The mechanism of inducing shear failure in the surrounding rock to produce earthquakes could be consistent with the double couple model. However, this requires the T-axis of the earthquake to be directed towards the implosion region. This necessitates the T-axes for deep focus earthquakes to be aligned in the seismic zone, which is contradictory to observations [17]. Alternatively, a combination of the above two mechanisms may be operative. Thus, implosions may become increasingly anisotropic and eventually lead to shear failure of the rock. This could happen because both the rock and the transition are anisotropic. The radiation pattern for this mechanism would be a combination of a predominant double couple component with some isotro-

pic component. The main phase of the deep focus earthquake will be preceded by hypocentral volume change. At least two deep focus earthquakes consistent with this type of radiation pattern have been identified [19]. Thus, although the olivine→spinel transition may not be responsible for the majority of deep focus earthquakes, the possibility of its generating some deep focus earthquakes is not eliminated [20].

REFERENCES

1. D.L. Anderson, Phase changes in the upper mantle, Science 157 (1967) 1165.

2. A.E. Ringwood, Phase transformations and the constitution of the mantle, Phys. Earth Planet. Inter. 3 (1970) 109.

3. S. Akimoto, M. Akaogi, K. Kawada, O. Nishizawa, Mineralogic distribution of iron in the upper-half of the transition zone in the earth's mantle. In preparation.

4. S. Akimoto, The system MgO-FeO-SiO_2 at high pressures and temperatures - phase equilibria and elastic properties, Tectonophysics 13 (1972) 16.

5. D.L. Turcotte, G. Schubert, Structure of the olivine→spinel phase boundary in the descending lithosphere, J. Geophys. Res. 76 (1971) 7980.

6. A.E. Ringwood, Phase transformations and mantle dynamics, Earth Planet. Sci. Lett. 14 (1972) 233.

7. J.W. Christian, The Theory of Phase Transformations in Metals and Alloys, Pergamon Press, Oxford (1965).

8. J.W. Cahn, The kinetics of grain boundary nucleated reactions, Acta Met. 4 (1956) 449.

9. A.E. Ringwood, A. Major, The system Mg_2SiO_4-Fe_2SiO_4 at high pressures and temperatures, Phys. Earth Planet. Inter. 3 (1970) 89.

10. C. Goetze, D.L. Kohlstedt, Laboratory study of dislocation climb and diffusion in olivine, J. Geophys. Res. 78 (1973) 5961.

11. D.L. Kohlstedt, C. Goetze, W.B. Durham, Plastic flow in olivine at low stresses, In: Petrophysics: The Physics and Chemistry of Minerals and Rocks, R.G.J. Strens, ed., John Wiley and Sons Ltd., London, in press.

12. D.L. Turcotte, G. Schubert, Fractional heating of the descending lithosphere, J. Geophys. Res. 78 (1973) 5876.

13. D.T. Griggs, The sinking lithosphere and the focal mechanism of deep earthquakes, In: The Nature of the Solid Earth, E.C. Robertson, ed., McGraw-Hill, New York (1972) p. 361.

14. M.N. Toksöz, J.W. Minear, B.R. Julian, Temperature field and geophysical effects of a downgoing slab, J. Geophys. Res., 76 (1971) 1113.

15. E.R. Engdahl, Relocation of intermediate depth earthquakes in the central Alentians by seismic ray tracing, Nature 245 (1973) 23.

16. M.N. Toksöz, N.H. Sleep, A.T. Smith, Evolution of the downgoing lithosphere and the mechanism of deep focus earthquakes, J. Roy. Astr. Soc. 35 (1973) 285.

17. B. Isacks, P. Molnar, Distribution of stresses in the descending lithosphere from a global survey of focal mechanism solutions of mantle earthquakes, Rev. Geophys. Space Phys. 9 (1971) 103.

18. C-M. Sung, R.G. Burns, Kinetics of high pressure phase transformations: implications to the evolution of the olivine→spinel transition in the downgoing lithosphere and its consequences on the dynamics of the mantle, Tectonophysics, in press (1976).

19. F. Gilbert, A.M. Dziewonski, An application of normal mode theory to the retrieval of structural parameters and source mechanisms from seismic spectra, Phil. Trans. Roy. Soc. London A278 (1975) 187.

20. We thank R. Regan for typing the manuscript. Research supported by the National Science Foundation (Grant No. EAR 75-20138).

FIGURE CAPTIONS

Figure 1: Possible composition-depth phase diagram of the pseudo-binary system Mg_2SiO_4 - Fe_2SiO_4 in the mantle. (a) Under oceanic or continental plates, (b) in the cold interior of downgoing slabs. Dotted lines indicate the composition of olivine and its pressure derivatives in the mantle. Symbols: α=olivine, β=modified spinel, γ=spinel, W=magnesiowüstite, S=stishovite. The composition of magnesiowüstite is projected from the SiO_2 apex in the ternary system MgO-FeO-SiO_2.

Figure 2: Proposed kinetic diagram for the olivine→spinel transition in the mantle. The coarse line is the equilibrium phase boundary. Cross-hatched bands are the regions of degree of transition between 10% (X=0.1) and 90% (X=0.9) for different mechanisms of nucleation; A=homogeneous nucleation with incoherent interphase boundaries; B= homogeneous nucleation with coherent interphase boundaries; C= nucleation on grain surfaces; D=nucleation on dislocations. For each mechanism of nucleation, there is a negligible degree of transition (<10%) on the low temperature side of the cross-hatched bands. X[12], Y[13], and Z[14] are different geotherms calculated for the cold interiors of downgoing slabs.

Figure 3: Proposed profiles of phase boundaries between X=0.1 to X=0.9 across downgoing slabs. Profiles A, B, and C correspond to geotherms X, Y, and Z, respectively, in Figure 2. Horizontal and vertical ellipses correspond to earthquakes with compression and tension axes aligned with the plunging direction of the downgoing slab.

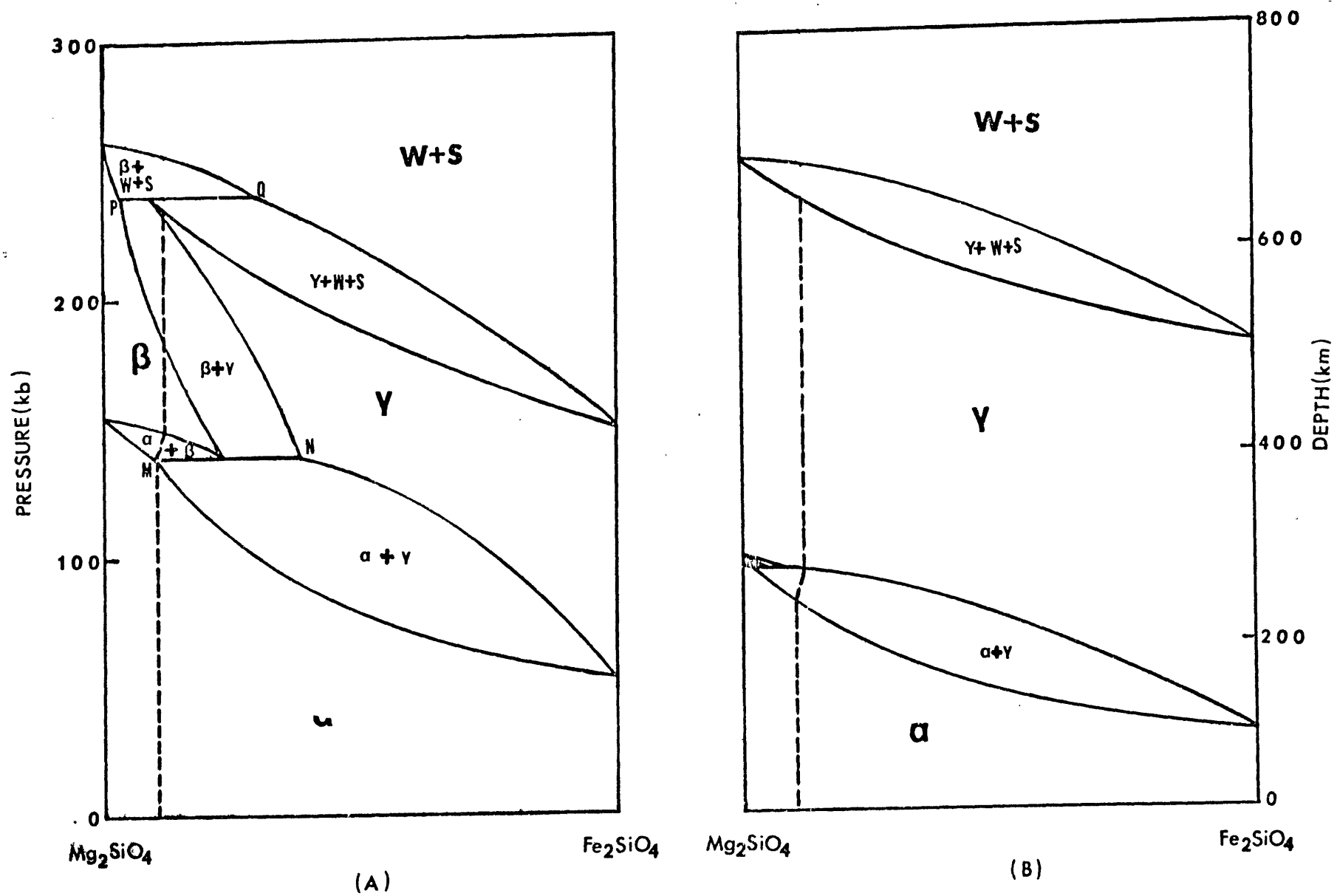
300
200
100
0
PRESSURE(kb)
W+S
β+
W+S
P
Q
Y+W+S
β
β+γ
γ
α
+ β
M
N
α + γ
α
Mg2SiO4
Fe2SiO4
(A)
800
600
400
200
0
DEPTH(km)
W+S
Y+ W+S
γ
α+γ
α
Mg2SiO4
Fe2SiO4
(B)

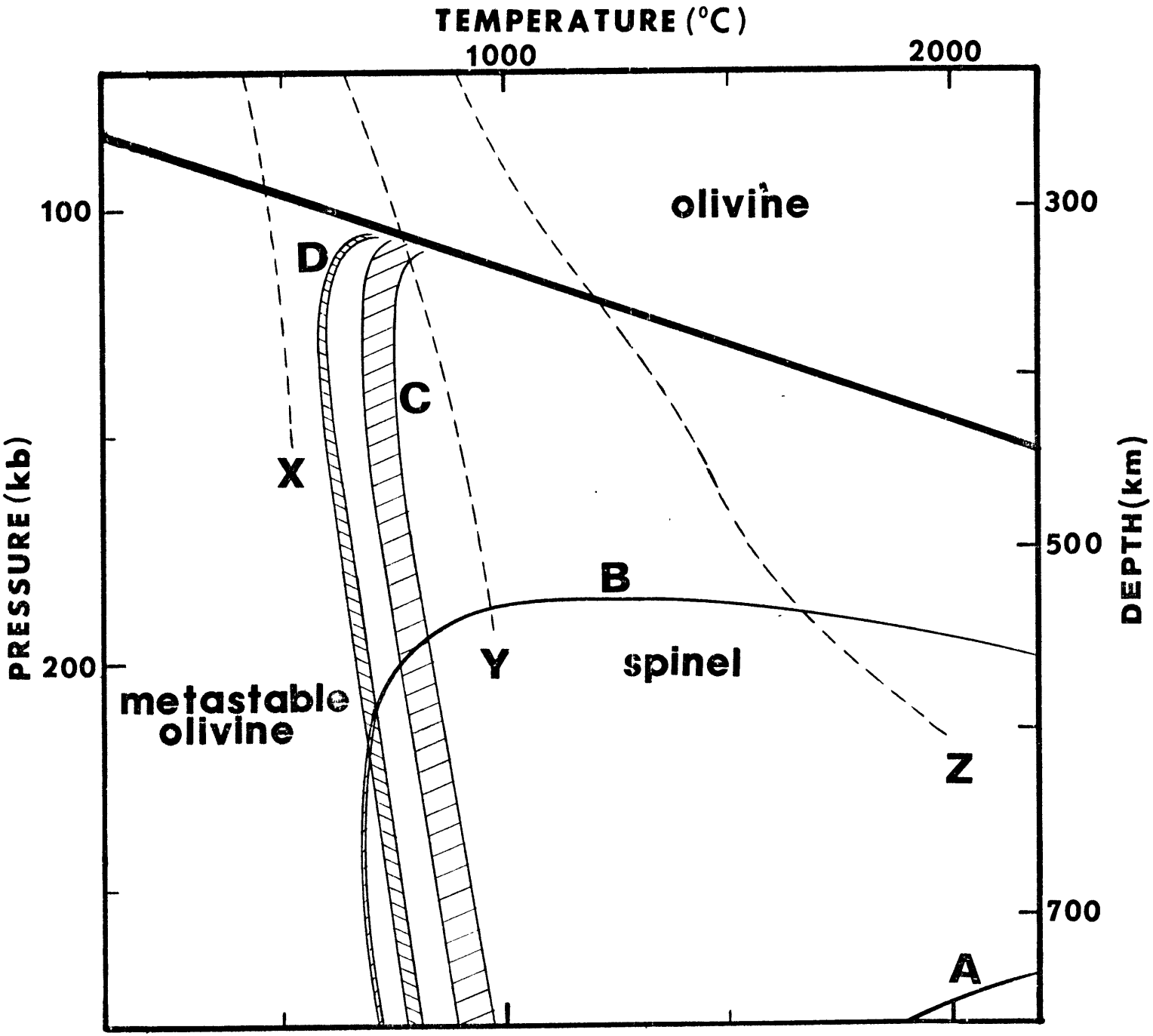
TEMPERATURE (°C)
1000
2000
100
200
PRESSURE (kb)
300
500
700
DEPTH (km)
olivine
D
C
X
Y
B
spinel
metastable
olivine
Z
A

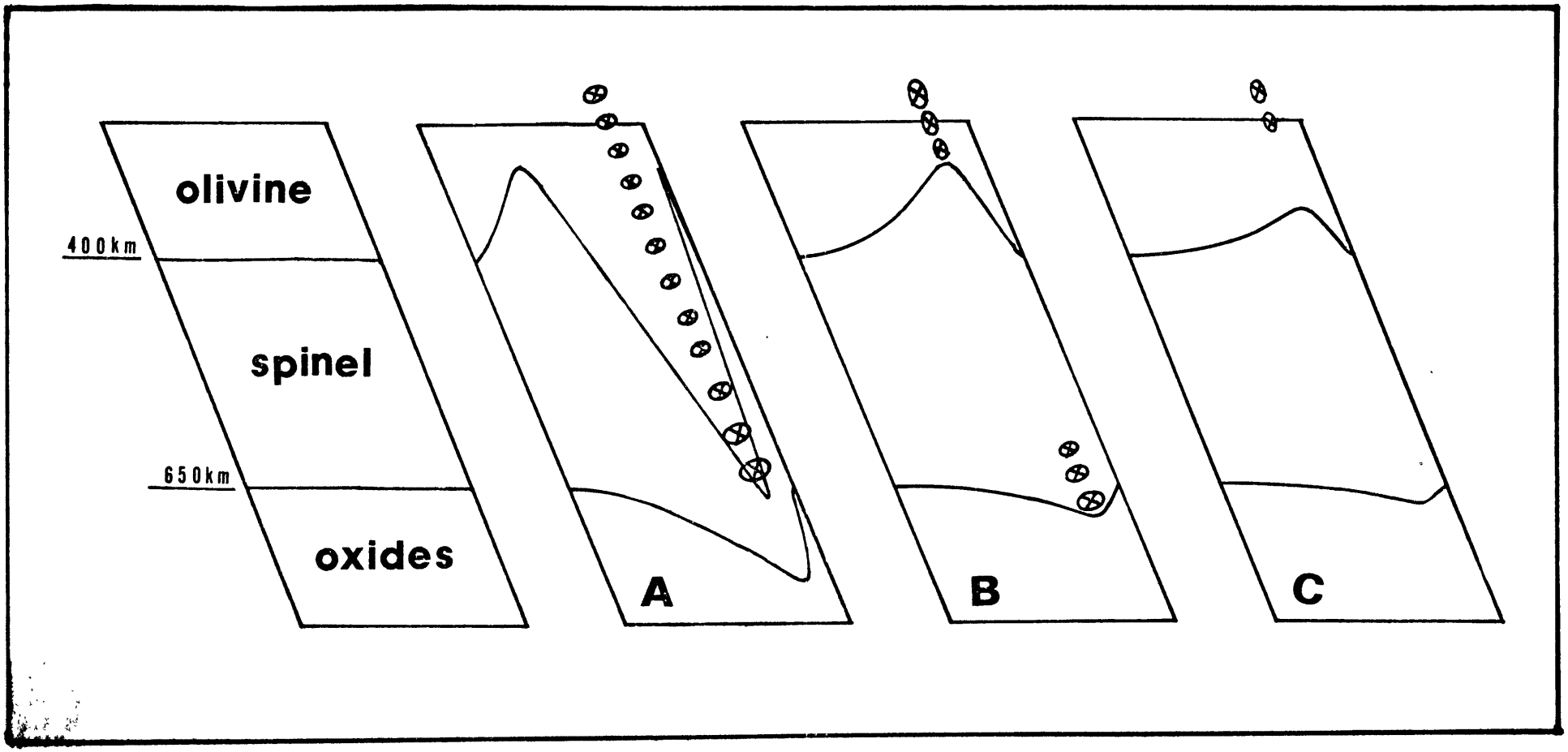
olivine
400km
spinel
650km
oxides
A
B
C

NEW MODIFICATION OF THE DIAMOND ANVIL PRESS: A VERSATILE APPARATUS FOR RESEARCH AT HIGH PRESSURE AND HIGH TEMPERATURE

Chïen-Min Sung

Department of Earth and Planetary Sciences
Massachusetts Institute of Technology
Cambridge, Massachusetts 02139

Submitted to Review of Scientific Instruments,

January 27, 1976

Abstract

A new modification of the diamond anvil press* which can achieve up to 300 kb and 1000°C is described. The new modification employs a new alignment technique and a new heating element and is a versatile apparatus for research at high pressure and high temperature.

Introduction

Since the introduction of opposed diamond anvils to achieve high pressure[1,2], diamond anvil presses have become the powerful tools in high pressure research. They have been used for high pressure measurements of optical spectroscopy[3,4], Mössbauer spectroscopy[5], x-ray diffraction[6,7], phase transitions[8,9], yield strength[10], conductivity[11], and other purposes. Different heating techniques have been employed in diamond anvil presses, thereby expanding their capabilities to high temperature measurements. Heating of diamond anvil presses has been achieved by using resistance coils[12,13], furnace[14], or YAG laser beams[14,15]. In this paper, we describe a new modification of the diamond anvil press in which heating is achieved by placing a resistance coil immediately around the two diamond anvils. This diamond press has the capability of achieving 300 kb and 1000°C over long periods of time.

Description of the Diamond Anvil Press

Our diamond anvil press is derived from the original design of Bassett and Takahashi[8], but employs a new mechanism for aligning the two diamonds and a new design of heating elements. The detailed assembly is shown in Figure 1. The two diamond anvils (A) are

*For more information about this equipment please write to the author.

mounted on the two pistons (B,C), using the high temperature cement such as Sauereisen No. 1 paste. The upper piston (B) is driven by the gimbal (D) and guided by the cylindrical sleeve (E). The pressure is achieved by squeezing the screw (F) on the spring (G) which ultimately transmits the force to the sample held between the two diamond anvils. There are holes through the center of the two pistons which allow the transmittance of radiation from optical light, x-ray, or Mössbauer γ-ray sources through the sample. The hole in the upper piston is a tapered slot which allows the passage of diffracted x-rays of up to $2\theta=35°$. The x-ray source is usually monochromatized Mo K_α radiation. It is collimated to a diameter of about 100 μm by a lead dispersed glass capillary tube (H) before entering the lower diamond and impinging on the sample. The position of the collimator (H) can be adjusted by turning the three equally spaced set screws (I) on the collimator holder (J). The latter is joined to the press by thread and can be easily detached or mounted without disturbing the original collimation. The x-ray camera (K) is a duplication of that designed by Bassett et al.[7]. The x-ray film is curved to a radius of 2.5" with its center coinciding with the sample. The camera is attached to the press by the four legs (M) and the sample-to-film distance can be adjusted before the heater (N) is placed around the two diamonds. The sample-to-film distance can be monitored by placing a platelet of NaCl outside the upper diamond. The whole press can be connected to a simple fixture (O) which fits to the track on the x-ray generator. Using NaCl as the internal standard to calibrate the pressure, the exposure time for Mo K_α radiation is about 400 hours. The exposure time can be

reduced by adapting a smaller film radius but this also reduces the precission of the pressure determination. Pressure can also be determined by using the ruby fluorescence technique[13]. In this case, neither the x-ray collimator or the camera is used and can be removed from the press.

The alignment of the two diamonds is achieved by translation and rotation of the lower diamond. Three equally spaced set screws (P) are used for the translational adjustment and the other three (Q) are used for the rotational adjustment. A similar alignment technique has been described before[13]. There are three alternative ways of arranging the six adjustment set screws as shown in Figure 2. The two sets of screws can both be located outside the lower piston (Figure 2a) or either set of screws can be located within the lower piston (Figure 2b, c). The latter arrangement is better because the two adjustments (translational and rotational) are independent and will not interfere with each other. This new design makes the alignment very easy and makes continuous adjustment under microscope possible. The alignment can also be performed in the middle of an experiment without unloading the sample. A good alignment of diamonds is indicated by the concentric phase boundaries of the sample and the centering of the isogyre cross of the uniaxially strained diamonds between cross polars.

The heater (N) is made of a fired pyrophyllite disc wound with thermocouple wire (0.4mm diameter 1m long) of platinum-rhodium (13%). The immediate surrounding of the heater around the sample has the advantage of rapid heating, e.g. 1 minute from 400°C to 600°C, without sacrificing the effectiveness of the quenching, e.g. 1 minute from 600°C to 300°C. Rapid heating during the first cycle

may cause the extrusion of the sample and may disturb the alignment of diamonds. These two difficulties may not be encountered during the recycled heatings. There are two holes penetrating horizontally through the heater. Two thermocouples can be used simultaneously to measure temperatures inside the heater. Temperature distribution inside the heater is quite homogeneous when the two diamonds are not inserted. The horizontal and the vertical temperature gradients inside the heater can both be very large, especially at high sample temperature, when the two diamonds are closed up as shown in Figure 3. Measured temperatures can be 50°C higher than the true sample temperature, even if the thermocouple head touches the diamonds. Because the diamond is a good thermal conductor (although it is a poor electrical conductor), and the sample is small and very thin (about 5 to 10 μm), the temperature gradient inside the sample may not be large. The true sample temperature can be measured by clamping the head of an ultrafine thermocouple(25μm wire diameter) at one edge, between the two diamonds. Because the pressure there is low, say below 30 kb, it will not increase the temperature reading by more than 4%.

The steady state power input for the heater to maintain a particular sample temperature as a function of the sample temperature is shown in Figure 4. The steady state power can be approached in a few hours of heating and is reproducible if the condition of the environment (ambient temperature, contact condition between the press and the ground, etc.) remains the same. The non-steady state power for the heater is higher and lower than the steady state power during heating and cooling, respectively, and the difference will increase with the rate of heating or cooling. Both the pistons (B,C) and the cylindrical sleeve (E) are made of inconel metal. If Corning

machinable glass is inserted in each of the pistons, the steady state power can be reduced up to 20% at a sample temperature of about 600°C.

When the diamond is heated above 600°C for a long period of time (several days or longer), its surface becomes frosted due to the slow burning in air. The oxidation of the diamond can be avoided by putting the whole press inside a box and purging with nitrogen or argon gas. Heating above 800°C may cause other problems, especially if the rate of heating is high. The anvil surface may become undulated due to the unevenness of the thermal expansion. This may cause pressure release on the sample. Prolonged heating may slso reduce the pressure by reducing the elastic constant of the spring (G). This problem is overcome by circulating cooling water through the hose fitting (R). In this case, the spring end and the hinge end (S) of the press remain cold during the heating of the sample.

Applications

There are several applications of our modified diamond anvil press. We have used them to study the kinetics of the olivine→spinel transition[17,18]. Two pictures of the unloaded samples are shown in Figure 5. An oriented single crystal (001) of fayalite is heated to 600°C for 50 minutes under a center pressure of approximately 140 kb (Figure 5a). The spinel is nucleated along the cleav-

age planes of olivine(010) and grows to form an annular ring in the region of the maximum pressure. Note that the pressure at the center is lower than that in the annular region in this particular run. A powdered fayalite of grain size approximately 5 μm is heated to 600°C for 1090 minutes under a center pressure near 100 kb (Figure 5b). The spinel is found to nucleate along the grain surfaces and grows inwards at the expense of fayalite crystals. The degree of transition at the center region has been estimated to be approximately 80% from the relative intensities of X-ray peaks of olivine and spinel. Figure 6 shows the polarized absorption spectra of an oriented fayalite single crystal at high temperature. In this measurement, samples of thickness about 20 μm are immersed in liquid held by a metal gasket and subjected to a pressure near 10 kb. Figure 7 shows the measured conductivity of a powdered fayalite sample as a function of temperature at a pressure of about 120 kb. The technique of measurement is otherwise similar to that described by others[11], except the sample is contained in a nitrogen atmosphere. The activation energy of conduction calculated from this measurement is about 0.3 ev at low temperatures (<300°C) and about 0.4 or higher at higher temperatures (300°C-500°C).

Acknowledgments

The author thanks Drs. W.A. Bassett, L.C. Ming, H.K. Mao, and G.J. Piermarini for introducing him to their diamond anvil presses and their techniques. He also thanks Dr. R.G. Burns and Mr. B.M. Loeffler for reviewing, and Ms. R. Regan for typing this manuscript. Research supported by grants from NASA (grant no. NGR-22-009-551) and NSF (grant no. EAR 75-20138).

References

1. J.C. Jamieson, A.W. Lawson, and N.D. Nachtrib, Rev. Sct. Instr., 30, 1016 (1959).

2. C.E. Weir, E.R. Lippincott, A. Van Valkenburg, and E.N. Bunting, J. Res. Natl. Bur. Stand. (U.S.), A 63, 55 (1959).

3. E.R. Lippincott, C.E. Weir, A. Van Valkenburg, and E.N. Bunting, Spectrochem. Acta, 16, 58 (1960).

4. R.M. Abu-Eid, Ph.D. Thesis, M.I.T. (1974).

5. F.E. Huggins, H.K. Mao, and D. Virgo, Year Book, Carnegie Inst. Wash., 405(1975).

6. G.J. Piermarini and C.E. Weir, J. Res. Nat. Bur. Stand.(U.S.), A 66, 323 (1962).

7. W.A. Bassett, T. Takahashi, and P.W. Stook, Rev. Sct. Instr., 38, 37 (1967).

8. W.A. Bassett and T. Takahashi, Amer. Mineral., 50, 1576 (1965).

9. L.G. Liu, W.A. Bassett, and M.S. Liu, J. Phys. Chem., 77, 1695 (1973).

10. G.L. Kinsland, Ph.D. Thesis, Univ. Rochester (1974).

11. H.K. Mao, Year Book, Carnegie Inst. Wash., 72, 552 (1973).

12. H.K. Mao and P. Bell, Year Book 71, Carnegie Inst. Wash., 176 (1971).

13. J.D. Barnett, S. Block, and G.J. Piermarini, Rev. Sct. Instr., 44, 1 (1973).

14. L.C. Ming, Ph.D. Thesis, Univ. of Rochester (1974).

15. L.C. Ming and W.A. Bassett, Rev. Sct. Instr., in press (1976).

16. G.J. Piermarini, S. Block, and J.D. Barnett, J. Appl. Phys., 44, 5377 (1973).

17. C.M. Sung and R.G. Burns, Tectonophysics, in press (1976).

18. C.M. Sung and R.G. Burns, Earth Planet. Sci. Lett., submitted.

Figure Captions

Figure 1. Detailed assembly for the new modification of the diamond anvil press.

Figure 2. Three alternative ways to align the lower diamond: (a) both translational and rotational adjustment set screws are located outside the lower piston; (b) translational adjustment set screws are located outside the lower piston; and (c) rotational adjustment set screws are located outside the lower piston. Rotational adjustment set screws can also be mounted on the upper piston[13]. The maximum pressure which can be achieved using these three alignment geometries is in the order c>b>a.

Figure 3. Temperature profile across the heater at sample temperature of 600°C. The lower figure shows the temperature distribution along the horizontal line passing through the center of the sample. Numbers are temperatures in °C. C and O mean the two diamonds are closed together and open, respectively.

Figure 4. Electrical power input (W) and current (I) versus sample temperature at thermal equilibrium. W and I will be higher and lower during heating and cooling, respectively.

Figure 5. Olivine→spinel transition at high pressures. (a) Oriented single crystal of fayalite (001) subjected to 140 kb and 600°C for 50 minutes. The dark, annular region is the transformed spinel. Note the spinel is preferentially nucleated on the cleavage plane (010); (b) powdered fayalite subjected to 100 kb and 600°C for 1090 minutes. Center

region is partially transformed olivine. Note the spinel is preferentially nucleated along the grain surfaces of olivine and grows inwards at the expense of the latter. The outermost dark rim is the oxidized fayalite. Both samples are approximately 500 μm across.

Figure 6. Polarized absorption spectra of an oriented fayalite single crystal at high temperatures and a pressure of near 10 kb. Vertical axis is the optical density in cm^{-1}. Numbers are temperature in °C. (a) β-spectra, and (b) γ-spectra. Note the spreading out of the M2 peaks, which indicates the increase of site distortion with temperature.

Figure 7. Electrical conductivity of powdered fayalite as a function of temperature at a pressure near 120 kb. The sample was under nitrogen during the measurement.

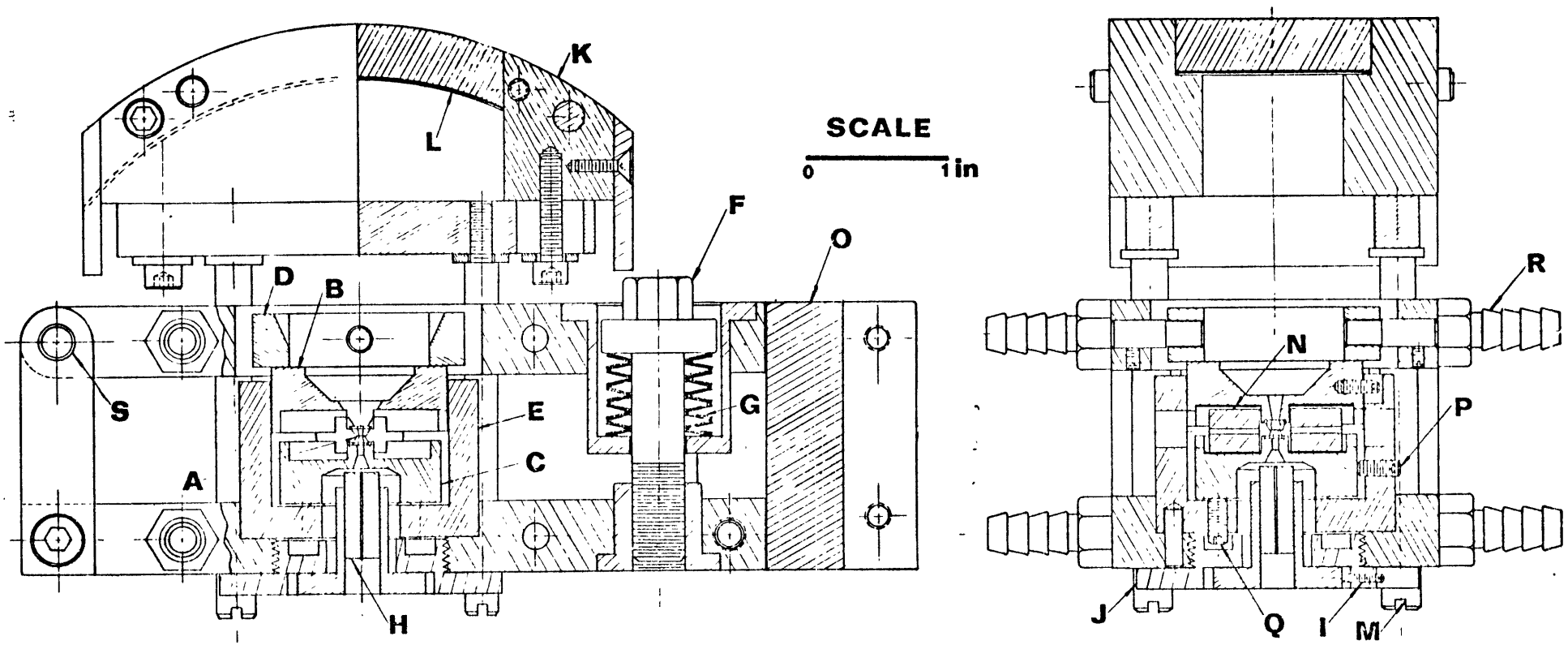
K
L
F
O
D
B
S
E
G
C
A
H
SCALE
0
1 in
R
N
P
J
Q
I
M

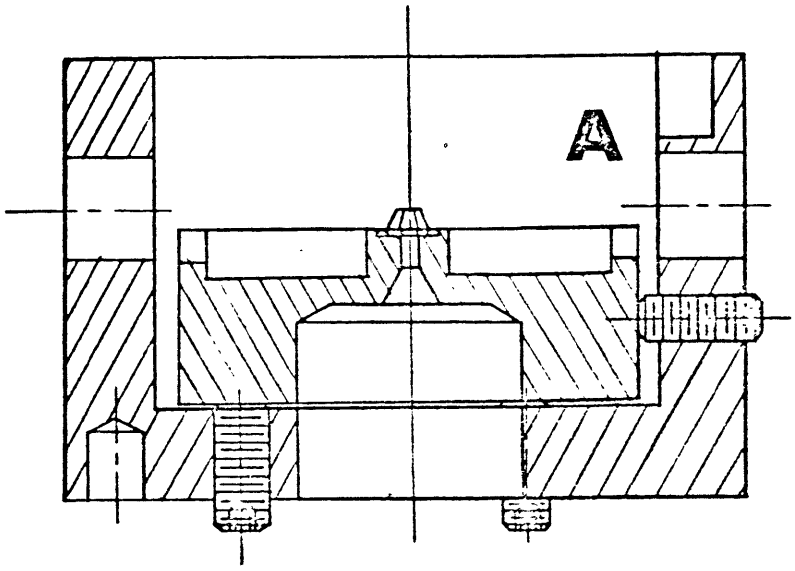
A

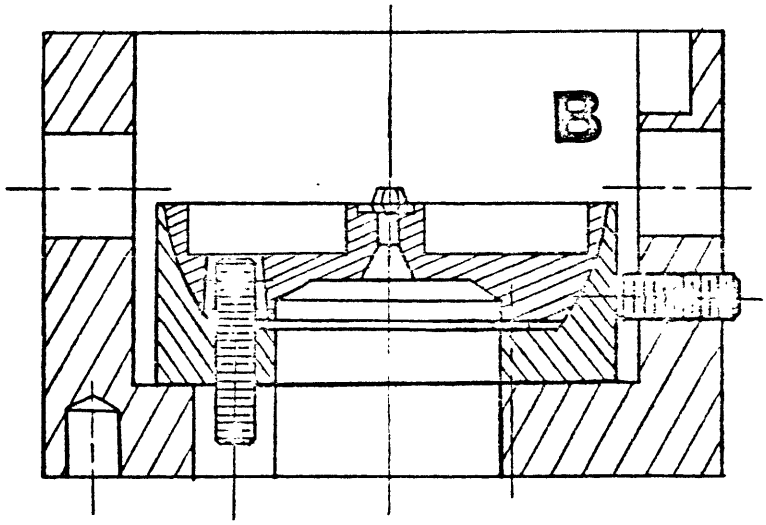
B

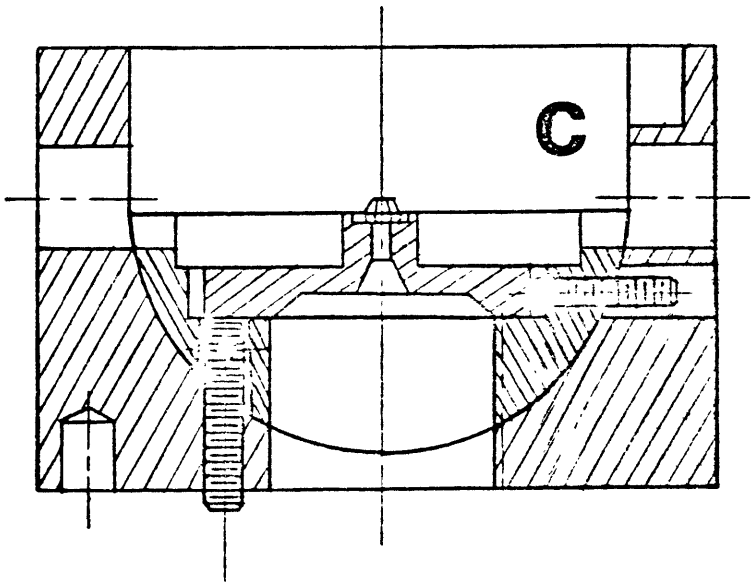
C

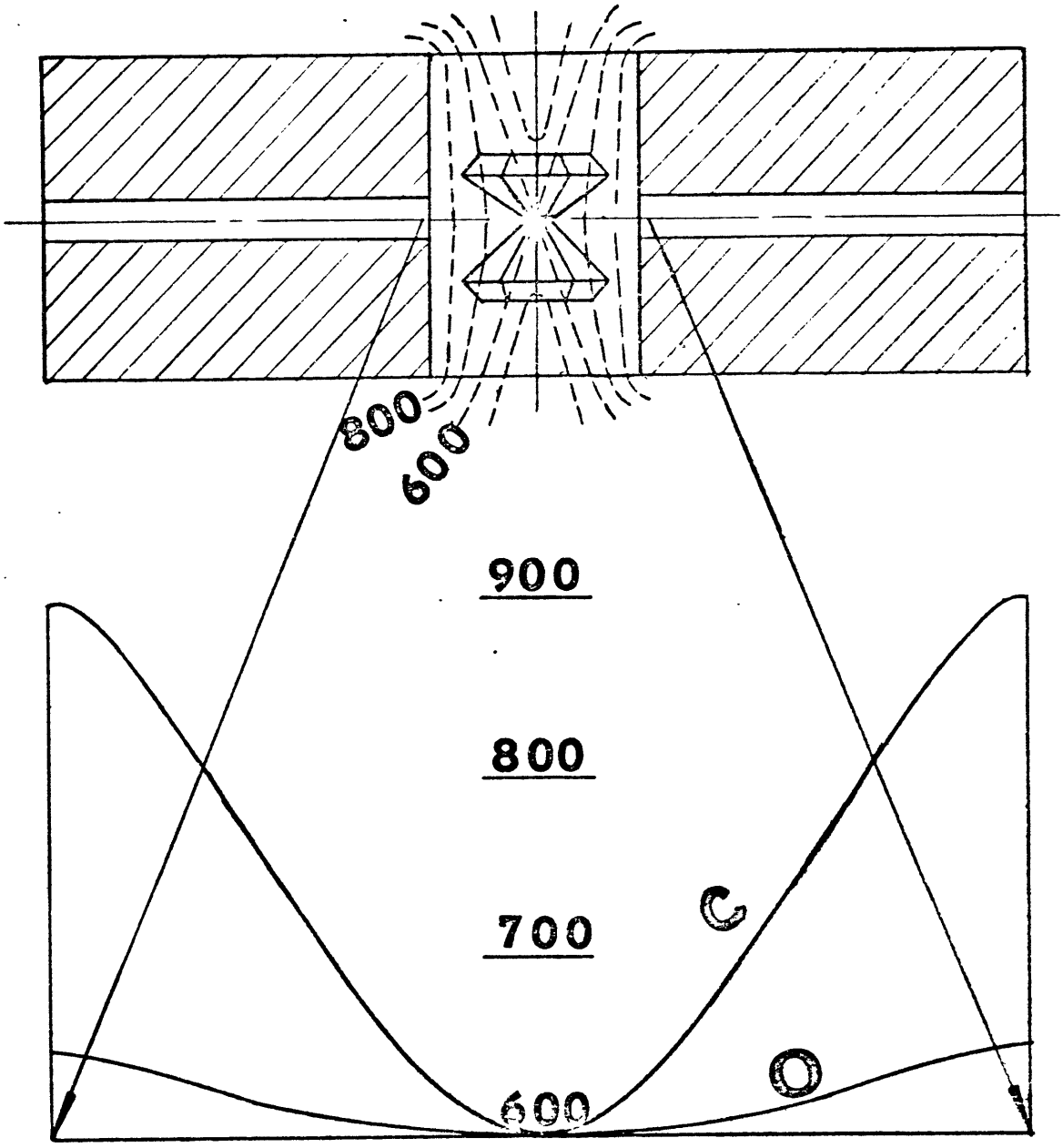
800
600
900
800
700
600
C
O

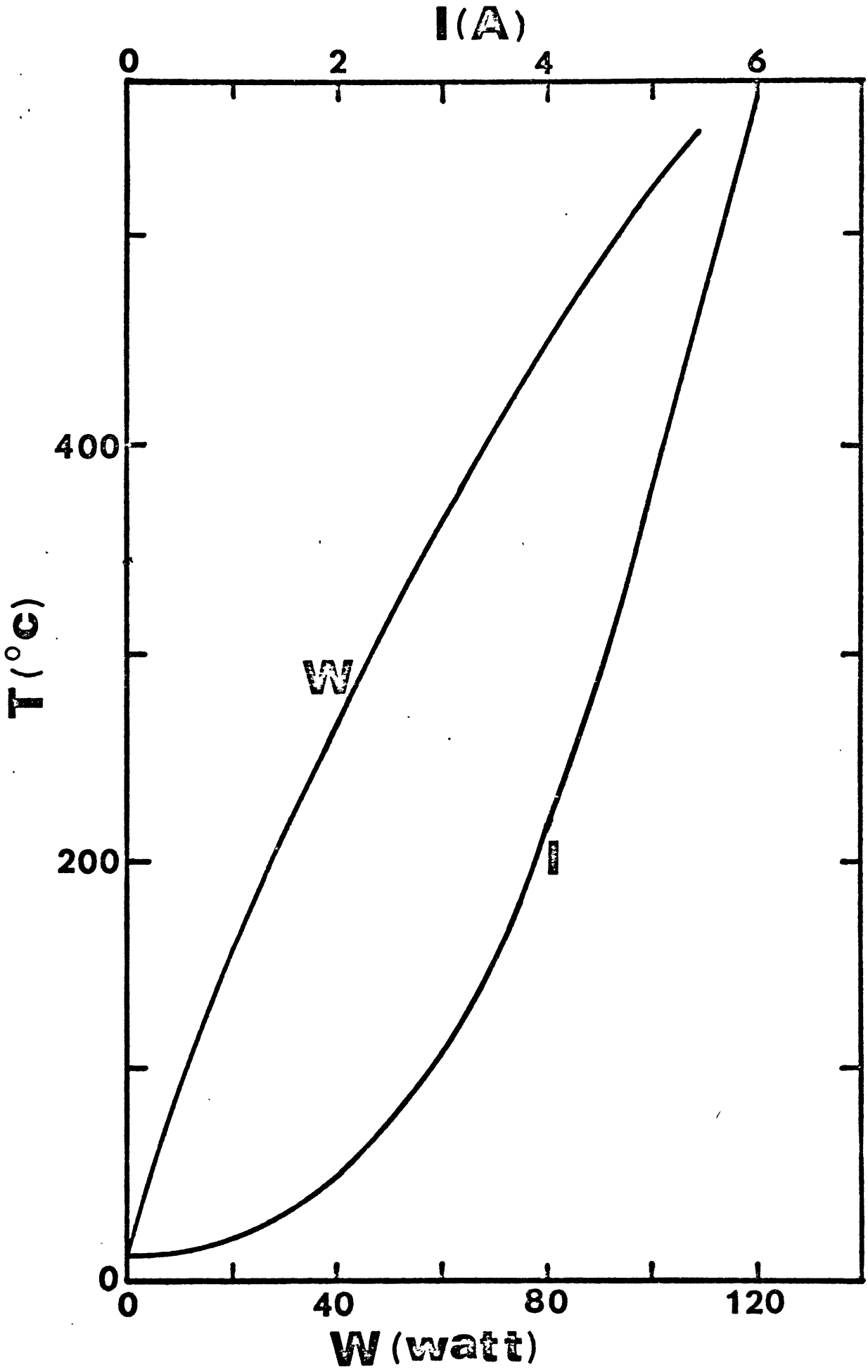
I(A)
0
2
4
6
400
200
0
T(°C)
W
I
0
40
80
120
W (watt)

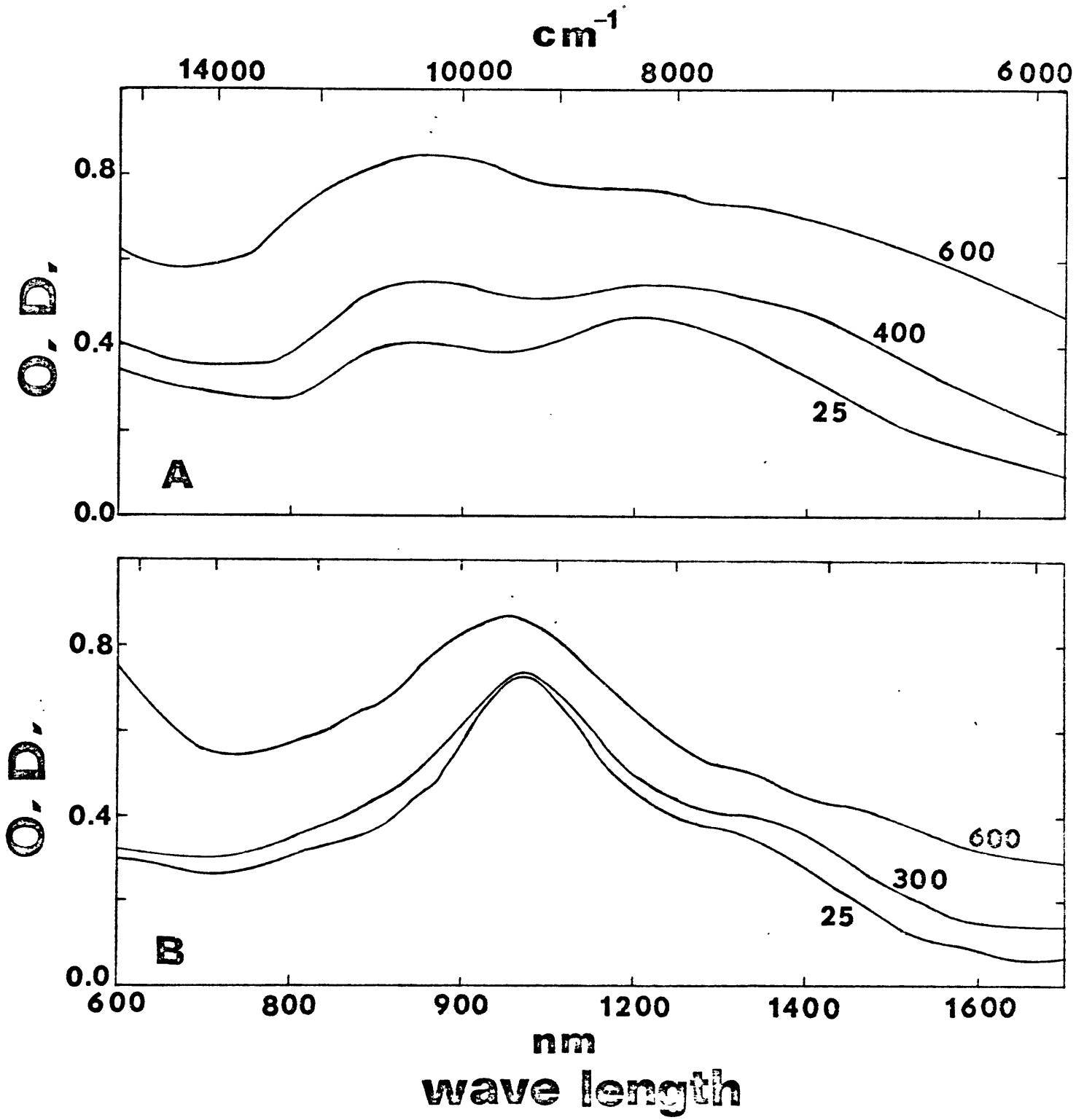
cm⁻¹
14000
10000
8000
6000
0.8
0.4
0.0
O. D.
600
400
25
A
0.8
0.4
0.0
O. D.
600
300
25
B
600
800
900
1200
1400
1600
nm
wave length

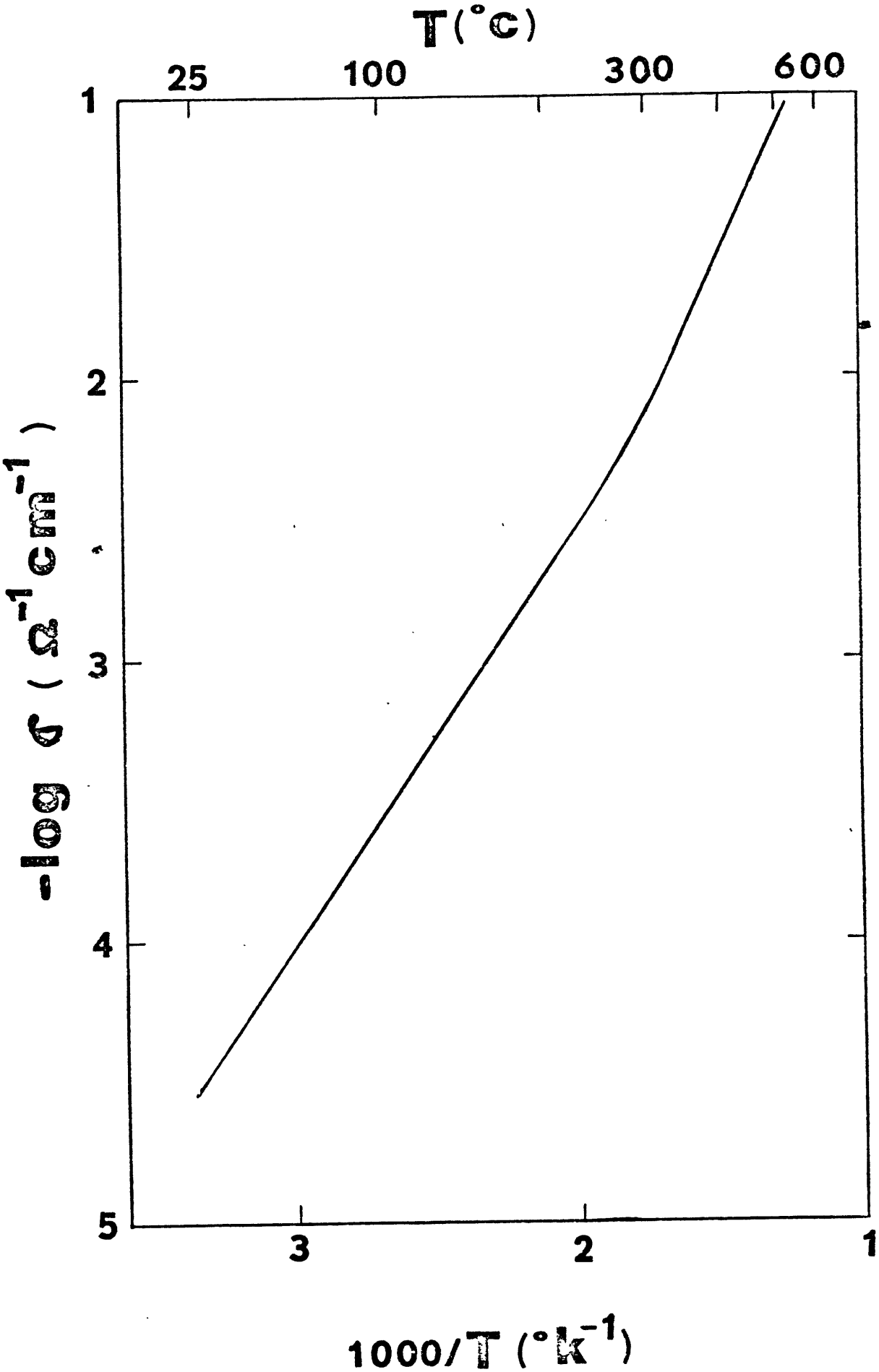
T(°C)
25
100
300
600
1
2
3
4
5
-log σ (Ω⁻¹ cm⁻¹)
3
2
1
1000/T (°k⁻¹)

PROCEEDINGS OF THE GEOLOGICAL SOCIETY OF CHINA
NO. 17, PP. 67-84, 10 FIGS., 1 TAB., APRIL, 1974

THE KINETICS OF HIGH PRESSURE PHASE TRANSFORMATIONS IN THE MANTLE: POSSIBLE SIGNIFICANCE ON DEEP EARTHQUAKE GENERATION

CHIEN-MIN SUNG

Department of Earth and Planetary Science
Massachusetts Institute of Technology

(With 10 text-figures and 1 table)

ABSTRACT

The rate equations for the olivine-spinel and pyroxene-garnet transformations, which are believed to cause the major seismic discontinuities found in the upper transition zone, have been semiquantitatively evaluated. The rates for these two transformations increase sensitively with temperature and superpressure (pressure beyond equilibrium). The rate of energy release for the olivine-spinel transformation under the physical conditions of the upper transition zone is then estimated based on this derived rate equation. It is found that in order for this rate of energy release to be comparable to that required for deep earthquake generation, the rate of superpressure accumulation would have to be as high as 1 kb/day. Since such a high rate of superpressure accumulation may never be attainable in the mantle, and since no suitable mechanism, which can efficiently convert heat into seismic energy, apparently exists, it appears unlikely that the high pressure phase transformations can directly generate deep earthquakes. However, the volume contraction and heat generation associated with the phase transformations may trigger catastrophic shear flow in the mantle, and thus may be indirectly responsible for deep earthquakes.

INTRODUCTION

Bridgman (1945) followed by Evison (1963) and Benioff (1963) have suggested that high pressure phase transformations may be the direct source for deep earthquakes and even the indirect source for some shallow earthquakes. Randall (1964 a, b) has calculated the possible energy released during a sudden phase transition and concluded that even for a small density increase, the energy concentration generated will be much higher than that produced in a sudden faulting responsible for common shallow earthquakes. Evison (1967) has found that the first motion of seismic waves from deep sources is dominantly dilational, indicating that they may be caused by the sudden contraction of material under high pressures. McKerrow *et al.* (1973) have further indicated that deep earthquakes are limited almost exclusively in certain belts associated with general surface subsidence and running parallel or subparallel to adjacent Benioff Zones. They attributed those features to high pressure phase transitions induced by downplunging oceanic plates. In addition, Kashara *et al.* (1971) have calculated from their kinetics experiments on nickel olivine that its transformation into nickel spinel may occur at such a high rate as to achieve 80% transition in 15 seconds, thus indicating that the rate of energy release accompaning with high pressure phase transitions may be high enough to generate deep earthquakes. All the evidence cited above suggests that catastrophic implosions produced by sudden polymorphic phase changes may be the important mechanism for deep earthquakes which are difficult to justify by elastic rebound theory. However, there is also much evidence against this possibility (e. g. Mendiguren, 1972; Aki, 1972; etc.) and controversy on the speculation that high pressure phase transformations may trigger deep earthquakes still exist.

The two major constituents in the mantle are believed to be $(Mg, Fe)_2 SiO_4$ and $(Mg, Fe) SiO_3$ with Mg/(Mg+Fe) atomic ratios close to 0.89 (Ringwood, 1970) At low pressures, the olivine structure is favored over the spinel structure for $(Mg, Fe)_2 SiO_4$ through shortening of polyhedral edges (Kamb, 1968) The pyroxene structure, on the other hand, is favored over the garnet structure for $(Mg, Fe) SiO_3$ by maintaining all the silicon ions in the tetrahedral sites. However as pressure increases, olivine and pyroxene become destabilized and transform into spinel and garnet, respectively. The pressures for these transformations are strongly dependent on mineral composition. If aluminium ions completely substitute both magnesium and silicon ions in the structure, spinel and garnet can be stable at zero pressure. The aluminous olivine and pyroxene may undergo transformations at the depth below 100 km as depicted by the stability field of pyrolite. For the majority alumina-free olivine and pyroxene in the Upper Mantle, their phase boundaries intersect the geotherm at the depth of about 400 km and have been correlated to the major seismic discontinuities found in the upper Transition Zone (Ringwood, 1970).

If high pressure phase transformations could generate deep earthquakes, olivine-spinel and possibly pyroxene-garnet transitions may be the best source candidates because they are the most drastic phase changes (density increase about 10%) observed in major Mantle minerals and occur within the depth range of deep earthquake foci. This paper attempts to evaluate the intrinsic properties (kinetics) of those two phase transformations under the physical conditions of their generation, and to compare the possible rate of energy release during these phase changes to that required for deep earthquakes.

THE RATE EQUATION FOR PYROXENE-GARNET TRANSFORMATION

The rate equation for pyroxene-garnet transformation is evaluated here by applying the model of nucleation and growth described in the appendix. Several crude approximations have been made in deriving this rate equation because of the complete lack of experimental data for kinetics of this transformation.

High pressure tends to increase the packing efficiency of a structure by increasing cation coordination number. The pyroxene-garnet transformation can be perceived by extending the coordination number from 6 to 8 for three quarters of Mg cations and from 4 to 6 for one quarter of Si cations as depicted by the following equation:

$$(Mg_3Mg)^{VI}(SiSi_3)^{IV}O_{12} \longrightarrow (Mg_3)^{VIII}(Mg,\ Si)^{VI}(Si_3)^{IV}O_{12}$$

where Roman superscripts denote coordination number.

The molar volume and bulk modulus of pyroxene of formula $(Mg_{0.89}Fe_{0.11})_4 Si_4O_{12}$ can be approximated from data of its endmembers (Nishizawa *et al.*, 1973) by interpolation to be 120.09 cm^3/GFW and 1,206 kb respectively. The molar volume of garnet of this composition is unknown, but from the cell edge of the least aluminous garnet synthesized by Ringwood *et al* (1966) (The ionic radius of Al^{+++} lies between Mg^{++} or Fe^{++} and Si^{++++}, therefore the cell edge won't change much if Al^{+++} substitute for the other ions), its molar volume is calculated to be 113.31 cm^3/GFW. The bulk modulus for this garnet is estimated to be 1,900 kb. The pressure and temperature at the depth of 400 km are about 130 kb and 1,200°C respectively (Fujisawa, 1966). Using Birch-Murnaghan equation of state

$$P = (3/2)\,K_0\,((V_0/V)^{7/3} - (V_0/V)^{5/3})$$

(where K_0 is the bulk modulus and the subscript "0" denotes zero pressure value) and making correction for thermal expansion of 3.70 and 3.24% (Clark, 1966), the molar volume of pyroxene and garnet at this possible transition depth are calculated to be 115.23 and 106.65 cm^3/GFW respectively. The average number of atoms (each formula contains 20 atoms) in the transforming matrix (pyroxene) per unit volume (N) is then calculated to be $1.05 \times 10^{23}\ cm^{-3}$. The average

atomic distance at the phase boundary or the average increment of thickness (l) due to the accretion of one layer of atoms is also calculated from the above molar volumes, which gives $l=2.10\times10^{-8}$ cm. The surface tension (σ) of the garnet nuclei is the difference of the surface energies between the average of granet and pyroxene and the interphase boundary. The surface energies for garnet and pyroxene are unknown and difficult to calculate from Gilman (1960) equation. However, the direct measurement (Brace, *et al.*, 1962) of these energies for most silicates fall around 500 ergs cm^{-2}. The surface tension of garnet nuclei in the pyroxene matrix may be much less than this value because of the compensation by the surface energy of the interphase boundary which may have nearly the same magnitude as for the individual phase. But here σ is tentatively assumed to be 500 ergs cm^{-2} in order to make some allowance for strain energy of the nuclei.

The free energy decrease, which is the driving force for the phase transition, of pyroxene-garnet transformation can be approximated by $\Delta G=-\Delta S\,\Delta T+\Delta V\,\Delta P$. ΔS is calculated by assuming $dP/dT=0.02$ kb $°K^{-1}$ of the average solid state transformation for major silicates (Ringwood, 1967) for pyroxene-garnet transition through Clapeyron relation, and ΔV from the above molar volume data. This gives $\Delta G=1.5\times10^{6}\,\Delta T-7.4\times10^{7}\,\Delta P$ erg cm^{-3}, where ΔT and ΔP in unit of °K and kb respectively. The compensation of the effect of 1 kb superpressure requires about 50°K of supertemperature which may never be attainable because the adiabat in the upper Transition Zone is too low (about 0.3°C/km, Hurley, 1972) to bring up this supertemperature. The effect of ΔT is negligible compared to ΔP, hence I put $\Delta G=-7.4\times10^{7}\,\Delta P$ erg cm^{-3} here for simplicity and make the allowance of ΔP to compensate the effect of ΔT.

The radius of critical-sized nucleus of garnet is then calculated from equation (2) of Appendix to be $1.35\times10^{-5}/\Delta P$ cm, from which the ratio of surface area to the average number of atoms in a critical-sized nucleus (A^*/n) is calculated to be $1.97\times10^{2}\,\Delta P$.

The activation energy ΔF^* is calculated from equation (1) of Appendix, which gives $3.28\times10^{-16}\,\Delta P$ erg/atom

The activation energy ΔE depends on the mechanism which is unknown for pyroxene-garnet transformation. Since the path of transition should always follow the one with minimum energy barrier, which is concievable from the equation of page 3 to be expanding the coordination spheres of Mg and Si cations. ΔE is here approximated by the work required to expand coordination sphere from CN=6 to CN=8 for three quarters of Mg ions and from CN=4 to CN=6 for one quarter of Si ions by assuming hard sphere model. The average Si-O distance under 130 kb pressure is calculated from the cell parameters of stishovite (Suito, 1972) through Birch-Murnaghan equation, this gives 1.75×10^{-8} cm. Assume that the cation oxygen radius ratio for stishovite is just enough for Si ion in CN=6 under this pressure (stishovite becomes stable when pressure increases above 100 kb at 1,200°C). This gives the radius of oxygen ion about 1.24×10^{-8} cm. The cation-oxygen distances for Mg^{VIII}, Mg^{VI} and Si^{IV} are then calculated by assuming oxygen ions are in contact in each coordination sphere. The average potential energy increase per atom for those expansion of coordination spheres is calculated to be 5.16×10^{-12} erg $atom^{-1}$.

Substitute all the above data into equation 4 of Appendix, the rate equation for pyroxene-garnet transformation is finally obtained as

$$K = 2.47\times10^{48}\,\Delta P^{3/2}\,T^{7/2}\exp\left(-(2.3732\,\Delta P+156522)/T\right)\left(1-\exp(-5.1561\,\Delta P/T)\right)^{3}$$

The only available experimental data for pyroxene-garnet transformation is from Ringwood *et al.* (1966). Their results indicated that for an aluminous pyroxene ($MgSiO_3\cdot5Al_2O_3$) under the pressure of 150 kb and temperature of 900°C, 30% of garnet wuld be formed in a period of about 4 minutes. Using equation (3) of Appendix, the rate constant K for this transition is calculated to be 1.4×10^{-3} min^{-4}. If ΔP is tentatively chosen to be 5 kb, the rate constant predicted by using the above equation under this physical condition is 1.7×10^{-3} min^{-4}. The effect

of alumina on the kinetics of pyroxene-garnet transformation is unknown but may not be very significant because of the intermediate characteristics (size, charge, etc.) of Al^{+++} between Mg^{++} and Si^{++++}. The agreement between the hypothetical rate equation for pyroxene-garnet transition and the experimental result is remarkable even though some crude approximations have been made in its derivation. The effect of ΔP and T on the behavion of this transformation based on the above rate equation is shown in Figs. 1 through 3. It can be seen that the rate of transformation depends sensitively on ΔP and T, especially the latter. The importance of temperature control on the rate of transformation can be seen in Fig. 3. If temperature drops below a crical value (T_{cr1} in Fig. 3), the vibrational energy in the atom may be so low that the activation energy for it transition becomes insurmountable and the process eventually stops no matter how high ΔP is. For a temperature as high as 1200°C which may prevail in the upper Transition

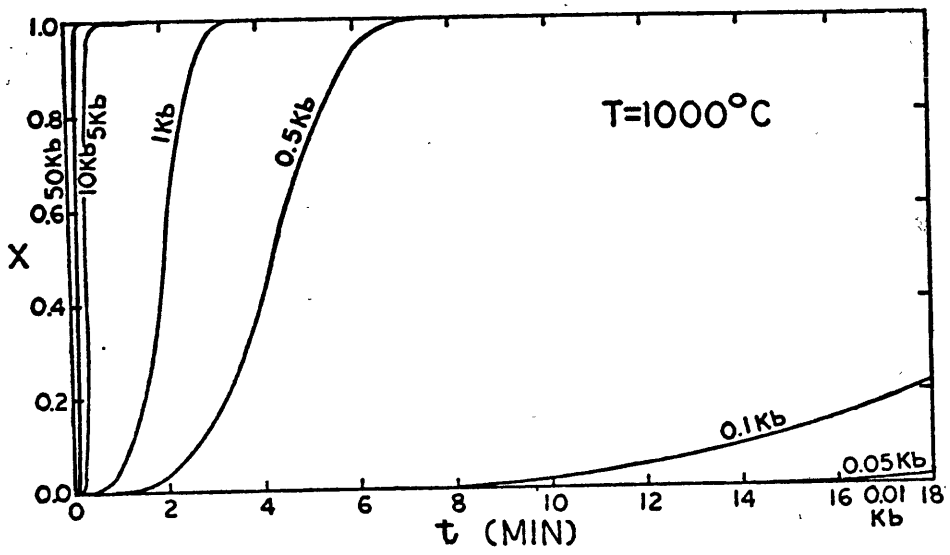

Fig. 1. The Superpressure dependence of the rate of pyroxene-garnet transformation.

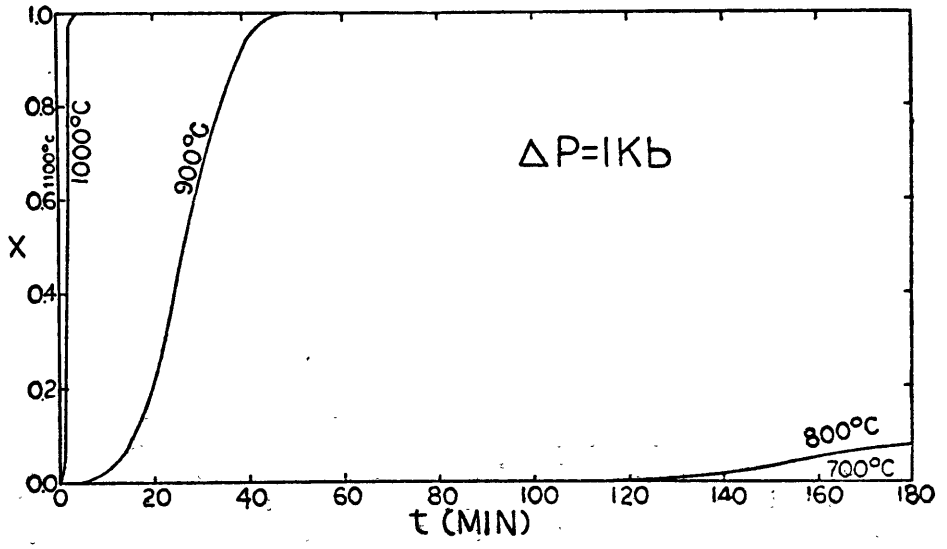

Fig. 2. The temperature dependence of the rate of pyroxene-garnet transformation.

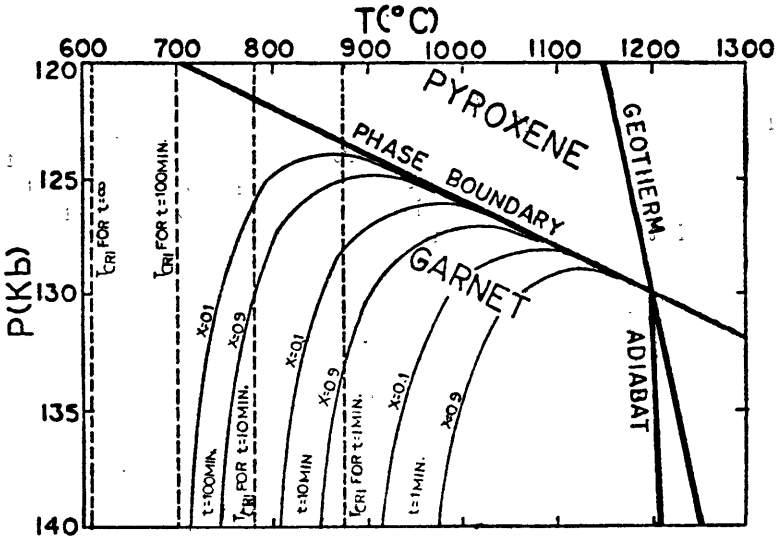

Fig. 3. The kinetics behavior of pyroxene-garnet transformation in the Mantle.

Zone, the rate of transformation becomes so fast that the completion of the whole process may be a matter of a few seconds (Figs. 2 and 3). In this case, the deep penetration of pyroxene into the metastability field becomes impossible.

THE RATE EQUATION FOR OLIVINE-SPINEL TRANSFORMATION

The magnitude of density increase in olivine-spinel transformation is same as that in pyroxene-garnet transformation. Since olivine is much more abundant than pyroxene (volume ratio about 4 to 1) in the Upper Mantle, the former transformation becomes more important in terms of possible mechanism for deep earthquakes.

The rate equation for olivine-spinel transformation can be derived in a manner similar to that described above for pyroxene-garnet transformation. However, since both σ and ΔE are difficult to estimate for the former transformation, the rate equation so derived may be very erroneous. Here a semi-empirical method is used in order to minimize the high uncertainty of pure theoretical derivation. Since no suitable experimental data are available for olivine-spinel transformation with the composition of Mg/(Mg+Fe) atomic ratio of 0, 89, the assumed ratio for Mantle olivine, data for Mg_2SiO_4 are used instead.

The thermodynamic properties (ΔV, ΔS, etc.) for olivine-spinel and pyroxene-garnet transformations are similar. Therefore the kinetics behaviors for these two transformations may be qualitatively similar. The rate equation for olivine-spinel transformation then can be tentatively written by analogy to that for pyroxene-garnet transformation as

$$K = C_1 P^{3/2} T^{7/2} \exp(-(C_2 \Delta P + C_3)/T)(1-\exp(-[\Delta G/N]/(kT)))^3$$

Where C_1, C_2 and C_3 are constants to be determined.

The molar volumes and bulk moduli for olivine and spinel of composition Mg_2SiO_4 are 43 68, 39.62 cm^3/mole and 1286, 2050 kb respectively. From Birch-Murnaghan equation of state and with thermal expansion of 4.10% and 3.24% up to 1200°C for olivine and spinel respectively, the volume change for this transformation in the environments of Upper Transition Zone is calculated to be $-3.10\ cm^3$/mole. The driving force for this transformation is then obtained as $\Delta G \doteqdot \Delta V \Delta P = -7.4 \times 10^7\ erg/cm^3$ (neglect ΔT effect as argued previously), which is found to be identical to that for the pyroxene-garnet transformation. The average atoms per unit volume for the trans-

forming phase (olivine) is next calculated from the above molar volume data to be 1.01×10^{23} atoms/cm^3. The exponent for the last term in the above rate equation ($-[\Delta G/N]/(kT)$) is then equal to $-5.3092\,\Delta P/T$.

Based on equation (3) of Appendix, the rate constant for each run of experiment on olivine-modified spinel (β-phase) transformation with coexisting transformed and transforming phases can be calculated. Three runs with possible maximum K's (minimum P or t) at different temperatures are chosen from literatures (Table 1) to solve the constants C_1, C_2 and C_3 in the above rate equation. Since no proportions of modified spinel are quoted by the authors, the volume fraction of transformation (X) is tentatively assumed the lowest possible value for each run, 1% for trace amount and 10% for unspecified amount of the transformed phase (β).

Table 1. The experimental runs for fosterite and the calculated superpressure (ΔP) and rate constant (K) for each run.

T (°C)	P (kb)	t (min)	ΔP (kb) Result	Reference	K (min^{-4})
740	230	20	132 $\alpha+\beta$ (trace)	Akimoto *et al.* (1968)	6.3×10^{-8}
1000	134	35	2 $\alpha+\beta$	Suito (1972)	3.4×10^{-8}
1100	150	5	5 $\alpha+\beta$	Suito (1972)	8.2×10^{-5}

The equilibrium pressure in olivine-modified spinel transition for the above three runs are calculated by the equation P(kb)$=0.13\,T$(°C)$+2$ determined by performing the reverse reaction of the transformation (Suito 1972), and the superpressure is obtained by subtraction. The rate constant for the three runs are calculated. The rate equation for olivine-modified spinel transformation is finally obtained by substituting the three rate constants into the above rate equation with unknown constants and solving simultaneously for those constants, which gives

$$K = 8.6\,10^9\,\Delta P^{3/2}\,T^{7/2}\exp\left(-(37.2173\,\Delta P+64898.2)/T\right)(1-\exp(-5.3092\,\Delta P/T))^3$$

When compared to the rate equation for pyroxene-garnet transformation, it is found that olivine-modified spinel transformation is characterized by possessing higher surface tension (σ) on its interphase boundary, which results in lower value of C_1 and higher value of C_2, and lower activation energy ΔE. The effect of ΔP and T on olivine-modified spinel transition is shown in Figs. 4 through 8. It can be seen that olivine-modified spinel transition is a much sluggish process and

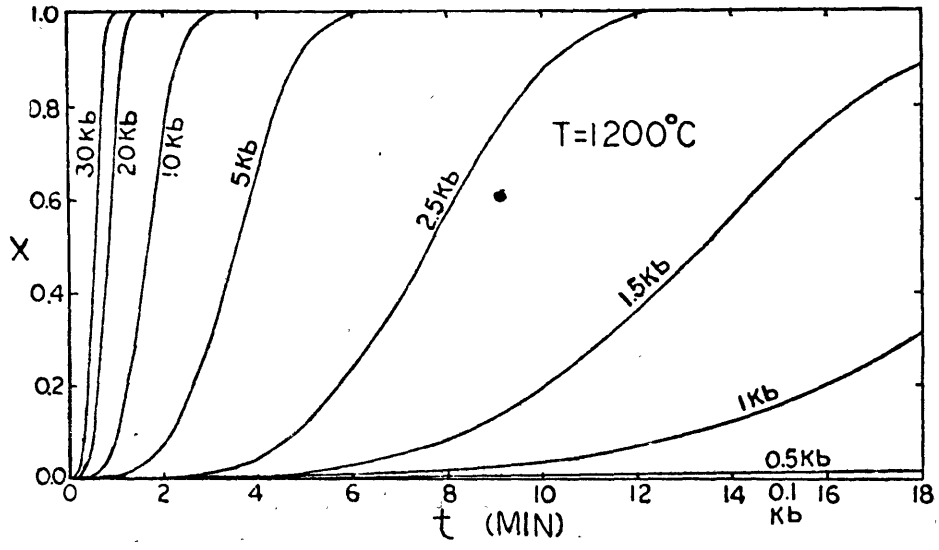

Fig. 4. The superpressure dependence of the rate of olivine-spinel transformation.

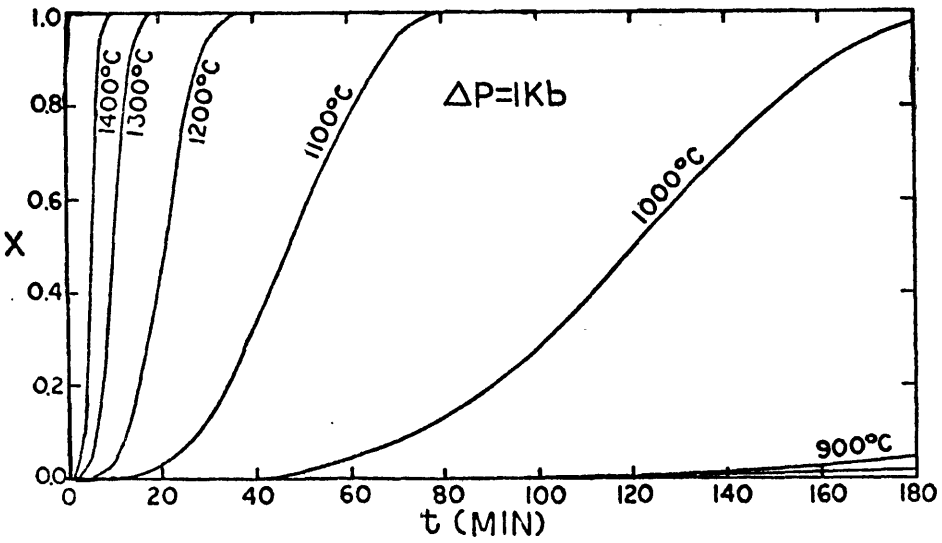

Fig. 5. temperature dependence of the rate of olivine-spinel transformation.

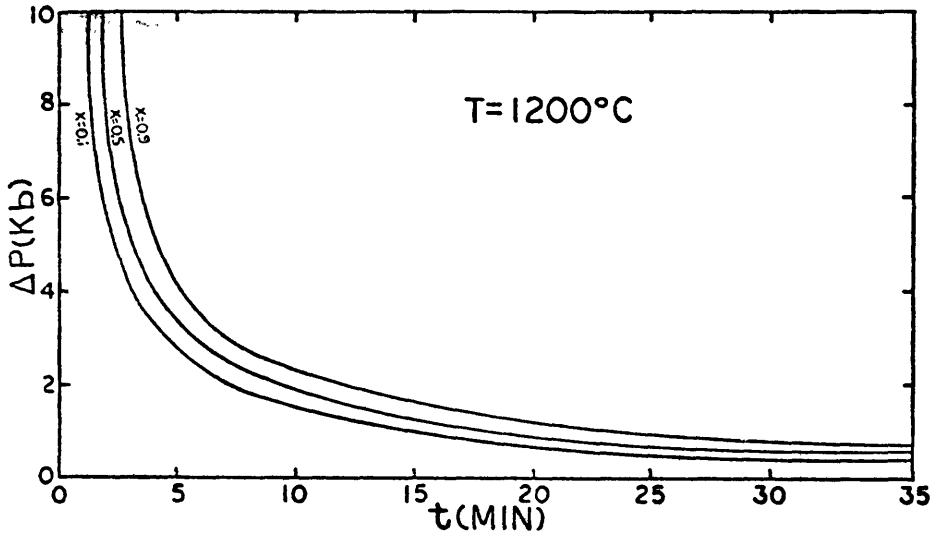

Fig. 6. The superpressure as a function of time for olivine-spinel transformation.

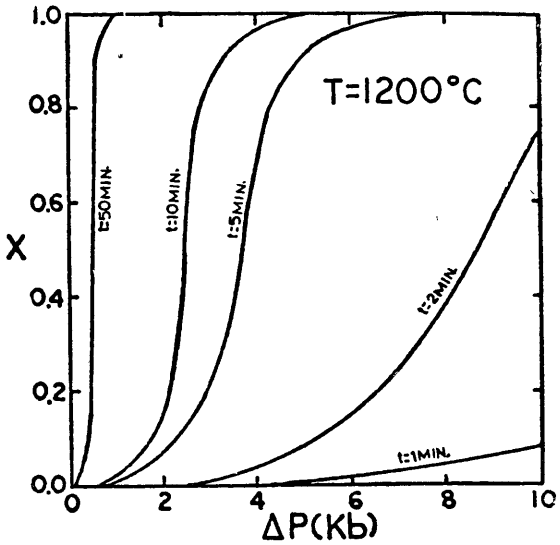

Fig. 7. The volume fraction of completion (X) as a function of superpressure for olivine-spinel transformation.

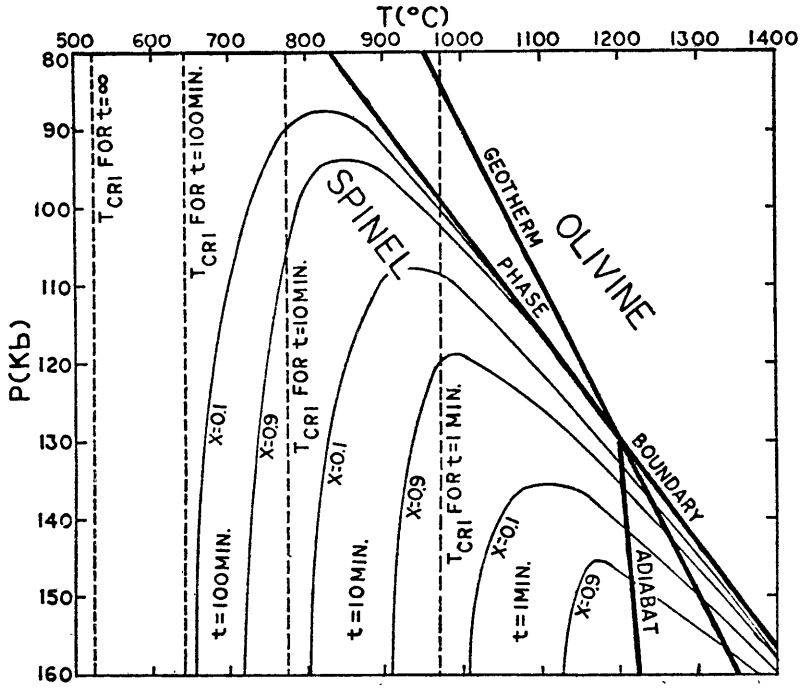

Fig. 8. The kinetics behavior of olivine-spinel transformation in the Mantle.

depends less sensitively on ΔP and T. However, the time for the completion of the whole process under very low superpressure at the temperature of upper Transition Zone is still short (about a few tens to a few hundred minutes), thus again prevent olivine from deep penetration into the metastability field.

Since the volume fractions of transformation (X's) for the experiments listed in Table 1 tend to be underestimated, the rate equation so derived may represent the lower limit of the real olivine-modified spinel transformation. This may be true even if X's for these experiments are really small because the slow nucleation rate at the incipient transformation may also result in small derived rate constants. If iron is added in the system, the olivine-spinel transformation can be facilitated due to crystal field stabilization. The isothermal phase diagram of the system Mg_2SiO_4—Fe_2SiO_4 (Fig. 9) suggests that the depression of free energy by adding iron into Mg_2SiO_4 is larger for spinel than olivine. If the surface tension (σ) between the two phases remain constant, the activation energy ΔF^* for the iron bearing olivine-spinel transformation may be less than that for pure Mg_2SiO_4. In addition, spinel is more stable than modified spinel under high pressures (Fig. 9), the driving force (ΔG) for olivine-spinel transformation is larger than that for olivine-modified spinel transformation, this may also reduce ΔF^*. However, the facilitation of olivine-spinel transformation with the presence of iron can be counterbalanced by the increase of ΔE due to the iron diffusion during its transformation. The rate constants estimated from the few experimental runs for the ovlivine-spinel transformation of the composition $(Mg_{0.93}, Fe_{0.07})_2SiO_4$ (Ito *et al.* 1971) are a little larger than that calculated from the derived rate equation. This suggests that the above rate equation may also represent the lower limit of olivine-spinel transformation for the natural mineral.

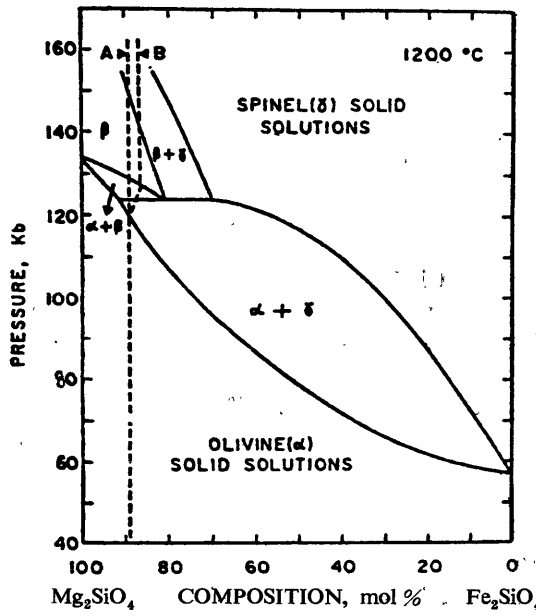

Fig. 9. The isothermal (1200°C) section of the system Mg_2Sio_4—Fe_2Sio_4. Dotted line (A) is the possible olivine composition and (B) is the spinel composition after correction for Fe^{++}/Mg^{++} partition between pyroxene and spinel (Nishizawa, *et al*, 1973).

DISCUSSION

If high pressure phase transformation could trigger deep earthquakes, they must occur very

fast and the heat loss through conduction becomes negligible during those transformations. The possible rate of heat generation for olivine-spinel transformation in a closed system under the physical conditions of upper Transition Zone is evaluated below and compared to that required for generating deep earthquakes.

The adiabat $(dP/dT)_S(=C_p/(V_\alpha T)$, where C_p and α are heat capacity and thermal expansion respectively) in the upper Transition Zone is about 1.2 kb/°C. The geotherm in this region is infened to be about 0.20 kb/°C (Fusisawa, 1968). The phase boundary of olivine-modified spinel transformation of composition Mg_2SiO_4 is not known accurately. Most of the data indicate that it has a slope of about 0.55 kb/°C (e. g. Ito *et al*, 1971). However, the latest experimental result (Suito, 1972) suggests a slope of 0 13 kb/°C. Here I tentatively use the average of these two, 0.093 kb/°C, for my discussion of the transition for natural olivine. Fig. 9 shows the relationship between the adiabat (*AE*), the geotherm (*AF*) and the phase boundary (*AI*) of olivine-spinel transformation at the intersection (point A) of the latter two in the upper Transition Zone. If the material at A is suddenly subjected to a superpressure, it may change following the adiabat. Heat then evolves due to olivine-spinel transformation and the material begins to heat up. If the transformation is complete, the final geotherm will be *ADCH*. However, as soon as the material recrosses the phase boundary, olivine becomes stable and the transformation stops. The geotherm is then limited by the phase boundary to be *ACH*. As heat dissipates through conduction, olivine may transform in equilibrium and the material stays on the phase boundary. However, after geological aging, the geotherm *ACH* will gradually move toward *ABE* (shown in fine line) and width of two phase region narrows. The temperature rise (ΔT_{100}) for total transformation can be calculated from heat evolved (ΔH) during this transformation and the heat capacity of the rock. Since the difference of heat capacity and thermal expansion between olivine and spinel is small, ΔH can be approximated by its value on the phase boundary, which equals to $T\Delta S$. ΔS is the entropy change in this transition and can be calculated through Clapeyron relation. The result gives $\Delta H \doteqdot 10105$ cal/mole $= 1.1 \times 10^{25}$ erg/km^3. Since the temperature in the upper Transition Zone has been well above the Debye temperatures for most of elements in silicates, C_p is then about 42 cal/mole for olivine. Assume the volume fraction of olivine in the rock is about 80%, this gives $\Delta T_{100} = 253$°C (no correction is made for the small contribution from the adiabat because of the existence of high uncertainty of this estimation). This correspond to the maximum width of the two phase region of 23 kb, which lies exactly in the middle of the range 18 to 28 kb proposed by Fujisawa (1968) and is in good agreement with some seismic studies (e. g. Kanamori, 1967, Johnson, 1967). If the superpressure ΔP is less than 23 kb, the proportion of rapid phase transformation, f, is limited by $f = \Delta P/23 = \Delta T/253$. This limitation can be relaxed, however, if the system is not closed and the energy transmitted through seismic waves.

If the superpressure for the olivine-spinel traniformation is tentatively assumed to be 1 kb. Then the temperature rise limitted by the phase boundary for this transformation will be 253/23 or 11°C. The maximum work extractable from the heat evolved during the transformation is then calculated from the second law of thermodynamics to be about 7.9×10^{22} erg/km^3. Bullen (1955) has estimated that the magnitude of energy density released by earthquakes of dislocation origin is no more than 10^{20} erg/km^3. If the generation of deep earthquakes requires the same magnitude of energy density, and if suitable mechanism, which can convert heat into seismic energy, exists, then this amount of energy density may correspond to a volume fraction (X) of olivine-spinel transformation of about 1.3×10^{-3}. Since $\Delta V/V$ for the total olivine-spinel transformation in the upper Transition Zone is about 0.074 and olivine comprises about 80% by volume in the Upper Mantle, this amounts a change of volume of 1.2×10^{-4} for the whole rock, which may be too small to be detectable by seismic means. Aki (1972) has estimated the fractional volume change associated with deep earthquakes to be about 10^{-4}, thus it seems possible to generate deep earthquakes by olivine-spinel transformation.

Bath (1966) has related the seismic energy E to the magnitude of earthquake M by log $E=12.24+1.44$. If the volume effected by the superpressure is 1 km^3, then the energy density of 10^{20} corresponds to an earthquake of magnitude 5.4. If this energy density is released in 1 minute, then the minimum rate of olivine-spinel transformation required to generate this earthquake is $dX/dt=1.6\times10^{-3}$/min. This rate of olivine-spinel transformation can be easily achieved with a superpressure greater than 0.1 kb at 1200°C from the rate equation derived previously. Even at $\Delta P=0.1$ kb, this rate of transformation can be attained after 150 min. of transformation. It seems possible for the natural processes to furnish this amount of superpressure, e. g. by collision of two plates or load filling of turbidites in the deep trenchs (the presence of superpressure does not necessary due to the increase of depth). Therefore, the generation of deep earthquakes by high pressure phase transformations seems to be possible. However, the superpressure can be applied gradually. The rate of phase transformation, and thus the rate of energy release is then limited by the rate of superpressure accumulation. The general kinetics equation for high pressure phase transformation with variable ΔP and T is

$$X=\int_{\Delta P_1}^{\Delta P_2}\int_{T_1}^{T_2}\int_{t_1}^{t_2}(1-\exp(-Kt^4))\,d\Delta P dT dt/((\Delta P_2-\Delta P_1)(T_2-T_1)(t_2-t_1)$$

For the olivine-spinel transformation with $dX/dt=1.6\times10^{-3}$/min. This may require a minimum rate of superpressure accumulation of about 0.006 kb/min or 1 kb/day. Since this high rate of superpressure accumulation may never be attainable in the mantle, it appears unlikely that the olivine-spinel transformation can directly generate deep earthquakes. In addition, even if the rate of heat generation is fast enough, it can only increase the internal energy and entropy of the rock because no suitable mechanism apparently exists to efficiently convert the heat into seismic energy.

Mendiguren (1970) has suggested a mechanism that the surrounding material may behave elastically when the interior material undertakes phase transition and collapse during the latter stage to generate earthquakes. In this case the earthquakes are preceded by the volume contraction as has been observed by Dziewonski *et al* (1974). Even though the fractional volume change associated with phase transformation is small, the total volume contraction may be enormous if the volume of the rock undertaking the phase transition is large. For example, if the rate of superpressure accumulation of 1 kb/year is applied to a volume of 1 km^3, the rate of total volume contraction will be about 5000 cm^3/year (the fractional volume change is about 10^{-4}/year). This rate of volume contraction is much higher than that can be compensated by the plastic flow of the surrounding rock, therefore it can creat or increase the stress in the surrounding rock and trigger the catastrophic shear flow as soon as the stress becomes higher than the creep strength of the rock. Since the temperature rise during the olivine-spinel transformation is limited by its phase boundary, being about 11°C for a superpressure of 1 kb, and the solidus of the rock in the upper Transition Zone may well be above the geotherm, it seems unlikely that the heat generated by phase transformation will result in partial melting of the rock. The heat required for shear melting, which was suggested by Griggs *et al.* (1968) as a possible mechanism for deep earthquakes, may not come from phase transformation but from the friction of the rocks. The high pressure phase transformations can, therefore, only be indirectly related to the deep earthquakes by inducing the shear flow through volume contraction.

Some seismologists tend to believe that the deep penetration into the metastability field for the phase transformation may store implosive potential energy for deep earthquakes. The impossibility of deep penetration into the metastability field for the olivine-spinel and pyroxene-spinel and pyroxene-garnet transformations has been described. Even this could happen, the transformation must be very sluguish and occur at temperature close to T_{cr1}. The path of the transformation will be $AB'C'$ in Fig. 10. In this case the catastrophic implosion may never occur because the rate of transformation is always slow although it is an accelerating process. The

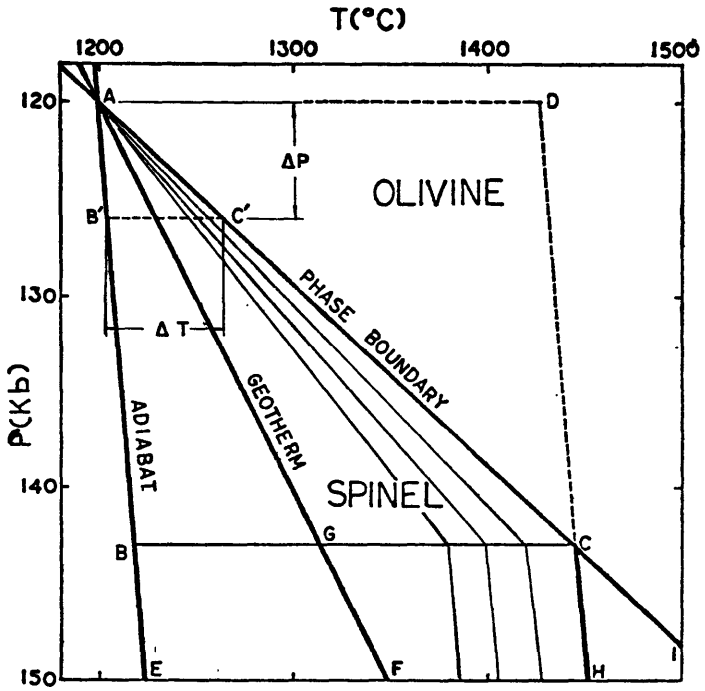

Fig. 10. The effect of olivine-spinel transformation on the geotherm in the Mantle.

present study indicates that the rate of transformation must be high throughout the process (path *AC'* in Fig. 10) in order to make this energy explosion possible. The rate of high pressure transformation depends on the rate of superpressure accumulation, which, therefore, determines the rate of implosion and thus the possibility of generation the deep earthquakes.

Other factors such as water content, grain size, heterogeneous nucleation and compositional variation of the transforming phase may also affect the kinetics of the high pressure phase transformations. The final understanding of the kinetics may rely on the experimental, results.

ACKNOWLEDGEMENTS

This study was motivated by Prof. R. G. Burns who has also carefully reviewed and criticized this manuscript. Prof. K. Aki and Messrs. J. Besancon, F. Huggins, M. Obata, and A. Smith have offered the author many constructive suggestions. Their efforts are fully appreciated.

REFERENCES

AKI, K. (1972) Earthquake mechanism: Tectonophysics, vol. 13, pp. 423-446.

AKIMOTO, S. and FUJISAWA, H. (1968) Olivine-spinel solid solution equilibria in the system Mg_2SiO_4—Fe_2SiO_4: J. Geophys. Res.' vol. 73, pp. 1467-1479.

_____ and KAWADA, K. (1973) Refinement of phase equilibrium study in the system Mg_2SiO_4—Fe_2SiO_4 at high pressures and temperatures: Phys. Earth Planet. Interiors (in press).

BATH, M. (1966) Earthquake Seismology: Earth Sci. Rev., vol. 1, p. 69.

BENIOFF, H. (1963) Source wave forms of three earthquakes: Bull. Seism. Soc. Am., vol. 53, pp. 893-903.

BRACE, W. F. and WALSH, J. B. (1962) Some direct measurements of the surface energy of quartz and orthoclase: Am. Mineral., vol. 47, pp. 1111-1112.

BRIDGMAN, P. W. (1945) Polymorphic transitions and geological phenomena: Am. J. Sci., vol. 243A, p. 90.

BULLEN, K. E. (1955) On the size of the strained region prior to an extreme earthquake: Bull. Seism. Soc. Am., vol. 45, pp. 43–46.

CLARK, JR. S. P. (EDITOR) (1966) Handbook of physical constants, revised edition: Geol. Soc. Am. Memoir 97.

DZIEWONSKI, A. M. and GILBERT, F. (1974) Temporal variation of the seismic moment tensor and the evidence of precursive composition for two deep earthquakes: Nature, vol. 247, p. 185.

EVISON, F. (1963) Earthquakes and faults: Bull. Seism. Soc. Am., vol. 53, pp. 873–891.

_____ (1967) On the occurrence of volume change at the earthquake source: Bull. Seism. Soc. Am., vol. 57, pp. 9–25.

FUJISAWA, H. (1968) Temperature and discontinuities in the Transition Layer within the earth's Mantle: J. Geophys. Res., vol. 73, pp. 3281–3294.

GILMAN, J. J. (1960) Direct measurement of the surface energies of crystals: J. Appl. Phys., vol. 31, pp. 2208–2218.

GRIGGS, D. T. and BAKER, D. W. (1969) in "Properties of Matter under Unusual Conditions", edit. by Mark, H. and Fernbach, S., Wiley, New York.

GUTENBERG, B. and RICHTER, C. F. (1956) Magnitude and energy of earthquakes: Annali di Geofisica, vol. 9, pp. 1–15.

HURLEY, P. M. (1972) Chemistry of the earth (lecture notes).

ITO, K., ENDO, S. and NAOTO, K. (1971) Olivine-spinel transformation in a natural fosterite: Phys. Earth Planet. Interiors, vol. 4, pp. 425–428.

KAMB, B. (1968) Structural basis of the olivine-spinel stability relation: Am. Mineral. vol. 53, pp. 1439–1455.

KASHARA and TSUKAHRA, H. (1971) Experimental measurements of reaction rate at the phase change of nickel olivine to nickel spinel: J. Phys. Earth, vol. 19, pp. 79–88.

KCKERROW, W. S. and LAMBERT, R. ST. J. (1973) Deep earthquakes, Surface subsidence and Mantle phase changes: J. Geol., vol. 81, pp. 157–175.

KANANORI, H. (1967) Upper Mantle structure: Bull. Earthquake Res. Inst., Tokyo Univ., vol. 45, p. 657.

JOHNSON, L. R. (1967) Array measurements of P velocities in the Upper Mantle: J. Geophys. Res. vol. 72, p. 6309.

MENDIGUREN, J. A. (1970) Speculations on phase changes in the earth's interior, Term paper, M. I. T.

_____ (1972) Source mechanism of a deep earthquake, Ph. D. thesis, M. I. T.

NISHIZAWA, O. and AKIMOTO, S. (1973) Partition of Mg and Fe between olivine and spinel and between pyroxene and spinel: Contr. Mineral. Petrol., vol. 41, pp. 217–230.

RANDALL, M. J. (1964) On the mechanisms of earthquakes: Bull. Seism. Soc. Am. vol. 54, pp. 1283–1289.

_____ (1964*a*) Seismic energy generated by a sudden volume change: Bull. Seism. Soc. Am. vol. 54, pp. 1291–1298.

RINGWOOD, A. E. (1967) The pyroxene-garnet transformation in the earth's Mantle: Earth Planet. Sci. Lett., vol. 2, pp. 255–263.

_____ (1970) Phase transformations and the constitution of the Mantle: Phys. Earth Planet. Interiors, vol. 3, pp. 109–155.

_____ and MAJOR, A. (1966) High pressure transformations in pyroxenes: Earth Planet. Sci. Lett. vol. 1, pp. 351–357.

SUITO, K. (1972) Phase transformations of pure Mg_2SiO_4 into a spinel structure under high pressures and temperatures, J. Phys. Earth, vol. 20, pp. 225–243.

地函內高溫相變之動力學與深源地震之可能相關性

宋　健　民

節　要

橄欖石—尖晶石，及輝石—石榴子石間之相變引起上部轉移帶中震波速度不連續關係，可由其相變之速率函數概略計算之。該二相變之速率隨溫度和超壓（超過平衡之壓力）而銳增。在上部轉移帶的物理條件下，橄欖石—尖晶石相變所放出之能量可由導出之速率函數加以估計。如使放出能量之速率與深源地震所需者相較，則累積超壓之速率必須高達每日一千粑 (1 kb/day)。由於地函中累積之超壓速率不可能達到此項數字，而且也無適當過程將熱能有效地轉換成地震能，如此，則高壓相變似乎不可能直接造成深源地震。然而由相變所引起之縮減體積及散發之熱能或可觸發地函內之塑性剪力流，因此可能間接引發深源地震。

APPENDIX

THEORY OF KINETICS FOR SOLID STATE PHASE TRANSFORMATIONS

Solid state phase transformations fall into two categories; those with compositional or structural fluctuations small in intensity but large in extensity and vice versa. The former occurs in transforming unstable phase into stable phase, therefore proceeds spontaneously without nucleation, such as spinodal decomposition and order-disorder transformation. The latter occurs in transforming metastable phase into stable phase, therefore requires to overcome an energy barrier by nucleation. Those nucleation-required transformations can be further divided into two types based on the presence or absence of cation diffusion. The diffusionless (martensitic) transformations proceed by distortion of the structures in such a way that all coordination relations are maintained. It can occur athermicly and propagate in such a fast rate as to approach the speed of sound. The diffusion (long or short ranged)—controlled transformations. Which include most of solid state reactions and polymorphic phase changes, are thermally agitable. Their behaviors, which can be described by classical models of nucleation and growth, are main objective of this paper.

The free energy decrease (ΔF) in forming a nucleus of a stable phase is

$$\Delta F = V\Delta G + A\sigma$$

Where V and A are volume and surface area of the nucleus, respectively; ΔG is the decrease of volume free energy; and σ is the surface tension (including strain energy) of the interphase boundary. If the transformed phase is isotropic, as assumed in spinel and garnet, the nucleus becomes spherical, and thus

$$\Delta F = (4/3)\pi r^3\Delta G + 4\pi r^2\sigma$$

Where r is the radius of the nucleus. A plot of ΔF versus r for metastable (saturated) and stable (undersaturated) transforming phases is shown in Fig. A. 1. It is found that the nucleus of the transformed phase in the metastable matrix becomes stable if it can grow larger than a critical size. The energy barrier (ΔF^*) for this nucleation and the radius (r^*) of the critical-sized nucleus can be found by $d\Delta F/dr=0$ at $r=r^*$, which gives

$$\Delta F^* = 16\pi\sigma^3/(3\Delta G^2) \quad \cdots\cdots(1)$$

$$\text{and } r^*=2\sigma/-\Delta G \quad \cdots\cdots(2)$$

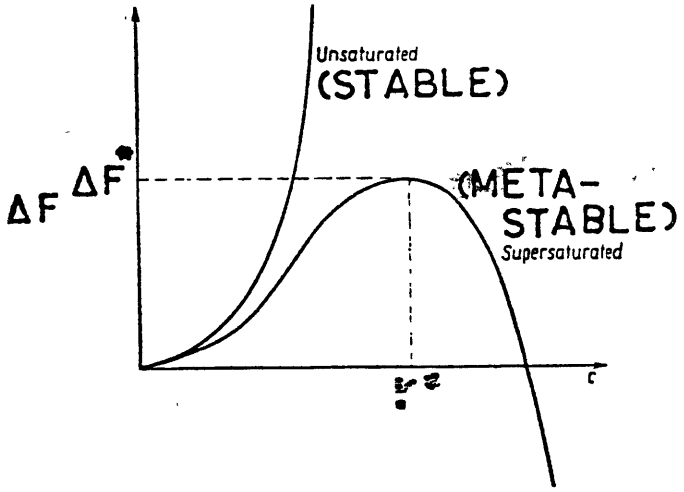

Fig. A. 1. Energy barrier for nucleation (F^*) as a function of size of nucleus

The activation energy ΔF^* lies at a multidimensional saddle point with maximum at r^* along the size coordinate and minima along all other coordinates. It decreases with the increasing of penetration into a metastable field (ΔG increases in equation (1)).

There is another kind of energy barrier to be overcome during nucleation and growth, i. e. the activation energy (ΔE) for diffusion or the energy barrier required to be surpassed during ion migration. If there is no chemical concentration gradient built up, i. e. during an isochemical transition, ΔE reduces to the energy required to detach ions from the transforming phase and is almost pressure and temperature independent as assumed in this paper for pyroxene-garnet transition. ΔE may be trivial compared to ΔF^* when the transformation occurs close to equilibrium, but it becomes more and more important as ΔF^* gradually vanishes during increasing of metastability. The combined effect of those two activation energies is shown by the projection of energy saddle region on energy vs r plane in Fig. A. 2.

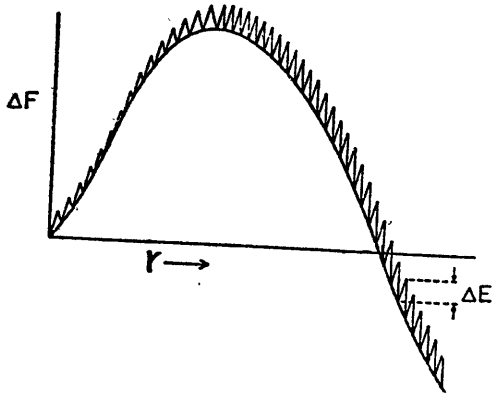

Fig. A. 2. The two kinds of activation energy for nucleation.

Since the average kinetic energy for an atom at temperature $T(°K)$ is kT, where k is Boltzman constant, the probability for an atom to surmount an energy barrier of Q is expressed by the Boltzman factor $\exp(-Q/(kT))$, where Q may stand for ΔF^* or ΔE. If the number of atoms per unit volume for a transforming phase is N, the number of critical sized nucleus of the transformed phase, when reaching steady state, will be $N\exp(-\Delta F^*/(kT))$ per unit volume. The probability of success for an atom to cross the phase boundary is $\exp(-\Delta E/(kT))$. The number of times an atom tries to jump across the boundary or the frequency of the atomic vibration at temperature T is about kT/h (Eyring theory), where h is Planck constant. If the number of atoms surrounding a critical sized nucleus is s^*, then the rate of adding atoms to the nuclei will be $s^*(kT/h)\exp(-\Delta E/(kT))$ per second. The homogeneous, steady state nucleation rate (I), i. e. the number of critical sized nucleus formed per second in an unit volume, will be the product of the critical sized nucleus and the rate of adding atoms to the nucleus or

$$I = Ns^*(kT/h)\exp(-(\Delta F^* + \Delta E)/(kT))$$

A more sophiscated equation known as Becker-Döring theory which takes into account the reversed reaction of the transformation is shown below

$$I = N(A^*/n)(kT/h)(\Delta F^*/(3\pi kT))^{1/2}\exp(-(\Delta F^* + \Delta E)/(kT))$$

Where A^* and n are surface area and number of atoms in the critical-sized nucleus respectively. A schematical representation of I versus the parameter to measure the metastability (ΔG) in terms of ΔP or ΔT, which are the pressure and temperature beyond the equilibrium, is shown in Fig. A. 3. The relation of time required to form a particular number of critical-sized nucleus to ΔP and ΔT is shown in Fig. A. 4.

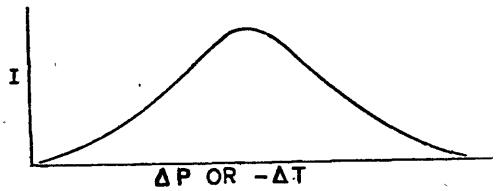

Fig. A. 3. The rate of nucleation as a function of metastability

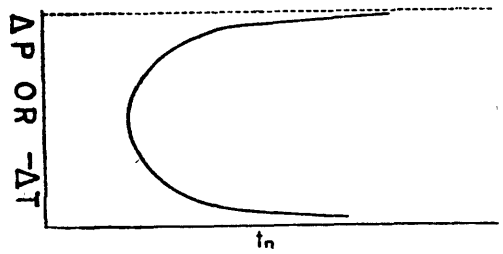

Fig. A. 4. The time to form a certain number of nuclei (t_n) as a function of metastability.

The activation energies for moving an atom from metastable to stable phase and the reversed reaction are ΔE and $\Delta E + [\Delta G]$ respectively (the bracket here denotes absolute value). Therefore the net rate of accretion of atoms to the nucleus is

$$s^*(kT/h)\exp(-\Delta E/(kT))(1-\exp(-[\Delta G/N]/(kT)))$$

Since for each increment of s^* atoms to the critical sized nucleus, It grows one unit of interphase boundary thickness (1), therefore the linear growth rate (Y) for the nucleus is

$$Y = 1\,(kT/h)\exp(-\Delta E/(kT))(1-\exp(-[\Delta G/N]/(kT)))$$

The variation of Y vs ΔP or ΔT is shown in Fig. A. 5.

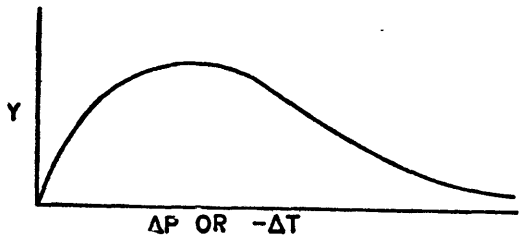

Fig. A. 5. The linear growth rate (Y) as a function of metastability.

For a steady state (constant I and Y) homogeneous nucleation process, the volume fraction (X) of the transformed phase as a function of time t for solid state polymorphic transformation can be expressed by

$$X = 1 - \exp(-Kt^4) \quad \cdots\cdots(3)$$

The rate constant K in the above equation can be related to nucleation (I) and growth (Y) rate by

$$K = wIY_1Y_2Y_3/4$$

Where w is a shape factor for the the nucleus and the subscripts of Y's denote the three spacial coordinates for growth. For the spheric nucleus, $w=(4\pi/3)$ and $Y_1=Y_2=Y_3=Y$, then

$$K = (\pi/3)IY^3$$
$$= (\pi/3)N1^3(A^*/n)(kT/h)^4(\Delta F^*/(3\pi kT))^{1/2}$$
$$\exp(-(\Delta F^* + 4\Delta E)/(kT))\,(1-\exp(-[\Delta G/N]/(kT))) \quad \cdots\cdots\cdots\cdots(4)$$

The rate constant K is seen to depend sensitively on composition, temperature and the volume free energy decrease (ΔG) of the transition. The last variable, which is the driving force of this transition, depends in turns on ΔP and ΔT. The volume fraction of completion (X) of this process is, therefore, a function of those variables and time. The dependence of X on ΔP, ΔT and t is schematically shown in Fig. A. 6.

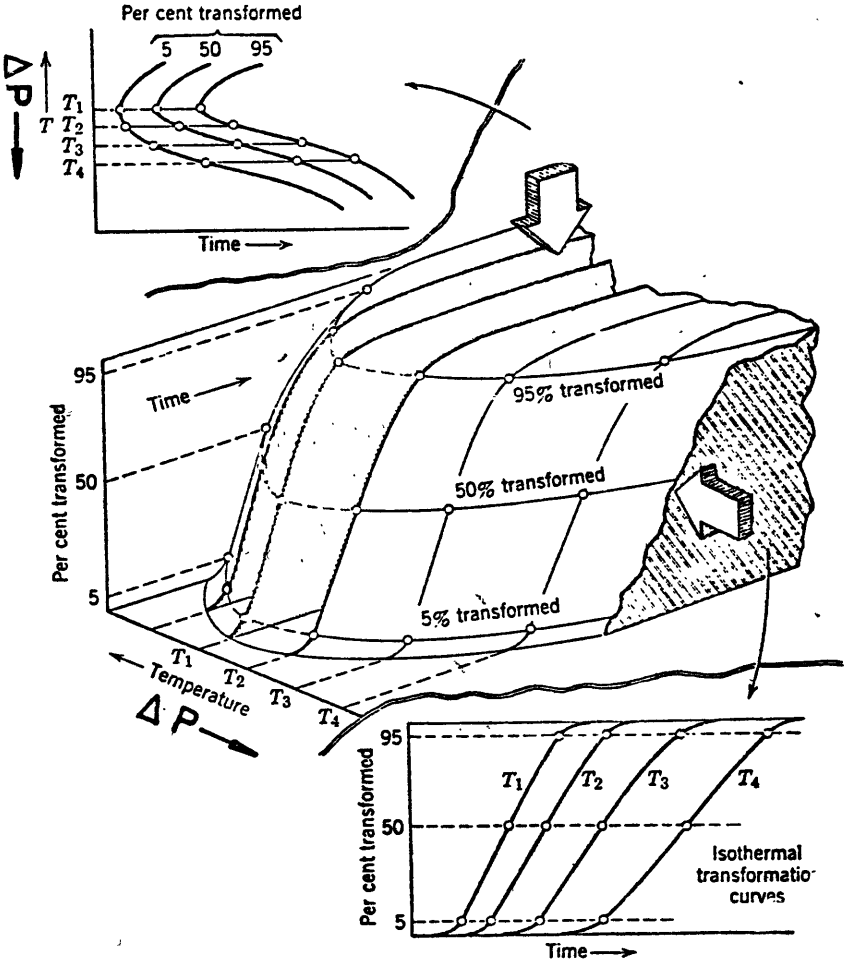

Fig. A. 6. The volume fraction of completion for a transformation as a function of metastability ans time.

REFERENCES

AARONSON, H. I., EDITOR (1970) Phase Transformations, Chapman and Hall Ltd., London.

CHRISTIAN, J. W. (1965) The Theory of Phase Transformations in Metals and Alloys, Pergamon Press, Oxford, London.

FINE, M. E. (1964) Introduction to Phase Transformations in Condensed Systems, The MacMillan Co., New York Collier-MacMillan Ltd., London.

Tectonophysics, 31 (1976) 1—32

KINETICS OF HIGH-PRESSURE PHASE TRANSFORMATIONS: IMPLICATIONS TO THE EVOLUTION OF THE OLIVINE → SPINEL TRANSITION IN THE DOWNGOING LITHOSPHERE AND ITS CONSEQUENCES ON THE DYNAMICS OF THE MANTLE

CHIEN-MIN SUNG and ROGER G. BURNS

Department of Earth and Planetary Sciences, Massachusetts Institute of Technology, Cambridge, Mass. (U.S.A.)

(Submitted May 24, 1975; accepted October 23, 1975)

ABSTRACT

Sung, C.-M. and Burns, R.G., 1976. Kinetics of high-pressure phase transformations: implications to the evolution of the olivine → spinel transition in the downgoing lithosphere and its consequences on the dynamics of the mantle. Tectonophysics, 31: 1—32.

The rate of a high-pressure phase transition increases exponentially with temperature (T) and overpressure or pressure beyond equilibrium (ΔP). It is also greatly promoted by introducing shear stress, diminishing grain size, and adding water or other catalysts to the reactants. For an isothermal and isobaric transition with no compositional change, if steady state of nucleation on grain surfaces is attained, the rate equation can be expressed: (1) before site saturation by: $X = 1 - \exp(-Kt^4)$, where $K = C_1 T^4 \exp[-\{C_2/(C_3 + C_4\Delta P)^2 + C_5/T\}][\exp(-C_6/T) - \exp\{-(C_7 + C_8\Delta P)/T\}]^3$; and (2) after site saturation by: $X = 1 - \exp(-K'T)$, where $K' = C_9 T[\exp(-C_6/T) - \exp\{-(C_7 + C_8\Delta P/T)\}]$, where X is volume fraction of completion of transformation, t is time, and the C's are characteristic constants. C_1 and C_9 are functions of grain size, C_3 and C_6 are functions of shear stress. All the C's are almost independent of temperature and pressure. Thus, if X as a function of T, ΔP, and t over a narrow P-T range can be experimentally determined, the C's can be calculated and the effect of grain size and shear stress on the rate of transformation can be evaluated. The isothermal and isobaric rate equations for a given composition, shear stress, and grain size are then experimentally determinable. The non-isothermal and non-isobaric rate equation can be calculated from the isothermal and isobaric ones if the rate of penetration into the metastability field is known. The important feature of the kinetics of high-pressure phase transitions predicted by these rate equations is that for a given rate of penetration into the metastability field, there can be defined a characteristic temperature, T_{ch}, below which the rate of the transition is virtually zero no matter how metastable the material is. For the olivine → spinel transition in the mantle, this characteristic temperature may be as high as 700°C. Thus, in a fast moving downgoing slab, the temperature at its cold center may remain below T_{ch} even down to depths in excess of 600 km, thereby greatly depressing the olivine—spinel phase boundary.

At an early stage in the development of a downgoing slab, the plunging speed is slow. This allows the interior of the slab to heat up and the olivine → spinel transition to proceed rapidly and near equilibrium. As a result, the olivine—spinel phase boundary in the slab will be distorted upwards. The rising of the denser spinel phase then provides an additional

driving force which accelerates the plate. Since the upper portion of the slab is pulled from below and the lower portion pushed from above, earthquakes of down-dip extension will occur in the upper mantle while those of down-dip compression will originate in the transition zone. Because the transformation occurs close to equilibrium, there will be an aseismic region separating the two seismic zones. When the plate velocity exceeds a certain limit, the temperature in the cold interior becomes low enough to depress the olivine → spinel transition. The phase boundary is then distorted downwards. The buoyant force thereby created will reduce the driving force, and the plunging speed of the plate will approach a steady state. In addition, the buoyant force will compress the slab from below and result in earthquakes of down-dip compression throughout the length of the slab. Now the olivine → spinel transition is so far from equilibrium that the reaction becomes implosive. A rise in frequency of deep earthquakes towards the implosion region in the lower transition zone is thus predicted. Therefore, as well as stabilizing the plate velocity, the olivine → spinel transition may also control earthquake distributions throughout the downgoing slab.

INTRODUCTION

Olivine (α-structure) is the dominant phase in the upper mantle. At depths around 400 km below normal tectonic provinces (oceanic and continental), it undergoes a series of transitions: olivine → olivine + spinel (γ-phase), olivine + spinel → olivine + modified spinel (β-phase), and olivine + β-phase → β-phase, thereby delineating the onset of the transition zone. Manifestations of these transitions are the rapid rises of seismic velocities, density, and possibly temperature gradient which mark the 400-km discontinuity. However, since the stability field of the β-phase is wedged out at low temperature, within the cold interior of a downgoing slab, olivine may transform directly into spinel. The olivine → spinel transition has been inferred to be a source of deep-focus earthquakes and a driving mechanism for downgoing slabs (Turcotte and Schubert, 1971; Ringwood, 1972, 1973; Schubert et al., in preparation). Although the consequences of the olivine → spinel transition in the mantle are generally well recognized, little attention has been paid to the effect of the kinetics of the transition on mantle dynamics (Sung, 1974; Burns and Sung, 1975; Sung, 1975). In this paper, we demonstrate that certain apparently contradictory geophysical observations in the mantle may be explained by variations in the rate of the olivine → spinel transition in the downgoing slab. Our approach calls for a general discussion of the kinetics of high-pressure phase transformations which are directly applicable to the mantle.

KINETICS OF FIRST-ORDER PHASE TRANSITIONS IN SOLIDS UNDER HIGH PRESSURES

The simplest kinetics equation for a chemical reaction is:

$$dX/dt = K(1 - X)^p \qquad (1)$$

where X is the degree of completion of the reaction; t is time; K is the rate

constant; and p is the order of the reaction. The large scatter of p-values in previous experimental data (e.g. Davis and Adams, 1965; Kasahara et al., 1971; Kasahara and Tsukahara, 1971) suggests that eq. 1 is inadequate for first-order solid-state transitions. Because no suitable rate equation exists for a first-order solid—solid transformation at high pressures, we derive here such a rate equation for a high-pressure solid → solid transition as a function of parameters such as shear stress, grain size, pressure, temperature, and overpressure (pressure beyond equilibrium) for each composition, which may be experimentally determined.

Phase transformations in solids are of two types: homogeneous and heterogeneous. Homogeneous transformations occur spontaneously over the entire material and there is no demarcation between the transforming and the transformed phases. Examples are order—disorder transformations. Heterogeneous transitions are larger in degree and smaller in extent and require an energy barrier to be overcome. This provides a high energy activated complex or transition state which separates the transformation into two recognizable stages: nucleation and growth. In heterogeneous or first-order phase transformations, the transforming and transformed phases are separated by a boundary which may be either sharp or diffuse. The olivine → β-phase and olivine → spinel (γ-phase) transitions are examples of heterogeneous transformations, and thus can be described by a model of nucleation and growth. We shall here extend the classical model of nucleation and growth to be applicable at high pressures. Because there are currently no suitable experimental data for quantitative kinetic calculations, and we are interested only in the qualitative behavior of high-pressure phase transformations in later discussions of mantle processes, we shall, for simplicity, restrict our derivation of a kinetics equation to an isochemical transformation.

Some energies may be released while the others may be absorbed during a phase transformation. In general, the total energy change, ΔG_T, for a solid—solid phase transformation under high pressure can be expressed by:

$$\Delta G_T = \Delta G + \Delta E^h + \Delta E^d + \xi + \sigma \qquad (2)$$

where ΔG is the Gibbs free energy decrease; ΔE^h is the energy of heterogeneity (grain surface, grain boundary, dislocation, point defect, etc.) which is released during the phase transformation; ΔE^d is the distortion energy (shear-strain energy) introduced by the application of high pressure; ξ is the strain energy created by the volume difference between the two phases; and σ is the surface energy created by the formation of the new interphase boundary.

Relationships among these energies are shown schematically in Fig. 1, in which the subscript "a" is used to denote quantities per atom or per molecule. The separation of these energies into components is for the convenience of evaluating their roles in the kinetics of transformation. It should be borne in mind that the component energy terms may not be independent of one another.

The first three terms in eq. 2 are negative and the last two terms are positive.

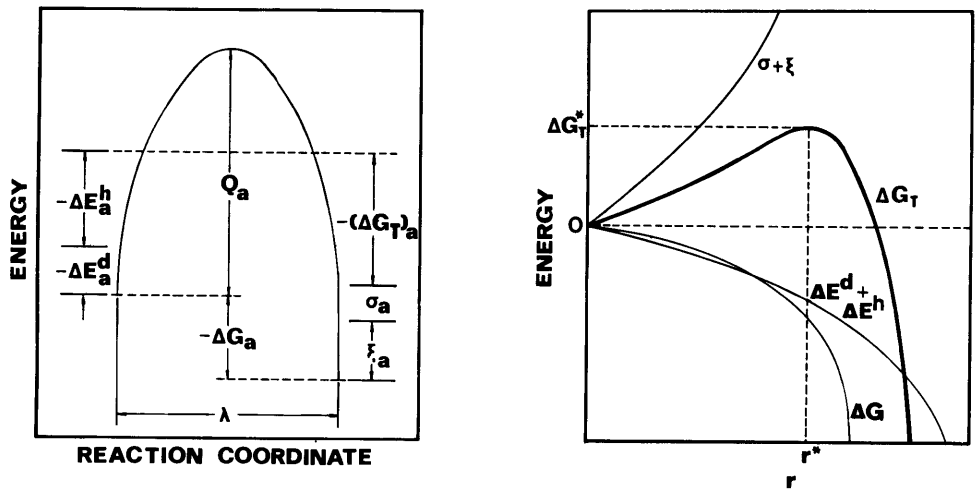

Fig. 1. Variation of energies during the migration of each atom from the metastable phase (left-hand side) to the stable phase (right-hand side). Note that ΔG_a, ΔE_a^h, and ΔE_a^d are released while σ_a and ξ_a are absorbed during the transformation. The overall energy change is $(\Delta G_T)_a$.

Fig. 2. Variation of released energy ($\Delta E^d + \Delta E^h$), absorbed energy ($\sigma + \xi$), and total energy change, ΔG_T with the nucleus size of the transformed phase, r. The zero energy refers to the original state before transformation.

The first three energy factors are thus positive driving forces and the last two negative driving forces for a phase transformation. A plot of these energies versus the average radius of the nucleus, r, of a transformed phase is shown schematically in Fig. 2. There exists a maximum value of ΔG_T (i.e. ΔG_T*) when the nucleus size reaches a critical value, $r = r^*$. This energy barrier is one of the two activation energies for nucleation. The other one, Q_a in Fig. 1, comes from the migration of atoms across the interphase boundary. If the chemical composition changes during a transformation, the activation energy of long-range diffusion will provide another energy barrier for nucleation. The nucleation path is such that it will minimize those energy barriers. For each of these activation energies, ΔG_T* will be important only when the transformation occurs close to equilibrium; the rate of the transformation will then be controlled by Q_a alone, especially when the penetration into the metastability field is deep. In a real transformation, ξ, σ, and Q will be anisotropic. The nucleus shape is such that it then minimizes these energies.

Several competing modes constitute the nucleation process. They include homogeneous or volume nucleation, and nucleation on grain surfaces, on grain boundaries, on dislocations, on point defects, etc. Homogeneous nucleation is important only when the crystal size is large and the driving force, $-\Delta G$, is large. For most high-pressure experiments, the starting material is in a powdered form. This will make nucleation on grain surfaces a dominant mode. Our preliminary experiments show that spinel nucleates predominantly

on the grain surfaces of fayalite powder. Hence, we shall consider only nucleation on grain surfaces and introduce $\Delta E^h = \Delta E^s$, where ΔE^s is the energy of grain surfaces, in the following discussion.

In the following equations, the superscript "—" applies to thermodynamic quantities per unit volume (for $\Delta\overline{V}$, $\Delta\overline{G}$, $\Delta\overline{E}^d$, $\overline{\xi}$, and $\overline{Q}$) or per unit area (for $\Delta\overline{E}^s$ and $\overline{\sigma}$), whereas the subscript "a" is used to denote quantities per atom or per molecule.

We have:

$$\Delta G = \eta_V r^3 \Delta\overline{G} \sim \eta_v r^3 \Delta\overline{V}\Delta P \tag{3}$$

$$\Delta E^s = \eta_A r^2 \Delta\overline{E}^s \tag{4}$$

$$\Delta E^d = \eta_V r^3 \overline{\xi} \tag{5}$$

$$\xi = \eta_V r^3 \overline{\xi} \tag{6}$$

$$\sigma = \eta_A r^2 \overline{\sigma} \tag{7}$$

where η_V and η_A are shape factors of the nucleus for volume and surface area, respectively.

$$\Delta G_T = \eta_V r^3 \Delta\overline{E}^V + \eta_A r^2 \Delta\overline{E}^A \tag{8}$$

where:

$$\Delta\overline{E}^V = \Delta\overline{V}\Delta P + \Delta\overline{E}^d + \overline{\xi} \tag{9}$$

$$\Delta\overline{E}^A = \Delta\overline{E}^s + \overline{\sigma} \tag{10}$$

$$\text{at } r = r^*, \quad \Delta G_T = \Delta G_T^*, \quad d\Delta G_T/dr = 0 \tag{11}$$

we get:

$$r^* = -(2\eta_A \Delta\overline{E}^A)/(3\eta_V \Delta\overline{E}^V) \tag{12}$$

$$\Delta G_T^* = (4\eta_A^3 \Delta\overline{E}^{A\,3})/(27\eta_V^2 \Delta\overline{E}^{V2}) \tag{13}$$

$$n^* = -(8\overline{N}_V/27)(\eta_A^3/\eta_V^2)(\Delta\overline{E}_A^3/\Delta\overline{E}^{V3}) \tag{14}$$

where n^* is the number of atoms or molecules in the critical-sized nucleus, and $\overline{N}_V$ is the number of atoms or molecules per unit volume. Also, we have:

$$\Delta G_a = (\Delta\overline{V}/\overline{N}_V)\Delta P \tag{15}$$

$$\Delta E_a^s = (\eta_A/\eta_V)(\Delta\overline{E}^s/\overline{N}_V)(1/r) \tag{16}$$

$$\Delta E_a^d = \Delta\overline{E}^d/\overline{N}_V \tag{17}$$

$$\xi_a = \overline{\xi}/\overline{N}_V \tag{18}$$

$$\sigma_a = (\eta_A/\eta_V)(\overline{\sigma}/\overline{N}_V)(1/r) \tag{19}$$

$$Q_a = \overline{Q}/\overline{N}_V \tag{20}$$

For an isothermal and isobaric transformation, if the shape of the nucleus

is independent of its size, the quantities $\Delta\overline{G}$, $\bar{\xi}$, $\Delta\overline{E}^{s}$, $\bar{\sigma}$, r^*, $\bar{\Delta}G_T^*$, n^*, and also ΔG_a, ξ_a, Q_a, $\Delta E_a^s \cdot r$, $\sigma_a \cdot r$ are all approximately constant. In general, material will yield under high pressure, so that the shear stress is then equal to its yield shear strength. If the transformed phase is free of shear stress, then:

$$\Delta\overline{E}^{d} = -[(\sigma_1 - \sigma_2)^2 + (\sigma_2 - \sigma_3)^2 + (\sigma_3 - \sigma_1)^2]/12\mu \tag{21}$$

where σ_1, σ_2, and σ_3 are the three principal stress values and μ is the shear modulus of the transforming phase. If, in particular, the stress is uniaxial, then this reduces to $\Delta\overline{E}^{d} = -(2/3)(\tau_{st}/\mu)$, where τ_{st} is the yield shear strength of the transforming phase.

The energy barrier for nucleation, ΔG_T^*, is created by both the surface energy of the interphase boundary, σ, and the strain energy due to the volume change of the transformation, ξ. The former will not displace the transition boundary but will decrease the nucleation rate by increasing the critical size of the nucleus (eq. 12). However, the latter will displace the transition pressure toward the direction of penetration into the metastability field by a pressure increment, $\Delta P = \xi/(-\Delta V)$ (Fig. 4). If shear distortion exists, ξ can be compensated by ΔE^{d}, and thus the displacement of the transition pressure is reduced. The strain energy, ξ, can also be released on grain surfaces. Therefore, the displacement of transition boundary in laboratory experiments will be negligible. On the other hand, if olivine crystals in the mantle are large and free from distortion, homogeneous nucleation may be the dominant transition process. The strain energy created will not be released and the displacement of the olivine → spinel transition in the downgoing slab towards the deeper region may be significant.

For a crude approximation, we estimated the increment of transition pressure for the homogeneous nucleation of the olivine → spinel transition with coherent interface by Bitter-Crum theory:

$$\bar{\xi} = (2\mu^{ol}K^{sp}/3K^{sp} + 4\mu^{ol}))(\Delta\overline{V})^2 \tag{22}$$

where μ^{ol} is the shear modulus for olivine, K^{sp} is the bulk modulus for spinel, $\Delta\overline{V} = \Delta V/V$, is the fractional volume change of the olivine → spinel transition. We have assumed the following data at the P-T conditions corresponding to the olivine → spinel transition in the downgoing slab: $\mu_{ol} = 811$ kbar, $K_{sp} = 2424$ kbar, $\Delta\overline{V} = 0.074$. This gives $\bar{\xi} \sim 2.0 \cdot 10^9$ erg/cm^3. Thus, $\Delta P \sim \bar{\xi}/\Delta\overline{V} \sim 27$ kbar, which corresponds to an increment of depth of about 70 km!

According to Christian (1965), the nucleation rate per unit volume, $\bar{I}$, for an isochemical solid—solid transformation can be expressed by:

$$\bar{I} = \overline{N}_s f(s^*/n^*)[\Delta G_T^*/(3\pi kT)]^{1/2} \exp[-(\Delta G_T^* + Q_a)/(kT)] \tag{23}$$

where N_s is the number of atoms (or molecules) on the grain surface per unit volume; s^* is the number of atoms (or molecules) on the surface of a critical-sized nucleus; $s^* = A^*/a^e$ where $A^* = \eta_A r^{*2}$ is the surface area of the critical-sized nucleus, a^e is the effective surface area of the atom (or molecule), k is

Boltzmann's constant; f is a frequency factor, and according the Eyring theory, $f = kT/h$, where h is Planck's constant. The quantity $S^*/n^* (\Delta G_T^*/3\pi kT)^{1/2}$ is within one or two orders of magnitude for all nucleation processes of interest, so that eq. 23 may be approximated as:

$$\bar{I} = \overline{N}_s kT/h \exp[-(\Delta G_T^* + Q_a)/(kT)] \tag{24}$$

Substituting the above quantities into eq. 2 and letting the C's be characteristic constants, we obtain:

$$\bar{I} = C_1' T \exp[-\{C_2'/(C_3' + C_4'\Delta P)^2 + C_5'\}/T] \tag{25}$$

where:

$$C_1' = \overline{N}_s k/h (>0) \tag{26}$$

$$C_2' = 4\eta_A^3(\Delta\overline{E}^s + \bar{\sigma})^3/(27\eta_V^2 k) \tag{27}$$

$$C_3' = \Delta\overline{E}^d + \bar{\xi} \tag{28}$$

$$C_4' = \Delta\overline{V} (<0) \tag{29}$$

$$C_5' = Q_a/k (>0) \tag{30}$$

From Fig. 1, we find that the energy barrier for the atom (or molecule) to join the nucleus is $Q_a + E_a^s + E_a^d$, and that for it to leave the nucleus is $Q_a - \Delta G_a - \xi_a - \sigma_a$. The net rate of growth, Y, can then be shown to be:

$$Y = \lambda f[\exp\{-(Q_a + \Delta E_a^s + \Delta E_a^d)/(kT)\} - \exp\{-(Q_a - \Delta G_a - \xi_a - \sigma_a)/(kT)\}] \tag{31}$$

where λ is the distance of atomic (or molecular) migration during the transformation. For homogeneous nucleation, $\Delta E_a^s = 0$. If the shear-strain energies, ΔE_a^d and ξ_a are negligible, then the growth rate reduces to the familiar form:

$$Y = \lambda f \exp\{-Q_a/(kT)\} [1 - \exp\{-\Delta G_a/(kT)\}] \tag{32}$$

As shown previously in eqs. 16 and 19, ΔE_a^s and σ_a are inversely proportional to r, so that they will have a negligible influence on the growth of the nucleus ($r > r^*$), although they are important during the nucleation stage ($r < r^*$). We have then:

$$Y \sim C_6' T[\exp(-C_7'/T) - \exp\{-(C_8' + C_9'\Delta P)/T\}] \tag{33}$$

where:

$$C_6' = \lambda(k/h) (>0) \tag{34}$$

$$C_7' = (Q_a + \Delta E_a^d)/k = C_5' + (\Delta E_a^d/k) (>0) \tag{35}$$

$$C_8' = (Q_a - \xi_a)/k (>0) \tag{36}$$

$$C_9' = (-\Delta\overline{V})/\overline{N} = -(C_4'/\overline{N}_V) (>0) \tag{37}$$

According to Cahn (1956), if a steady state of transformation is attained

(i.e. both $\bar{I}$ and Y become constants) for the nucleation on grain surfaces of an equigranular material at constant P and T, then, before site saturation (i.e. before the nucleation sites on the grain surface are exhausted), the kinetic equation can be expressed by:

$$X = 1 - \exp[-\{(\eta_V/4)\bar{I}Y^3t^4\}] \tag{38}$$

where X is the degree (volume fraction) of completion of the transformation, and t is the time. After site saturation, the transformation will proceed only by growth, and the kinetic equation becomes:

$$X = 1 - \exp(-\eta_g\bar{S}Yt) \tag{39}$$

where η_g is a geometric factor related to the shape of the grain, and $\bar{S}$ is the area of the grain surface per unit volume. In general:

$$X = 1 - \exp(-Kt^n) \tag{40}$$

where K is the rate constant and n is an integer. Before site saturation, $n = 4$:

$$K = (\eta_V/4)\bar{I}Y^3 = C_1T^4 \exp[-\{C_2/(C_3 + C_4\Delta P)^2 + C_5\}/T] [\exp(-C_6/T) - \exp\{-(C_7 + C_8\Delta P)/T\}]^3 \tag{41}$$

where:

$$C_1 = \eta_V C_1' C_6'^3/4, \quad C_2 = C_2', \quad C_3 = C_3', \quad C_4 = C_4', \quad C_5 = C_5', \quad C_6 = C_7', \quad C_7 = C_8', \quad C_8 = C_9' \tag{42}$$

After site saturation, $n = 1$:

$$K = \eta_g\bar{S}Y = C_9T[\exp(-C_6/T) - \exp\{-(C_7 + C_8\Delta P)/T\}] \tag{43}$$

where:

$$C_9 = \eta_g\bar{S}C_6' \tag{44}$$

Equation 40 can be rewritten as:

$$\ln \ln [1/(1 - X)] = \ln K + n \ln t \tag{45}$$

A $\ln \ln [1/(1 - X)]$ versus $\ln t$ plot for the experimental data for nucleation on grain surfaces of an isothermal and isobaric transformation will fall on a curve with initial slope $n = 4$ and final slope $n = 1$. The intercepts of these two slopes on the $\ln \ln [1/(1 - X)]$ coordinate give the values of $\ln K$ corresponding to the two stages before site saturation ($n = 4$) and after site saturation ($n = 1$). The transition state between these two stages occupies only a very brief portion of the whole transformation process (Cahn, 1956), so that almost all the observable experimental data should fall on either of the straight line portions corresponding to slopes $n = 4$ or $n = 1$ in the $\ln \ln [1 - (1 - X)]$ versus $\ln t$ plot.

The C's in eqs. 41 and 43 are almost independent of pressure and temperature changes over a narrow P-T range at high pressures and temperatures. If experimental data for X as a function of T, ΔP, and t are available over a restricted range of P and T, the K and n in eq. 40, and hence the C's in eqs. 41

and 43 can then be determined. It is then possible to evaluate the quantities $\overline{N}_s$, $\Delta\overline{E}^s$, $\overline{\sigma}$, a^e, $\Delta\overline{E}^d$, $\overline{\xi}$, Q_a, λ, by solving the simultaneous equations involving the C's (eqs. 26—30; 34—37; 42, 44). Also, the quantities r^*, ΔG_T^*, n^* can be calculated from eqs. 12—14. After eqs. 41 and 43 are solved, the rate constant at any P-T condition close to the region where the experimental data were obtained can be calculated. The effect of grain size and shear stress on the rate constant may also be calculated by assigning appropriate values to $\overline{N}_s$ and $\Delta\overline{E}^d$. The dependence of the C's on P and T can be evaluated if experimental data are available over wider ranges of P and T.

The above model assumes that the material is monatomic and that each atom moves independently across the interphase boundary during the transformation. When the model is applied to the olivine → β-phase or olivine → spinel transitions, however, it describes the average behavior of the transformation, so that each parameter calculated will be the average for all atoms involved. Furthermore, if long-term diffusion takes place in these transformations, the growth rate Y might not be constant, and may be proportional to $t^{1/2}$. A further complication is that we are mainly interested in the kinetics of the transformation under continuous heating and compression rather than isothermal and isobarical conditions. However, the former can be obtained from the latter if the rate of penetration into the metastability field is known.

Although the above model is too simple to describe fully the kinetics of a real transformation, it nevertheless provides a useful semi-empirical equation which can be determined experimentally. Important features of the kinetics of high-pressure phase transformations predicted by eq. 41 are as follows (see Figs. 3 and 4): If all other variables not discussed are held constant for a given transition, then:

(1) $K \propto T^4 \exp(-C_{10}/T)[\exp(-C_6/T) - \exp(-C_{11}/T)]^3$

where C_{10}, C_6, and C_{11} are positive; thus, the rate of transition will increase drastically with temperature (Fig. 3).

(2) $K \propto \exp[-\{C_{12}/(C_3 + C_4\Delta P)^2 + C_{13}\}][C_{14} - \exp\{-(C_{15} + C_{16}\Delta P)\}]^3$

where the C's except C_{12} are positive. C_{12} can be negative if $(\Delta\overline{E}^s + \overline{\sigma})$ is negative, but $[C_{12}/(C_3 + C_4\Delta P)^2 + C_{13}]$ is positive. Thus, the rate of transition will also increase drastically with overpressure (Fig. 3). However, since $dQ_a/dP = V_a^{act}$, where V_a^{act} is the activation volume per atom, beyond a certain pressure, the effect of increasing Q_a outweighs that of increasing ΔP. Thus, the rate of transition decreases with further pressure increase (Fig. 4).

(3) $K \propto \overline{N}_s \propto \overline{S} \propto (1/d)$

where d is the average diameter of the grain size. Thus, the rate of transition is inversely proportional to the grain size (Fig. 4).

(4) $K \propto \exp[-\{(\Delta\overline{E}^s + \overline{\sigma})^3/C_{17} + C_{13}\}]$

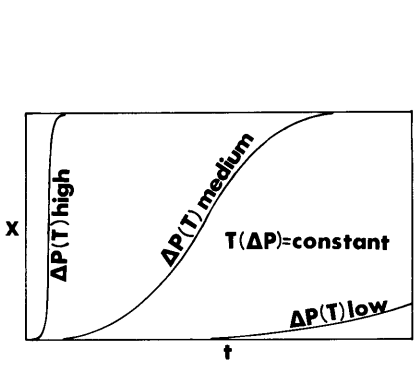

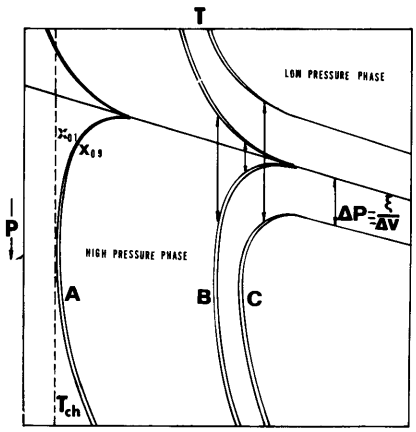

Fig. 3. Degree of isothermal and isobaric transformation (X) as a function of temperature (T), overpressure (ΔP), and time (t).

Fig. 4. Kinetic diagram of high-pressure phase transformation. Narrow bands between isograds $X_{0.1}$ and $X_{0.9}$ are regions where the transformation is 10%—90% complete. A = isograds for a transformation with heterogeneous nucleation for small grain size, high shear stress, long transformation time or slow penetration into the metastability field, and/or with catalyst. B = isograds for a transformation of heterogeneous nucleation for large grain size, low shear stress, short transformation time or fast penetration into the metastability field, and/or without catalyst. C = isograds for a transformation of homogeneous nucleation.

Notes: (1) For a given condition of transformation, there exists a characteristic temperature (T_{ch}) below which it is impossible to attain a certain degree of transformation (X = 10% in the above diagram).

(2) For a given condition of transformation, hysteresis (arrows in the above diagram) increases rapidly when T_{ch} is approached.

(3) Isograds will bend towards the direction of increasing temperature under very high pressure because of the increasing of the activation energy, Q_a.

(4) Homogeneous nucleation will deviate by an overpressure $\Delta P = \xi/(-\Delta V)$ from the equilibrium phase boundary.

where $\bar{\sigma}$, C_{17}, and C_{13} are positive. Thus, the rate of transition increases with $\Delta\overline{E}^s$. Grain surfaces (solid-air contact) provide a more important catalyst for the transition than grain boundaries (solid—solid contact).

$$(5)\ K \propto \exp[-\{C_{12}/(C_{18} + \Delta\overline{E}^d) + C_{13}\}][\exp\{-(C_{19} + C_{20}\Delta\overline{E}^d)\} - C_{21}]^3$$

thus the rate of transition will increase with $\Delta\overline{E}^d$ or shear stress (Fig. 4).

(6) For an isothermal and isobaric transition, isograds (contours of constant X) will move towards the direction of decreasing temperature with increasing time, i.e. the longer the time for a material to transform at constant P and T, the lower the ΔP and T required to attain a certain degree of transition (X) (Fig. 4).

(7) For an isothermal and isobaric transition, there exists a characteristic

temperature T_{ch}, below which it becomes impossible to attain a certain degree of transformation in a given time. T_{ch} can be calculated by eq. 41, using ΔP = infinite and K obtained from eq. 40.

(8) For a polythermal and polybaric transition, isograds will move towards the direction of increasing temperature with the rate of penetration into the metastability field. Thus, if the heating and compression is fast, higher P and T will be reached before a certain amount of olivine can transform into spinel (Fig. 4).

(9) For a given rate of penetration into the metastability field, the overpressure, ΔP, or the underpressure, $-\Delta P$, required to start the transformation at a perceivable rate or to attain a certain degree of transformation increases drastically with decreasing T, i.e. the hysteresis of the transformation (arrows in Fig. 4) increases drastically with decreasing T.

(10) For a given rate of penetration into the metastability field, there also exists a characteristic temperature T_{ch} below which it is impossible to attain a certain degree of transformation, no matter how high is the driving force (ΔP or $-\Delta P$). We shall emphasize this property in the following discussion of the kinetics of the olivine → spinel transition in the mantle.

SPECULATIONS ON THE EVOLUTION OF THE OLIVINE → SPINEL TRANSITION IN DOWNGOING LITHOSPHERIC PLATES

Following the earliest synthesis of Fe_2SiO_4 spinel by Ringwood in 1958, extensive high pressure experiments on the olivine → spinel transition have been performed in the system, Mg_2SiO_4—Fe_2SiO_4 (Akimoto et al., 1965, 1967; Akimoto and Fujisawa, 1966, 1968; Akimoto and Ida, 1966; Akimoto, 1972; Ringwood and Major, 1966, 1970; Kawai et al., 1970; Ito et al., 1971; Suito, 1972). As a consequence of the increased CFSE acquired by Fe^{2+} in the spinel structure, the transition pressure for the olivine → spinel transition in fayalite is significantly smaller than that for forsterite (Syono et al., 1971). Furthermore, the negligible hysteresis of the olivine → spinel transition in Fe_2SiO_4 implies that T_{ch} for this transformation is much lower than that for Mg_2SiO_4. Thus, the equilibrium phase boundary for Fe_2SiO_4 can be more accurately determined. On the other hand, phase relationships in Mg_2SiO_4 are more complicated because: (1) a β-phase exists and is stable over a finite P-T range; (2) the transitions: olivine → β-phase; β-phase → spinel (γ-phase), and olivine → spinel occur at higher pressures, so that high uncertainties exist over measured pressures and temperatures; and (3) the transformations are very sluggish because T_{ch} is so high. As a result, the stability fields of the α-, β-, and γ-phases of Mg_2SiO_4 are not well established. From available experimental data, the slopes of all three phase boundaries α—β, β—γ, and α—γ appear to be positive and the field of the β-phase expands with temperature. Furthermore, the γ-phase has been shown to decompose into magnesiowüstite solid solutions and stishovite at very high pressures (Ming and Bassett, 1975; Kumazawa et al., 1974). Extrapolation of experimental data for Mg_2SiO_4

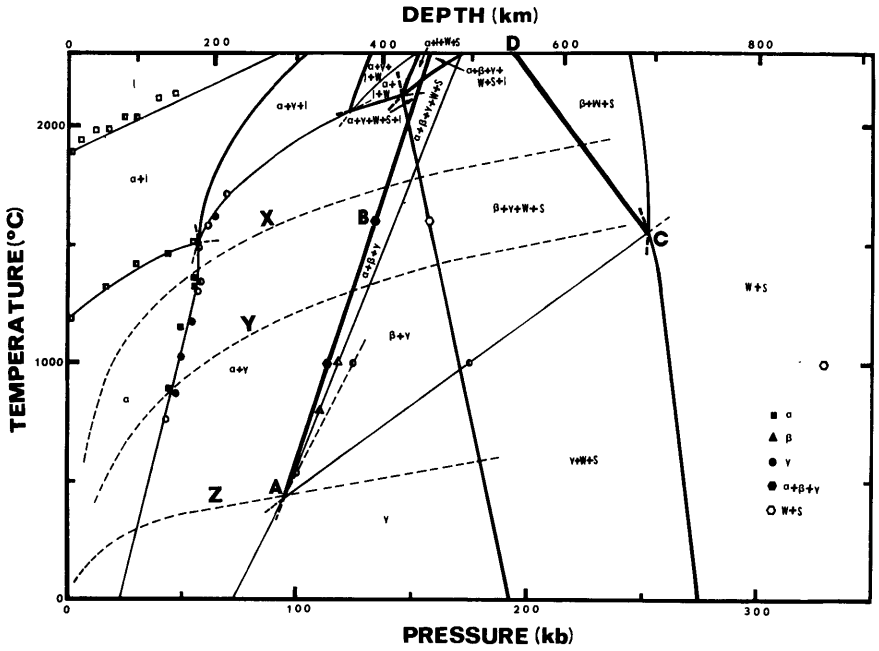

Fig. 5. Proposed phase diagram for the pseudo-binary system Mg_2SiO_4—Fe_2SiO_4. Plotted data and symbols for the phases are shown in Table I. Fine and coarse lines are univariant lines for one component system (Mg_2SiO_4 or Fe_2SiO_4), and for two (Mg_2SiO_4—Fe_2SiO_4, MgO—SiO_2, or FeO—SiO_2) or three (MgO—FeO—SiO_2) component systems, respectively. $AB(\alpha + \beta + \gamma)$ and $CD(\beta + \gamma + w + s)$ are univariant lines responsible for 400-km and 650-km discontinuities, respectively. X and Y are the range of geotherms under continental and oceanic plates (Ahrens, 1972). Z is the geotherm of the coldest part of a fast plunging downgoing slab (Turcotte and Schubert, 1973).

suggests that the β-Mg_2SiO_4 phase may decompose to periclase plus stishovite at very high temperatures before it transforms to the spinel (γ-Mg_2SiO_4) phase. On the basis of these assumptions, we propose a phase diagram for the system Mg_2SiO_4—Fe_2SiO_4 illustrated in Fig. 5. Note that the high P-T portion of this diagram is purely speculative, and is subject to modifications as new data become available.

Summarized in Table I are the experimental data used to construct Fig. 5. The data selected are such that for each corresponding run temperature, the pressure chosen is that which has the minimum value for the transformation in the forward direction: low-pressure phase → high-pressure phase. Conversely, the maximum pressure value is chosen for the transformation taking place in the reverse direction. These data usually correspond to runs with longest duration and the least degree of transformation. The purpose of selecting data this way is to minimize the hysteresis of the transformation, although the experimental uncertainties cannot be reduced.

The equilibrium phase boundary should lie between the normal transformation and its reversed reaction in a P-T plot. In the case of transformations that

occur at higher pressures, the experimental data available are always those going from the low-pressure phase to the high-pressure phase, the phase boundary so determined thus representing the limit towards the direction of increasing pressure. We have assumed that the 650-km discontinuity in the mantle is caused by the decomposition of β-phase or spinel into magnesiowüstite (w) and stishovite (s). Thus, in Fig. 5, we have arbitrarily drawn the three univariant lines, γ + w + s and β + w + s in Mg_2SiO_4 and β + γ + w + s (*CD*) in the pseudobinary system Mg_2SiO_4—Fe_2SiO_4, to fulfill this assumption.

Since shear stress can greatly promote the rate of transformation without disturbing the phase boundary (Dachille and Roy, 1961), its effect on reducing the hysteresis of the transformation parallels that of rising temperature. Shear stress is higher in anvil-type pressure apparatus than in others. Thus, anvils may be more useful in studying the phase equilibrium of Mg_2SiO_4 which has large hysteresis even at temperatures up to 1,200°C, provided that the accuracy of a P-T measurement is not reduced by the presence of high shear stress. Therefore, all the experimental data shown in Table 1 for transformations performed at higher pressures were selected from anvil-type high-pressure measurements.

Also superimposed in Fig. 5 are geotherms of different tectonic provinces. Thus, curves *X* and *Y* are the ranges of oceanic and continental geotherms (Ahrens, 1972). Curve *Z* is the geotherm for the coldest part of a downgoing slab corresponding to constant shear stress on the slip zone (Turcotte and Schubert, 1973). The dip angle and velocity of the slab in their calculations are 45° and 8 cm/year, respectively. The polythermal and polybaric sections along geotherms of the two different tectonic provinces are shown in Fig. 6. The dotted lines in Fig. 6 correspond to the proposed mantle compositions with atomic ratio, Mg/(Mg + Fe) = 0.89 for olivine coexisting with pyroxene and Mg/(Mg + Fe) = 0.87 for β-phase or spinel coexisting with garnet solid solution (Akimoto et al., in preparation). Note from Fig. 6A, that the dominant phase in the upper transition zone under the stable tectonic provinces (oceanic and continental) is the β-phase. It will partially or completely transform into the γ-phase before it decomposes into magnesiowüstite and stishovite in the lower transition zone. If Fe can preferentially partition into the β-phase or the γ-phase relative to pyroxene (Nishizawa and Akimoto, 1973) or garnet (Akimoto et al., in preparation), then the γ-phase will be stable at shallower depths. On the other hand, the dominant phase in the downgoing slab of the whole transition zone will be the γ-phase (Fig. 6B). The decomposition of the γ-phase into magnesiowüstite and stishovite in the downgoing slab will occur at a deeper level, possibly in the lower mantle, due to the negative P-T slope of this phase boundary (Ming and Bassett, 1975; Kumazawa et al., (1974).

Since the oxygen ions in both the β- and γ-phases are in cubic closest packing, whereas in the olivine (α-phase) structure they are in hexagonal closest packing, the structural differences between the β- and γ-phases are much smaller than those between the α- and β-phases and the α- and γ-phases. The cation sites

TABLE I

Selected data to construct the phase diagram of the system Mg_2SiO_4—Fe_2SiO_4 shown in Fig. 5

P(kbar)	T(°C)	t(minute)	Composition	Reaction	Method	Reference
42.7 ± 0.5	755 ± 10	120	Fe_2SiO_4	$\alpha \rightarrow \alpha + \gamma$ (small amount)	exp.	Akimoto et al. (1967)
47.2 ± 0.5	870 ± 10	45	Fe_2SiO_4	$\alpha \rightarrow \alpha + \gamma$ (80%)	exp.	Akimoto et al. (1967)
44.3 ± 0.5	885 ± 10	26	Fe_2SiO_4	$\gamma \rightarrow \alpha$	exp.	Akimoto et al. (1965)
49.3 ± 0.5	1025 ± 15	30	Fe_2SiO_4	$\alpha \rightarrow$ r	exp.	Akimoto et al. (1967)
49.3 ± 0.5	1145 ± 10	15	Fe_2SiO_4	$\gamma \rightarrow \alpha$	exp.	Akimoto et al. (1967)
54.2 ± 0.5	1170 ± 10	10	Fe_2SiO_4	$\alpha \rightarrow \alpha + \gamma$ (60%)	exp.	Akimoto et al. (1967)
57 ± 1	1300 ± 5	10	Fe_2SiO_4	$\alpha \rightarrow \alpha + \gamma$ (30%)	exp.	Akimoto et al. (1967)
55.8 ± 0.5	1320 ± 5	10	Fe_2SiO_4	$\gamma \rightarrow \alpha$	exp.	Akimoto et al. (1967)
58.3 ± 0.5	1340 ± 5	10	Fe_2SiO_4	$\alpha \rightarrow \alpha + \gamma$ (80%)	exp.	Akimoto et al. (1967)
54.2 ± 0.5	1355 ± 5	10	Fe_2SiO_4	$\gamma \rightarrow \alpha$	exp.	Akimoto et al. (1967)
57.5 ± 0.5	1485 ± 5	5	Fe_2SiO_4	$\alpha \rightarrow \alpha + \gamma$ (80%)	exp.	Akimoto et al. (1967)
0.001	1205 ± 5	—	Fe_2SiO_4	$\alpha \rightarrow \alpha +$ l	exp.	Akimoto et al. (1967)
17.0 ± 0.5	1315 ± 5	5	Fe_2SiO_4	$\alpha \rightarrow \alpha +$ l (50%)	exp.	Akimoto et al. (1967)
30.0 ± 0.5	1415 ± 10	5	Fe_2SiO_4	$\alpha \rightarrow \alpha +$ l (40%)	exp.	Akimoto et al. (1967)
43.5 ± 0.5	1455 ± 5	5	Fe_2SiO_4	$\alpha \rightarrow \alpha +$ l (30%)	exp.	Akimoto et al. (1967)
54.2 ± 0.5	1505 ± 10	5	Fe_2SiO_4	$\alpha \rightarrow \alpha +$ l (80%)	exp.	Akimoto et al. (1967)
61.2 ± 0.5	1575 ± 5	4	Fe_2SiO_4	$\alpha \rightarrow \gamma$ (small amount) + l	exp.	Akimoto et al. (1967)
64.0 ± 0.5	1615 ± 10	4	Fe_2SiO_4	$\alpha \rightarrow \gamma +$ l (rare)	exp.	Akimoto et al. (1967)
69.0 ± 0.5	1710 ± 10	3	Fe_2SiO_4	$\alpha \rightarrow \gamma +$ l (60%?)	exp.	Akimoto et al. (1967)
158 ± 5	1600 ± 100	—	Fe_2SiO_4	$\alpha \rightarrow$ w + s	exp.	Ming and Bassett (1975)
100 ± 15	530	—	Mg_2SiO_4	$\alpha \rightarrow \alpha + \gamma$	ext.	Ringwood and Major (1966)
125 ± 13	1000 ± 200	—	Mg_2SiO_4	$\alpha \rightarrow \alpha + \gamma$	ext.	Ringwood and Major (1966)
110 ± 11	800 ± 20	60	Mg_2SiO_4	$\alpha \rightarrow \alpha + \beta$	exp.	Suito (1972)

118 ± 12	1000	3—5	Mg_2SiO_4	$\alpha \rightarrow \beta$	exp.	Ringwood and Major (1970)
175	1000	—	Mg_2SiO_4	$\alpha \rightarrow \beta + \gamma$	ext.	Akimoto (1972)
0.001	1890 ± 20	—	Mg_2SiO_4	$\alpha \rightarrow \alpha + l$	exp.	Bowen and Anderson (1914)
5.5	1930	1	Mg_2SiO_4	$\alpha \rightarrow l$	exp.	Davis and England (1964)
12.5	1975	1	Mg_2SiO_4	$\alpha \rightarrow l$	exp.	Davis and England (1964)
18	1980	2	Mg_2SiO_4	$\alpha \rightarrow \alpha$ (33%) + l	exp.	Davis and England (1964)
25	2030	2	Mg_2SiO_4	$\alpha \rightarrow \alpha$ (50%) + l	exp.	Davis and England (1964)
30.5	2030	1	Mg_2SiO_4	$\alpha \rightarrow \alpha$ (33%) + l	exp.	Davis and England (1964)
39.5	2105	1	Mg_2SiO_4	$\alpha \rightarrow l$	exp.	Davis and England (1964)
330	1000	30	Mg_2SiO_4	$\alpha \rightarrow w + s$	exp.	Kumazawa et al. (1974)
114 ± 12	1000 ± 200	3—5	$(Mg_{0.9}Fe_{0.1})_2SiO_4$	$\alpha \rightarrow \alpha + \beta + \gamma$	exp.	Ringwood and Major (1970)
134	1600	—	$(Mg_{0.9}Fe_{0.1})_2SiO_4$	$\alpha \rightarrow \alpha + \beta + \gamma$	est.	Ringwood and Major (1970)

Notes:

(1) The pressure calibration for Akimoto et al. (1965, 1967) was based on the Tl II → III transition at 36.7 kbar and Ba II → IV transition at 59 kbar. The pressure for the latter transition has been revised to 55 kbar (see Mao et al., 1969). Pressures between 36.7 and 55 kbar in their works have been recalculated by $P' = 36.7 + (P - 36.7) \times [(55 - 36.7)/(59 - 36.7)]$, where P' and P are pressures listed in this table and reported in their literature, respectively.

(2) Slopes of the phase boundary $\gamma \rightarrow w + s$ shown in Fig. 5 are: −0.022 kbar/°C for Fe_2SiO_4 (Ming and Bassett, 1975); and −0.013 kbar/°C for Mg_2SiO_4 (Ahrens and Syono, 1967).

(3) Symbols in this table are:
α = olivine, β = modified spinel, γ = spinel, w = wüstite of magnesiowüstite, s = stishovite, l = liquid, exp. = experimental, ext. = extrapolated from the Fe_2SiO_4-rich compositions in a pressure-composition phase diagram, est. = estimated.

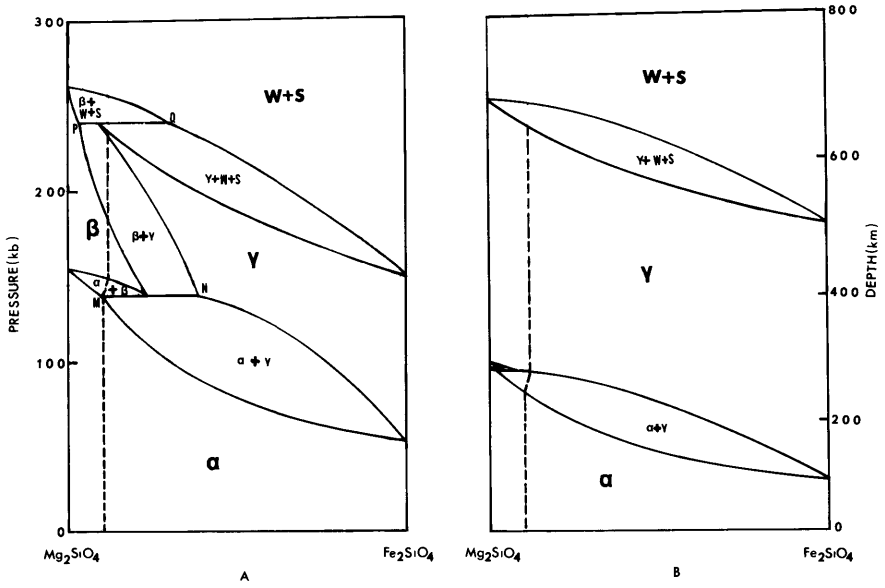

Fig. 6. Polythermal and polybaric sections through the phase diagrams shown in Fig. 5. A. Along geotherms under normal tectonic provinces (between *X* and *Y* in Fig. 5). B. Along the cold interior of a fast plunging downgoing slab (along *Z* in Fig. 5). *MN* and *PQ* in A are traces of univariant lines *AB* and *CD* in Fig. 5, respectively. The composition of magnesiowüstite is projected from the silica end member in the ternary system MgO–FeO–SiO_2. Dotted lines are the proposed compositions for the system Mg_2SiO_4—Fe_2SiO_4 in the mantle with Mg/(Mg + Fe) atomic ratio of 0.89 in olivine and 0.87 in β-phase or spinel (Akimoto et al., in preparation). Note that the 400-km discontinuity is caused by the $\alpha \rightarrow \beta$ transition under normal tectonic provinces. The corresponding transition in the cold interior of a fast plunging downgoing slab is the $\alpha \rightarrow \gamma$ transition.

are similar for the β- and γ-structures, too, and are quite different from the olivine structure (Table II). As a result, thermodynamic properties of the β- and γ-phases are rather similar, but are different from those of the α-phase. Therefore, the kinetics of the $\alpha \rightarrow \beta$ and $\alpha \rightarrow \gamma$ transformations are probably similar and slower than the rate of the faster $\beta \rightarrow \gamma$ transition. Since only the qualitative features of the kinetics of the olivine → spinel transition are under consideration, we shall neglect the small differences between the β- and γ-phases in the discussion which follows.

The temperature in the lower part of the upper mantle may be sufficiently high for olivine to recrystallize and thus relieve the accumulation of shear stress, so that olivine crystals are probably large and stress-free. In this case, homogeneous nucleation will dominate and the activation energy, ΔG_T^*, for the transformation will be very high. On the other hand, heterogeneous nucleation is the dominant mode for the olivine → spinel transition performed in the laboratory because material used in experimental runs is in a powdered form. In addition, shear stresses in high-pressure apparatus are much higher than

TABLE II

Structural differences of cation sites in the three polymorphs: α, β, and γ Mg_2SiO_4

Polymorph	Site	Number of shared corners per site			Number of shared edges per slite	
		O—O	O—T	T—T	O—O	O—T
α	M1	4(4M2)	2	—	4(2M1, 2M2)	2
	M2	8(4M1, 4M2)	4	—	2(2M1)	1
	T	—	6(2M1, 4M2)	0	—	3(2M1, 1M2)
β	M1	0	6	—	6(4M3, 2M2)	0
	M2	0	6	—	6(5M3, 1M1)	0
	M3	0	4	—	7(4M3, 2M2, 1M1)	0
	T	—	10	1	—	0
γ	O	0	6	—	6	0
	T	—	12	0	—	0

O = octahedral site (Mg,Fe), T = tetrahedral site (Si).

those expected at depths in the mantle where the olivine → spinel transition occurs. Furthermore, reduction of overpressure at a transition point due to volume contraction during the phase change is compensated for immediately in high-pressure apparatus but only very slowly by the creep of the rock in the mantle. Because of the sluggishness of the transformations in Mg_2SiO_4, Akimoto (1972) and Ringwood and Major (1970) used "reactive forsterite", and sometimes added water to catalyze the transformation. As a result, rates of the olivine → spinel transition performed in the laboratory are expected to be orders of magnitude higher than the reaction rate in the mantle.

Yet, experimental syntheses of Mg-rich spinels below 700°C have been unsuccessful to date, even though the overpressure was very high. Thus, it seems that the T_{ch} for a highly catalyzed olivine → spinel transition performed in the laboratory is close to 700°C. The T_{ch} for the non-catalyzed transition in the mantle will be much higher. However, this may be compensated for by the extremely slow rate of penetration of olivine into the spinel field in the downgoing slab. In addition, the impurities in natural olivine may promote the rate of transition and lower the T_{ch}. As a crude approximation, we may estimate the T_{ch} for the olivine → spinel transition in the downgoing slab as follows: The olivine → spinel transition will proceed by two consecutive

processes in such a way that local charge balance is maintained. These two processes are: the rearrangement of oxygen anions by transforming the hexagonal closest packing (h.c.p.) of olivine into the cubic closest packing (c.c.p.) of spinel; and the rearrangement of cations by transforming M_1, M_2, and tetrahedral (T) sites of olivine into octahedral (O) and T sites of spinel. The structural differences of the cation sites among the three polymorphs α, β, and γ are listed in Table II. Both processes may proceed by diffusion, but because the oxygen ions are considerably larger than the cations, the diffusion of oxygen ions will be the rate-determining process. Unfortunately, the activation energy of diffusion of oxygen ions is not known. Here we have assumed that the olivine → spinel transition proceeds by diffusion of large cations (Mg, Fe) only; the transformation rate thus estimated will be the upper limit of the real case. Because olivine crystals in the lower portion of the upper mantle are probably large, there is a limited number of sites available for nucleation on grain surfaces, so that site saturation will occur at an early stage during the transformation through heterogeneous nucleation. We thus consider only the growth contribution to the olivine → spinel transition, and neglect the small amount of spinel formed on the grain surfaces of olivine. Thus, eq. 39 is applicable. We shall approximate the shape of the olivine grains by tetrakaidecahedra. Equation 39 then becomes (Cahn, 1956):

$$X = 1 - e^{-2\bar{s}Yt} \tag{46}$$

where $\bar{s} \sim 3.4/d$. If we tentatively assume the average diameter (d) of olivine grains to be about 100 cm, then $\bar{s} \sim 0.034$ cm^2/cm^3. Let us now put $X = 0.1$ and t = one million years for the olivine → spinel transition in a downgoing slab. Then, from eq. 40 ($n = 1$):

$$K = -\ln(1 - X)/t = 3.3 \cdot 10^{-15}\ \text{sec}^{-1} \tag{47}$$

Let ΔP = large, $T = T_{ch}$, $\exp[-\Delta G_a/(kT)] \sim 0$, from eq. 32 we get:

$$Y \sim \lambda(kT_{ch}/h)\exp[-Q_a/(kT_{ch})] \tag{48}$$

Let us now approximate the thickness of the interphase boundary by the average interatomic distances of divalent cations between olivine and spinel, which gives $\lambda \sim 3.3 \cdot 10^{-8}$ cm. Substituting the above data into eq. 43, yields:

$$K = 2\bar{s}Y \sim 47T_{ch}\exp[-Q_a/(kT_{ch})] = 3.3 \cdot 10^{-15}\ \text{sec}^{-1} \tag{49}$$

For $T_{ch} = 700°C$ (973°K), this gives $Q_a \sim 6.0 \cdot 10^{-12}$ erg or about 3.7 eV. Let us now consider homogeneous nucleation as the competing process for the olivine → spinel transition in the downgoing slab. From eq. 40 ($n = 4$):

$$K = -\ln(1 - X)/t^4 = 1.1 \cdot 10^{-55}\ \text{sec}^{-4} \tag{50}$$

From eq. 41:

$$K = (\eta_V/4)\bar{N}_V(k/h)(\lambda k/h)^3 T_{ch}^4[\exp\{-4Q_a/(kT_{ch})\}] \tag{51}$$

Let us approximate the shape of spinel nuclei by spheres, then $\eta_V = 4\pi/3$;

and approximate $\overline{N}_V$ by the number of divalent cations per unit volume in olivine; this gives $\overline{N}_V \sim 2.9 \cdot 10^{22}/\text{cm}^3$. Thus:

$$K = 2.2 \cdot 10^{41} T_{ch}^4 \exp[-4Q_a/(kT_{ch})] = 1.1 \cdot 10^{-55} \text{ sec}^{-4} \quad (52)$$

If $T_{ch} = 700°\text{C}$, then $Q_a = 8.5 \cdot 10^{-12}$ erg or 5.3 eV. This value is higher than that for nucleation on grain surfaces calculated previously. Thus, we conclude that homogeneous nucleation will be more efficient than nucleation on grain surfaces for the olivine → spinel transition in the downgoing slab. However, had we assumed a grain size smaller than $d = 100$ cm, then nucleation on grain surfaces would become more important.

Buening and Buseck (1973) have measured the activation energy of intrinsic lattice diffusion for divalent cations in Mg-rich olivine at high temperature and 1 atm. to be 2.9 eV, which is close to the Q_a just calculated by assuming $T_{ch} \sim 700°\text{C}$ for the two nucleation processes of the olivine → spinel transition in the downgoing slab. Since the activation energy Q_a may increase with pressure and because we have neglected the activation energy of migration of oxygen ions in the above calculation, the actual activation energy for the olivine → spinel transition in the downgoing slab under the pressure condition of the transition zone may have a value consistent with that which we calculated by assuming $T_{ch} \sim 700°\text{C}$. In the following discussion, we shall tentatively assume that the T_{ch} for the olivine → spinel transition in the downgoing slab is 700°C and that negligible transformation will occur below this temperature.

The proposed kinetics diagram for the olivine → spinel transition in the mantle is shown in Fig. 7B. The line AQ marks the very onset of the olivine → spinel transition at the low-temperature side (Fig. 6B) and the series of transitions: $\alpha \rightarrow \alpha + \gamma$; $\alpha + \gamma \rightarrow \alpha + \beta$; and $\alpha + \beta \rightarrow \beta$ at the high-temperature side. According to the experimental results of Akimoto et al. (in preparation), the point M in Fig. 6A in their isothermal sections of the system Mg_2SiO_4—Fe_2SiO_4 moves towards the direction of increasing Fe_2SiO_4 with temperature. Thus, above a certain temperature, say 1500°C, the $\alpha \rightarrow \beta$ transition may occur directly and bypass the other reactions in the mantle. Therefore, under very high temperatures, AQ in Fig. 7B may mark the very onset of the $\alpha \rightarrow \beta$ transition.

Isograds $X_{0.1}$ and $X_{0.9}$ in Fig. 7B mark the positions for initiation, say $X = 0.1$, and completion, say $X = 0.9$, of the olivine → spinel transition in the mantle, respectively. The area on the left side of the isograd $X_{0.1}$ in the spinel field is the region where the major portion of olivine can exist metastably at the rate of penetration into the spinel field determined by the plunging velocity of the downgoing slab because of the negligible amount of transformation ($X < 0.1$). The isograd $X_{0.1}$ is drawn on the assumption that its asymptote at the low-temperature side is $T_{ch} = 700°\text{C}$. Because the transitions involve compositional change, the separations between $X_{0.1}$ and AQ, and between $X_{0.9}$ and $X_{0.1}$ are determined by the pressure ranges for equilibrium transformation to attain 10% and 90% of spinel, respectively, at the higher-tempera-

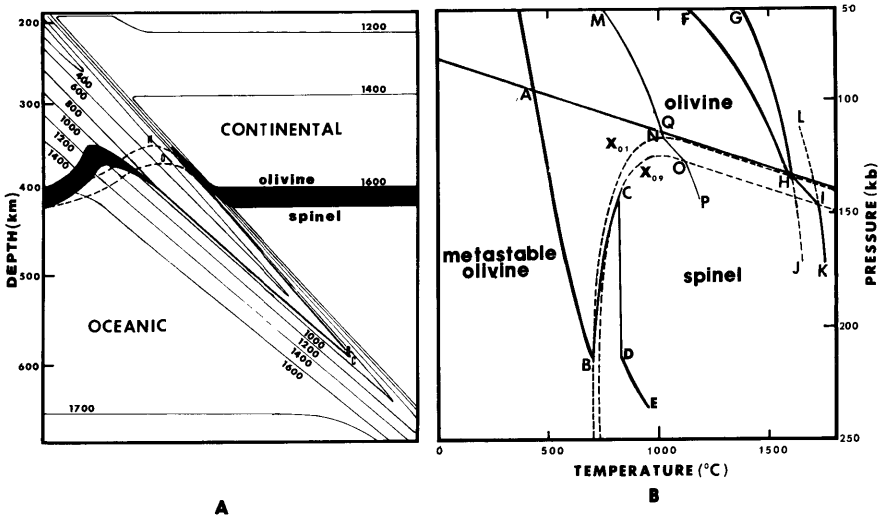

Fig. 7. A. Thermal structure and the distortion of the olivine—spinel phase boundary in a fast plunging downgoing slab. Numbers are temperatures of isotherms in °C. The blackened band is the region of coexistence of olivine and spinel (X = 0.1—0.9). Note the downward distortion of the olivine—spinel phase boundary and the offset of isotherms across it. Dotted lines are the phase boundary for a slower plunging downgoing slab which has the geotherm *MNOP* in its coldest interior. B. Effect of the olivine → spinel transition on different geotherms. *FH* and *GH* are geotherms under continental and oceanic plates, respectively. *MN* and *AB* are geotherms of the coldest parts of downgoing slabs with slow and fast plunging velocities, respectively. Note the tremendous overpressure drop, *BC*, due to the olivine → spinel transition in the cold interior of a fast plunging downgoing slab. The pre-transformational thermal structure and geotherms *AB*, *FH*, and *GH* are based on Schubert et al. (in preparation).

ture side where the rate of transformation is fast. As soon as temperature is low enough to allow olivine to move deeply into the spinel field, the olivine → spinel transition, if taking place, will involve no compositional change. In this case, the isograd $X_{0.9}$ will lie immediately adjacent to $X_{0.1}$ (Fig. 7B). Curves *FH* and *GH* are geotherms under the continental plate and the oceanic plate, respectively. Curve *AB* is the geotherm in the coldest part of a downgoing slab. All the geotherms are based on Turcotte and Schubert (1973). When the geotherms cross the isograd $X_{0.1}$, the rate of the olivine → spinel transition becomes very fast. Because the transformation is exothermic, heat will be evolved and temperature will suddenly increase. As a result, geotherms will bend towards the direction of increasing temperature (Fig. 7B).

The adiabatic temperature increase, ΔT (temperature between *BD* or *HI*), is estimated as follows: Let $Cp \sim 40$ cal/mol and $\Delta V = -4$ cm^3/mol, where Cp is the heat capacity of olivine and ΔV is the molar volume change for the olivine → spinel transition. Then, the heat released during the complete transformation is $\Delta H \sim T\Delta S \sim T\Delta V(dP/dT) \sim -4590$ cal/mol. Assuming the temperature at 400 km depth to be 1600°C, this gives $\Delta T = \Delta H/Cp \sim 115$°C. In

reality, the adiabatic temperature increase due to the olivine → spinel transition may be lower than 115°C, however, because of the presence of other minerals, lower temperatures in the downgoing lithosphere, and a smaller $\Delta\overline{V}$ at high pressure.

At the two margins of the downgoing slab, geotherms will follow *FH* (continental side) or *GH* (oceanic side). As soon as geotherms cross $X_{0.1}$, phase transformation occurs very fast. Although the transformation may not be isochemical and may involve several reactions, qualitatively the kinetics of these reactions still follow the curves shown in Figs. 3 and 4, but the curves may no longer be smooth and continuous. In the mantle, the rate of the olivine → spinel transition may depend not only on its intrinsic kinetics, but also on superimposed physical conditions. At the two margins of a downgoing slab, the transitions will take place fast and close to equilibrium. However, as soon as the transition occurs, overpressure drops due to the volume contraction and temperature increases due to the generation of latent heat. This will force the geotherm to cross the isograds in the direction of decreasing X (see Fig. 7B), which is inhibited because as soon as this happens the transition will automatically stop. The rate of the olivine → spinel transition at the two margins of the downgoing slab is then controlled by the two competing processes, namely the overpressure accumulation and the temperature increase. The former depends mainly on the plunging velocity of the slab, and the latter on the rate of heat dissipation. If the plate moves fast, the geotherm will follow *FHIK* or *GHIK* in Fig. 7B. On the other hand, if the plate moves very slowly, the latent heat generated by the olivine → spinel transition will dissipate before pressure increases further. In this case, the geotherm will be *FHJ* or *GHJ*. The actual geotherm for the plate margins will lie between the two extremes. For the opposite direction of movement of mantle material, e.g. rising of a mantle plume, the geotherm will be parallel to either *KIHF*(*G*) or *KIL* or inbetween, depending on the ascending rate of the mantle plume, or the two competing rates between decompression and heat dissipation.

The geotherm in the coldest part of a downgoing slab is *AB* (Fig. 7B). As soon as it hits $X_{0.1}$ at *B*, the rate of the olivine → spinel transition drastically increases. Pressure then drops and temperature rises, but this time the temperature rise will not curb the transformation because it moves the geotherm in the direction of increasing X. The rate of the olivine → spinel transition is then controlled solely by the rate of overpressure accumulation, which is determined by several competing rates. They include: plunging velocity of the plate, rate of elastic deformation and creep of the wall rock, and rate of thermal expansion. The dominant factors at the beginning, the intermediate, and the final stages of the transformation are rate of elastic deformation, rate of creep, and the plunging velocity of the slab, respectively. Because the kinetics of the transformation is fast and the volume contraction is much faster than that which can be compensated for by the above factors, the geotherm between the two isograds $X_{0.1}$ and $X_{0.9}$ will follow such a path that although ΔP drops, it moves in the direction of increasing X (Fig. 7B). This gives the geotherm a

negative P-T slope. Because the isograds are nearly vertical and the separation of $X_{0.1}$ and $X_{0.9}$ is very small, the allowed overpressure drop could be tremendous. As a result, it builds up a narrow zone of very high pressure gradient which separates the transformed spinel from the untransformed olivine. The zone of high-pressure gradient will greatly enhance the shear stress or accelerate the creep rate of the wall rock. As soon as the transformation is complete, the volume contraction will be compensated and the pressure will soon increase to the previous value at *B* (*D* in Fig. 7B). The geotherm then follows the original trend before transformation but is displaced by ΔT (*BD* in Fig. 7B). Based on the above model, the pressure for a fixed point at the center of the plate as a function of time is schematically shown in Fig. 8. It should be noted that the drop of pressure from *B* to *C* and the resumption of pressure from *C* to *D* are almost instantaneous compared to the time required to build up the pressures (*AB* and *DE*).

Geotherms along other parts of the downgoing lithosphere will lie between the two curves *F*(*G*)*HIK* and *ABCDE*.

The distortion of the olivine—spinel phase boundary across the downgoing lithosphere, based on Fig. 7B, is shown in Fig. 7A. The thermal structure above the phase boundary in Fig. 7A is taken from Schubert et al. (in preparation). They calculated the thermal structure based on Turcotte and Schubert (1973) for the downgoing slab of dip angle 45° and plunging velocity, 8 cm/year, respectively. Under these conditions, the distortion of the olivine—spinel phase boundary could be downward instead of upward as proposed by previous workers (Ringwood, 1973; Turcotte and Schubert, 1971; Schubert et al., in preparation). It should be noted that both the pressure gradient and the temperature gradient increase drastically toward the tip of the tongue-shaped cold center, and this tip (*BC* in Fig. 7A) is a region where the high pressure—low

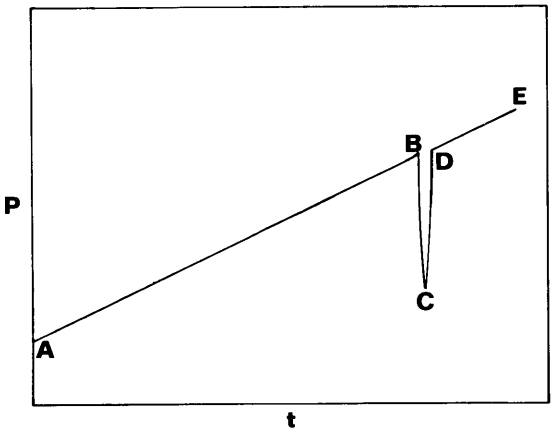

Fig. 8. History of compression for the cold interior in a fast plunging downgoing slab (along the path of *ABCDE* in Fig. 7B). Note the sudden drop (*BC*) and resumption (*CD*) of pressure across the olivine—spinel phase boundary.

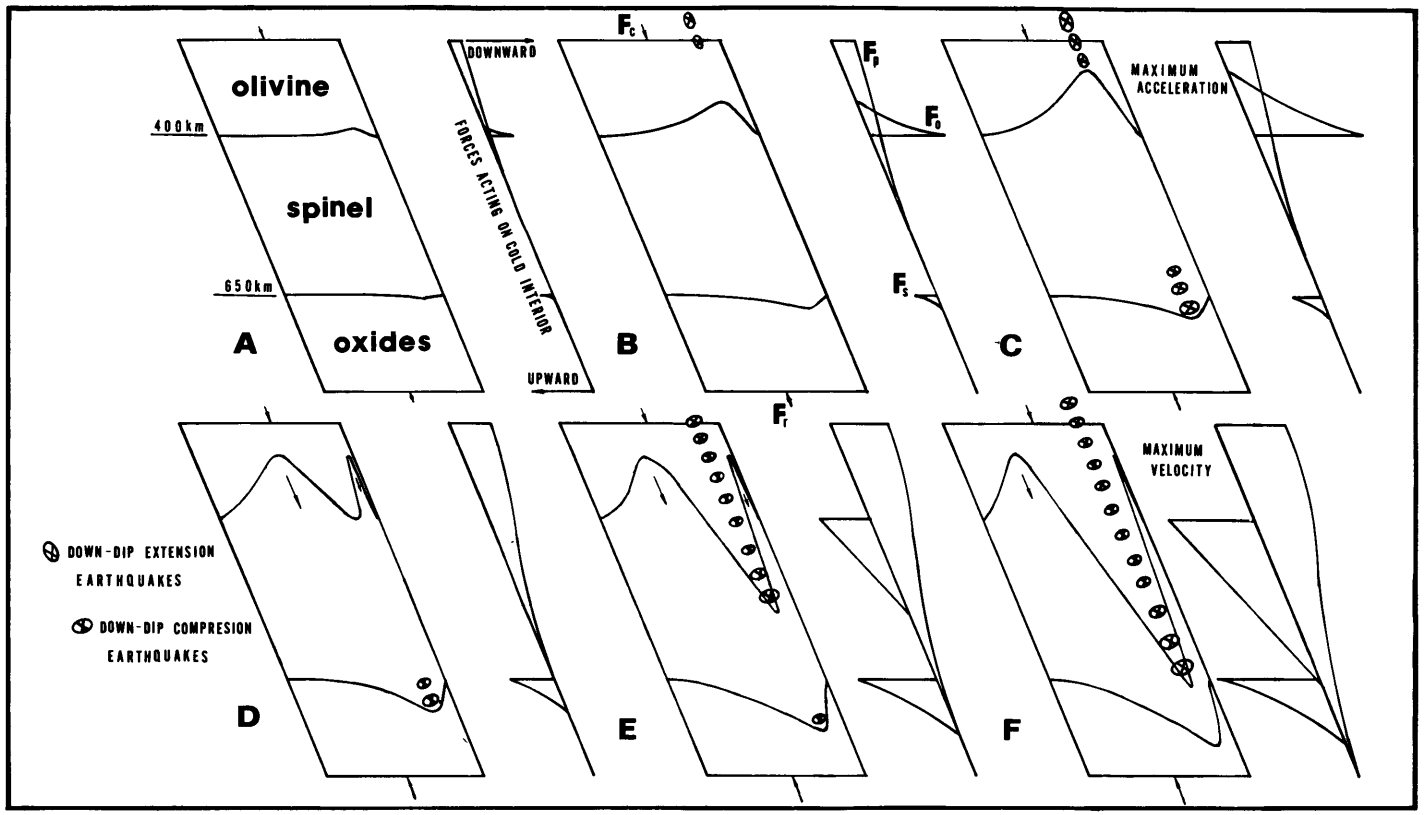

Fig. 9. Evolution of phase boundaries during the development of a downgoing slab. The plunging velocity of the downgoing slab increases from *A* to *F*. Forces acting on the cold interior are shown schematically on the right-hand side of each stage of the evolution of phase boundaries. The effect of the latent heat associated with phase transformations on the force F_c is neglected. The size of the ellipse is intended to correlate with the seismicity. Note the effect of the distortion of the olivine—spinel phase boundary (spinel 10%—90%) on the patterns of the earthquake distribution. Note also the increase of seismicity towards the region of high-pressure gradient where the shear stress is greatly enhanced.

temperature olivine (*B*) is in contact with the low pressure—high temperature spinel (*C*). This may introduce mechanical instability and have important consequences on plate dynamics discussed later.

The geotherm, *AB*, taken from Turcotte and Schubert (1973), has the lowest temperature gradient compared to those proposed by the other workers (McKenzie, 1970; Minear and Toksöz, 1970 a, b; Toksöz et al., 1971, 1973; Griggs, 1972). If the geotherm has a higher temperature gradient, e.g. curve *MNOP* in Fig. 7B, then the distortion of the olivine—spinel phase boundary will be upward instead of downward as shown by the dotted line in Fig. 7A. The uppermost point of the phase boundary should be *N* instead of *Q*. The temperature gradient at the coldest part of a downgoing slab is a function of several variables of which the plunging velocity is the most critical. The center temperature is low when the plate moves rapidly and high when the plate moves slowly. The distortion of the olivine—spinel phase boundary is then downward when the plate moves rapidly and upward when the plate moves slowly. The degree of distortion from upward to downward increases with plate velocity (Fig. 9), as will be discussed later. If Fig. 7 represents to some extent what may actually happen in the mantle, then there is a possibility that the cold olivine tongue may eventually reach a depth of 650 km in a fast plunging slab and olivine may eventually decompose directly into magnesiowüstite and stishovite, without going through the β- or γ-phase, provided T_{ch} for the olivine → oxides transition is not very high.

POSSIBLE CONSEQUENCES ON MANTLE DYNAMICS

At low pressure, the creep strengths of rocks exceed their (shear) rupture strength so that rocks become brittle. This forms the basis of the elastic rebound theory (Reid, 1910) in which earthquakes are proposed to be produced by sudden faulting. Creep strengths and rupture strengths of rocks both go through a minimum at the low-velocity zone and rise slowly again with depth. At the region where deep-focus earthquakes occur, the creep strengths of rocks are believed to be lower then their rupture strengths. Rocks will then creep before rupture. Shear stress is relieved so that rupture will not occur. This led Bridgeman (1945), and later Evison (1963) and Benioff (1963), to propose that high-pressure phase transformations may be an alternative mechanism for deep-focus earthquakes. Subsequently, this topic has become the subject of a hot debate (Mendiguren, 1972).

The basic requirement for a high-pressure phase transition to generate deep-focus earthquakes is that the transition rate be negligible at the earliest stages. This enables the low-pressure phase to penetrate deeply into the stability field of the high-pressure phase, and to store the implosive chemical energy. At a later stage, the transition occurs suddenly and releases the stored energy as seismic waves (Dennis and Walker, 1965). Randall (1964a, b) calculated the energy released in such a process, and concluded that the energy was more than sufficient to generate deep-focus earthquakes. Experimental evidence to support this hypothesis stems from the work of Kasahara and Tsukahara (1971),

who demonstrated that a sudden phase transition in NH_4F under pressure could generate elastic shocks directly. Ringwood (1973) also reported an example of explosive devitrification of metastable silicate glasses at room temperature.

If high-pressure transformations do generate deep-focus earthquakes, then the olivine → spinel transition is undoubtedly the most likely dominant source. Not only is olivine the most extensive phase in the upper mantle, but the olivine → spinel transition with $\Delta V/V \sim 0.8$ is one of the most intensive phase transformations taking place between the Mohorovičič discontinuity and the 650-km discontinuity, within which deep-focus earthquakes occur. We shall now explore the possible role of the olivine → spinel transition on deep-focus earthquake generation.

At the two margins of a downgoing lithosphere, the olivine → spinel transition is so rapid that deep penetration of olivine into the spinel field, which is required to generate deep-focus earthquakes, becomes impossible. However, at the cold interior of the downgoing slab, metastable olivine can penetrate very deeply into the spinel field (Fig. 7). As discussed earlier, although the olivine → spinel transition is predicted to be implosive, the rate of the transformation is controlled by the rate of elastical deformation of the wall rock at the very beginning of the transformation and by the rate of creep of the wall rock at later stages. At the onset of the olivine → spinel transition, although the fractional volume change may be small (say less then 10^{-4}), the rate of transition, and hence the rate of decrease of overpressure, is a maximum (*B* in Fig. 8). If the transition takes place simultaneously over a large volume of the slab, it seems possible that the sudden contraction may elastically deform the wall rock at such a fast rate that it generates a seismic shock. If this does occur, the first motion of seismic waves will be predominantly dilational (monopolarity). This type of radiation pattern was claimed for some deep-focus earthquakes (Evison, 1967). However, an overwhelming number of deep-focus earthquakes are consistent with a double-couple or shear dislocation model (e.g. Ritsema, 1970; Isacks and Molnar, 1971). This might appear to eliminate phase transformations as a mechanism for generating deep-focus earthquakes. However, Knopoff and Randall (1970) demonstrated that the double-couple model may not be the unique description of the quadrupole radiation pattern for deep earthquakes. Randall and Knopoff (1970) further indicated that linear dipole solutions, which are compatible with a phase transformation origin, may exist in many deep-focus earthquakes. In addition, Gilbert and Dziewonski (1975) have also pointed out the possibility of neglecting an isotropic component in the focal-mechanism solution in which the double-couple model was assumed. They also observed precursor hypocentral volume changes for two multiple event deep-focus earthquakes. Thus, the possibility that some deep-focus earthquakes are generated by sudden phase transformations cannot be eliminated.

If phase transitions do generate deep-focus earthquakes, then uniform implosions and monopolar focal solutions for deep-focus earthquakes should

not be expected because neither the transition nor the wall rock is isotropic. The collapse of wall rock will always follow a plane of weakness, and lead to further weakening upon collapse, which may develop into a plane of shear dislocation. Thus, double couple or double couple combined with single force, linear dipole, etc. will also be focal solutions for deep-focus earthquakes induced by phase transformations. Under these conditions, strong shear waves associated with deep-focus earthquakes can also be explained. A similar model has been suggested by Ringwood (1973), and is consistent with the observation of large shear waves generated by underground nuclear explosions (Toksöz et al., 1965), which are analogous to phase transformations in the mantle.

We have noted earlier that there exists a zone of mechanical instability along the tongue-shaped olivine—spinel phase boundary in a fast plunging slab (*B* and *C* in Fig. 7A). This mechanical instability is created by the close contact between the cold, highly compressed olivine above the phase boundary, and the hot, less compressed spinel at lower levels during the olivine → spinel transition. The pressure and temperature gradients between the two incompatible phases are highest at the cold center of the downgoing slab, and taper off toward the two margins. Smith and Toksöz (1972) and Toksöz et al. (1973) have calculated the shear-stress distribution in downgoing slabs. They concluded that shear stress may accumulate to as high as 500—1000 bars in the cold interior of the downgoing slab. The stress in the cold olivine near the vicinity of the high-pressure gradient will be greatly enhanced, and this will eventually lead to shear rupture of the rock and of the generation of deep-focus earthquakes. Once shear rupture occurs, local shear stress drops, but new shear stresses develop upwards and deep-focus earthquakes at higher levels ensue. The stress in the hot spinel may not build up because the creep rate is greatly promoted by high temperature. However, the creep rate can be accelerated at the vicinity of the high-pressure gradient, and a narrow zone of virtually zero friction may form due to shear melting (Griggs and Baker, 1969), to transformation superplasticity (Sammis and Dein, 1974) or to other effects. This may also produce deep-focus earthquakes of double-couple solutions. We thus propose the following processes which may contribute to the mechanism of deep earthquakes:

$$\text{PHASE TRANSFORMATION} \rightarrow \left\{\begin{array}{l}\text{VOLUME CONTRACTION} \\ \\ \text{HEATING}\end{array}\right\} \rightarrow \text{PRESSURE DROP}$$

$$\rightarrow \left\{\begin{array}{l}\text{STRESS ENHANCED IN THE COLD OLIVINE} \rightarrow \text{SHEAR RUPTURE} \\ \text{CREEP ACCELERATED IN THE HOT SPINEL} \rightarrow \text{SHEAR MELTING}\end{array}\right\} \rightarrow \text{STRESS DROP}$$

$$\rightarrow \text{DEEP EARTHQUAKES WITH FOCAL SOLUTIONS OF DOUBLE COUPLE} \pm \text{OTHER COMPONENTS}$$

We showed earlier that the distortion of the olivine—spinel phase boundary is mainly dependent on the plunging speed of the downgoing slab, and that a region of high-pressure gradient can occur at any place in the cold interior of

the downgoing slab between 300 km and 650 km. When the plunging velocity of the slab is high, both the degree of downward distortion of the olivine—spinel phase boundary and the pressure gradient will be high. If our model is correct, we should expect seismicity to decrease initially and then to increase toward the region of the maximum pressure gradient. The high seismicity upwards towards the crust above is due to the high stress associated with the interaction of the two plates at low temperatures, whereas the decreasing seismicity is due to decreasing creep strength of the rocks, and the reincreasing of the seismicity due to the increasing number of earthquakes induced by phase transformations towards the region of high-pressure gradient. Indeed, downgoing slabs in several regions do show this distribution of seismicity, e.g. Tonga—Fiji—Kermadec Plate, Kuril—Kamchatka Plate, and Japan Plate (Isacks et al., 1968). On the other hand, if the downgoing slab is moving slowly, the distortion of the olivine—spinel phase boundary will be upward instead of downward, and the pressure gradient between the two phases will be negligible. Under these conditions, we would expect the seismicity to decrease with depth and eventually terminate at some place above the distorted phase boundary (about 300 km). Examples of slabs with seismicity terminated at about 300 km are numerous (see Isacks and Molnar, 1971).

Forsyth and Uyeda (in preparation) have shown that among the possible driving forces of plates, those acting on the downgoing slab are an order of magnitude stronger than the other forces, and thus control the velocity of plate motions. Two major forces oppose one another on the downgoing slab: one is the downward pulling force, F_p, which comes from the extra density due to the cold contraction of the slab interior and thus is part of the convecting force; the other is the upward resistant force, F_r, which comes from the viscous drag of the plunging slab. The distortion of the olivine—spinel and the spinel—oxides phase boundaries will provide two additional forces, F_o and F_s, respectively, to the downgoing slab. F_o is a downward pulling force when the plunging velocity of the slab is slow to moderate and it changes to an upward resistant force (buoyant force) when the plunging velocity is high. F_s is always an upward buoyant force. F_p, F_r, and F_s will increase with the plunging velocity. F_o may increase then decrease and again increase, but with the opposite sign, with the plunging velocity. F_p, F_r, and F_o have comparable magnitudes (several kilobars when the plunging velocity is high). Because both the temperature difference between the margins and the cold interior of the slab, as well as the absolute value of dP/dT of the phase boundary, are smaller at the 650-km discontinuity than at the 400-km discontinuity, F_s turns out to be smaller than F_o when the plunging velocity of the slab is either slow or fast. F_p will concentrate on the upper portion of the downgoing slab (about 650 km depth), but F_r and F_s will concentrate on the lower portion of the downgoing slab (about 650 km depth). The center of F_o is variable, depending on the plunging velocity of the slab. The distribution of these forces along the downgoing slab as a function of plunging velocity of the slab is shown schematically in Fig. 9.

By taking into account the effect of phase transformations on plate dynamics, we picture the evolution of a downgoing slab as shown schematically in Fig. 9: At the early stage of development of a downgoing slab, the plate is driven by the convective force, F_c, which can either be in a form of so called "ridge push" due to the elevation of the mid-oceanic ridge or in a form of drag force acting on the bottom of the horizontally advected plate. At this stage, the plunging velocity of a slab is slow and the distortion of phase boundaries is small. All the forces acting on the downgoing slab, F_p, F_r, F_o, and F_s are small at this stage (*A* in Fig. 9). As the plate velocity increases, the olivine—spinel phase boundary begins to rise, while the spinel—oxides phase boundary, which has a negative P-T slope, begins to depress down. The plate is then accelerated by the total force $F_T = F_c + F_p + F_o - F_r - F_s$ (*B* in Fig. 9).

At some stage, the rising of the olivine—spinel phase boundary becomes a maximum; the accelerating force is also a maximum (*C* in Fig. 9). When the plate velocity is higher, the olivine—spinel phase boundary becomes depressed while the spinel—oxides phase boundary is further depressed (*D* in Fig. 9). F_o begins to reduce and finally change sign and also becomes a buoyant force (*E* in Fig. 9). When the plate velocity is at a maximum (*F* in Fig. 9), the depression of the two phase boundaries and thus the buoyant force is a maximum. F_r also attains its maximum value at this stage. The total driving force, F_T, is reduced to zero and the plunging velocity of the slab reaches a steady state (terminal velocity). The above simplified model thus indicates the possible role of the evolution of phase transformation in plate dynamics.

From a world-wide analysis of focal-mechanism solutions for earthquakes occurring in downgoing slabs, Isacks and Molnar (1971) have shown that usually either the compressional axes or the tensional axes are parallel to the seismic zone, that is the plunging direction of the downgoing slab. The distributions of these two types of earthquakes, down-dip compression and down-dip extension, along the downgoing slab fall, in general, into three groups: (1) earthquakes of down-dip extension which occur down to 300 km depth only; (2) earthquakes of down-dip extension which occur above 300 km and earthquakes of down-dip compression which occur below 400 km. There is a clear aseismic region separating these two seismic zones; and (3) earthquakes of down-dip compression which occur all the way down to about 700 km depth. The first group of earthquake distributions is consistent with stage B of plate evolution in Fig. 9. At this stage, relative coldness of the central part of the newly developed downgoing slab is accentuated so that the degree of upward distortion of the olivine—spinel phase boundary is moderate. Because of the rapid enhancement of the downward forces F_p and F_o, the portion of the slab below the olivine—spinel phase boundary begins to pull the portion above it and results in earthquakes of down-dip extension within the latter. The second group of earthquake distributions is consistent with stage *C* in Fig. 9. At this stage, the downward force $F_p + F_o$ is a maximum. The portion of the slab above the olivine—spinel phase boundary is again pulled from below and results in earthquakes of down-dip extension. The portion of the slab below the olivine—

spinel phase boundary is subjected to the high compressional force between F_p + F_o and F_r + F_s, and thus results in earthquakes down-dip compression. Up to this stage, the olivine → spinel transition occurs nearly at equilibrium, and the high-pressure gradient has not yet been developed. Consequently, the seismicity may not increase toward, or even occur at, the region of the olivine—spinel phase boundary. The seismicity below the olivine—spinel phase boundary may be due to the volume contraction of the spinel → oxides transition. The existence of the aseismic zone between these two types of earthquakes can also be due to the breaking off of the lower portion of the downgoing slab (Isacks and Molnar, 1971) due to the large pulling force F_o. The third group of the earthquake distributions is consistent with the stage of the plate evolution corresponding to *E* or *F* in Fig. 9. At this stage, the resistant force F_o + F_s + F_r reaches a maximum, so that the whole length of the downgoing slab is under compression, resulting in earthquakes of down-dip compression throughout its length. With the development of a high-pressure gradient in the lower transition zone (Fig. 7), seismicity which initially diminished rises again. Below a depth of about 700 km, the temperature at the center of the downgoing slab may rise sufficiently to prevent the accumulation of stress and preferential creep along a restricted plane. Therefore, deep earthquakes are eliminated below this depth. Toksöz et al. (1973) have shown that deep-focus earthquakes are localized along the cold interior of downgoing slabs. They attribute this to the low temperature at this region. The low temperature can allow either brittle fracture or accelerated creep to occur, which are necessary conditions for deep-earthquake generation. In addition, as we have shown above, it also localizes the pressures, F_p, F_o, F_s, and the high-pressure gradient at the cold interior of the downgoing slab, thereby providing the source for stress concentrations required to generate deep-focus earthquakes.

CONCLUSION

We have shown that phase transformations may play a vital role in plate dynamics. The model presented here is consistent qualitatively with geophysical observations. The concepts presented here suggest that those mantle models which neglect the dynamic effects of phase transformations should be re-evaluated. Such models include: thermal structure, thermal and electrical conductivities, gravity anomaly, and elasticity in downgoing slabs. To understand more quantitatively the role of phase transformations in plate dynamics, further experimental data are required on both the stability fields and the kinetics of high-pressure transitions for Mg-rich olivines.

ACKNOWLEDGMENTS

The authors benefited from discussions with Dr. J.W. Cahn on the kinetics of phase transformations; with Mr. M. Obata on phase diagrams; and with Mr. W.P. Chen on earthquake mechanism. We thank Dr. Peter Molnar and Dr.

K. Aki for critically reviewing the manuscript, Mr. Bruce Loeffler for helpful comments, and Ms. Roxane Regan for typing the paper. The research is supported by a grant from the National Science Foundation (grant No. EAR75-20138).

REFERENCES

Ahrens, T.J., 1972. The mineralogic distribution of iron in the upper mantle. Phys. Earth Planet. Inter., 5: 267—281.

Ahrens, T.J. and Syono, Y., 1967. Calculated mineral reactions in the earth's mantle. J. Geophys. Res., 72: 4181—4188.

Akimoto, S., 1972. The system MgO—FeO—SiO_2 at high pressures and temperatures — phase equilibria and elastic properties. Tectonophysics, 13: 161—187.

Akimoto, S. and Fujisawa, H., 1966. Olivine—spinel transition in the system Mg_2SiO_4—Fe_2SiO_4 at 800°C. Earth Planet. Sci. Let., 1: 237—240.

Akimoto, S. and Fujisawa, H., 1968. Olivine—spinel solid solution equilibria in the system Mg_2SiO_4—Fe_2SiO_4. J. Geophys. Res., 73: 1467—1479.

Akimoto, S. and Ida, Y., 1966. High-pressure synthesis of Mg_2SiO_4 spinel. Earth Planet. Sci. Let., 1: 358—359.

Akimoto, S., Fujisawa, H. and Katsura, T., 1965. The olivine—spinel transition in Fe_2SiO_4 and Ni_2SiO_4. J. Geophys. Res., 70: 1969—1977.

Akimoto, S., Komada, E. and Kushiro, I., 1967. Effect of pressure on the melting of olivine and spinel polymorph of Fe_2SiO_4. J. Geophys. Res., 72: 679—686.

Akimoto, S., Akaogi, M., Kawada, K. and Nishizawa, O., in preparation. Mineralogic distribution of iron in the upper half of the transition zone in the earth's mantle.

Benioff, H., 1963. Source wave forms of three earthquakes. Bull. Seismol. Soc. Am., 53: 893—903.

Bowen, N.L. and Anderson, O., 1914. The binary system MgO—SiO_2. Am. J. Sci., 37: 487—500.

Bridgman, P.W., 1945, Polymorphic transitions and geological phenomena. Am. J. Sci., 243A: 90—97.

Buening, D.K. and Buseck, P.R., 1973. Fe—Mg lattice diffusion in olivine. J. Geophys. Res., 78: 6852—6862.

Burns, R.G. and Sung, C.M., 1975. Kinetics of the olivine → spinel transition in downgoing lithosphere: implications to deep earthquake genesis. Trans. A.G.U., Abstr., 56: 453—454.

Cahn, J.W., 1956. The kinetics of grain boundary nucleated reactions. Acta Metall., 4: 449—459.

Christian, J.W., 1965. The Theory of Phase Transformations in Metals and Alloys. Pergamon Press, Oxford.

Dachille, F. and Roy, R., 1961. Influence of displacive-shearing stresses on the kinetics of reconstructive transformations effected by pressure in the range 1—100,000 bars. In: J.H. Boer et al. (Editors), Reactivity of Solids. Elsevier, Amsterdam, pp. 502—511.

Davis, B.L. and Adams, L.H., 1965. Kinetics of the calcite—aragonite transformation. J. Geophys. Res., 70: 433—441.

Davis, B.T.C. and England, J.L., 1964. The melting of forsterite up to 50 kilobars. J. Geophys. Res., 69: 1113—1116.

Dennis, J.G. and Walker, C.T., 1965. Earthquakes resulting from metastable phase transitions. Tectonophysics, 2: 401—407.

Evison, F., 1963. Earthquakes and faults. Bull. Seismol. Soc. Am., 53: 873—891.

Evison, F., 1967. On the occurrence of volume change at the earthquake source. Bull. Seismol. Soc. Am., 57: 9—25.

Forsyth, D. and Uyeda, S., in preparation. On the relative importance of driving forces of plate motion.

Gilbert, F. and Djiewonski, A.M., 1975. An application of normal mode theory to the retrieval of structural parameters and source mechanisms for seismic spectra. Philos. Trans. R. Soc. London, Ser. A, 278 : 187—269.

Griggs, D.T., 1972. The sinking lithosphere and the focal mechanism of deep earthquakes. In: E.C. Robertson (Editor), The Nature of The Solid Earth. McGraw-Hill, New York, pp. 361—384.

Griggs, D.T. and Baker, D.W. 1969. The origin of deep focus earthquakes. In: H. Mark and S. Fernbach (Editors), Properties of Matter under Unusual Conditions. Wiley, New York, pp. 23—41.

Isacks, B. and Molnar, P., 1971. Distribution of stresses in the descending lithosphere from a global survey of focal mechanism solutions of mantle earthquakes. Rev. Geophys. Space Phys., 9: 103—174.

Isacks, B., Oliver, J. and Sykes, L., 1968. Seismology and the new global tectonics. J. Geophys. Res., 73: 5885—5899.

Ito, K., Endo, S. and Kawai, N., 1971. Olivine—spinel transformation in a natural forsterite. Phys. Earth Planet. Inter., 4: 425—428.

Kasahara, J. and Tsukahara, H., 1971. Experimental measurements of reaction rate at the phase of nickel olivine to nickel spinel. J. Phys. Earth, 19: 79—88.

Kasahara, J., Ohno, I. and Iida, K., 1971. Generation of elastic shocks accompanied with a phase change on NH_4F. J. Phys. Earth, 19: 47—58.

Kawai, N., Endo, S. and Ito, K., 1970. Split sphere high pressure vessel and phase equilibrium relation in the system Mg_2SiO_4—Fe_2SiO_4. Phys. Earth Planet. Inter., 3: 182—185.

Knopoff, L. and Randall, M.J., 1970. The compensated linear-vector dipole: a possible mechanism for deep earthquakes. J. Geophys. Res., 75: 4957—4963.

Kumazawa, M., Sawamoto, J., Ohtani, E. and Masaki, K., 1974. Post-spinel phases of forsterite and evolution of the earth's mantle. Nature, 247: 356—358.

Mao, H.K., Takahashi, T., Bassett, W.A., Weaver, J.S. and Akimoto, S., 1969. Effect of pressure and temperature on the molar volumes of wüstite and of three $(Fe,Mg)_2SiO_4$ spinel solid solutions. J. Geophys. Res., 74: 1061—1069.

McKenzie, D.P., 1970. Temperature and potential temperature beneath island arcs. Tectonophysics, 10: 357—366.

Mendiguren, J.A., 1972. Speculations on phase changes in the earth's interior. Unpublished manuscript.

Minear, J.W. and Toksöz, M.N., 1970a. Thermal regime of a downgoing slab and new global tectonics. J. Geophys. Res., 75: 1397—1419.

Minear, J.W. and Toksöz, M.N., 1970b. Thermal regime of a downgoing slab. Tectonophysics, 10: 367—390.

Ming, L.C. and Bassett, W.A., 1975. The postspinel phases in the Mg_2SiO_4—Fe_2SiO_4 system. Science, 187: 66—68.

Nishizawa, O. and Akimoto, S., 1973. Partition of magnesium and iron between olivine and spinel, and between pyroxene and spinel. Contrib. Mineral. Petrol., 41: 217—230.

Randall, M.J., 1964a. On the mechanisms of earthquakes. Bull. Seismol. Soc. Am., 54: 1283—1289.

Randall, M.J., 1964b. Seismic energy generated by a sudden volume change. Bull. Seismol. Soc. Am., 54: 1291—1298.

Randall, M.J. and Knopoff, L., 1970. The mechanism at the focus of deep earthquakes. J. Geophys. Res., 75: 4965—4976.

Reid, H.F., 1910. The mechanism of earthquakes, the California earthquake of April 18, 1906. Report of the State Earthquake Commission, 2. Carnegie Institution of Washington, Washington, D.C.

Ringwood, A.E., 1958. The constitution of the mantle. II: Further data on the olivine—spinel transition. Geochim. Cosmochim. Acta, 15: 18—29.

Ringwood, A.E., 1972. Phase transformations and mantle dynamics. Earth Planet Sci. Lett., 14: 233—241.
Ringwood, A.E., 1973. Phase transformations and their bearing on the dynamics of the mantle. Fortschr. Mineral., 50: 113—139.
Ringwood, A.E. and Major, A., 1966. Some high-pressure transformations: synthesis of Mg_2SiO_4—Fe_2SiO_4 solid solutions. Earth Planet. Sci. Lett., 1: 241—245.
Ringwood, A.E. and Major, A., 1970. The system Mg_2SiO_4—Fe_2SiO_4 at high pressures and temperatures. Phys. Earth Planet. Inter., 3: 89—108.
Ritsema, A.R., 1970. The mechanism of mantle earthquake in relation to phase transformation process. Phys. Earth Planet. Inter., 3: 503—510.
Sammis, C.G. and Dein, J.L., 1974. On the possibility of transformal superplasticity in the earth's mantle. J. Geophys. Res., 79: 2961—2965.
Schubert, G., Yuen, D.A. and Turcotte, D., in preparation. Role of phase transitions in a dynamic mantle.
Smith, A.T. and Toksöz, M.N., 1972. Stress distribution beneath island arcs. Geophys. J.R. Astron. Soc., 29: 289—318.
Suito, K., 1972. Phase transformations of pure Mg_2SiO_4 into a spinel structure under high pressure and temperatures. J. Phys. Earth, 20: 225—243.
Sung, C.M., 1974. The kinetics of high-pressure phase transformations in the mantle: possible significance on deep earthquake generation. Proc. Geol. Soc. China, 17: 67—84.
Sung, C.M., 1975. Role of the olivine → spinel transition in plate dynamics. Trans. A.G.U., Abstr., 56: 454.
Syono, Y., Tokonami, M. and Matsui, Y., 1971. Crystal field effect on the olivine—spinel transformation. Phys. Earth Planet. Inter., 4: 347—352.
Toksöz, M.N., Harkrider, D. and Ben-Menaheem, A., 1965. Determination of source parameters by amplitude equalization of seismic waves, 2. J. Geophys. Res., 70: 907—929.
Toksöz, M.N., Minear, J.W. and Julian, B.R., 1971. Temperature field and geophysical effects of a downgoing slab. J. Geophys. Res., 76: 1113—1138.
Toksöz, M.N., Sleep, N.H. and Smith, A.T., 1973. Evolution of the downgoing lithosphere and the mechanism of deep focus earthquakes. Geophys. J.R. Astron. Soc., 35: 285—310.
Turcotte, D.L. and Schubert, G., 1971. Structure of the olivine—spinel phase boundary in the descending lithosphere. J. Geophys. Res., 76: 7980—7987.
Turcotte, D.L. and Schubert, G., 1973. Frictional heating of the descending lithosphere. J. Geophys. Res., 78: 5876—5886.